ICCEE2021 Proceedings

for zanzibar island in tanzania state up to 2100

Mostafa A. El-Manzalawy, Mohamed M. ElGohary, Maged M.AbdElnaby, Technical and environmental performance investigation of Marine Alternative fuels

Will be submitted to Journal

Amira Ahmed, Asmaa Hasan, and Khalid Al Hagla, "Active School Travel (AST): A Comprehensive Approach Towards Examining Factors Influencing Children's Travel Mode Choice in Alexandria"

Enneth Mensah, Hatem Mahmoud, Manabu Fujii, and Hassan Shokry,"Assessing the Potential of Upcycling Waste Plastics into Mechanically Strong Water-resistant Thermal Insulation Carbon Foam via Chemical Blowing Method and Low-Temperature Carbonization"

H. D. Gohoho, H. Noby, J. I. Hayashi, A. H. El-shazly, "Adsorption of Methylene Blue using Raw and Carbonized Peanut Shell".

Sondos Jehad Juneidi1, Mohamed Tarek Sorour, and Samia Ahmed Aly, "Design and Estimation of Greenhouse Gas of Wastewater Treatment Plant Types: Activated Sludge, Aerated Lagoon, and Membrane Bioreactor Using GPS-X Simulator Program: Case Study of Aqaba City (South Jordan)"

R. Mahrous, E. Giancola, A. Osman, H. Mahmoud, "Bio-receptive Facades as an Innovative Solution for Sustainable Cities: A Review on Conscious Design in Hot-Humid Climate."

M. Bahaa, D. A. Elgayar, H. A. Farag, M. F. Elkady "Adsorption of Methylene Blue Dye from Aqueous Solutions Using Low Cost and Novel Zeolite/ PES Composite from Natural Egyptian Clay"

Mahmoud Samy, and Mona G. Ibrahim, "Suspended and coated iron waste for photo-Fenton-like degradation of industrial effluents under neutral condition"

.Mahmoud M. Mansour , Mona G. Ibrahim , Manabu Fuji , Mahmoud Nasr, EJUST, Recent Applications of Flash Flood Hazard Assessment Techniques: Case Studies from Egypt and Saudi Arabia"

Hani Ezz, Mona Gamal Ibrahim , Manabu Fujii, Mahmoud Nasr, "Application of biochar synthesized from anaerobically digested rice straw for methylene blue removal""

Esraa Abdel-Gawad, Alexandria, Egypt, "Mass and heat transfer at the bottom of cylindrical stirred tank reactor and possible applications"

M.M.Elgohary, A.Banawan , M.M.Omar Alexandria, Egypt "Jack-up rigs foundation integrity using artificial intelligence

A.U. Zeid, A.H. Elshazly, M.F. Elkady, "Novel PVDF/UIO-66 Hybrid Membrane for Cation Separation in Electrodialysis System"

Ahmed Mohamed Saqr, Mona Gamal Ibrahim, Manabu Fujii, Mahmoud Nasr "Recent Applications of Simulation-Optimization Modeling Techniques for Groundwater Management and Sustainability"

Hadeer Emad Sobhy, Omar Mohamed Galal. and Hatem Mahmoud, " Benchmarking Of Outdoor Thermal Comfort"

Shinji Kudo, Xin Huang, Sakura Sakai, Kyoi Fujiki, Shusaku Asano, Jun-ichiro Hayashi, "Hydrolysis of anhydrosugars over a solid acid catalyst for saccharification of cellulose via pyrolysis"

3rd International conference of Chemical, Energy and Environmental Engineering
July 2021 Egypt Japan University of Science and Technology, Alexandria, Egypt.

Countermeasures Against Local Scouring around Bridge Piers: Embedded Sill

Ahmed A. Elsawy[1,a], Ahmed M. Abdelrazek[1,b], Magdy M. Aboelela[1,c] and M.A. Abourohiem[1,d]

[1]Irrigation Engineering and Hydraulics Dept., Faculty of Engineering, Alexandria University, Alexandria, Egypt.

[a]ahmedabdelazizelsawy@gmail.com, [b]ahmedmrazek@alexu.edu.eg, [c]magdyabo@yahoo.com, [d]mohammed.abourohiem@gmail.com

Keywords: Countermeasures, Embedded sill, Bridge piers, Local scour, Scour reduction

Abstract. Local scour at bridge piers will weaken the bed material underneath the pier's foundation, causing the entire structure to collapse. The current study focuses on using an embedded sill as a countermeasure to reduce the overall scour depth across the bridge pier. The presence of a sill embedded in the bed material reduces the scour depth by increasing stream bed resistance. An experiment is carried out to determine the effect of the sill location on the scour depth. Three models for a rectangular pier with a round nose of the same length (L = 20 cm) and different widths (b = 2,3 and 4 cm) are checked, and they are fixed in a layer of uniform distribution sand as bed material. Experiments are carried out in a horizontal flume with a clear water flow permitted to discharge between 0.2 and 0.45 Froude numbers. The study found that the embedded sill has a significant impact, particularly when placed near the pier nose, reducing the maximum scour depth by up to 50%.

Introduction

Local scour refers to the erosion of the streambed material around bridge piers, which considers a major obstacle in water streams. The interference of the pier with the coming flow creates downflow and a horseshoe vortex at the pier nose, which can remove the bed material around the pier foundation, particularly at its nose. With time, successive scour may undermine the soil below the pier base, causing failure of the bridge. Scour depth must be controlled using some countermeasures to be within the minimum values to avoid such failure. The local scour problem around bridge piers was extensively investigated in different approaches, classified as (i) scour mechanism, (ii) bridge supports arrangement. (iii) method of scour depth estimation, and (iv) local scour countermeasures. We will only present the recent investigation dealing with the scour countermeasures since the current study is interested in a new measure in such a field.

A large depth of the pier foundation is required to avoid the scour effect, which is a costly proportion. So, for safety and economy, scour depth must be controlled using some countermeasures. In recent times, efforts had been oriented towards developing methods for reducing scour depth. These methods can be grouped as direct and indirect countermeasures. Direct scour countermeasures increase the stream bed resistance using riprap, as studied by [1]. In the indirect scour countermeasures, the flow pattern around the pier nose is changed and diverts its direction to reduce the downflow and horseshoe vortex strength. Active countermeasures had been achieved using (i) sacrificial pile, (ii) collar, (iii) slots, and (iv) bed sill. Location of the sacrificial column, with a relative diameter dc/b = 1.0, at a relative distance xc/b = 2.5 upstream the pier nose, results in a reduction up to 70 % in scour depth [2]. A wider collar at lower levels causes a scour reduction of about 75 % [3] and 95 % when located at bed level -0.1 of the pier diameter [4]. An experimental study showed that using collars around multi-vents bridge piers reduces the local scour depth by 65% [5]. The effect of both angle and diameter of slots on the scour depth is experimentally studied; thus, the location of slots, at angle β

= 90, gives a maximum scour depth of about 30 % [6]. At rectangular pier groups, the installation of slots reduces the scour depth by about 92% [7]. Experimentally, the scour depth around the circular pier becomes negligible when a bed sill is placed just upstream of the pier [8].
However, the above countermeasures possess a significant reduction in the maximum scour depth, a higher cost, and great care in construction present the main disadvantages of such measures. The collar may separate from the pier due to erosion of the pier surface by the flow's interaction. The danger of choking the slot space by debris and floating materials is severe and may also reduce the strength of the pier structure. Hence, the above countermeasures cannot be considered the best scour countermeasures [9]. In the present study, an embedded sill is used to control the scour depth around a rectangular bridge pier since it processes at a low cost and more straightforward in construction.

Statement of The Problem

The present study is intended to control the local scour depth at the rectangular pier with a round nose, using a sill embedded in the bed material. The main target is to establish the best sill location, giving the minimum scour depth. Location of the sill upstream the pier nose will create a scour hole just upstream of the sill. The eroded sediments from the sill's scour hole will transport by the flow and deposit in the scour hole formed at the pier nose, which compensates part of its eroded soil, and then reduces its volume. On the other hand, the location of the sill downstream the pier nose will back up the flow upstream the sill, which reduces flow velocity and thus reduces the scour depth at the pier nose. For this purpose, an experimental study is conducted to declare the effect of sill location on the scour depth, as shown in Fig. (1).

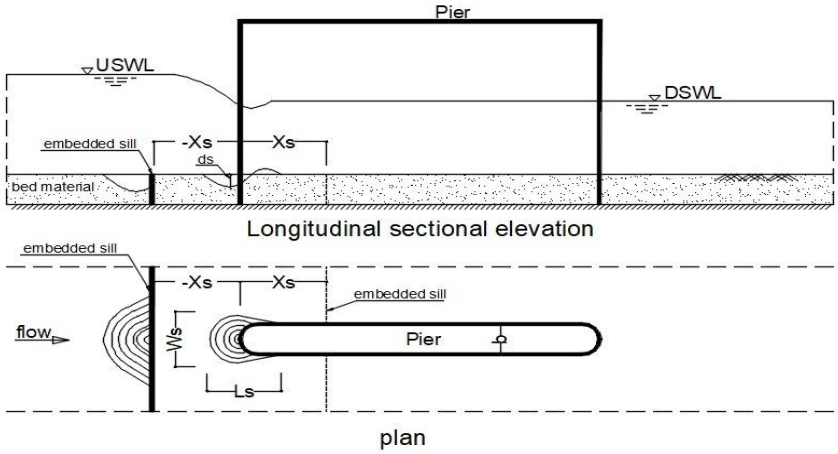

Fig (1) Effect of the embedded sill on the local scour around a rectangular pier.

Main parameters involved in the current problem

The parameters affecting the scour depth (d_s), maybe expressed as,

$$d_s = f_1(\mathrm{h, v, \rho, \mu, L, b, x_s}, d_{50}, g, \mathrm{T}), \quad (1)$$

where, (h) and (v) are depth and velocity of flow, (ρ) and (μ) are density and dynamic viscosity of water, (L) and (b) are length and thickness of pier, (x_s) is the sill location, (d_{50}) is the median diameter of sediments grains, (g) is the acceleration gravity, and (T) is the duration time.
Excluding the parameters; L and T since they kept constant throughout the experiments, and applying Buckingham theorem (π – theory), Eq. (1) becomes,

$$\frac{d_s}{b} = f_2\left(\frac{v}{\sqrt{g\,h}}, \frac{\rho\, v\, b}{\mu}, \frac{x_s}{b}, \frac{d_{50}}{b}\right). \quad (2)$$

where, $\frac{v}{\sqrt{g\,h}}$, and $\frac{\rho\, v\, b}{\mu}$ present Froude (F_n) and pier Reynolds numbers (R_n), respectively, then

$$\frac{d_s}{b} = f_3\left(F_n, R_n, \frac{x_s}{b}, \frac{b}{d_{50}}\right). \quad (3)$$

These are the main parameters that would be tested to declare the resulted effect on the scour depth, due to the existence of the embedded sill.

Experimental study

The experimental study is conducted in a horizontal flume, fabricated from fiberglass, with 5.7 m length, 0.6 m width, and 0.2 m depth, as shown in Fig. (2). Three models of coated wood for the pier are tested, having 20 cm length and height, but with different widths b =2.0, 3.0, and 4.0 cm. The sill model is a perspex plate 0.6m long, 10cm depth, and 0.6cm thick. The flume is filled with a sand layer of 10cm depth and having d_{10}= 0.23mm, d_{16}= 0.3 mm, d_{50}= 0.4 mm, d_{60}= 0.45 mm, and d_{84}= 0.6 mm. The geometric standard deviation for the grain size distribution, $\delta = d_{84}/d_{16}$= 0.2, and the uniformity coefficient $C_u = d_{60}/d_{10}$=1.96, so the soil is considered uniform distribution.

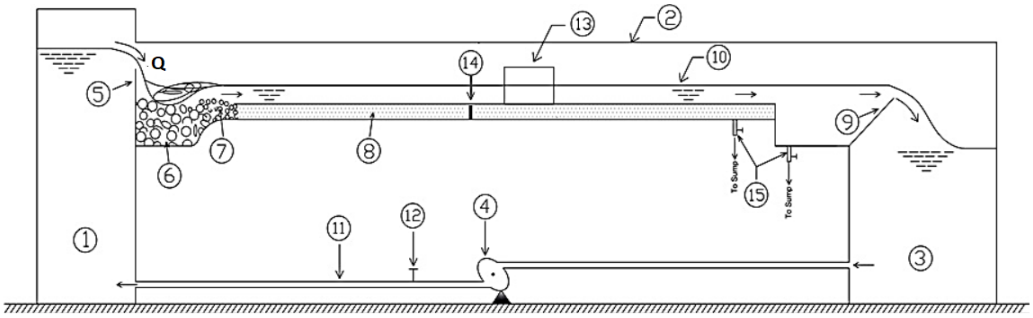

Fig. (2) The experimental set up: (1) Inlet tank (2) Working section (3) Outlet tank (4) Pump (5) Triangular weir (6) Gravel (7) Riprap (8) Sand layer (9) Tailgate (10) Water surface (11) Feeding pipe (12) Control valve (13) Pier model (14) Embedded sill model (15) Pipe drain.

The experiments were conducted considering two cases, (i) pier models fixed in the sand layer, without the embedded sill, and (ii) with the sill's existence. The embedded sill is located at relative distances upstream of the pier nose where x_s/b = -1.0, - 0.5, just at the pier nose where x_s/b = 0.0, and the downstream the pier nose where x_s/b = 0.5, and 1.0. For each location, different discharges are allowed to pass, with corresponding Froude number F_n= 0.20, 0.25, 0.30, 0.35, 0.40, and 0.45, considering a duration time T = 2.0 hours for each discharge.

Analysis and discussion of results

The analysis of the obtained results includes the effect of the main parameters, expressed by Eq. (3), on the scour depth, considering the two cases, without and with the existence of the embedded sill. Calculations showed that, effect Reynolds number (R_n), on the scour depth, not exceed 2.0 %; therefore, it will be excluded. Thus, the following analysis includes only the effect of Froude number (F_n), relative sill location (x_s/b), and the relative width of the pier($\frac{b}{d_{50}}$).

Cases without the embedded sill. The measured values of the scour depth, in such a case, are considered reference data to be used as a base of comparison with those obtained due to the existence of the sill. Referring to Eq. (3), the relative scour depth (d_{so}/b) depends on Froude number (F_n), in addition to the relative pier width (b/d_{50}). The experimental results, graphically presented in Fig. (3), in which the scour depth increases as values of F_n increase, while it decreases with increasing the

relative pier width $\frac{b}{d_{50}}$. Reduction of scour depth due to increasing the pier width is referred to that the heading up of flow, at the pier nose, is higher for larger pier widths, and then the lower velocity of flow, and lower the effect of both downflow and horseshoe vortex.

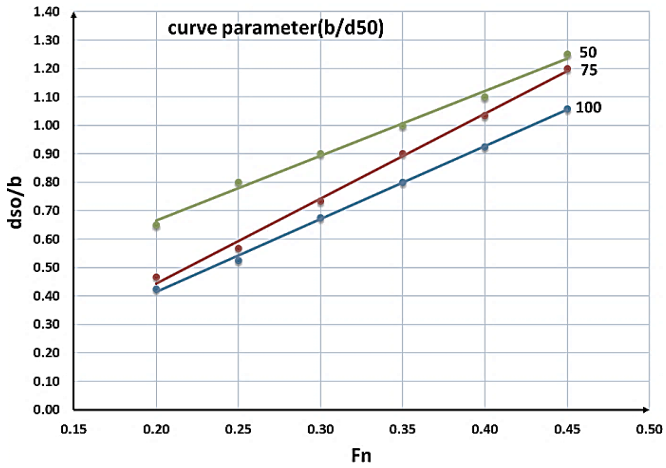

Fig. (3) Effect of Froude number and the relative width of the pier on scour depth for the case without sill.

Cases with the embedded sill. The embedded sill is located at relative distances x_s/b = -1.0, -0.5, 0.0, 0.5, and 1.0 with respect to the pier nose as mentioned above. Values of scour depth are affected by F_n, x_s/b, and b/d_{50}As shown in Fig. (4). It is seen that location of sill just at the pier nose, where $x_s/$ b = 0.0, gives the minimum scour depth, with a scour reduction ranges from 30% ~ 50% corresponding of F_n= 0.20 ~ 0.45. Figure (5) shows a comparison between the scour depth resulted when the embedded sill is located just at the pier nose and the case without sill.

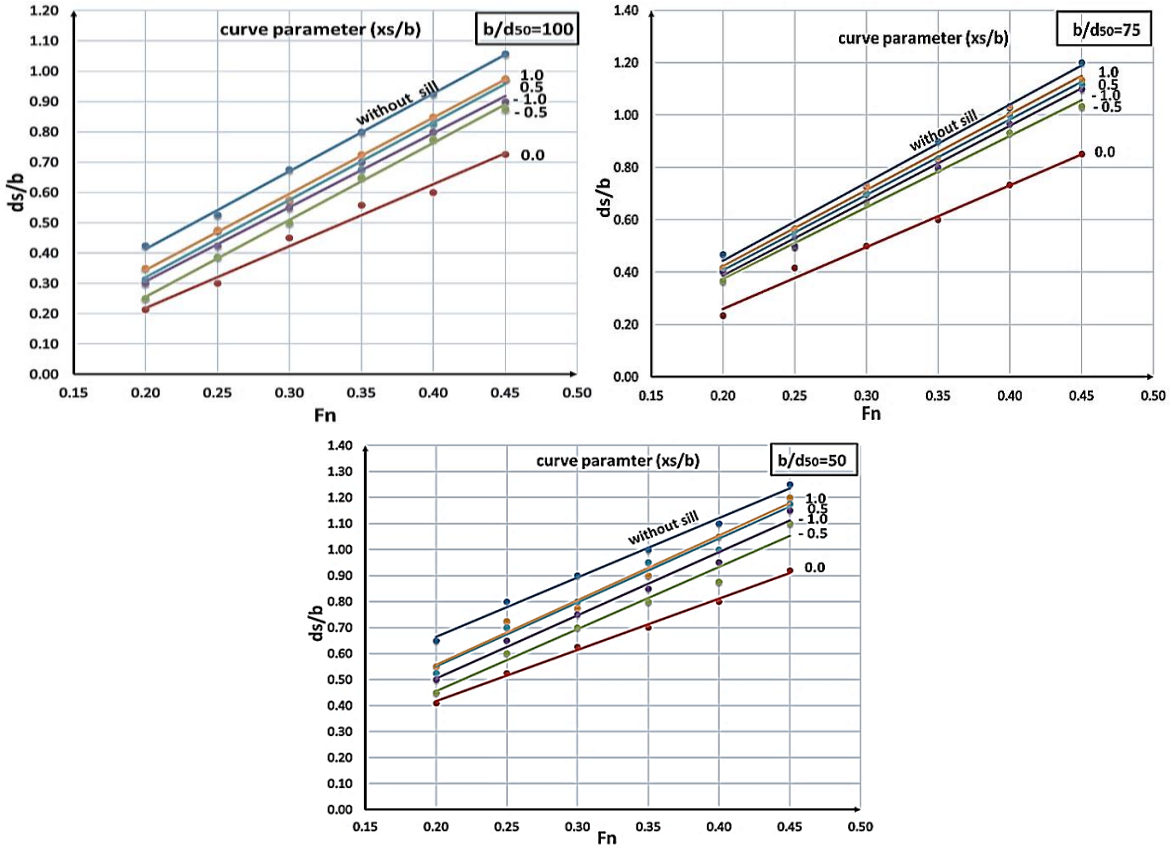

Fig.(4) Effect Fn, x_s/b and b/d_{50} on the relative scour depth (ds/b).

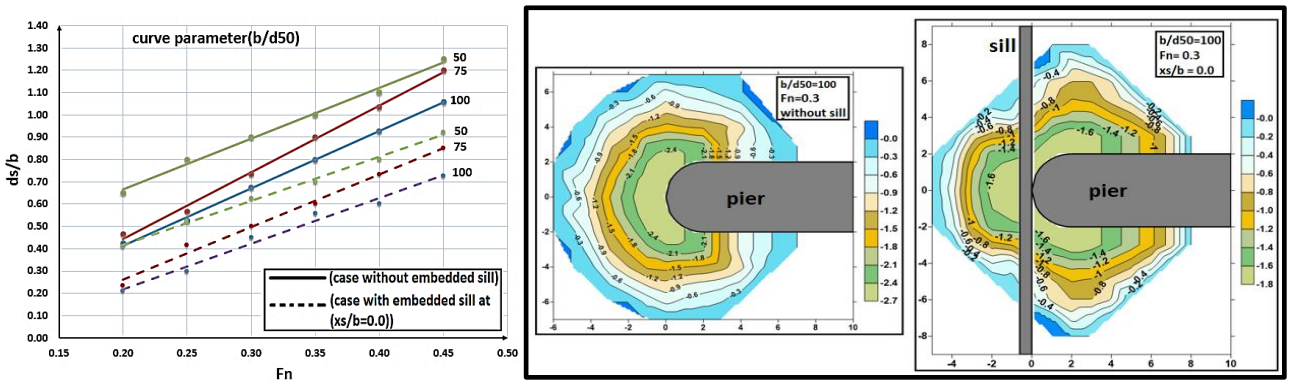

Fig (5) Comparison between values of the scour depth for cases without and with sill located at the pier nose.

Formulation of results in general equations

It's helpful to formulate the results in empirical equations to predict, in advance, the scour depth at a pier nose if an embedded sill is used as a countermeasure. Therefore, the multiple linear regression is applied to correlate the scour depth (*ds*) with the main parameters; F_n, R_n, x_s/b, and b/d_{50}. From the above analysis, it is obvious that the location of the sill upstream of the pier is the most effective since it produces lower values of scour depth. Therefore, the results obtained for the sill location downstream of the pier will be excluded throughout the regression analysis. Thus, two-thirds of the data, considering the sill's location upstream of the pier and just at its nose, are randomly chosen to develop the required Eqs. (4) and (5).

Sill location upstream the pier

$$\frac{d_s}{b} = 0.0499 + 2.4882\ (\mathrm{F_n}) - 0.1654\ \left(\frac{\mathrm{x_s}}{\mathrm{b}}\right) - 0.003842\left(\frac{\mathrm{b}}{\mathrm{d_{50}}}\right), \qquad R^2 = 97\ \% \tag{4}$$

Sill location just at the pier nose

$$\frac{d_s}{b} = 0.1672 + 2.131\ (\mathrm{F_n}) - 0.004063\left(\frac{\mathrm{b}}{\mathrm{d_{50}}}\right), \qquad R^2 = 98\ \%. \tag{5}$$

Equations (4) and (5) are checked using the remained one-third of the experimental data. Figure (6) shows a comparison between the measured values of (*ds/b*) with those obtained using Eqs. (4) and (5). It is found that an acceptable agreement is found with a maximum deviation of 15 %.

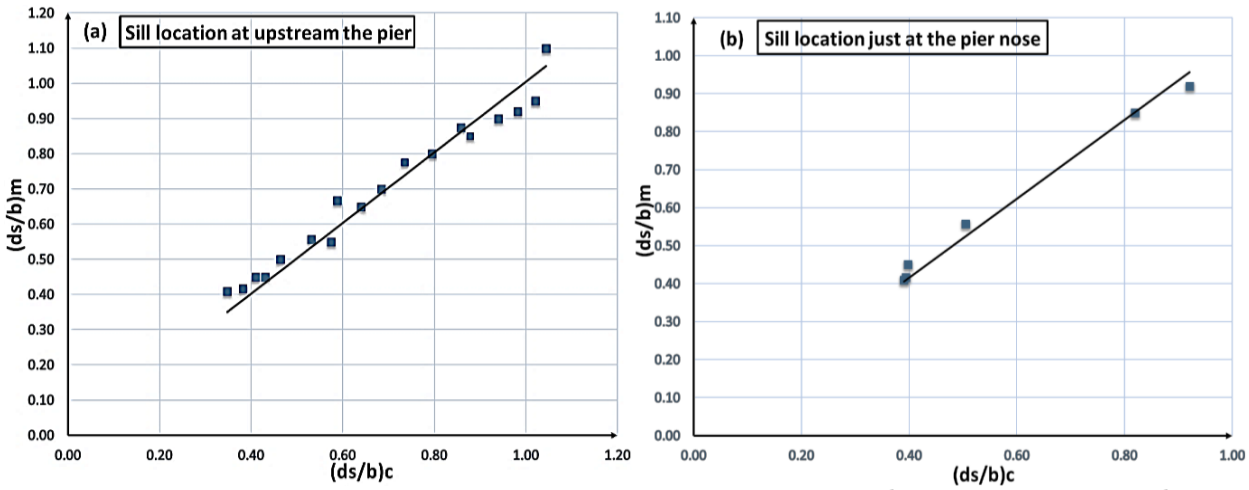

Fig. (6) Comparison between the relative scour depth, measured $(\frac{d_s}{b})_m$ and calculated $(\frac{d_s}{b})_c$.

The predicted empirical Eqs. (4) and (5) are valid within the ranges of the experimental data; $0.20 \leq F_n \leq 0.45$, $-1.0 \leq \frac{x_s}{b} \leq 0.0$, and $50 \leq \frac{b}{d_{50}} \leq 100$. The agreement between Eqs. (4) and (5) is checked by substituting for $\frac{x_s}{b} = 0.0$ in Eq. (4). The resulting values of $\frac{d_s}{b}$ are compared to those given by Eq. (5) since a maximum deviation of 10 % is found.

Conclusions

The effect of pier width, sill location, and Froude number on the scour depth at the pier nose is analyzed within the ranges of F_n = 0.20 to 0.45, and $\frac{b}{d_{50}}$ = 50 to 100. As a result, the following conclusions are obtained:

1- The scour depth is being lower for piers with a large width.
2- Compared to those obtained downstream of the pier, scour depths are smaller when sill positions upstream.
3- The location of the embedded sill, just at the pier nose, produces the minimum scour depth since it reduced by about 50 %.
4- The scour depth, for sill location upstream the pier, can be predicted using Eq. (4), while Eq. (5) is used for the location of sill just at the pier nose.
5- The highest effective parameter is the sill location, whereas F_n and $\frac{b}{d_{50}}$ are of the second and third orders, while R_n has very no influence.

References

[1] Bhalerao, A. R., & Garde, R. J., Design of Riprap for protection against scour around bridge pier. ISH Journal of Hydraulic Engineering, 16(1), (2010), 79–92.

[2] Abuflgha, B. M., Protection of Bridge Piers Against Local Scour Using Upstream column, Msc Thesis, Almergeb University, Libya, (2014).

[3] Zarrati, A. R., Gholami, H., & Mashahir, M. B., Application of collar to control scouring around rectangular bridge piers. Journal of Hydraulic Research, 42(1) (2004), 97–103.

[4] Masjedi, A., Bejestan, M. S., & Esfandi, A., Reduction of local scour at a bridge pier using collar in a 180degree flume bend. Journal of Applied Sciences, 10(2010), 124–13.

[5] Mohammed, Y. A., Saleh, Y. K., & Ali, A.-A. M., Experimental investigation of local scour around multi-vents bridge piers. Alexandria Engineering Journal, 54(2) (2015), 197–203.

[6] Abd El-Razek, M., Abd El-Motaleb, M., & Bayoumy, M., Scour reduction around bridge piers using internal openings through the pier. Alexandria Engineering Journal, 42(2) (2003), 241–248.

[7] H Saleh, H., Abozeid, G., & S Darweesh, M., REDUCTION OF LOCAL SCOUR AROUND OBLONG BRIDGE PIERS USING SLOTS. Journal of Advanced Engineering Trends, 39(1) (2020), 45–62.

[8] Razi, S., Salmasi, F., Hosseinzadeh Dalir, A., & Farsadizaeh, D., Application of Bed Sill to Control Scouring Around Cylindrical Bridge Piers. Journal of Civil Engineering and Urbanism, 2 (2011), 115–121.

[9] Beg, M., & Beg, S., Scour reduction around bridge piers: A review. International Journal of Engineering Inventions, 2(7) (2013), 7–15.

Environmental Revitalization of Neglected Urban Open Spaces (NUOS) in Community Development: School Farm Approach

Ali Fouad Bakr[1, a] , Nehad Abd EL Gawad[2,b]

[1] *Department of architecture, Faculty of Engineering, Alexandria University, Alexandria, Egypt*

[2] *Department of architecture, Faculty of Engineering, Alexandria University, Alexandria, Egypt*

[a]*alibakr@alexu.edu.eg,* [b]*nehad.abdelgawad@alexu.edu.eg*

Keywords: Neglected Urban Open Spaces (NUOS), Food Accessibility, Environmental Revitalization, School Farm (SF) &Sustainability.

Abstract

The majority of contemporary cities prefer modern urban planning schemes, creating inconsistent urban fabric and consequently generating Neglected Urban Open Spaces (NUOS). NUOS appear across cities as meaningless, abandoned, and in-developed spaces such as vacant plots, industrial sites, deteriorated waterfronts, and infrastructure leftover spaces. In mid of endless challenges; climate change, resources' scarcity, and food insecurity, developing NUOS could enhance city resilience and sustainability. The environmental revitalization of NUOS can develop urban agriculture models in form of School Farm (SF). SF is an innovative approach to improve food accessibility and security. An ultimate objective of this paper is to revitalize NUOS as a new environmental urban space by applying the SF approach through providing an inclusive strategy to understand and underpin the synergy between various forms of NUOS, the applicability of SF, and consequently leads to reimagining sustainability in urban planning. This paper discusses the complexity, various factors, and ultimate use of NUOS in urban development. A proposed model of NUOS-revitalization provides a dynamic model of SF enhancing the environmental dimension of urban development. It connects nonetheless food security and urban planning within the context of the modern city in offering a multisectoral-sustainable society of environmental, social, and economic development.

1. Introduction

City planning has been subject to many urban problems as a result of rapid urbanization, overpopulation, and economic crisis. One of these problems is the rise of the percentage of Neglected Urban Open Spaces (NUOS) within the urban fabric. These spaces have taken different forms in the city such as military sites, industrial sites, leftover space, and oversized streets. NUOS could break the continuity of the urban fabric, creating meaningless spaces, and vacant unsafe landscapes. which threaten citizens' safety, and increase economical and social, and environmental deterioration of neighborhoods.

Recently, urban developers have recognized the potentials of NUOS in creating sustainable communities in environmental, economic, and sociocultural aspects [1 ،2]. They have followed the functional, social, and environmental dimensions of urban design through the revitalization process. From the perspective of environmental revitalization, NUOS can be integrated with the urban fabric by the Urban Agriculture (UA) approach [3, 4]. This form of revitalization converts these spaces into different forms of green vegetated spaces like Community Gardens (CG) For example, CG are constructed in abandoned spaces within low-income neighborhoods to strengthen their access to healthy foods [5]. One of these vegetated spaces forms is School Farm (SF), which confronts some challenges compared to the other forms of (UA) approach. The challenges are a lack of financial resources and adequate infrastructure in schools for greening spaces [6].

Hence, the argument of this research is based on the applicability of revitalizing NUOS to create new models of SF as new resources of organic food in the urban food system, as well as to meet the need of schools. To achieve this plan, this research is methodically constructed into three main sections. Section 1: explains NUOS into the urban fabric, Section 2: examines how NUOS would be converted to active urban spaces. Finally, Section 3: presents the environmental revitalization of NUOS as SF. To conclude, NUOS could play a fundamental role in delivering sustainable SF concepts by developing new models, which act as a catalyst in community resilience. Furthermore, the hypothesized model will enrich the community with a healthy interactive environment.

2. NUOS into The Urban Fabric

The emergence of NUOS is a cumulative process, where it is synchronized with the continuous development of a city. In 1986, Roger Trancik explained the rotted causes of NUOS; The automobile, modern movement in design, urban renewal policies, and privatization of public space [7, 8]. Other causes contribute to NUOS are the lack of attractive activities & amenities within urban spaces [2], and the lack of regulations, which define the property rights or ownership [9]. NUOS are thoroughly discussed earlier conveying several perceptions and viewpoints [10, 7, 8, 5]. However, within the aimed scope, Roger (1986) has defined NUOS as spaces that are undesirable urban areas, which need to be redesigned to impact positively on surroundings [7]. These multi contributions have created confusion in investigating and classifying NUOS into the urban fabric [11, 12]. Thus, this research provides the classification of NUOS, which includes 3 main compartments: Vacant Land (VL), Social Unfamiliar Space (SUS), and Transport Infrastructure Leftover Space (TILS).

NUOS as VL involves numerous types of unutilized lots in the fringes of cities and may involve abandoned structures, which may vary between being totally or partially destroyed [5, 13]. As a result of development, VL comes in two forms: Permanent Vacant Land **(PVL)**, and Temporary Vacant Land **(TVL) TVL** involves previously developed & undeveloped land [13, 14]. The previously developed land refers to the previous activity industrial, commercial, residential been conducted, which is absent currently [15]. This VL comes with an environmental cost of contamination VL as brownfields [13], which demands more financial resources for remediation and remove the contaminates [12]. Concerning the previously undeveloped land, it refers to VL with random green growth without previous activity [11, 13]. This type exists in cities on two levels: city-scale, and neighborhood-scale according to scale, and location [11, 15]. At the city scale, this type includes three types remnant parcels, corporate reserve parcels, and VL for speculation [16]. Then, at the neighborhood scale, this type involves four types according to their locations to the surrounding buildings [12]. They are vacant corner lot, vacant block, suburban yards, and VL system [17]. Regarding Temporary Vacant Land (TVL), it refers to dual and single-use spaces at specific times, which are converted to VL eventually [14]. It includes two forms; the first relates to the building block, and the other relates to the community [8] The first form of TVL involves inactive sidewalks that have lost their environmental, and social benefits for users [8, 18]. As for, the second type related to the community scale, it involves surfaces of parking lots, which often interrupt the pedestrian connection in cities [12, 8].

As for NUOS as SUS, it discusses the scope of SUS composed of neglected paths, nodes, and green spaces, which are all defined as NUOS of the contemporary city [8, 19]. In this sense, The hierarchical structure of Boulevard St, Main ST, and arterial roads have contributed to NUOS formation by the propagation of vacant, and underutilized spaces [8, 16]. Despite, they can represent complete streets, which can strengthen the sustainability concept by applying green stormwater infrastructure of the streetscape, and buildings [12, 20]. Likewise, neighboring streets and pedestrian streets have significantly featured with blank walls, which can be revitalized as green facades to add the greening style to the neighborhoods [21].

As for, Nodes are converted to NUOS by strengthening the sense of insecurity due to the dominance of random plants [18, 7]. Other forms of nodes have emerged by the development of mobility and building regulations such as *amorphous square, and* traffic square [20] The *amorphous square is described as* an unorganized and formless space with no specific shape [8, 14]. Despite urban green spaces are expected to improve the quality of lives cities' inhabitants, they were converted to NUOS with poor management and limited maintenance [22, 2].

Finally, NUOS as a TILS describes a residual or Leftover space (LS), which are generally neglected due to the oddity of shape and location related to Transport Infrastructure (TI) [2, 12]. The location of LS varies between waterfront, and within the residential territories [18]. Furthermore, the psychical form of LS could be classified into four categories; at grade, depressed, elevated stacked, and elevated side by side [12]. Depressed LS is explained earlier as a remnant parcel-as a form of VL [2]. As for, At grade LS includes vacant sideways, which are narrow spaces compared to their length Then, Elevated LS refers to ambivalent landscapes located adjacent, along, and beneath flyovers of highway structures [11, 20].

3. From NUOS to Active Urban Spaces

With the limitless challenges of the twenty-first century, the Urban Revitalization Strategy (URS) had to be envolved simultaneously to include environmental risk management, heritage preservation, and maximizing the societal, and environmental returns [23, 4]. URS has succeeded to transform NUOS into active urban Spaces to deliver economic, social, environmental, outcomes [24, 25, 18]. From the perspective of economic revitalization, NUOS open new business chances by pumping new activities like local markets, and investment farms [12, 20]. Similarly, social revitalization develops NUOS as attractive public spaces by the innovative design of activities, and landscape [2, 12].

4. The Environmental Revitalization of NUOS as SF

Environmental revitalization is a cleanup strategy that offers a solution to improve the condition of neglected spaces [12, 26]. Hence, NUOS can be new sources of urban green lungs to provide the communities with healthy environments, and a comfortable climate [18]. These lungs would be productive green space by the UA approach as School Farm (SF) [21, 3]. SF is a significant green strategy that can develop the urban food system of communities with new sources of growing food [21, 27]. Furthermore, SF can provide the communities with a wide range of ecosystem services such as solve soil loss, create wildlife habitats, besides improving air and water quality [12, 20].

SF can serve as either Farm-To-School and/ or School Gardens to connect children with local farming [28, 29]. Farm-to-School is a program that aims at increasing the integration of fresh food from local, and regional farms into school meals [28]; including other activities of harvest festivals, field trips, and educational visits from the farmers [21, 3]. As for School Garden (SG), it refers to a wide range of farm activities according to the scale, and category of schools [6]. These gardens involve chicken coops and beehives besides green gardens and aquaculture facilities [21]. The form of SG varies from windowsill boxes, few containers in a side alley, to a full garden in unused space [12, 20]. SG aims at enhancing "learning by doing" to explore the entire food ecosystem [29, 27]. Thereafter, students capture the real-life experience of the farming industry [28].

More importantly, SF can achieve social, economic, environmental, and health outcomes [29, 15]. On the social scale, SF is a new social movement that brings various participants together; farmers, farmworkers, community residents, or students, parents, teachers, and school food staff [28, 3]. It builds a strong sense of place and ownership towards the community as well as a sense of responsibility to preserve the agricultural heritage [30]. Speaking of the economic benefits, SF can strengthen the local, and regional food economies; particularly the Farm to School program by promoting their nutritious food to schools [17, 28]. Therefore, farmers get rid of the pressures of real estate developers to sell their land for development projects [6, 27]. On the educational aspect, SF is

served as a real-life laboratory, where students gain the hands-on experience of cultivation [21]. In this sense, SF generates a student, who values agriculture as an essential part of a learning culture by engaging youth in growing, harvesting, and cooking food [28, 29]. Regarding the health benefits, SF is a chance to decrease the exposure to different diseases like diabetes, and obesity [21, 3]. Besides, SF enhances food safety by growing food based on organic fertilizer, and fewer pesticides [21, 27].

To clearly understand the environmental revitalization of NUOS as SF, the following Table 1 illustrates that by linking the following;
1. The classifications of NUOS: To includes NUOS as Vl, SUS, and TILS.
2. The two sectors of SF; Farm to School, and School Garden: investigate the different typologies of activities, which vary between growing, and holding festivals as mentioned before.
3. The scale of SF: To provide a lot of related to the built environment, and urban spaces; involving micro-scale (backyard, balcony, courtyards, wall's structure, patio pots, street verges, and green roof of buildings), mesoscale (urban farms, and farmscrapers), and macro-scale (urban food forest, and nurseries') [31].
4. The impacts associated with SF achieve a lot of benefits including; Sustainable food production, Education of students, Local food economies, Social commitment, and Urban requalification [21, 3, 21].

Classifications of NUOS				Description	Sectors of School Farms: Farm To school	Sectors of School Farms: School garden	Scale of school farm according to gardens in the urban community agriculture	Description	Impacts of constructing School farms
Vacant Land	Permanent vacant land	Previous developed	Contaminated	Natural Mining sites	Non-Used for School Farms, it's considered as a part of cultural landscape.				
				Post-industrial sites as a result of urban sprawl, they may be including abandoned building with destroyed or non-destroyed state. It's always located inside the city.		✓	Varied between Micro, Meso of School Farms related to the built environment, besides providing Macro scale of School Farms related to urban spaces.	**School Farms** by NUOS related to **the built environment**; 1. **Micro scale**: involves • ***Re-activating Rooftop*** to produce on structurally suitable and accessible green zones. • ***Use Wall Structure*** by structurally sound exterior to grow types of agricultural climbing and potted plants. 2. **Meso scale**: involves ***practicing sustainable urban agriculture in the Whole Unused Buildings*** to produce specific products under artificial and/or natural lighting. As for **School Farms** by NUOS related to **urban space;** 1. **Macro scale**: It involves constructing ***Urban Forest, and farm of Greenhouses with*** adding certain forms of gardening, and soil amendments to address the problem of contamination.	☑ Urban requalification. ☑ Education students ☑ Education students
			Non contaminated	Derelict sites involve abandoned constructions surrounded with non-used vacant land. It's always located **inside the city.**	✓	✓			☑ Sustainable food production. ☑ Local food economies. ☑ Education students
				Un-attended space, which involves natural vegetations, and eco system items. It's always located **outside the city.**	✓		Macro scale of School Farms related to urban space	**School Farms** by NUOS related to **urban space;** **1. Macro scale: involves** constructing ***Urban Food Forests*** to provide larger-scale agriculture activities ***designed to provide commercial, and educational products***, leading to resilient community.	
		Previous un developed	City scale	Vacant land with different forms; remnant parcels, corporate reserve parcels, vacant land for speculation.	✓	✓	Varied between Micro, and Macro scale of School Farms related to urban space	**School Farms** by NUOS related to **urban space;** 1. **Micro** scale: involves ***Green Ways, And Street Verges.*** 2. **Macro scale:** involves ***Urban Food Forest*** to provide larger-scale agriculture activities to ***provide commercial, and educational, and community products***, leading to resilient community.	☑ Sustainable food production. ☑ Local food economies. ☑ Education students
			District scale	Vacant land with different forms; vacant corner lot, vacant block, suburban yards, and vacant land system.		✓	Varied between Meso and Macro scale of School Farms related to urban space.	**School Farms** by NUOS related to **urban spaces;** 1. **Meso scale:** involves ***small- sized Urban Farm*** **by greening both** vacant corner lot, and vacant block. 2. **Macro scale:** involves ***medium-sized Urban Farm*** **by greening to** suburban yards, and vacant land system to provide ***Medium-scale agriculture activities designed to provide educational products, and community.*** Because of the proximity to educational institutions.	
	Temporary vacant Land	Community scale	Parking lots	Passive Parking Buildings with multi-levels.		✓	Micro scale of School Farms related to the built environment.	**School Farms** by NUOS related to **the built environment**; 1. **Micro scale**: Use ***Wall Structure*** by structurally sound exterior for growing types of agricultural climbing and potted plants to re-active parking building.	☑ Urban requalification. ☑ Education students
				Separated vacant spaces between spaces of parking cars.		✓	Micro scale of School Farms related to urban space.	**School Farms** by NUOS related to **urban spaces;** **1. Micro scale**: involves ***Green Backyards, Street Verges, or adding Patio Pots.***	
		Building scale	Sidewalks and front edges.	Passive pedestrian paths, and inactive front facades of buildings.		✓	Micro scale of School Farms related to both the built environment, and urban space.	**School Farms** by NUOS related to **the built environment**; **Micro scale: involves using** by ***Wall Structure*** structurally sound exterior to grow types of agricultural climbing and potted plants. Besides, ***Installing Wall Hangers*** as a system of specific plants in pots fastened to exterior `and connected to a constructed irrigation/feeding pipe system. **School Farms** by NUOS related to **urban space**; **1. Micro scale:** involves adding ***Patio Pots within sidewalks, or Street verges*** to grow vegetable and fruits in small pots in limited spaces.	☑ Urban requalification. ☑ Social commitment: ☑ Education students
Social Unfamiliar Space	Paths	Oversized streets " Boulevard- Main ST"		They are large scale streets with passive sidewalks, also some of these streets may include vacant land, and abandoned constructions.	✓	✓	Varied between Micro, Macro scale of School Farms related to urban space; creating complete street , besides Meso, and Micro scale of School Farms related to the built environment.	**School Farms** by NUOS related to **the built environment;** 1. **Meso scale**: involves practicing sustainable urban agriculture in ***Whole Unused Buildings*** to produce specific products under artificial and/or natural lighting.	☑ Sustainable food production ☑ Local food economies ☑ Education students
								2. **Micro scale: involves** • ***Re-activating Rooftop*** to produce on structurally suitable and accessible green zones. • ***Use Wall Structure*** by structurally sound exterior to grow types of agricultural climbing and potted plants.	☑ Urban requalification. ☑ Education students.
								School Farms by NUOS related to **urban space**; 1. **Micro scale: involves adding Patio Pots within sidewalks, or Street verges** to grow vegetable and fruits in small pots in limited spaces. 2. **Macro scale**: constructing ***Urban Forest, and Farm of Greenhouses*** to produce sustainable agricultural products.	☑ Sustainable food production ☑ Local food economies ☑ Education students
		Residential ST		They are presenting in passive sidewalks with poor frontage.		✓	Micro scale of School Farms related to the built environment, and urban space.	**School Farms** by NUOS related to **the built environment**; 1. **Micro scale**: involves • ***Re-activating Rooftop*** to produce on structurally suitable and accessible green zones. • **Use Wall Structure** by structurally sound exterior to grow types of agricultural climbing and potted plants. Besides, Installing Wall Hangers as a system of specific plants in pots fastened to exterior `and connected to a constructed irrigation/feeding pipe system.	☑ Urban requalification. ☑ Social commitment
		Pedestrian ST				✓		**School Farms** by NUOS related to **urban space**; **1. Micro scale** related to urban space: involves **adding Patio Pots within sidewalks, or Street verges** to grow vegetable and fruits in small pots in limited spaces.	
	Nodes	Amorphous square, traffic Square.		They are modern nodes, which have been converted to NUOS mainly by the poor design of landscape intervention, and the dominance of random plants.	✓	✓	Micro scale of School Farms related to urban space.	**School Farms** by NUOS related to **urban space**; 1. **Micro scale**: involves creating ***Mini-Parks*** according to the scale of nodes.	☑ Urban requalification ☑ Education students.

Continued

	Green spaces	Neighborhood urban green	Use only Neighborhood garden, which involve nonuse green spaces.	✓	✓	Meso scale of School Farms related to urban space.	**School Farms** by NUOS related to **urban space;** 1. **Meso scale:** involves medium-***sized Urban Farm*** to provide Medium-scale agriculture activities designed to provide educational products Because of the proximity to educational institutions.	
		Metropolitan urban green space	Use both city scale garden and natural reserves.			Macro scale of School Farms related to urban space.	**School Farms** by NUOS related to **urban space;** 1. **Macro scale**: involves Constructing both urban Food forest, ***Farm of Greenhouses to provide*** large-scale agriculture activities.	
Transport Infrastructure Leftover space	At Grade LS		It refers to wayside spaces, which form linear vacant space. It also includes abandoned railways spaces.	✓	✓	Varied between Meso, Macro, and Micro scale of School Farms related to urban space.	**School Farms** by NUOS related to **urban space;** 1. **Micro scale** involves using ***Wall Structure*** by structurally sound exterior to grow types of agricultural climbing and potted plants, besides ***Installing Wall Hangers*** as a system of plants in pots.	☑ Sustainable food production ☑ Local food economies ☑ Education students ☑ Urban requalification
	Elevate LS	On waterfront	It involves three forms of LS related to the location of flyover; adjacent space curtilage, and Linear space.				2. **Meso scale**: involves ***Medium-Sized Urban Farm*** to provide medium-scale agriculture activities designed to provide educational products because of the proximity to educational institutions. 3. **Macro scale** involves; Installing ***Communal Greenhouses***, ***Urban Food orest*** to produce sustainable agricultural products.	
		Between neighborhoods	It involves three forms of LS related to the location of flyover; Outside Penetrating, and Integrating with the urban form of neighborhoods	✓	✓			

Table 1 how the revitalization of NUOS can provide different forms of SF(The authors-2021)

5. Conclusion

Within the research, the environmental revitalization of NUOS presents in providing the communities with SF to enrich them with the new possibility of a sustainable food system. This approach aims to facilitate the production, accessibility, and sustainability of local food by empowering communities to tackle inequalities and limited urban capacities. It aims to curb poverty and improve food security by maximizing the utility of NUOS to produce a sustainable food system, and preserving farmland, nonetheless, to achieve economic and sociocultural gains.

The research has presented both NUOS and SF thoroughly by discussing their forms, and potentials in the communities. Regarding the synergy between SF and NUOS, SF can convert the unpleasant image of NUOS; vacant land, social unfamiliar space, and transport infrastructure leftover spaces, to a sustainable and productive space. Besides, SF can decrease the negative environmental impacts of NUOS on the community such as the impacts of contamination. Therefore, the proposed approach combines the elements of SF, classifications of NUOS, and forms of new gardens related to the scale of urban agriculture with various forms of agricultural products according to the scale of SF; green roofs, sidewalks, and grand urban forest. Thus, SF is an innovative strategy that achieves a wide range of environmental, educational, social, economic, and health benefits for the communities and individuals.zz

References

[1] J. Monclús and C. . D. Medina, "Urban Voids and 'in-between' Landscapes," in Urban Visions From Planning Culture to Landscape Urbanism, C. . D. Medina and J. Monclús, Eds., Springer International Publishing, 2018.
[2] N. E. S. Abd EL Gawad, K. S. Al-Hagla and D. M. Nassara, "Place making as an approach to revitalize Neglected Urban Open Spaces (NUOS): A case study on Rod El Farag Flyover in Shoubra, Cairo," Alexandria Engineering Journal, Volume 58, Issue 3, 2019.
[3] S. Krishnan, D. Nandwani, G. Smith and V. Kankarta, "Sustainable Urban Agriculture: A Growing Solution to Urban Food Deserts," in Organic Farming for Sustainable Agriculture, D. Nandwani, Ed., Switzerland , Springer, 2016 .
[4] Y. Egercioğlu, N. Yakıcı and T. Ertan, "Urban Decline and Revitalization Project in Izmir-Tire Historical City Center," Procedia - Social and Behavioral Sciences, 2016 .
[5] M. Pagano and A. O. Bowman, "Vacant Land in Cities: An Urban Resource," https://www.brookings.edu, Washington, DC , 2001.
[6] A. Bonannoa and S. . S. Mendis, "Too cool for farm to school? Analyzing the determinants of farm to school programming continuation," Food Policy, 2021.
[7] T. Roger, Finding lost space:Theories of Urban Design, New York : Wiley, 1986.
[8] J. Jacobs, The Death and Life of the Great American Cities., New York: Random House, 1961
[9] A. Haas and . M. Kopanyi, "Taxation of Vacant Urban Land: From Theory to Practice," international growth centre , London , 2017.

[10] K. Lynch , The image of city, Cambridge, Massachusetts, and London, England : MIT, 1960.
[11] P. Hamil and S. Lucas, "Vacant land: The new urban green?," Cities, 2013.
[12] N. E. S. Abd El Gawad , "Urban Revitalization of Neglected Urban Open Spaces (NUOS): Place making as an approach," Faculty of Engineering, Egypt, 2020.
[13] G. Kim, "The Public Value of Urban Vacant Land: Social Responses and Ecological Value," sustainability, 2016 .
[14] K. Ghotb, "Evaluation of the Lost Spaces in Karakol and Sakarya Districts of Famagusta, North Cyprus," Eastern Mediterranean University, Gazimağusa, North Cyprus, 2014.
[15] G. . ,. Newman, A. O. Bowman, R. . J. Lee and B. Kim, "A current inventory of vacant urban land in America," Journal of Urban Design, 2016 .
[16] L. Najjar and S. Ghadban, "In-between forgotten spaces in Palestinian cities: the twin cities of Ramallah and Al-Bireh as a case study," WIT Transactions on Ecology and The Environment,, 2015
[17] C. Brodsky, C. Nilon and P. Warren, "Balancing Urban Biodiversity Needs and Resident Preferences for Vacant Lot Management," Sustainability , 2018 .
[18] L. García and Esmeralda, "From Void to Opportunity," Procedia Environmental Sciences, vol. 37,2017 .
[19] J. Massengale and V. Dover, Street Design The Secret to Great Cities and Towns, Canada: John Wiley & Sons , 2014 .
[20] J. Azhar and . M. Gjerde, "Re-Thinking the role of Urban In-Between Spaces," in 50th International Conference of the Architectural Science Association , 2016 .
[21] B. . T. Izumi, K. Alaimo and M. . W. Hamm, "Farm-to-School Programs: Perspectives of School Food Service Professionals," Journal of Nutrition Education and Behavior, Volume 42, no. Issue 2, 2010.
[22] T. Maruani and I. A. Cohen, "Open space planning models: A review of approaches and methods," Landscape and Urban Planning, 2007.
[23] M. Spandou, C. Garcia and R. Macário, "Urban revitalization and Transport: local factors and," in CITTA 3rd Annual Conference on Planning Research Bringing City Form Back Into Planning , Portugal , 2010 .
[24] K. Bohn and A. Viljoen, "More space with less space: An urban design strategy," 2005.
[25] M. Ramlee, D. Omar, R. . M. Yunus and Z. Samadi, "Revitalization of Urban Public Spaces:An Overview," in Asian Conference on Environement - Behaviour Studies , Iran , 2015.
[26] R. Cybriwsky, "Changing patterns of urban public space: Observations and assessments from the Tokyo and New York metropolitan area," Cities , vol. Volume 16, no. Issue 4, 1999.
[27] M. . R. Savoie-Roskos, H. Wengreen and C. Durward, "Increasing Fruit and Vegetable Intake among Children and Youth through Gardening-Based Interventions: A Systematic Review," Journal of the Academy of Nutrition and Dietetics , vol. Volume 117 , no. Issue 2 , 2016
[28] J. . R. Hermann, S. . P. Parker, B. . J. Brown, Y. . J. Siewe, B. . A. Denney and S. . J. Walker, "After-School Gardening Improves Children's Reported Vegetable Intake and Physical Activity," The journal of Nutrition Education and Behavior, vol. Volume 38, no. Issue 3, 2006.
[29] C. . K. Berezowitz, A. B. B. Yoder and D. A. Schoeller, "School Gardens Enhance Academic Performance and Dietary Outcomes in Children," Journal of School Health,Volume 9 , issue 7 , 2015.
[30] Z. Wua, R. Chena, M. Meadowsa, D. Senguptaa and D. Xu, "Changing urban green spaces in Shanghai: trends, drivers and policy implications," Land Use Policy , 2019.
[31] L. . J. Pearson, L. Pearson and C. Pearson, "Sustainable urban agriculture: Stocktake and opportunities," 2010

Synergy between Light Pollution Control, and Concrete-Nano-Based Materials: Remodeling Urban Nightscape

Ali Fouad Bakr [1,a] **,Nehad Abd EL Gawad** [2,b]

[1] *Department of architecture, Faculty of Engineering, Alexandria University, Alexandria, Egypt*

[2] *Department of architecture, Faculty of Engineering, Alexandria University, Alexandria, Egypt*

[a]*alibakr@alexu.edu.eg,* [b]*nehad.abdelgawad@alexu.edu.eg.*

Keywords*: Light Pollution (LP), Concrete-Nano-Based Material, Light-Emitting Concrete (LEC), Pollution Control &Urban Nightscape.*

Abstract

Rapid urbanization and population growth have emphasized the exaggerated consumption of artificial light causing higher levels of carbon footprints and Light Pollution (LP), and consequently fueling up the global warming. LP is the excessive brightening of the night sky by artificial lighting for illuminating roadways, landmark buildings, and public spaces. It aims at enhancing the sense of security and enhanced visibility at night. However, LP can have far-reaching negative consequences for the human organism and the ecosystem in urban areas. Despite the debatable underuse of Concrete-Nano-Based Material, the application of Light-Emitting Concrete (LEC) enables light to be transmitted through opaque concrete, accordingly reduces building energy consumptions and ultimately solving that dilemma. Yet, still, urban designers and architects neglect the aesthetic value and the light transmittance properties of LMC. Hence, this paper aspires to remodel the city's urban nightscape by shedding the light on the applicability of LMC as a Concrete-Nano-Based Materials approach to reinforce pollution control in the city. The paper investigates that the overuse of energy-efficient bulbs usually overshadows the LP problem. By focusing on the scalability and useability of LMC, this material can be applied to the following sections; sustainable environment for construction and decoration, lighting infrastructure of roads and highways, plus the use in public open spaces; including streets, squares, and waterfronts. Hence, this research capitalizes on the synergy between LP and LMC in delivering more sustainable cities, and less light-polluted environments.

1. Introduction

Light is one of the fundamental infrastructures, which is substantially associated with urbanization growth. It plays an important role in enhancing the uniqueness of the architecture, and urban life in the cities. Therefore, electric lights have drastically reordered nightscapes across the city to be significantly brighter and more illuminated at night. Unfortunately, the nightscapes have caused Light pollution (LP) as a result of the excessive use of outdoor illumination. LP has a wide range of negative impacts on the urban environment including; human health, wildlife behavior, astronomy sciences, and climate change, and energy consumption. In other words, lighting the concrete buildings and roads requires more electricity consumption, which leads to increasing the emissions of carbon dioxide. Likewise, LP can disturb and exhaust the wild creatures by dazzling their eyes and shattering the circadian clocks. Despite, all these negative impacts, LP remains largely overlooked and unregulated compared to other pollution forms. Therefore, there is a strong need for an innovative model Lighting for LP control, besides the preceding contribution of LED lighting, and The Cut-Off Light.

In other respect, materials science, and the construction process are in continuous acceleration towards generating new innovative building materials. To end with creating a sustainable community. For this reason, a lot of materials are produced based on nanotechnology to be termed as nano-based material. Recently, a lot of architects have used this material in many architectural applications including; interior design, and façade forming. This technology could modify the chemical and

physical behavior of materials to be more adaptable for the changes of the surrounding environmental conditions. In this sense, they are featured with high-performance efficiency and low negative impacts on humans and the environment.

From the environmental perspective of the city, and the vitality of Nano-Based materials towards decreasing the percentage of LP, this paper aims to remodel the nightscape of the city based on applying light-emitting concrete (LEC) as a type of cement nano-based material to cope with pollution control and energy shortages. To achieve this aim, the paper follows the reviewing method to cover the sides of LP and the new LEC material. Hence, it is theoretically structured as follows; Section (1) gives an overall overview of the nightscape of the city, Section (2): discusses LP in the city. Then Section 3 investigates both nano-based materials especially LEC. Finally, Section 4: purposes a conceptual framework of LEC as an innovative, and complementary approach with other approaches to overcome the LP problem. To conclude that LEC can be applied in different sectors of architectural design, and urban design; especially the landscape of open spaces. Hence, the integration between LEC application and the traditional method can create sustainable and less polluted spaces.

2. Nightscapes and Light Pollution

A nightscape is a lighting-based approach for re-introducing the image of the city at night This approach is based on the concept of "City As A Scene" by converting the cityscapes into living scape with multi-sensories [1]. A nightscape approach simulates the perceptual, and visual aspects of the city [2] by reflecting various sides of the urban environment such as identity, ancientness, modernity, size, safety, and density, as well as the architectural designs [3, 4]. By investigating the illumination design in the urban environment, consists of thousands of artificial light sources, hence, the nightscape of the city is classified into 4 types [5, 6]. First, Architecture Nightscape involves lighting the building façade, and interior spaces [1]. Second, Urban Public Spaces Nightscape: involves lighting a wide range of public open spaces such as squares, gardens, streets, and parks; including the main elements of the landscape to provide a safe, and walkable environment [7, 6]. Third, Infrastructures Nightscape: aims to keep specific facilities works well during the night such as towers, bridges, tunnels, chimneys, and city gates [3]. Finally Marketing Nightscape: is a tool to send attractive messages to the public by the lightened boards of business advertisements [8].

LP is defined as the human-made environmental pollution caused by the excess use of artificial lighting [9]. In this sense, LP is wasted light, which scatters across the atmosphere leading to brightening the night sky [7, 2]. According to the International Commission on Illumination (CIE), LP results from two root causes; the focus of infrastructure planning within urban development plans [10]. Therefore, the downtown is the most light-polluted zone because of the presence of commercial activities, institutional buildings, and traffic jams [4, 2]. The other cause is the lack of social awareness among the population how the unconstrained use of electricity boosts the percentages of LP in the city [11].

LP involves three main forms; Urban Sky Glow, Light Trespass, and, Glare [12, 13]. Skyglow is a combination of reflected and refracted light, created by the over-illumination of the floodlights outside the buildings [9]. Therefore, it weakens the visibility of astronomical objects in the night sky based on light's reflection [5]. Then, Light Trespass is uncontrolled light that spills onto private property; resulting in substantial health problems for inhabitants [4]. Finally, Light Glare results from the excessive contrast between bright and dark areas in one's field of personal view [5]. It results in scattering in the eye [13]. Regarding the scope of sustainability, LP, unfortunately, creates serious physiological consequences for humans, and ecological impacts on animal and plant populations. That may end with reshaping the entire ecosystem [14, 5]. Accordingly, discussing the effects of LP concentrates on three aspects: Waste of energy and money, and wildlife & Human health issues [10, 11].

Nearly all living organisms, including human beings, have evolved under a natural rhythm of day and night. For example, about 30% of all vertebrates and more than 60% of all invertebrates worldwide are nocturnal [11, 15]. In the case that the night becomes brighter, and the light extends farther into rural areas, wild animal, and marine ecosystems cannot differentiate between day and night [5]. Hence, this creates the disturbance of the natural day, and night cycle, and physiology, including hormonal balance, as well as organism fitness, food web interactions, and biotope connectivity [5, 13]. Furthermore, LP leads to changing changes in animal behaviors, such as migration patterns, and competitive interactions [16, 17]. For example, sea turtles and birds get confused, lose their way, and often die because they cannot be guided by the moonlight during their migration [18, 17].

As for the human health issue, exposure to light can change the 24-h circadian rhythms. For example, the secretion of the hormone melatonin is a biochemical signal, which is secreted during the hours of darkness into the blood by the pineal gland in the brain [11, 15]. That causes sleep deprivation, fatigue, headaches, stress, and anxiety y [11]. Also, there are many biological effects connected with this hormone as the activation of melatonin receptors [5]. These receptors are acting as a powerful antioxidant, scavenging free radicals and thereby helping to prevent cancer cell damage and proliferation [11, 15]. Furthermore, these receptors organize the efficiency of the immune systems and protect the nuclear and mitochondrial DNA [4, 16].

Concerning the last aspect of waste of energy and money, energy specialists consider the overconsumption of electricity releases millions of tons of carbon dioxide into the atmosphere. This gas increases the climate change progress. This extreme consumption represents a costly drain for the city by the enormous use of coal [10]. For example, The International Dark-Sky Association reported that the American production of electricity approximately requires 30 million barrels of oil and 8.2 million tons of coal. That costs the country in the region $2 billion a year. Hence, it must cut down on the energy that we use, and waste, before searching for alternative energy sources [16, 15].

3. Nano Based Material and Light Pollution: Light Cement Approach

Notably, Nanotechnology is one of the most significant practical approaches that has enhanced the development of building materials for architectural and urban design–[19, 20]. This approach works on transforming the chemical and physical features of materials to improve the efficiency of their performance to be more responsive and adaptable to external and internal environmental conditions (i.e., light, temperature, etc.) [21]. To end with providing Smart Nano-Materials with low negative impacts on the human and the environment [22], such as concrete. Smart nano-based concrete can achieve a lot of goals in architectural and urban design in terms of structural, economic, aesthetic, environmental, and functional sides [23, 24].

Because the key objective of this research focuses on the environmental side to increase LP control, Light-Emitting Concrete (LEC) is selected in between the various forms of Smart Nano-Based Concrete [20, 23]. LEC is a type of smart and multifunctional concrete that possesses the ability to trap solar energy in the daytime to re-emitting it as visible light in the dark [25, 26]. This material contributes to energy conservation and the creation of a low-carbon environment [21, 20]. Furthermore, LEC enhances the aesthetical aspects of the urban environment [25].

More importantly, this paper discusses LEC as a good chance to enhancing LP control, therefore, it doesn't discuss the chemical features of LEC quantitatively. LEC has two forms according to the method of applying Nano Technology through the production process [27], as shown in Fig.1. The first form is Light Transmitting Concrete (LTC), which is produced by incorporating optical fibers into conventional concrete. The function of these fibers is to transmit and pass sunlight

through the concrete [21]. The other form is Self-Luminous Concrete, which is created by mixing luminous materials as phosphor powers with the conventional concrete [20, 22, 27].

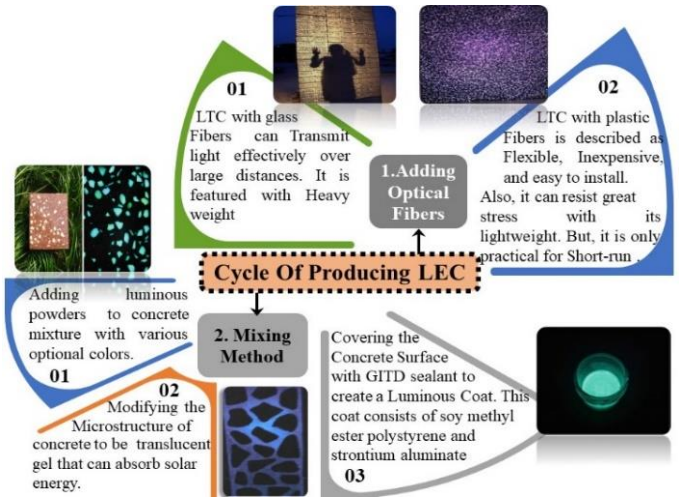

Fig1 two methods of producing LEC (The authors-2021)

4. Conceptual Proposal to Integrate Light Cement Approach Within The Nightscape

Despite, there are other technological innovations, which could contribute to increasing energy control, and reduce percentages of LP, such as luminaries with high-pressure sodium, LED lighting, and the motion sensor, as well as changing the design of light fixtures "The Cut-Off Light" [28, 12]. However, LP stills a critical environmental problem. That suppose obligation for architects, and urban designers to search for new alternatives depended mainly on sunlight. Hence, LEC can be a catalyst in remodeling the nightscape of the city.

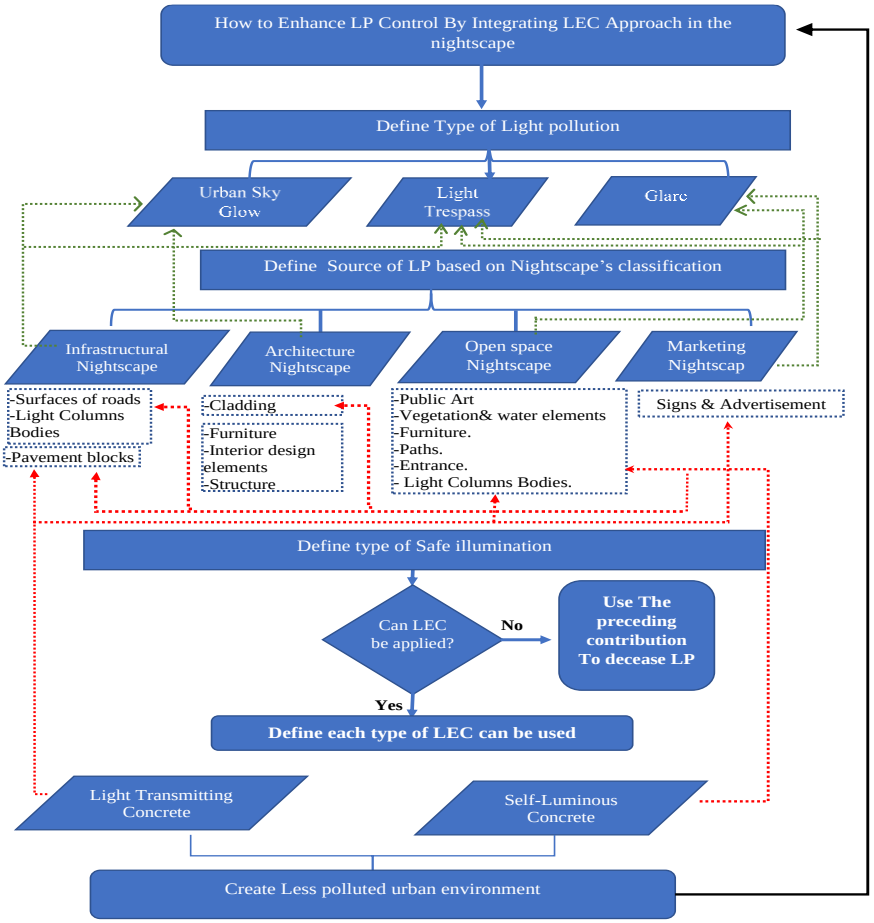

Fig 2 integrate Light Cement Approach within The Nightscape (The authors-2021)

As illustrated in Fig. 2, LEC can contribute to decreasing the percentage of LP with the other used approaches within the three classifications of nightscape as mentioned before. The objective of LEC represents in converting the elements of each nightscape into batteries that store solar light during daylight hours and discharge at night. Hence, this application of LEC as a non-biased material approach depends on the determination of the type of LEC including; Light Transmitting Concrete and Self-Luminous Concrete that will be added to the selected elements of the nightscape. For example, Self-Luminous Concrete can remodel all elements of Open space Nightscape and Infrastructural Nightscape. Also, it can remodel cladding elements of Architecture Nightscape such as facades. Therefore, lighting design should be integrated with the architectural design process.

5. Conclusion

This research reviews the problem of Light Pollution in the nightscape of the city, and how it can cause harm to human health, and disrupt the ecological and socio-economic aspects of the cities. Consequently, managing darkness should be an integral part of planning the urban areas in the city. Hence, this paper sheds light on the significance of nano-based materials; especially Light Emitting concrete as a safe and sustainable approach for the nightscape of the city to manage light pollution. by reviewing this material, its application can reinforce the concept of sustainability in architecture, and urban design by reducing energy consumption, and enhance pollution control. Therefore, the two types of Light Emitting concrete can remodel the three classifications of nightscapes related to architecture, infrastructure spaces, open public urban open spaces, and marketing services. Thus, this applicability of the Light Emitting concrete approach can integrate with other approaches in overcoming the Light Pollution problem. To end with providing less polluted, and sustainable environment. Hence, future researches should embrace the quantitative methodology to analyze Light Emitting concrete based on tests, and programs.

References

[1] M. . A. Tzimopoulou and A. Bourlidou, "Urban Landscape Architecture in the Reshaping of the Contemporary Cityscape," in IOP Conf. Series: Materials Science and Engineering, 2017.
[2] A. Radicchi and D. Henckel, "Combined Sound-& Lightwalks. A perception based method to analyze and evaluate the sonic and light environment of our cities at night," in Euronoise, Heraklion, Greece, 2018 .
[3] F. . S. Abdelbaky , "Cityscape as an Inspiration for Contemporary Painting," in The International Conference : Cities' Identity Through Architecture and Arts (CITAA) , 2017 .
[4] C. Calleri, A. Astolfi, A. Pellegrino, F. Aletta, L. Shtrepi, E. Bo, M. D. Stefano and P. Orecchia, "The Effect of Soundscapes and Lightscapes on the Perception of Safety and Social Presence Analyzed in a Laboratory Experiment," sustainability , 2019 .
[5] D. Casciani, The Human and Social Dimension of Urban Lightscapes, Switzerland: Springer, 2020 .
[6] G. Dobler, M. Ghandehari, S. . E. Koonin, R. Nazari, A. Patrinos, M. . S. Sharm, A. Tafvizi, H. T. Vo and J. . S. Wurtele, "Dynamics of the urban lightscape," Information Systems, no. Article In Press , 2015.
[7] F. Falchia, P. Cinzano, C. . D. Elvidge, D. . M. Keith and A. Haimd, "Limiting the impact of light pollution on human health, environment and stellar visibility," Journal of Environmental Management, 2011.
[8] J. . D. Hale, G. Davies, A. . J. Fairbrass, T. . J. Matthews, C. D. F. Rogers and J. P. Sadler, "Mapping Lightscapes: Spatial Patterning of Artificial Lighting in an Urban Landscape," plosone , 2013 .
[9] A. Jechow, C. C. Kyba and F. Hölker, "Mapping the brightness and color of urban to rural skyglow with all-sky photometry," Journal of Quantitative Spectroscopy & Radiative Transfer , 2020
[10] T. Ma , "Multi-Level Relationships between Satellite-Derived Nighttime Lighting Signals and Social Media–Derived Human Population Dynamics," Remote Sens , 2018 .
[11] A. Łopuszyńska, "Reducing the light pollution in settlement units areas – comparative case studies," in E3S Web of Conferences , 2018.
[12] P. Tabaka and P. Rozga, "Influence of a Light Source Installed in a Luminaire of Opal Sphere Type on the Effect Of Light Pollution," energies, 2020 .
[13] K. M. Z. ´. Dabkowska, K. Xavia and K. Bobkowska, "Assessment of Citizens' Actions against Light Pollution with Guidelines for Future Initiatives," Sustainability, 2020 .
[14] A. F. Bakr, E. Diab and D. Saadallah, "Inefficient Lighting Solutions: step-by-step Geographic information system (GIS) Technique," in The 3rd international conference of the Arab Society for Computer Aided Architectural Design (ASCAAD) , Alexandria, Egypt, 2007.

[15] R. . G. Stevens and Y. Zhu, "Electric light, particularly at night, disrupts human circadian rhythmicity: is that a problem?," Philosophical Transactions B, 2015 .
[16] T. Longcore and C. Rich, "Ecological light pollution," Frontiers in Ecology and the Environment, 2004 .
[17] B. Mizon, Light Pollution: Responses and Remedies, Second Edition ed., Wimborne, UK: Springer , 2012.
[18] A. E. Schirmer, C. Gallemore, T. Liu, S. Magle, E. DiNello, H. Ahmed and T. Gilday , "Mapping behaviorally relevant light pollution levels to improve urban habitat planning," Scientific Reports, 2019.
[19] B. Konarzewska, "Smart Materials in Architecture: Useful Tools with Practical Applications or Fascinating Inventions for Experimental Design?," in Materials Science and Engineering , 2017 .
[20 N. Al-Kurdi, D. Abdel-Aziz and A. Alshboul, "The Impact of Using Light Transmitting Concrete on Energy Saving in Office," Research Journal of Applied Sciences, Engineering and Technology, 2014 .
[21] M. Addington and D. Schodek, Smart Materials and New Technologies, London : Architectural Press, 2005.
[22] M. M. Alobeidi and A. . A. Alsarraf, "The Impact of the use of Smart Materials on the Facades of Contemporary Buildings," International Journal of Engineering & Technology , 2018
[23] R. . A. Ali and O. H. Kharofa, "The impact of nanomaterials on sustainable architectural applications smart concrete as a model," Materials Today: Proceedings , 2021 .
[24] B. Han, L. Zhang and J. Ou, Smart and Multifunctional Concrete Toward Sustainable Infrastructures, B. Han, L. Zhang and J. Ou, Eds., Singapore : Springer , 2017 .
[25 S. M. Chiew, I. . S. Ibrahim, M. A. M. Ariffin, H. S. Lee and J. . K. Singh, "Development and properties of light-transmitting concrete (LTC) e A review," Journal of Cleaner Production, 2020 .
[26] H. Barghlame and H. . H. Gavgani, "Light emitting concrete composition and method of synthesizing light emitting concrete structure". United States Patent US 9 , 777 , 212 B2 , 2017 .
[27] N. Baig, I. Kammakakam and W. Falath, "Nanomaterials: a review of synthesis methods, properties, recent progress, and challenges," Materials Advances , 2021.
[28] A. Łopuszyńska, "Reducing the light pollution in settlement units areas – comparative case studies," in E3S Web of Conferences, 2018.

Energy analysis for an integrated solar-powered adsorption-based cogeneration system

Ahmed A. Hassan[1, a], Ahmed E. Elwardany[1,b] , Shinichi Ookawara[1,2,c], Ibrahim I. El-Sharkawy[1,d]

[1]Energy Resources Engineering Department, Egypt-Japan University of Science and Technology (E-JUST), New Borg El-Arab City, Alexandria 21934, Egypt.
[2]Department of Chemical Science and Engineering, Tokyo Institute of Technology, Tokyo 152-8552, Japan.
[a]ahmed.hassan@ejust.edu.eg, [b]ahmed.elwardany@ejust.edu.eg, [c]ookawara.s.aa@m.titech.ac.jp, [d]ibrahim.elsharkawy@ejust.edu.eg

Keywords: Adsorption chiller, Cogeneration system, Flat plate collectors, PVT collectors, Organic Rankine cycle (ORC).

Abstract. Global warming is a major life-threatening problem in many countries worldwide. Extensive carbon dioxide emissions associated with various separate generation systems for different human needs such as electricity, cooling are of the main contributors to the problem. One major solution is to utilize integrated multigeneration system to increase efficiency and reduce emissions. Additionally, driving these systems with renewable energy sources such as solar and wind energy represents ultimate solution to substantially reduce the associated carbon emissions. In this paper, theoretical performance investigation of a cogeneration system intended to provide cooling and electricity for a building in Alexandria, Egypt is performed. The system comprises commercially-available solar collectors for electricity generation and solar thermal energy capture, silica gel/water pair-based adsorption chiller for cooling production, and organic Rankine cycle (ORC) employing R134a as a refrigerant and driven by hot water exiting adsorption bed during desorption process. A novel hybrid solar collector configuration, composed of photovoltaic/thermal (PVT) collectors and flat plate thermal (FPT) collectors linked together in a parallel configuration, is used for this study. The generated electricity by PVT collectors and ORC is used for building needs or supplied to the grid. MATLAB software is used to simulate the developed mathematical model of the system under the climate conditions of Alexandria during summer months. The results of the current investigation show that the best cooling performance is during July with maximum and average cooling capacity of about 9 and 6.45 kW, respectively. ORC generates about 7.09 kWh/day during summer months and it has an efficiency of about 5.6%. PVT collectors generates about 44.56 kWh/day electric energy during the month of July.

Introduction

Global warming is a major life-threatening problem in many countries worldwide. The increasing massive quantities of carbon dioxide emissions and other high global warming potential (GWP) gases is engraving the problem. Conventional separate production systems that provide the human needs of electricity and cooling are considered one of the top contributors of harmful emissions. One solution that started to gain attention in the last two decades are using cogeneration and multigeneration system, which help increase overall system efficiency and reduce associated emissions. Furthermore, driving these integrated system with renewable energy resources such as solar energy represent a major solution to emissions problem [1,2]. Egypt has a great potential in utilizing solar energy as it is considered one of the sunbelt countries with abundant solar radiation and long sunny hours for most of the year.

Photovoltaic/thermal (PVT) solar collectors are hybrid type that is developed to generate electricity similar to conventional photovoltaic (PV) collectors, and capture solar thermal energy but at lower efficiency compared to conventional thermal collectors such as flat plate thermal collectors (FPT)

and evacuated tube collectors. However, PVT usually has better overall efficiency compared to conventional collectors. That is why researchers studied PVT collectors in order to increase their performance and efficiency in electricity and heat production [3].
Thermally-driven chillers such as adsorption chillers have the advantages of using natural refrigerants with no negative effect on the environment such as water, and can be driven by solar energy or waste heat. Additionally, adsorption chillers can be driven with a temperature as low as 50℃, have long lifetime, require minimal maintenance because they have almost no moving parts, and do not encounter crystallization or corrosion problems compared to other thermally-driven chillers such as absorption chiller [1,4]. However, the main drawbacks of these systems are their relatively low COP and bulkiness due to the limitation of sorption capacity of adsorbent material and the low heat transfer rate inside adsorber/desorber reactors. Many researchers investigated theoretically and experimentally how to improve the performance of adsorption chillers and reduce its footprint []. Additionally, Researchers studied extensively many adsorbent/adsorbate pairs to be employed in adsorption chillers to enhance its performance [5].
Organic Rankine cycle are similar to conventional Rankine cycle that is used in steam power plant. However, the working fluid used is organic fluid such as R134a, R290, butane and R245a etc. Thus, it can be driven by low-grade temperature source unlike steam cycle that is driven by high temperature sources only. Consequently, ORC is used to generate electricity from waste heat or solar energy, and many researchers employ them into multigeneration systems [6].
In this paper, theoretical performance investigation of a cogeneration system intended to provide cooling and electricity for a building in Alexandria, Egypt (31.2°N, 31.23°E) is performed during summer months. The system comprises a novel solar collector configuration composed of commercially-available solar collectors for electricity generation and solar thermal energy capture, silica gel/water pair-based adsorption chiller for cooling production, and organic Rankine cycle (ORC) employing R134a as a refrigerant. The adsorption chiller is driven by hot water in the storage tank, and the hot water exiting adsorption bed during desorption process is driving the ORC evaporator. A novel hybrid solar collector configuration, composed of photovoltaic/thermal (PVT) collectors and flat plate thermal collectors (FPT) linked together in a parallel configuration, is used for this study. The generated electricity by PVT collectors and ORC is used for building needs or supplied to the grid.

System description
Schematic of the proposed cogeneration system is illustrated in Fig. 1.

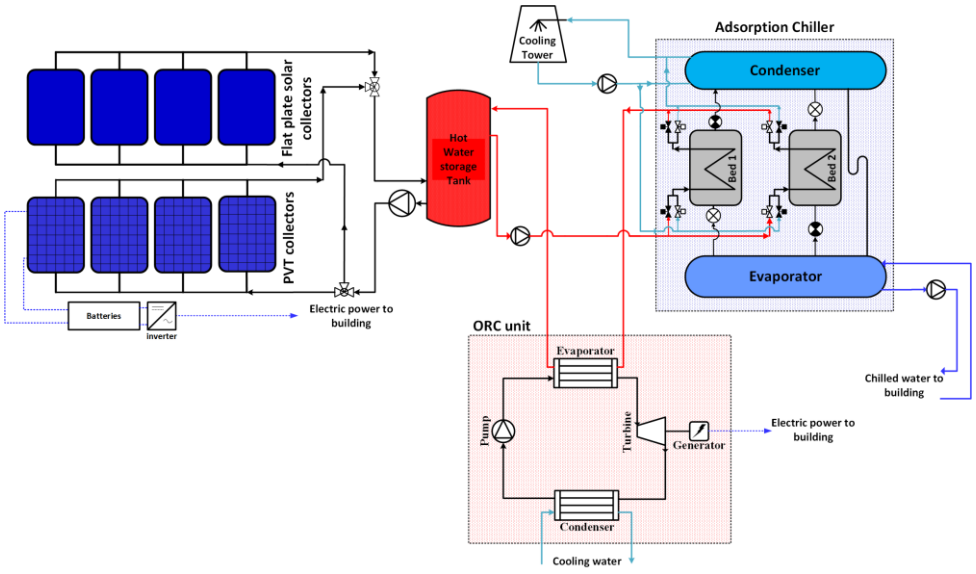

Figure 3: Schematic of the proposed cogeneration system

The novel solar collector configuration comprises two groups of commercial collectors available on the market. The first one is the PVT collectors made by FOTOTHERM company in Italy, while the other group is flat plate thermal solar collectors FPT made by Apricus Company in USA. The two commercial collectors used in the investigation are tested and certified by many certification agencies in Europe and North America such as Solar Keymark and Solar Rating & Certification Corporation (SRCC). The specifications of both collectors used in the investigation are illustrated in Table 1.

Table 1. Specifications of the solar collectors used in the study [7,8].

Criteria	PVT collector	FPT collector
Model	FT300AL	FPC-A32
Manufacturer	FOTOTHERM, Italy	Apricus, USA
Number of collectors used	20	20
Aperture area (A_{sc})	1.58 m^2	2.8 m^2
Optical efficiency (η_0)	58.3%	75.5%
Heat loss Coefficient (a_1)	6.08 $Wm^{-2}k^{-1}$	3.738 $Wm^{-2}k^{-1}$
Heat loss Coefficient (a_2)	0.0 $Wm^{-2}k^{-2}$	0.007 $Wm^{-2}k^{-2}$
Nominal electrical efficiency (η_n)	18.3%	---
Power temperature Coefficient (β)	-0.4%	---

The adsorption chiller used in the current investigation for cooling production is a single effect, double-bed chiller, which employs silica gel/water as the working pair. The specifications of the utilized adsorption chiller and silica gel/water pair used can be found in El-Sharkawy et. al [9].
The hot water storage tank is a 1.25 m^3 capacity made by a German company named Solarfocus. The tank employs a hard polyurethane thermal insulation to reduce the thermal losses to the environment. The ORC unit that employs R134a as a refrigerant is used to generate more electricity from the captured solar thermal energy and increase overall system efficiency. ORC evaporator is driven by the hot water exiting the adsorption beds during desorption process. Turbine and pump efficiencies are assumed to be 85%. The refrigerant pump inlet condition is assumed to be saturated liquid, while at the evaporator exit is saturated vapor. Furthermore, refrigerant flow through the evaporator and condenser is assumed isobaric. The operating parameters of the ORC are shown in Table 2.

Table 2. Operating parameters of the ORC used in the present study.

Criteria	Value
Evaporator pressure	17 bar
Condenser pressure	9 bar
Minimum operational hot water Temperature ($T_{hw,min}$)	66°C
Refrigerant mass flow rate ($\dot{m}_R$)	0.16 kg/s
Turbine efficiency ($\eta_{ORC,Tur}$)	85%
Pump efficiency ($\eta_{ORC,pump}$)	85%
ORC evaporator efficiency ($\eta_{ORC,evap}$)	95%

Mathematical Model

Energy balance method is used to model thermal performance of both PVT and FPT solar collectors. The PVT collector can be modeled as a conventional solar thermal collector with its absorber covered by the PV layer. The following assumptions are made for the PVT collectors to provide sufficiently accurate description of the thermal efficiency of the PVT collectors and simplify the model [10]: I) The absorber surface and the PV layer are at thermal equilibrium, II) one-dimensional heat transfer.

The thermal efficiency $\eta_{th,sc}$ of the FPT and PVT solar collectors can be calculated based on the incident solar radiation (G_t), ambient temperature (T_{amb}) and the average solar collector heat transfer fluid temperature ($\bar{T}_{hw}$), which here is water, as in Eq. 1.

$$\eta_{th} = \eta_0 - a_1\left(\frac{\bar{T}_{hw}-T_{amb}}{G_t}\right) - a_2\left(\frac{(\bar{T}_{hw}-T_{amb})^2}{G_t}\right) \quad (1)$$

Electrical efficiency of the PVT collectors is calculated by Eq. 2 to estimate their electric performance as follows:

$$\eta_{elec} = \frac{P_{elec}}{G_t \,.\, A_{sc}} \quad (2)$$

where P_{elec} is the generated electrical power by the PVT collectors. It is worth noting that the PVT collectors manufacturers provide the values of η_{elec} at the standard testing conditions (STC), in which the G_t is 1000 W/m^2 and a reference PV cell temperature T_{ref} is 25℃. However, these conditions are changing continuously throughout any operational day. Therefore, Eq. 3 is used to get the value of η_{elec} at different G_t and PV cell temperature T_{sc}.

$$\eta_{elec} = \eta_n + \beta(T_{sc} - 25℃) \quad (3)$$

The energy balance equations of the solar collectors and the hot water storage tank are taken as presented by El-Sharkawy et. al [9] and are used to estimate the temperatures of the solar collector and hot water in the storage tank.
All the equations regarding the simulation of the dynamic performance of the silica gel/water pair adsorption equilibrium and kinetics in addition to constants required can be found in []. Additionally, all the energy balance equations of the evaporator, condenser and the two adsorption beds of the adsorption chiller are also taken as in [9].
Adsorption chiller performance parameters such as the average cyclic cooling capacity ($\dot{Q}_c$) and coefficient of performance (COP_c) are calculated by Eqs. 4 and 5.

$$\dot{Q}_c = \frac{\int_{t_{0,c}}^{t_{f,c}} (\dot{m}\, C_p\, (T_{in}-T_{out})\, dt)_{chill}}{\int_{t_{0,c}}^{t_{f,c}} dt} \quad (4)$$

$$COP_c = \frac{\int_{t_{0,c}}^{t_{f,c}} (\dot{m}\, C_p\, (T_{in}-T_{out})\, dt)_{chill}}{\int_{t_{0,c}}^{t_{f,c}} (\dot{m}\, C_p\, (T_{in}-T_{out})\, dt)_{hw}} \quad (5)$$

Where t_0, c and $t_{f,c}$ is cycle starting and finishing times, respectively.
CoolProp open source library is used to define the thermal properties of R134a refrigerant in MATLAB software. Energy balance of the ORC evaporator is used to estimate the hot water exit temperature as in Eq. 6. The net power generated by the ORC and its efficiency is calculated by Eqs. 7 and 8.

$$\dot{Q}_{in,ORC} = \dot{m}_{R134a}\Delta h_{ORC,Evap} = \dot{m}_{hw} C_p (T_{hw,in} - T_{hw,out})\eta_{ORC,evap} \quad (6)$$

$$\dot{W}_{net,ORC} = \dot{W}_{Tur,ORC} - \dot{W}_{pump,ORC} \quad (7)$$

$$\eta_{ORC} = \frac{\dot{W}_{net,ORC}}{\dot{Q}_{in,ORC}} \quad (8)$$

Results

Climate conditions

The climate conditions at building location in Alexandria (31.2°N, 31.23°E) during the summer months for solar collector tilted by 30° are estimated using Meteonorm software. Figure 2 shows the total solar radiation and the ambient temperature for the three months of summer for Alexandria.

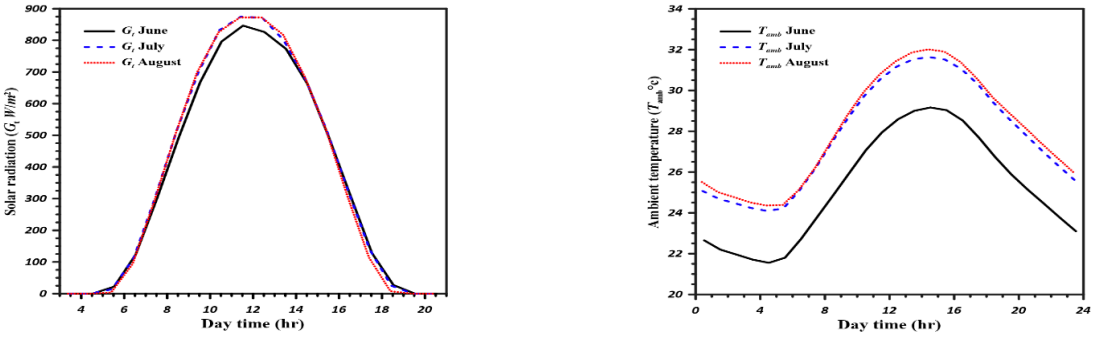

(a) (b)

Figure 2. (a) Solar radiation during summer months, (b) Ambient temperature during summer months

ORC performance

ORC has been adjusted to start operation when the hot water temperature reaches 66℃ with respect to the chosen evaporator pressure. ORC generates a net power $\dot{W}_{net,ORC}$ of about 1.58 kW between 11:00 AM to about 15:15 PM, at which the temperature of the hot water in the tank becomes lower than 66℃. Additionally, the ORC has an efficiency of about 5.6 % which is expectedly low due to lower driving temperature. Figs. 4a and 4b illustrates the generated power by ORC in a typical day in July, and the generated electric energy during summer months, respectively.

PVT electric performance

Figure 4a illustrates the electric power generated by PVT collectors, ORC and the total electric power in the month of July, while Fig. 4b shows the electric energy generated in a typical day during the three months of summer.

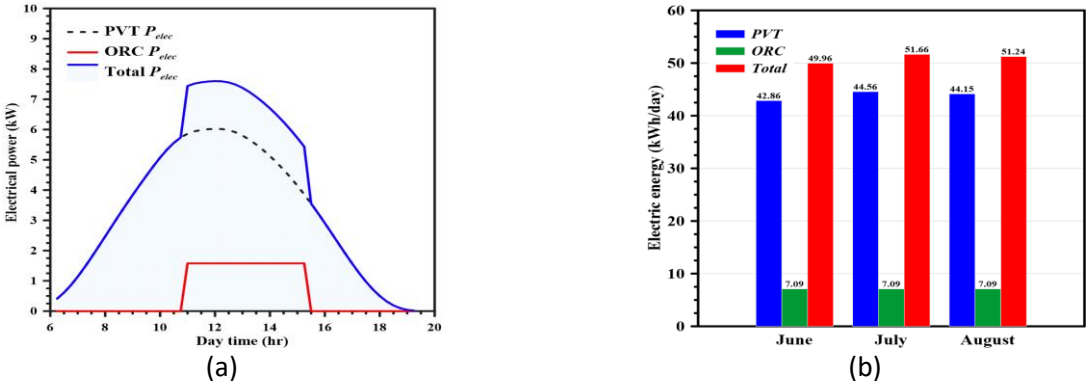

(a) (b)

Figure 4. (a) Generated electric power during a typical day in July, (b) Generated electric energy in a typical day during summer months

The month of July has the highest PVT and total electric power production of 44.56 and 51.66 kWh/day, respectively as shown in Fig. 4b. This is because it has almost the same solar radiation as the month of August while having less ambient temperature which help reducing the temperature of the PV modules in the PVT collectors and thus increasing the electric power generation.

Adsorption chiller performance

Figure 3a shows the $\dot{Q}_c$ and COP_c in a typical day during the month of July, while Fig. 3b illustrates the maximum and average values of the $\dot{Q}_c$ during the three months of summer, and Fig. 3c show the maximum and average values of the COP_c during summer months.

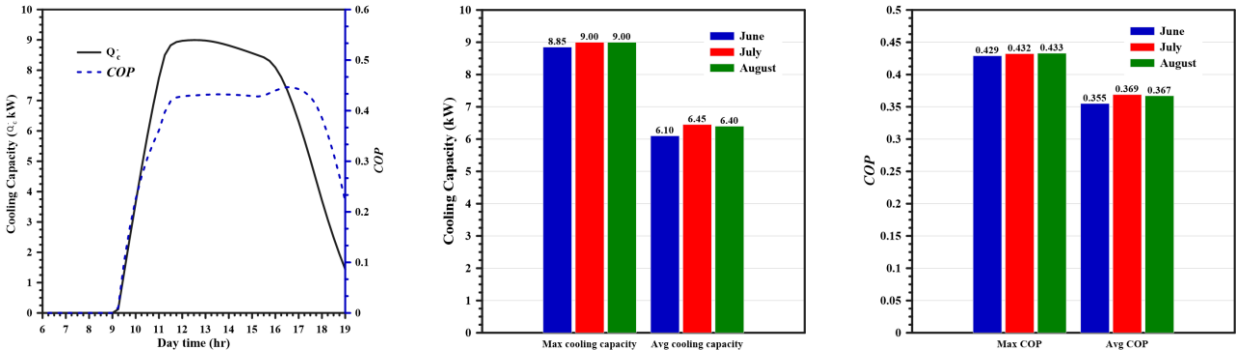

Figure 3. (a) $\dot{Q}_c$ and *COPc* in a typical day during the month of July, (b) Maximum and Average $\dot{Q}_c$ during summer months, (c) Maximum and Average COPc during summer months.

As shown in Fig. 3a, the cooling production starts at about 9:00 AM when the temperature in the hot water storage tank become high enough to drive the silica gel beds at about 52°C. Then, the cooling capacity starts to increase gradually as the temperature of the hot water increases in the tank, until it reaches its maximum value of 9 kW at about 11:00 PM, before it start to decrease due to the starting of the operation of the ORC at this time. Otherwise, it is expected that cooling continues increasing for the case of no ORC included in the system. COP_c takes the same trend as the $\dot{Q}_c$ and reaches a maximum value of about 0.432. The month of July has almost the highest average $\dot{Q}_c$ and COP_c of about 6.45 kW and 0.369, respectively. However, August also has a very close cooling performance because both months have almost same climate conditions.

References

[1] A.A. Hassan, A.E. Elwardany, S. Ookawara, M. Ahmed, I.I. El-Sharkawy: Int. J. Refrig. 116 (2020), p. 129–145.

[2] S. Murugan, B. Horák: Renew. Sustain. Energy Rev. 60 (2016), p. 1032–1051.

[3] S.S. Joshi, A.S. Dhoble: Renew. Sustain. Energy Rev. 92 (2018), p. 848–882.

[4] B.B. Saha, I.I. El-Sharkawy, in: Heat Pipes Solid Sorption Transform. Fundam. Pract. Appl., CRC Press, (2013), p. 29.

[5] M.M. Younes, I.I. El-Sharkawy, A.E. Kabeel, B.B. Saha: Appl. Therm. Eng. 114 (2017), p. 394–414.

[6] J.S. Pereira, J.B. Ribeiro, R. Mendes, G.C. Vaz, J.C. André: Renew. Sustain. Energy Rev. 92 (2018), p. 728–743.

[7] Information on http://www.apricus.com/upload/userfiles/downloads/Apricus_FPC-A32_Tech_Info.pdf.

[8] Information on http://www.fototherm.com/en/our-products/al-series/

[9] I.I. El-Sharkawy, H. AbdelMeguid, B.B. Saha: Appl. Energy 126 (2014), p. 235–245.

[10] A. Buonomano, F. Calise, A. Palombo: Renew. Sustain. Energy Rev. 82 (2018), p. 1874–1908.

Towards Adapted Heritage Buildings to Sea Level Rise in Egypt: The Citadel of Qaitbay as a Case Study

Sherein El-Shahat [1, a] and Nehad A. Gawad [2,b]

[1,2] Nile Higher Institute for Engineering and Technology, Mansoura, Egypt.

[a] sherein.shahat@yahoo.com,

[b] nehadabdelgawad@gmail.com

Keywords: heritage building, sea level rise, adaptation, policies, strategies.

Abstract. The heritage areas carry the identity and culture of our past nations. They tell us what happened to our great ancients and how they obligated the cruel circumstances for their hard living. Heritage buildings remind us of our great roots, which reflect on their architecture and spaces. So, the research aims to put a group of SLR adapatation policies and strategies be maintain on the remains for next generations. The Citadel of Qaitbay has been selected as a case study that classified as category (A) in the value degree. It is obligated to a protection strategy for the shoreline and few modifications inside the citadel to be restored to its good state. The analytical approach will be used in the research. SLR adaptation and conservation mechanisms are vital approaches to preserve the history and culture of nations in the coastal zones. Besides these approaches, it could be integrating with other programs (e.g. special development programs). Soft protection is the main process of SLR adaptation strategies and is more sustained in such areas. The accommodation strategy is considered the rehabilitation process of the building. Retreat strategy is used rarely when treating the heritage areas.

Introduction

What remained from ancient lives carries the heritage identity of every nation. These remains tell us the story of how ancients adapted and tolerated their physical and socio-economic aspects. Therefore, they should be conserved from different hazards that threatening their existence to be maintained to the coming generations.

There are many threats to heritage areas resulting from natural risks and human intervention. Natural hazards are various; such as climatic hazards (humidity, heat waves, heavy precipitation, …), tectonics (earthquakes, landslides, …), marine actions (SLR, storm surges, saltwater intrusion, erosion, inundation, …), riverine forces (floods, erosion in stream body, …). Hazards from human intervention are more damaged and more dangerous, which can be resulting from wars, political conflicts, purposed corruption, urban and population growth, pollution, neglect, unawareness, gaps in land value, unsustainable development, unwise management, etc.

Climate change and its association with sea-level rise 'SLR' have become a fact that increasingly challenge coastal zones all over the world (El-Shahat et. al., 2020). These impacts work on losing each of coastal lands and assets, including the valued items (e.g. natural protected areas, heritage buildings). Therefore, they should be adapted. There are many strategies of adaptation, such as protection, accommodation, and retreat (El-Shahat, 2018).

Used Category, Case Study, and Method:

Based on the value degree of heritage buildings, it could be classified into the followings:

- Category (A): It is allowed to make restoration without any internal or external modification, except in rare conditions.

- Category (B): It is allowed only to make minor internal modifications.
- Category (C): It is allowed to make major modifications with keeping only on structure and elevations of building.

Accordingly, the interfering levels by the adaptation strategies for the three classifications:

- Protection strategy could be used for category (A);
- Strategies of protection and minor accommodation could be used for category (B);
- Strategies of protection and major accommodation could be used for category (C).

The Citadel of Qaitbay has been selected as a case study, which exists in the margin of Pharos Island, and adjacent directly to the Mediterranean Sea as in fig (1). The citadel is classified as category (A) due to its high value, which obligated to a protection strategy for the shoreline and few modifications inside the citadel to be restored its good state. The analytical approach will be used in the research to configure a group of adaptation strategies and policies to sustain coastal heritage buildings.

Fig (1): The recent site of Citadel of Qaitbay (Based on Google Earth).

Sea Level Rise Impacts on The Citadel:

Due to the direct exposure to sea motion as in fig (2), the citadel has witnessed major devasting events from marine actions, such as SLR, tsunami, and storm surges. These hazards have generated an inundation and an erosion of the citadel body. Besides, currents and tides have resulted in severe immigration of sandy soil surrounding the citadel as in fig (3). Recently, waves have caused a big hole in the northern wall of the citadel as in fig (4). There is a saltwater intrusion into the basement floor through openings, which impacted the internal parts and foundation of the building as in fig (5). As well as, the elevation had been eroded in many parts due to high humidity in the atmosphere and high dynamic waves action as in fig (6).

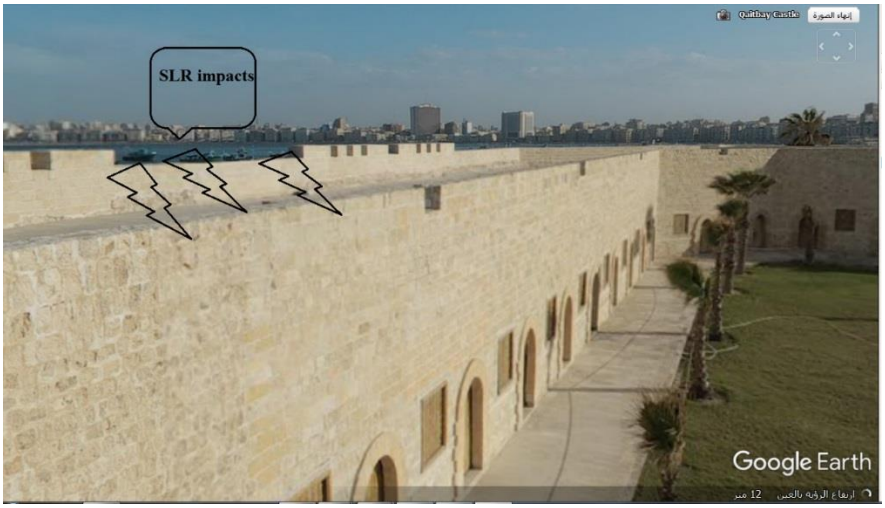

Fig (2): The direct exposure of SLR on the citadel.
Source: Based on photos of Google Earth.

Fig (3): The sand immigration surrounding the citadel.
Source: Based on photos of El-Youm El-Sabea Journal (accessed on 23, Sept 2020).

Fig (4): The hole on the northern wall of the citadel.
Source: Based on photos of El-Youm El-Sabea Journal (accessed on 23, Sept 2020).

Fig (5): Saltwater intrusion inside the citadel.
Source: Based on photos of El-Youm El-Sabea Journal (accessed on 23, Sept 2020).

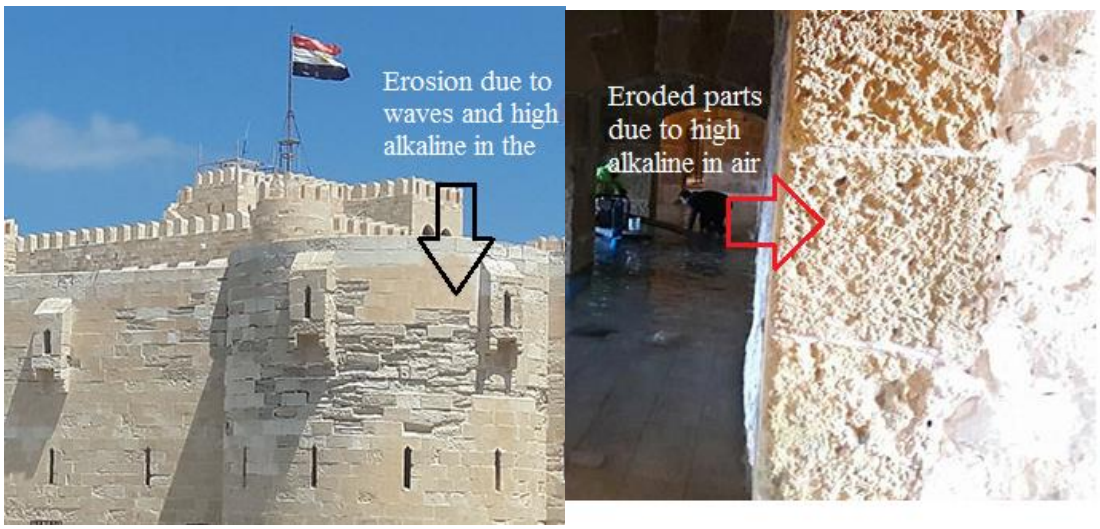

Fig (6): Erosion in walls due to high alkaline in the air and waves action.
Source: Based on photos of El-Youm El-Sabea Journal (accessed on 23, Sept 2020).

The Local Solutions:

The antiques Minister with the supervision of the organization of shores protection investigates a big project for reinforcement of existed seawall in front of the citadel by blocking the gaps between rocks in the seawall, which resulting in erosion in another adjacent unprotected area. Also, they already constructing drowned breakwaters from 250m distancing from the shoreline with 7-9 m height of the breakwaters to accumulate sand around them, which disturbing the navigation marine paths of boats for creation or fishers. At the scale of the building, there is a restoration to eroded material in some parts only, also there is bumping to the intruded saltwater out the citadel.

The Optimized Solutions:

It is required to make a precise restoration to its lost material than happening now to innovate the citadel. Also, it should make a rehabilitation to the citadel by making more celebrations and social events in day and nights to get feasible money to spend on its maintenance cautiously. It should make a managed plan in emergency cases with many procedures, such as blocking the openings before the periods of storm surges to preserve the internal spaces in a good state.

Due to its high priority to our national inheritance, there will be urgent protection to the shoreline by soft coastal engineering, such as nourishment dunes stabilized with vegetation to keep a

livability shoreline, which will raise the tourism. It also should raise people's awareness of the citadel's importance using media and websites to keep on the citadel health by public interest and efforts.

As for the context of the citadel, it should be linked it to the valuables in the surrounding areas, such as Ras El-Tin Palace, Abu Abbas Mosque, Al-Attarin Market, Al-Mansheya Square, traffic stations, Corniche streets, ... This link is recomended by upgraded pathes, which should be upgrading their softscape (e.g. trees, water features), hardscape (e.g. pavement, carvings, furnitures).

Moreover, it could be adopted a framework for adaptation as the followings:

- Mapping of future shorelines according to SLR scenarios, topography, and morphology of the area.
- Defining other acceleration forces to SLR risk at the historical area (tsunami, …).
- Studying socioeconomic aspects of the area to identify local abilities and interesting points (services, shops, ...).
- Studying governmental plans for the area to integrate the efforts of both local authorities and stockholders.
- Intervening by protection strategies after studying the impact of this intervention.
- Activating the building with many supported programs (i.e. social events).
- Activating the conservation mechanisms, for example, using the new material with the same type and shape as the existing one in a heritage building (conservation programs).
- Activating social participation in the preservation of the buildings.

Conclusion:

The heritage areas carry the identity and culture of our past nations. They are socially valued and sensitive areas, which need to be considered. SLR adaptation and conservation mechanisms are vital approaches to preserve the history and culture of nations in the coastal zones. Besides these approaches, it could be integrating with other programs (e.g. special development programs). Soft protection is the main process of SLR adaptation strategies and is more sustained in such areas. The accommodation strategy is considered the rehabilitation process of the building. Retreat strategy is used rarely when treating the heritage areas.

The research recommends the following:

- Assessing the SLR vulnerability to all coastal heritage areas at the national scale.
- Giving priority to strategies to risked heritage areas such as those in low-lying areas.
- Providing and using precise data to make flexible and modified plans.
- Effective plans aim with area condition.
- Encouraging and supporting research studies for vulnerable areas.
- Awareness and education for more national capacity (e.g. individuals, governmental bodies).

1.

References:

Agrawala, Shardul, Annett Moehner, Mohamed El Raey, Declan Conway, Maarten Van Aalst, Marca Hagenstad, and Joel Smith. "Development and climate change in Egypt: focus on coastal resources and the Nile." *Organisation for Economic Co-operation and Development* (2004).

Akeil, Sherein. "Adaptation with climate change as an opportunity to raise the quality standards of life in our communities." Bulletin de la Société de Géographie d'Egypte 92.1 (2019): 76-89.

Bigio, Anthony G. "Cities and climate change." *Building safer cities: The future of disaster risk* (2003): 91-100.

Carabelli, Romeo. "Recent architectural inheritance in the Mediterranean: Temporalities and territories." (2005).

Dasgupta, Susmita, Benoit Laplante, Siobhan Murray, and David Wheeler. "Sea-level rise and storm surges: A comparative analysis of impacts in developing countries." (2009).

Dean, Robert G., and Robert A. Dalrymple. *Coastal processes with engineering applications*. Cambridge University Press, 2004.

Drost, Anne. "Developing sustainable tourism for world heritage sites." *Annals of tourism research* 23, no. 2 (1996): 479-484.

El-Raey, Mohamed, Dia H. El-Quosy, Mahmoud El-Shaer, Osama A. El Kholy, and Eng Ayat Soliman. "Egypt: inventory and mitigation options, and vulnerability and adaptation assessment." *CSP Interim Report—Egypt, US Country Studies Program Google Scholar* (1995).

El-Raey, Mohamed, K. R. Dewidar, and Mamdouh El-Hattab. "Adaptation to the impacts of sea level rise in Egypt." *Mitigation and Adaptation Strategies for Global Change* 4, no. 3-4 (1999): 343-361.

El-Raey, Mohamed, Samir Nasr, Omran Frihy, Sahar Desouki, and Kh Dewidar. "Potential impacts of accelerated sea-level rise on Alexandria Governorate, Egypt." *Journal of Coastal Research* (1995): 190-204.

El-Raey, Mohamed. "Vulnerability assessment of the coastal zone of the Nile delta of Egypt, to the impacts of sea level rise." *Ocean & coastal management* 37, no. 1 (1997): 29-40.

El-Shahat, Sherein, et al. "Vulnerability assessment of African coasts to sea level rise using GIS and remote sensing." Environment, Development and Sustainability (2020): 1-19.

Frihy, Omran E., Khalid M. Dewidar, and Mohamed M. El Raey. "Evaluation of coastal problems at Alexandria, Egypt." *Ocean & coastal management* 30, no. 2-3 (1996): 281-295.

Hansen, Liane. "Rising Sea Levels Threaten Egypt's Ancient Cities." *Retrieved July* 28 (2008): 2009.

Inman, Douglas L., M. Hany, S. Elwany, Ahmed A. Khafagy, and Abraham Golik. "Nile Delta profiles and migrating sand blankets." *Coastal Engineering Proceedings* 1, no. 23 (1992).

Intergovernmental Panel on Climate Change. (2015). *Climate change 2014: mitigation of climate change* (Vol. 3). Cambridge University Press.

Jokilehto, Jukka. "World heritage: observations on decisions related to cultural heritage." *Journal of Cultural Heritage Management and Sustainable Development* 1, no. 1 (2011): 61-74.

Mitchell, Nora, Mechtild Rossler, and Pierre-Marie Tricaud. *World Heritage paper№ 26. World Heritage Cultural Landscapes. A hand book for conservation and management*. 4/2/UNESCO/Cult/09/E, 2009.

Mowforth, Martin, and Ian Munt. *Tourism and sustainability: Development, globalisation and new tourism in the third world*. Routledge, 2015.

Simmonds, Julia. "UNESCO world heritage convention." *Art Antiquity & L.* 2 (1997): 251.

Solar concentration for pesticide-containing wastewater combat: Can solar energy meets a green costless goal for treating agriculture waste stream?

RAHMA Hussain Thabet[1,a], MAI Kamal Fouad[2,b], ISMAEL Abd-elrahem Ali[3,c], SHAKINAZ Aly El-Din El Sherbiny[2,d] and MAHA Abdelbaset Tony[1,e]

[1]*Advanced Materials/Solar Energy and Environmental Sustainability (AMSEES) Laboratory, Basic Engineering Science Department, Faculty of Engineering, Menoufia University, Shebin El-Kom, Egypt*

[2]*Chemical Engineering Department, Faculty of Engineering, Cairo University, Egypt*

[3]*Cyclotron project, Nuclear Physics Department, Nuclear Research Center, Atomic Energy Authority, Egypt*

[a] eng.rahma.197@gmail.com, [b]maifouad86@gmail.com, [c] ismail_phy@yahoo.com
[d] shakinaz@gmail.com, [e] dr.maha.tony@gmail.com

Keywords: Methomyl; Magnetite; oxidation; Fenton's reagent; Solar energy

Abstract: Pesticides are attained through the environment via a direct discharge of the agriculture stream in massive amounts. Basically, the precise estimation of pesticide release into the ecosystem is quite uncertain. But, recent studies state its toxicity to the biosphere. Thereby, treating such effluent is a must. Heterogeneous catalytic oxidation systems showed a superior activity due to *in-site* oxidation. Magnetite nanocrystals (Fe_3O_4) were synthesized using a cost-efficient co-precipitation technique and the structure and morphology of the nanostructured particles were studied using X-ray diffraction (XRD) characterized and transmission electron microscopy (TEM). The produced Magnetite was used as a source of Fenton's reaction for oxidizing methomyl in aqueous stream. The effect of multivariable system parameters were investigated, and the optimal system conditions were monitored at pH 3.0 and 100 and 40 mg/L of H_2O_2 and, magnetite, respectively which recorded 72% of mehtomyl removal within 80 min time of reaction at a lab-scale ultraviolet reactor. To add up, for large scale applications, parabolic trough solar concentrator mounted with a tubular reactor is used in a pilot scale facility during the summer periods in Menoufia Governorate, Egypt to conduct the solar experiments which recorded a hgher removal efficiency through augmented facility.

Introduction

Ecosystem pollution is in increase due to numerous human activities. Certainly, such pollution is creating a serious hazard to human and aquatic life. Wastewaters containing pesticides include hazardous and occasionally non-biodegradable chemicals that persist in the environment even after being processed conventionally [1].

Methomyl is an insecticide in the carbamate group of pesticide that is commonly used in agriculture due to its effective control of many types of pests. However, because of its high solubility [2], it is harmful to surface and groundwater in agricultural areas. Thus, the European Commission (EC) and World Health Organization (WHO) are categorized it as a restricted, very toxic, and hazard [3, 4].

Advanced oxidation processes (AOPs) have been developed to provide a sustainable and practical wastewater management solutions without the use of harmful chemicals to completely mild compounds such as CO_2, H_2O, and inorganic salts [5]. Fenton's reagent depends on using salts and H_2O_2 to create highly reactive hydroxyl used for the treatment different types of pollutants including pesticides [6].

To add up, organic pollutant oxidation by Fenton's reagent may be greatly expedited and enhanced by ultraviolet and visible light, as well as solar radiation. Commercially, the use of solar energy as a source of UV irradiation is a very attractive and promising technology [7].

Massive energy consumption is recorded through wastewater treatment plants. Worldwide, energy is required to deliver water to humanity. About one percent of the whole energy demand is used yearly

in the water sector for water activities. 14% from such energy is only consumed for wastewater treatment plants as seen in Fig. 1 [8]. Solar energy is a superior candidate for enhancing Fenton system in a cost-efficient, clean and green technique [9]. Ultraviolet source from solar energy makes the magnetite based-Fenton reaction meets the sustainability concept.

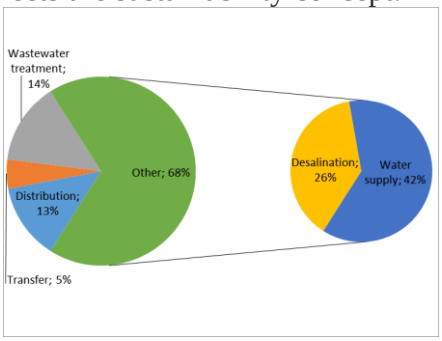

Fig. 1 Worldwide energy consumption with related water sector's intake (adopted from [8])

Herein, nanostructured Fe_3O_4 were synthesized and applied as a photocatalyst for methomyl elimination. Nonetheless, there is a gap in the study that focuses on utilizing nanoparticles as a source of a solar photo-Fenton reagent for treating pesticide wastewater in a pilot-scale application, according to the literature referenced. As a result, the current study focuses on eco-sustainable solar-catalytic reactors for the treatment of methomyl wastewater via pilot-scale Fenton-based system under natural sunlight.

2. Materials and Methods

2.1. Chemicals

Ccommercial methomyl pesticide with a formula of $C_5H_{10}N_2O_2S$ is supplied by the agriculture chemicals company in Menoufia Governorate, Egypt. The magnetite nanoparticles were prepared via co-precipitation technique and used as Fenton catalyst. H_2O_2, 40% was used to initiate the Fenton reaction. Diluted solutions were prepared from NaOH and H_2SO_4 were used for pH adjustment. All chemicals were used as received without any further treatment or purification. Distilled water was also used along this study for preparing solutions.

2.2. Characterization

X-ray diffraction pattern, XRD, the Fe_3O_4 precipitate was dried and analyzed using an X-ray diffractometer. The instrument applied for the analysis was X-lab Shimadzu X-6000), and identified with Cu-Kα radiation. Furthermore, a high-resolution Transmission Electron Microscope (TEM) has been applied to investigate the particle size of the as-synthesized Fe_3O_4 nanoparticles.

2.3. Magnetite nanocatalyst preparation

Fe_3O_4 nanoparticles were synthesize via cost efficient co-precipitation methodology. Such technique has been highlighted before [10]. In this process Ferric Sulphate, $Fe_2(SO_4)_3$ and Ferrous Sulphate, $FeSO_4$ were dissolved in deionized water of 1.5 L volume. Drop by drop, pure sodium hydroxide (NaOH) solution was added with stirring until the pH of the solution reached 11.0. The obtained precipitate was filtered and heated to 80 ^oC. The resultant particles then subjected for repetitive washing with distilled water to assure the removal of any chemicals, sodium hydroxide and sodium sulphate till the resultant pH of the solution recorded neutral pH (7.0). Finally, the obtained nano-magnetite Fe_3O_4 was dried to 60 °C and grounded.

2.4. Methomyl oxidation test

Initially, 50 mL of Methomyl pesticide (50 ppm) was subjected to the simulated photo-reactor using a ultraviolet (UV) illumination (254 nm wavelength) for conducting the photo-oxidation test. The Fenton's is added and pH is adjusted, if required. Then, at a defined time

intervals the treated samples are subjected for spectrophotometer analysis. Furthermore, for a pilot scale solar reactor a parabolic trough solar collector augmented with a tubular reactor is used. Methomyl is allowed to be circulated through a peristaltic pump (Shenchen, model LABN6) to the tubular reactor where the sun is collected and reflected to the reactor where the Fenton's occurs. The photograph f the pilot scale experimental set-up is illustrated in Fig. 2 (with the schematic representation inset of Fig. 2).

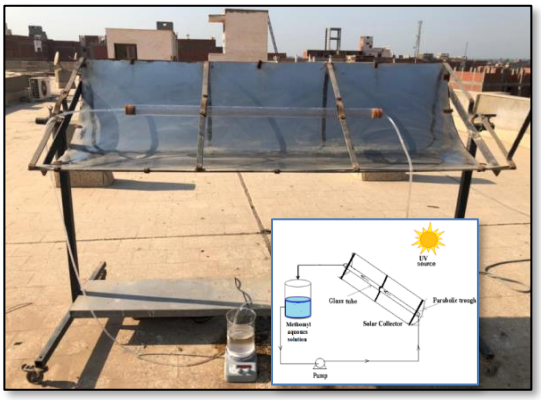

Fig. 2 Pilot Scale Solar reactor

2.5. Analysis technique

(Unico UV-2100 spectrophotometer, USA was used for methmoyl analysis. Solarmeter (KIPP ZONEN ISO 9060, Pyranometer CMP 3) was used to monitor solar radiation through the day-time of study.

3. Results and Discussions:

3.1. Morphological and structural characterization of Magnetite:

The TEM micrographs of the produced Fe_3O_4 nanoparticles shown in the Fig. 3 revealed that the majority of the nano-magnetite are spherical in shape, with the exception of tiny edges connected to specific nanoparticles. Also, the XRD graph (adopted from the previously published by the authors [11] displayed the peaks in the graph corresponding to a single phase of spinel structure for magnetite nanosturucture.

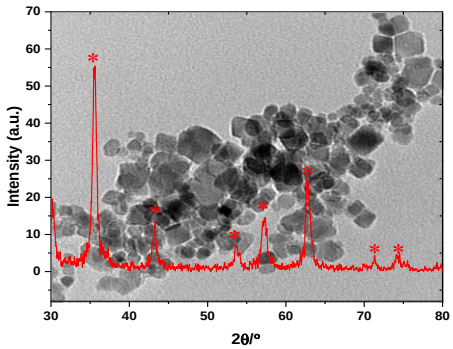

Fig. 3 TEM micrograph and XRD of the synethsized magnetite samples

3.2. Artificial UV- illumination Fenton test

Effect of magnetite dose

Under the UV-illumination, series of experiments are carried out to examine the effect of magnetite nanoparticles dose on methomyl oxidation. A 50 mg/L of the methyl solution was subjected to various magnetite nanoparticles concentrations ranged from 10 to 80 mg/L, (at 100 mg/L of H_2O_2 and pH 3.0). As illustrated in Fig. 4, increasing magnetite results in an increment in oxidation of methomyl. However, further catalyst increase results in a decline in oxidation rate. 40 mg/L was recorded as the optimal magnetite dose. This is illustrated by the presence of Fe_3O_4 over or lower the optimal limit could affect $OH^{\bullet}$ radicals production which is the main responsible of oxidation [12]. Hence, the overall reaction yield is scavenged.

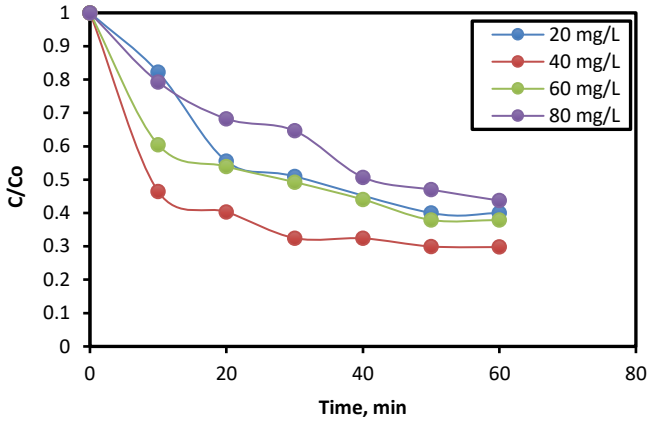

Fig. 4 Effect of magnetite dose on oxidation

Effect of H_2O_2 concentration:

Fig. 5 displays the effect of different doses of H_2O_2 reagent at constant 40 mg/ L of megnetite and pH 3.0. The results reveal that changing the peroxide concentration from 100 to 1600 mg /L changing the oxidation rate, however, the best oxidation value of methomyl elimination rate is corresponding to 100 mg/L of H_2O_2 concentration. This is linked to the $OH^{\bullet}$ radicals' generated. As H_2O_2 is a key parameter that possess a terminal effect on the radicals produced. Contrary, the reaction yield is declined with unoptimal H_2O_2 since the unoptimal peroxide results in a low $OH^{\bullet}$ radicals that hinder the reaction.[13, 14].

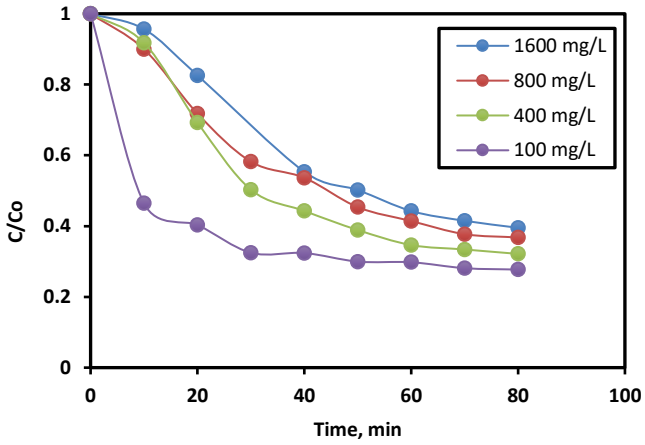

Fig. 5 Effect of H_2O_2 dose on oxidation

Initial pH Effect:

Fenton oxidation is highly dependent reaction on pH conditions. Thus, such effect was studied by varying the initial pH value of methoyl solution (3.0-8.0) keeping peroxide and magnetite 400 and 40 mg/L, respectively. Fig. 6 clearly displays the oxidation is affected with the starting pH of the solution. Decreasing the pH from to 3.0 increases the oxidation rat. This observation is most likely due to the maximal $OH^{\bullet}$ radicals' production within the acidic medium. Hwover, unfavourable radicals are created at higher pH values [15, 16].

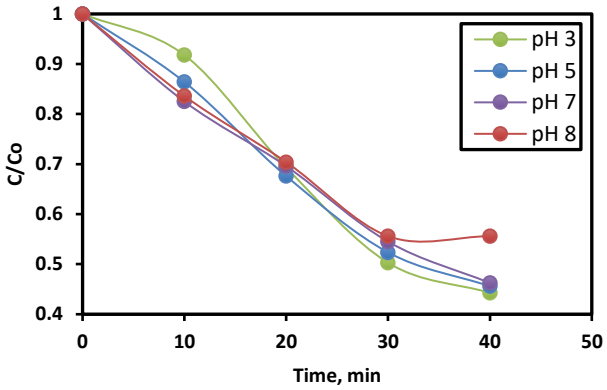

Fig. 6 Effect of pH dose on oxidation

3.3. Solar Oxidation:

In Menoufia Governorate in the north of Egypt in the Nile Delta Region, like most cities in Egypt, well endowed with the natural solar radiation especially in the sum season the sun enhanced Fenton oxidation experiments is conducted. During July, the time of study, the solar radiation is monitored to reach to 942 W/m^2. The solar experiment test is given in Fig. 7 show that the pre-natural solar irradiance test helps in almost complete methomyl removal which is more than 95% due to photons attained from the sunlight initiating the Fenton's reaction more than that gained from artificial UV illumination source [17].

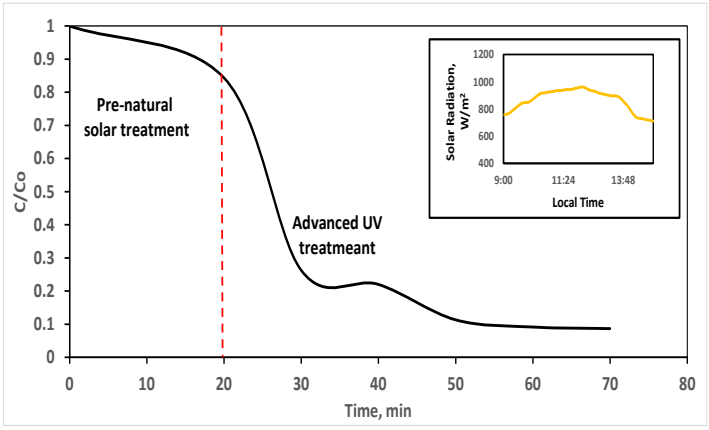

Fig. 7 Effect of natural solar treatment augmented UV oxidation on methomyl oxidation

Conclusion

Fenton reagent that is so-called solar Fenton reaction revealed a good treatability in oxidizing methomyl pesticide. Augmented natural radiation with artificial UV radiation recorded a good efficiency compared to UV radiation only and the reaction well working at pH 3.0 and the optimized conditions affects the removal efficiency.

References

[1] M.A. Tony, H.L. Parker, J.H. Clark, Journal of Environmental Science and Health, Part A, 51 (2016) 974-979.

[2] M. Tamimi, S. Qourzal, A. Assabbane, J.M. Chovelon, C. Ferronato, Y. Ait-Ichou, Photochemical & Photobiological Sciences, 5 (2006) 477-482.

[3] S. Malato, J. Blanco, J. Cáceres, A.R. Fernández-Alba, A. Agüera, A. Rodrıguez, Catalysis Today, 76 (2002) 209-220.

[4] C. Zhang, Z. Yang, W. Jin, X. Wang, Y. Zhang, S. Zhu, X. Yu, G. Hu, Q. Hong, Letters in applied microbiology, 64 (2017) 289-296.

[5] M.A. Tony, P.J. Purcell, S.A. Mansour, Chemical Engineering Communications, (2020) 1-15.

[6] M.A. Tony, S.A. Mansour, International Journal of Environmental Science and Technology, 17 (2020) 161-174.

[7] M.A. Tony, S.A. Mansour, International Journal of Environmental Science and Technology, 17 (2020) 1337-1350.

[8] K. Wydra, M. Jaskolski, L. Wagner, E.S. Mohamed, Journal of Photonics for Energy, 9 (2019) 043108.

[9] M.A. Tony, International Journal of Environmental Analytical Chemistry, (2021) 1-33.

[10] P.L. Hariani, M. Faizal, R. Ridwan, M. Marsi, D. Setiabudidaya, International Journal of Environmental Science and Development, 4 (2013) 336-340.

[11] R.H. Thabet, M.K. Fouad, I.A. Ali, S.A. El Sherbiney, M.A. Tony, International Journal of Environmental Analytical Chemistry, (2021) 1-23.

[12] H.S. El-Desoky, M.M. Ghoneim, R. El-Sheikh, N.M. Zidan, Journal of hazardous materials, 175 (2010) 858-865.

[13] W. Chu, Chemosphere, 44 (2001) 935-941.

[14] W. Sabaikai, M. Sekine, M. Tokumura, Y. Kawase, Journal of Environmental Science and Health, Part A, 49 (2014) 193-202.

[15] F. Akbal, A. Kuleyin, Environmental Progress & Sustainable Energy, 30 (2011) 29-36.

[16] M.A. Tony, P.J. Purcell, Y. Zhao, Journal of Environmental Science and Health, Part A, 47 (2012) 435-440.

[17] M.A. Tony, Energy Storage, (2021) e238.

Lithium-Ion Batteries Thermal Management based on Nanomaterials Technology and Cooling Strategies

Marwa Mahmoud Hamed[1], Jackleen S. Same[1], Walid A. Hussien[1], A. El-Tayeb[*1], I. Moukhtar[1], Esam H. Abdelhameed[1], A.Z. El Dein[1]

[1]Electric Engineering Department, Faculty of Energy Engineering,

Aswan University, Aswan, Egypt.

*E-mail: Ahmed_al_tayeb@aswu.edu.eg

Keywords: Lithium-Ion Batteries, Nanotechnology Materials, Battery Thermal Management Systems, Phase Change Material and Simulation Model.

Abstract. This article presents nanotechnology materials and different cooling methods as a practical solution for improving the thermal management of lithium-ion batteries. These batteries are very sensitive to frequent temperature changes, which affects the battery life. Hence, designing effective battery thermal management systems is very important for enhancing heat dissipation and extend battery life. During the charging and discharging process of the battery, the unequal heat generated at every cell inside the pack and the generated convection coefficient, which is higher at the surface than the center of the battery, cause a non-uniform in the battery temperature. The irregular temperature distribution has negative impacts on the overall performance of the battery pack. Therefore, the rapid changes of the batteries had to be monitored carefully and managed to avoid safety and thermal-related issues. Until now, many researchers developed various battery thermal management systems to meet the requirements such as high power, fast charging rates, and improved driving performance. This paper summarizes the recent research studies of thermal management of lithium-ion batteries. The management strategies classify into two categories: internal cooling strategies, which depends on nanotechnology materials such as phase change material cooling methodology, and external cooling strategies, which relies primarily on-air cooling or liquid cooling methodologies. Furthermore, numerous thermal models have been discussed for better understanding of the heat transfer mechanisms within the battery enclosure, where the thermal radiation and natural convection from all free surfaces were modeled. in addition, propagation of thermal runaway of all cells in the battery pack is predicted through the analysis of the thermal simulation model.

1. Introduction

Li-ion batteries (LIBs) are the powerhouse for the digital electronic revolution in the modern mobile society, which exclusively used in mobile phones and laptop computers. The success of commercial LIBs in the 1990s was not an overnight achievement, but a result of intensive research and contribution by many great scientists and engineers. Then many efforts have been put to further improve the performance of LIBs that achieved certain significant progress. To meet the increasing demand for energy storage, particularly from increasingly popular electric vehicles, intensified research is required to develop next generation LIBs with dramatically improved performances, including improved specific energy and volumetric energy density, cyclability, charging rate, stability, and safety [1, 2]. There are still notable challenges in the development of next-generation LIBs. New battery concepts must be further developed to go beyond LIBs in the future. Although the lithium-ion battery is the most energy promising new energy sources but many problems at the side of safety view on the thermal hazards can be caused by several factors such as electrical, chemical, physical, and thermal factors. The generated internal heat is the main cause of the security issues in LIBs [1, 3]. Due to abuse conditions such as electrical, thermal, or mechanical abuse, a series of side reactions are excited, and a huge amount of heat is released. When this amount of generated heat cannot be dissipated in time, the internal temperature in LIBs quickly increases. The highly internal temperature causes decomposition of solid electrolyte interface on anodes, collapse of separators, and

oxygen evolution in cathodes. Eventually, these reactions lead to thermal runaway and consequently safety accidents such as combustion and explosion [4, 5]. Many types of research are doing to overcome the thermal hazard and improvement the electrical, chemical, and physical properties [3]. Some measures are reviewed including the application of safety devices, fire-retardant additives, battery management systems, hazard warnings, and firefighting should a hazard occur [6, 7]. This research will discuss the thermal problem enhancement inside the battery, includes electrolyte, cathode, anode, and separator parts, and outside the battery using different cooling strategies. Various battery thermal management systems (BTMSs are designed to control the operating temperature of LIBs and ensure performance and safety. For batteries operating in high temperature conditions, current cooling strategies rely primarily on air cooling, liquid cooling, and phase change material (PCM) cooling [8, 9].

2. Internal Cooling of Lithium-Ion Batteries

Within the final two decades, a wide assortment of nanomaterials (measured or structured) was arranged in several forms by either physical or chemical “bottom-up” or “top-down” strategies [10, 11]. The foremost curiously portion approximately these structures at the nanoscale is that size-related marvels and forms can happen, and consequently changes in properties or improvement of unused ones emerge as it were since of size, that cannot be seen in their large-scale partner [12]. Also, over the past two decades, there has been quick progress in the field of nanoelectronics to get the behavior of limited electrons in solids and to a lesser degree in nanoionics for the behavior of restricted particles in solids [13]. The application of nanomaterials standards in electrochemical storage devices and energy conversion in common caught on at an awfully early organize due to the self-evident benefits in catalysis for fuel cells or upgrading charge and release in batteries and capacitors [12]. Lithium-Ion battery innovation was no exception, and as talked about within the past segment, one or two of the terminals are blended ionic or electronic strong conductors and the electrolyte is a particle conductor. Subsequently, it is exceptionally imperative to get it the behavior of particles and electrons when limited in strong materials at the nanoscale and its impact on battery execution.

2.1 Nanomaterials for Separator in Lithium-Ion Battery:

The separator is an important part in the battery to ensure the safety of lithium-ion batteries and prevent direct electric contact between the cathode and anode while allowing ion transport see figure (1). The separators are not an element in the electrochemical reactions but determine the performance of the electrochemical reaction and the safety of LIBs.

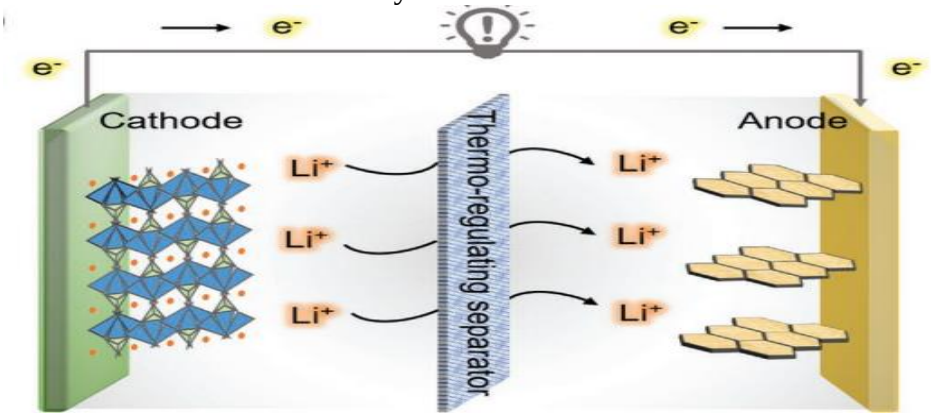

Figure (1) Separator in lithium-ion battery

The separator with phase change material (PCM) of paraffin wax encapsulated in hollow polyacrylonitrile nanofibers can prevent the internal temperature rise of LIBs. It is indispensable to build safer LIBs from the separator aspect. Currently, polyolefin-based microporous membranes are the most widely used separators in LIBs. However, the poor thermal stability and wettability with electrolytes of these low-melting-point and nonpolar polymers need to be overcome. Recently, inorganic, and organic materials have been coated onto separators to improve thermal resistance and

wettability. Nevertheless, the coating layer may increase the thickness and decrease the porosity of the separators. More importantly, rationally designed separators with multiple functions are proposed to improve the safety of LIBs. For example, it is beneficial to suppress the dendrite growth of lithium by altering the pore structure or engineering the surface properties of separators. When the dendrite growth of lithium is inevitable, a dendrite detecting separator is constructed to alert of Li dendrite formation by sensing of the voltage change. The separator with a phase-change material (PCM) of paraffin wax encapsulated in hollow polyacrylonitrile nanofibers renders a wide range of enthalpy (0–135.3 J g−1), capable of alleviating the internal temperature rise of LIBs in a timely manner. Under abuse conditions, the generated heat in batteries stimulates the melting of the encapsulated PCM, which absorbs large amounts of heat without creating a significant rise in temperature.

2.2 Nanomaterials for Anode in Lithium-Ion Battery

There are many promising materials that can be used as electrodes of the anode. The Sn anode which can be formed with the lithium alloy. The Sn material is expensive and nontoxic. Because of graphene characteristics it can be used to enhance the Sn anode performance. A 3D carbon anode lattice designed and covered with Sn/graphene porous nanosized by Lian et al [14]. The merits of this composite are its high reverse capacity which is nearly 600mAhg^{-1} at 50 cycles. In recent research, encapsulation process is used to encapsulate the Sn nanoparticle (Sn/NPs) which synthesized by microwave irradiation of SnO_2, which gives reversible capacities of 1037 mAhg^{-1}. The cycling ability exceeds 5000 times in half-cells at a 6 C rate while retaining 400 mAhg $^{-1}$ reversible capacities [15]. From this, the graphene composite with the tin can enhance the performance of the anode lithium-ion battery and treatment the problem of the volume expansion during Li cycling. Junke Ou& Shugen Wu and Hao Wang [16] use the cobalt oxide CO_3O_2 nanomaterial to enhance the performance of the anode as indicated in Figure (2). This material gives good electrochemical properties, which has a large capacity of nearly 890 mahg^{-1} nanomaterial synthesis with hydrothermal synthesis.

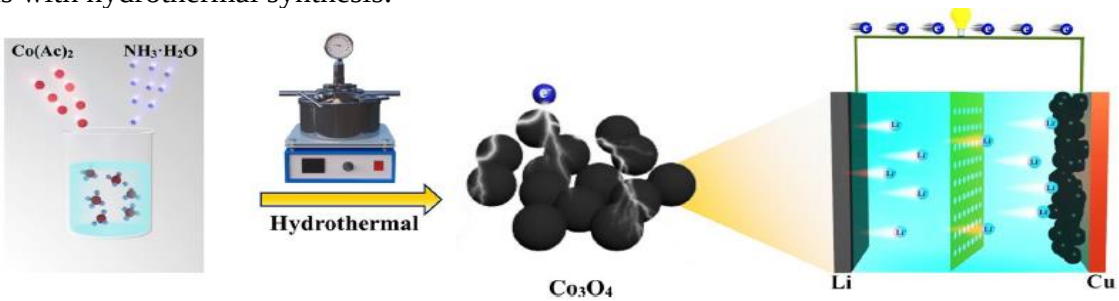

Figure (2) CO_3O_4 Nanoparticles in lithium-ion battery

2.3 Nanomaterials for Cathode in Lithium-Ion Battery:

More advanced research operates on the battery cathode to enhance the performance of the battery as more cycles, thermal treatment problem, and high capacity. The required properties of materials that used as a cathode have more attention due to their merits such as cheap material, high capacity, high cycle stability, and nontoxic. This material could achievement by coating the cathode surface with an inorganic material as TiO_2, Li_2ZrO_3, Al_2O_3, but the inorganic material has a problem of resist the diffusion of li^+. This problem can avoid by doing a modification on its surface by polymers. Yoon-Sung Lee, Won-Kyung Shin and Aravindaraj G Kannan [17], synthesized Layered LiNi0.6Co0.2Mn0.2O_2 cathode material and double-layer coated with Al_2O_3 nanoparticles and conductive PEDOT-co-PEG copolymer.

2.4 Nanomaterials for Electrolyte in Lithium-Ion Battery:

The electrolyte is one of the critical components within the lithium-ion battery but, has several demerits. For organic solvent-based electrolytes, their problems are flammability and intrinsically poor cycling efficiency. For ionic liquid-based electrolytes, their demerit is the relatively high

viscosity, which limits the attainable ionic conductivity. Composite polymer electrolytes (CPEs) can enhance the performance of the lithium-ion battery, they have good electromechanical properties and can increase the mobility ions [18]. CPEs can improve the structure and interactions between atoms/ions/nanoparticles within the system, and dielectric

3. External Cooling of Lithium-Ion Batteries

3.1 Air Cooling in Lithium-Ion Batteries:

Air cooling strategies can be classified into natural cooling and forced cooling when the intake air can be either direct from the atmosphere (that called passive air system) or be conditioned after an air conditioner heater or evaporator (that called active air system). Figure (3) shows a schematic description of the systems. Both called forced air system because in both cases the air is supplied by a blower. The forced air-cooling system with simple structure has the advantage of high reliability, low cost as well as easy maintenance, while it has poor thermal management, that is, beyond the operating temperature, uneven uniformity of temperature distribution and thermal escape diffusion. At high ambient temperatures such as 45°C - 50°C, the temperature inside the battery pack exceeds 55°C which exceeds the operating temperature and causes thermal escape. The uniformity of the temperature distribution is also important because of degradation and life cycle. As the flow rate increases, the maximum temperature difference of the cell will degrade and reduce the cycle life because heat transfer between cells is faster than heat transfer from the battery pack to the air. So, if one of the cells fails, then thermal escape will spread on the battery pack [2].

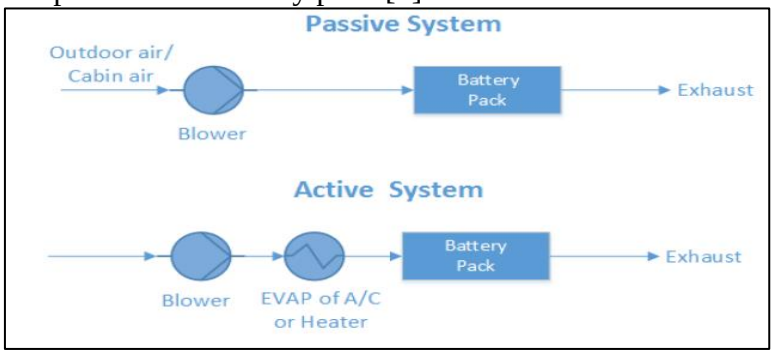

Fig (3) Forced air system (passive & active)

3.2 Liquid Cooling in Lithium-Ion Batteries:

Liquid cooling strategies can be further classified into direct cooling and indirect cooling. Direct liquid cooling is the immersion of the battery unit in the dielectric cooler (such as oil) while indirect cooling is achieved by the liquid flowing through the tubes/separate casing around the unit or cold plate where the units are placed on. Since the heat must pass through the surface of the tubes/panels before the coolant takes it away, the thermal resistance of indirect cooling inevitably increases.

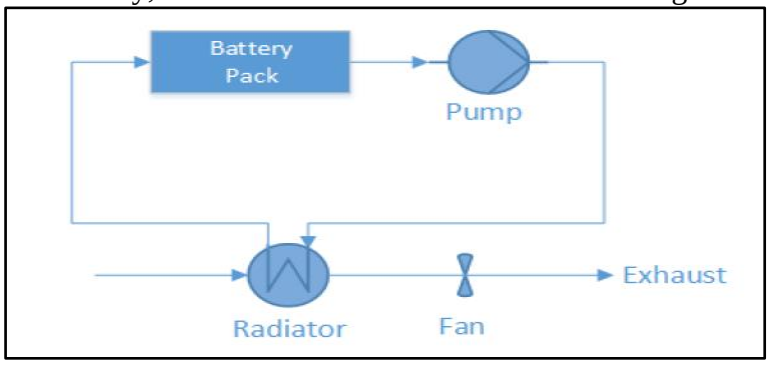

Fig (4) Passive liquid system

In contrast, the heat transfer process in direct liquid cooling is more efficient due to the direct contact between the coolant and the batteries. However, the high viscosity of dielectric fluids such as mineral

oil leads to large energy consumption when a high forced flow rate is required. Things are different with indirect cooling that can use low-viscosity liquids such as water. Liquid Coolant has a higher thermal conductivity which makes it a more attractive choice as a cooling medium [3]. Liquid systems can also be categorized into passive systems or active systems. In a passive fluid system, the heat sink for cooling is a radiator. This system does not have the ability to heat up. Fig (4) shows the regular diagram of a passive fluid system. The heat transfer fluid is circulated by the pump inside a closed system. The circulating fluid absorbs heat from the battery pack and releases heat through the radiator. The cooling power is strongly dependent on the temperature between the surrounding air and the battery. Fans behind the radiator can improve cooling performance, but if the ambient air is higher than the battery temperature or the difference between them is too small, the passive fluid system becomes ineffective. Active liquid system consists of two loops as shown in fig (5). The upper part is called the primary loop and the lower part is called the secondary loop. The primary loop is like that of a passive fluid system, in which the heat transfer fluid is circulated by the pump. The secondary loop is the air conditioning loop (A/C loop). The upper heat exchanger instead of the cooler acts as an evaporator (EVAP) for the cooling process and connects both loops. During the heating process, the four-way valve will be switched; the upper exchanger acts as a condenser (COND) and the lower heat exchanger acts as an evaporator. The heating operation loop is also called the heat pump loop.

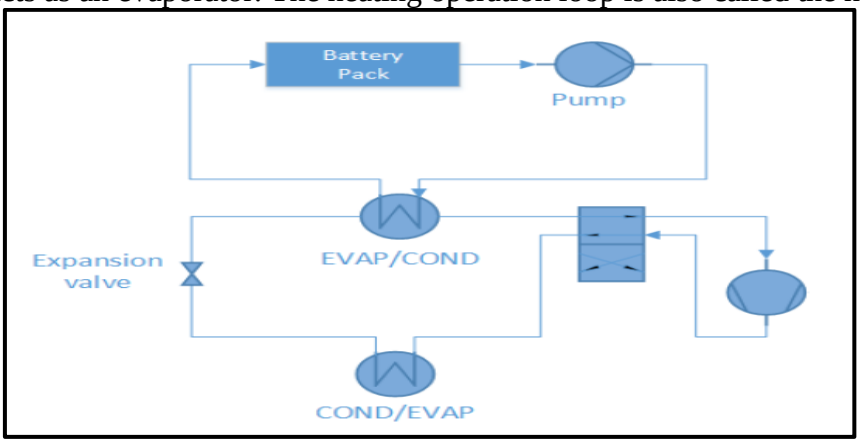

Fig (5) Active liquid system

3.3 Phase Change Material (PCM) in Lithium-Ion Batteries

PCM cooling systems perform well for thermal management. Even under high ambient temperatures from 45 ° C to 50 ° C, the temperature inside the cell bundle is always below 55 ° C due to the high thermal conductivity and latent heat. PCMs can absorb and release a large amount of thermal energy during their melting and freezing process, with outstanding advantages of storing or releasing the thermal energy at a constant temperature or with a narrow temperature range, communication technologies have been rapidly progressed. If a single cell fails, the thermal escape will not propagate because the PCM graphite matrix rapidly absorbs and distributes heat. The weakness of PCM is that it is more suitable for cold conditions or in space. PCM structure is simple, light and space-saving. But it still has flammability and electrical conductivity as well as resizing due to graphite PCM property. Recently, proposed the utilization of paraffin phase change material (PCM) with graphene fillers to enhance the performance of lithium-ion (Li-ion) batteries versus intense self-heating [13].

4. Simulation analysis of air cooling

This paper presents a review of batteries' thermal field simulation by studying the structure and working principle of monomer battery and the thermal field distribution of the battery pack using suitable simulation software and applied on the battery back. the thermal simulation of a single battery it is necessary to study the heat generation of a single battery by 3D- parameters of the battery, there a lot of software was used to build the three-dimensional model. Various parameters influence thermal distribution inside and outside the batteries such as the thickness of the battery, the material inside the

battery is regarded as uniform heating, the heat generation rate of the battery when the battery is discharged, and using the material parameters of the battery, the battery heating rate, the boundary conditions, it found the maximum temperature difference. By monomer battery simulation it could be seen that the highest temperature of the surface of the battery was 47.05 ℃, and the lowest temperature was 34.25 ℃, the difference of the temperature of was 12.8 ℃, and the temperature difference of 12.8 ℃ was more than reasonable temperature difference of 5 ℃ battery pack. Therefore, it was necessary to install the cooling system when the battery works in the battery pack.

5. Conclusion

The Li-ion battery is a promising alternative in many application of electrical devices such as mobile phones, laptop computers, and electric vehicles. However, the lifespan, performance and safety of Li-ion battery are strongly depended on their operating temperature. Inappropriate temperature will cause the power/capacity degradation, shorten the cycle life and may even cause the thermal runaway. Also, large unequal temperature among cells or within each cell may lead to the failure of battery. Therefore, Li-ion batteries should be maintained in a speceified temperature range. To this end, an effective thermal management system is critical to control the batteries within a desired temperature range. Additionally, it is essential to develop an accurate thermal model for Li-ion batteries to conduct numerical simulations. The cooling strategies are categorized into: internal cooling of lithium-ion batteries such as nanomaterials for separator, anode, cathode, and electrolyte, and external cooling of lithium-ion batteries such as air cooling, liquid cooling, and PCM. Among these approaches, the air cooling is the best way in electric vehicle power system, while liquid coolant has a higher thermal conductivity which makes it a more attractive choice as a cooling medium. As well, the nanomaterial play an important role for enhancing the performance of the lithium ion battery, many properties mentioned in the review enhanced by nanomaterials like electromechanical, thermal, capacity voltage and conductivity.

6. Acknowledgments

The authors appreciatively recognize the Egyptian Science and Technology Development Fund (STDF) for subsidizing this work among the STDF project with ID no. 43247.

7. References

[1]Z. Liu, Q. Hu, S. Guo, L. Yu, and X. J. A. M. Hu, "Thermoregulating Separators Based on Phase‐Change Materials for Safe Lithium‐Ion Batteries," vol. 33, no. 15, p. 2008088, 2021.
[2]G. Duan, S. Liu, and H. J. e.-P. Hou, "Synthesis of polyacrylonitrile and mechanical properties of its electrospun nanofibers," vol. 18, no. 6, pp. 569-573, 2018.
[3]K. Liu, Y. Liu, D. Lin, A. Pei, and Y. J. S. a. Cui, "Materials for lithium-ion battery safety," vol. 4, no. 6, p. eaas9820, 2018.
[4]X. Feng, M. Ouyang, X. Liu, L. Lu, Y. Xia, and X. J. E. S. M. He, "Thermal runaway mechanism of lithium ion battery for electric vehicles: A review," vol. 10, pp. 246-267, 2018.
[5]X. Feng, D. Ren, X. He, and M. J. J. Ouyang, "Mitigating thermal runaway of lithium-ion batteries," vol. 4, no. 4, pp. 743-770, 2020.
[6]M. Yuan and K. J. J. o. E. C. Liu, "Rational design on separators and liquid electrolytes for safer lithium-ion batteries," vol. 43, pp. 58-70, 2020.
[7]Q. Wang, L. Jiang, Y. Yu, and J. J. N. E. Sun, "Progress of enhancing the safety of lithium ion battery from the electrolyte aspect," vol. 55, pp. 93-114, 2019.
[8]J. Ou, S. Wu, and H. Wang, "Hydrothermal Preparation of Homogeneous Cobalt Nanomaterials as Stable Anodes for Superior Lithium Ion Batteries," vol. 34, no. 3, pp. 383-389, 2021.
[9]P. Lian *et al.*, "Design and synthesis of porous nano-sized Sn@ C/graphene electrode material with 3D carbon network for high-performance lithium-ion batteries," vol. 604, pp. 188-195, 2014.

[10] W. Wang and P. J. P. Alexandridis, "Composite polymer electrolytes: Nanoparticles affect structure and properties," vol. 8, no. 11, p. 387, 2016.
[11] Y.-S. Lee, W.-K. Shin, A. G. Kannan, S. M. Koo, D.-W. J. A. a. m. Kim, and interfaces, "Improvement of the cycling performance and thermal stability of lithium-ion cells by double-layer coating of cathode materials with Al2O3 nanoparticles and conductive polymer," vol. 7, no. 25, pp. 13944-13951, 2015.
[12] Y. Abu-Lebdeh and I. Davidson, *Nanotechnology for lithium-ion batteries*. Springer Science & Business Media, 2012.
[13] K. E. Drexled, "Engines of creation: the coming era of nanotechnology," 1986.
[14] G. A. Ozin and A. Arsenault, *Nanochemistry: a chemical approach to nanomaterials*. Royal Society of Chemistry, 2015.
[15] E. Roduner, *Nanoscopic materials: Size-dependent phenomena and growth principles*. Royal Society of Chemistry, 2015.
[16] H. Liu, Z. Wei, W. He, J. J. E. c. Zhao, and management, "Thermal issues about Li-ion batteries and recent progress in battery thermal management systems: A review," vol. 150, pp. 304-330, 2017.
[17] L. S. Wickramaratne, "Battery Thermal Management System," 2017.
[18] A. A. J. B. M. Pesaran, "Battery thermal management in EV and HEVs: issues and solutions," vol. 43, no. 5, pp. 34-49, 2001.

Hydraulic Performance of the Semi-Circular Breakwater for Coastal Protection

Ahmed A. Romya[1,a], Ahmed M. Abdelrazek[2,b], M.M. Iskander[1,c] and Hossam M. Moghazy[2,d]

[1]Coastal Research Institute, The National Water Research Center, Egyptian Ministry of Water Resources and Irrigation, Alexandria, Egypt.

[2]Irrigation Engineering and Hydraulics Dept., Faculty of Engineering, Alexandria University, Alexandria, Egypt.

[a]ahmedromya12@yahoo.com, [b]ahmedmrazek@alexu.edu.eg, [c]coastal_alex@yahoo.com, [d]hossam_moghazy@yahoo.com

Keywords: *Computational fluid dynamics, Flow-3D, Numerical simulation, Semi-circular breakwater*

Abstract. Breakwaters, for example, are structures designed to sustain and dissipate the energy produced by waves. They help stabilize the coast and preserving ports, beaches, and other coastal resources and habitats. Due to their aesthetic advantages and high structural efficiency, semi-circular breakwaters have been used in various locations worldwide. Coastal structures are subject to hydrodynamic forces usually estimated through physical models and experiments, which still a realising tool to study and design such systems. However, these models are difficult to implement, requiring high costs and long experimental procedures. Thus, alternative methodologies for analysing the hydrodynamic efficiency of these structures are extremely beneficial. In this study, a two-dimension wave flume model and the computational fluid dynamics tool (Flow-3D) are used to study the efficiency of the semi-circular breakwater (SBW). The numerical model was calibrated and tested using experimental data, taking into account the effects of water depth and wave characteristics. The results show that the numerical model accurately simulates wave flume and semi-circular breakwater interaction with the fluid. Furthermore, SBW has demonstrated its high efficiency in dissipating waves by 65 to 80% when partially submerged.

Introduction

There are three approaches to study the coastal structures by measuring and observing from the field, laboratory study, and mathematic models. Although the expansion of using numerical models in coastal engineering; has not made physical models outdated. Recently, a new concept of "hybrid modeling" appeared where physical model results were used as input for numerical models and alternately [1]. [1,2] classified the physical models into several types, Fig. 1.

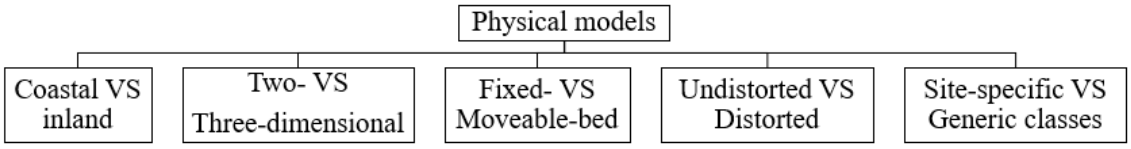

Fig. 1: Classification of the physical model types.

[3] compared between Physical Simulation (PS) and Numerical Simulation (NS), and reported that once the methodology of numerical code is learned, it can take a short time by mouse clicks to simulate any coastal conditions. In PS, wave data is recorded at defined locations by wave gauges or optical readings. While numerical data is extracted at any point of the grid, it gives the entire image for any complex problem. Additionally, all types of waves can be generated in NS, unlike PS. Roughly 71 % of the earth's surface area covers the blue water of oceans and seas. The position at

which these waters met land is the coastline. Coastal protection is an urgent need in many coastal areas to retrieve the land depleted by sea attacks. The SBW is characterized by a lightweight hollow structure for weak bed soil, curvature shape which reduces wave force and dissipates wave energy as wave run-up. This structure is also prefabricated, which decreases construction time. This paper aims to study the hydraulic performance of the semi-circular breakwater using physical and numerical models. The structure will be installed directly on the bed without a rubble mound base to exclude the effect of base.

Experiment Work

The physical modeling mission is to understand structure behavior and its effect on the hydrodynamic parameters and bed morphology within controlled conditions [2]. Most of the coastal structures are model tested to reach the optimum design where all the available design equations are empirical formulas with many limitations.

Wave Flume. The experiments were carried out in the physics lab of the Coastal Research Institute at the Abu - Quir research station in Alexandria, Egypt. It is executed in a wide wave flume of 40 m long, 1.20 m wide, and 1.20 m deep, Fig. 2. The flume bed was reshaped with a sand layer with a maximum height of 0.30 m and a ramp of 1:10, both covered by cement mortar to create deep and transition zones with a fixed bed.

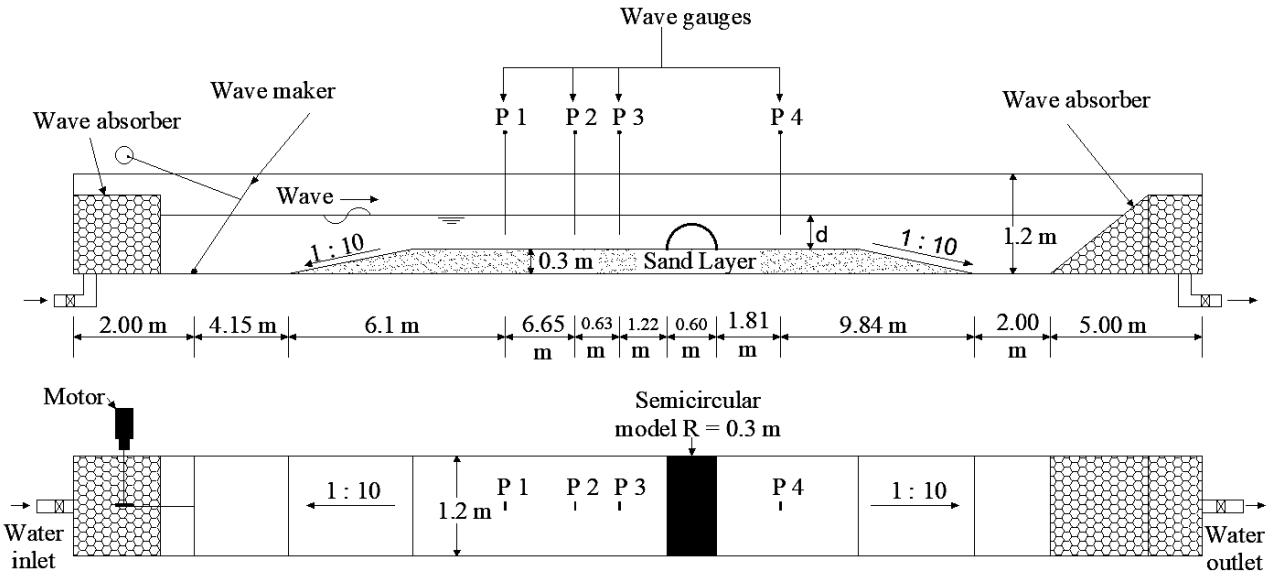

Fig. 2. Schematic diagram of the experiment setup.

Regular waves up to 30 cm height and 3.0 sec period were generated by a flap stainless-steel paddle plate that hinged at one end of the flume bed. Passive wave absorbers are installed to reduce the amount of reflection from end walls and enhance the quality of wave generation. In this work, four-wave gauges (P1, P2, P3, and P4) were installed at the flume center alignment at 10.25 m, 16.9 m, 17.53 m, and 21.16 m from wave paddle to measure the fast changes in water level. The first and the last gauges measure incident and transmitted wave properties, respectively. The second and third gauges obtain the incident regular and reflected irregular waves, which can be separated by measuring the wave elevations at two known positions on a line parallel to the direction of wave propagation [4]. At the beginning and end of each series of experiments, all the wave probes were carefully calibrated.

Model Installation. The wide flume model is used to check the efficiency of the smooth solid semi-circular breakwater (SBW) of radius R= 0.30 m and long l= 1.18 m installed and fixed on the flume fixed bed, Fig. 3 – a. It was constructed on a scale of 1:10 from a steel frame covered by a cladding

aluminum sheet of 0.40 mm thickness. Radial stiffeners were added to brace the model from sway. Fig. 3 – b presents model installation.

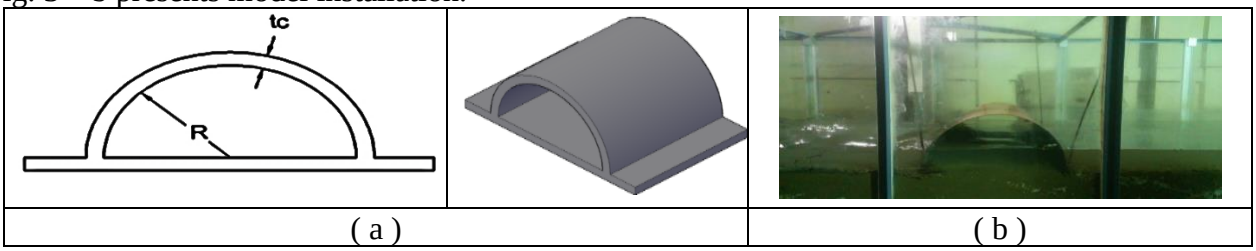

Fig. 3: a - Isometric view and cross-section for SBW, b - Structure installation during physical model experiments.

Test Series. The experiments were divided into; Group A without structure and Group B with semi-circular structure. The two series of experiments were conducted under the same conditions. All experiments are subjected to a group of wave periods (T) range from 1.25 to 3 sec. with 0.25 sec. interval and water depths (d) equal 0.20, 0.30, and 0.40 m, corresponding to merged, crest with still water level and submerged structure respectively.

Numerical Model

Flow-3D software [5] is used to solve governing equations to simulate the fluid characteristics based on solving RANSE (Reynolds-averaged Navier-Stokes Equation). This software implements the Volume of Fluid VoF method applied to track the free surface [6]. Computational hardware used for all the simulations presented as follows: Computational Specifications = Dual Intel Xeon Processor E5-2687W V3 (10C HT, 25MB Cache, 3.1 GHz Turbo) with 128GB 2133MHz DDR4 Memory.

Model Setup. The geometries used in this research were exported as a stereolithographic (.stl) format from Auto-CAD 3D to the Flow-3D model. Regular structured grid cells are employed with varying sizes according to the zone's weightiness, fine at fascinating places, and course at inlet and outflow gradually to achieve high accuracy, low simulation time, and good grid skewness ratio.

Many trials have been conducted to settle grid resolution. The trials show that 0.005 m, 0.01 m, and 0.05 m cell dimensions around structure, at relaxation zones and boundaries, respectively, are the best for our case Fig. 4. Simulation time was 20 seconds, with an initial time step 0.01 sec., which is sufficient to catch the rapid change in free surface.

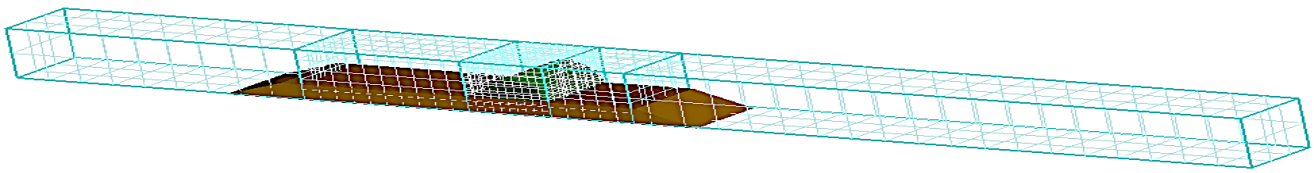

Fig. 4: Numerical domain of the model and the domain discretized grid.

In our simulation, the water is considered a Newtonian fluid, the LES turbulence model is used to simulate the turbulency and details of flow fluctuation. One fluid was used, which means that the upper region of fluid has negligible inertia relative to the water inertia. The stokes wave ('Fenton's 5th-order theory) is generated at the inlet boundary [7]. Wave absorbing layer is installed before an outflow boundary reduces wave reflection from the boundary on the right [5]. Symmetry boundary type is applied at the sidewall, the top of the domain, and each mesh block's edges to decrease calculations, while the bottom is a wall type [7,8]. Four probes are applied at the exact locations in the physical experiments for monitoring free water surface elevation, which is used in model calibration, validation, and wave series analysis.

Calibration and Validation. The target of verification and validation guarantees reasonable results for a specific range of flow problems produced using the Computional Fluid Dynamics CFD code.

The experimental study within the flume without structures was used to calibrate the numerical model. In contrast, experimental studies with the structure were used for the model verifications. The results show strong correlation coefficients R^2 between the numerical and physical models range between 0.93 and 0.98 at the four locations of wave probes, Table 1 and Fig. 5. The numerical model success in simulating the semicircle structure interaction with the fluid with high accuracy.

Table 1: Calibration and validation of the numerical model using the experimental results.

Case	Action	d (m)	T (sec)	R^2
No structure	Calibration	0.20	2.55	0.93,0.98,0.98,0.92
	Validation	0.40		0.97,0.97,0.96,0.97
SBW	Validation	0.20	1.9	0.95,0.93,0.97

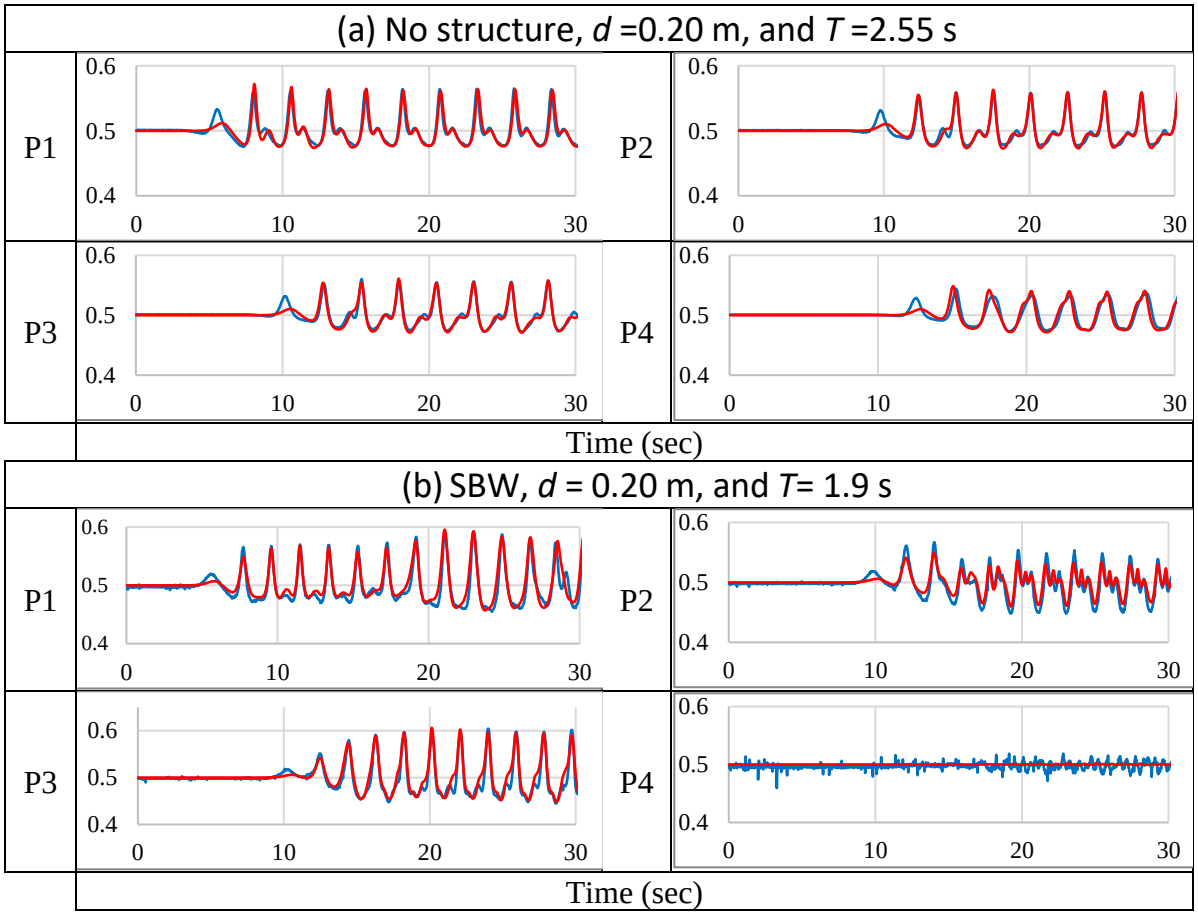

Fig. 5: Numerical model (Red) calibration and verification for the free surface elevation at probes 1, 2, 3, and 4 for (a) No structure, (b) SBW compared with physical model results (Blue).

Results and Discussion

After calibration, the numerical model is used to study the structure efficiency for the different submergence values (d/R) and the wave steepness (Hi/gT^2). Twenty-five numerical model runs were carried out for the dominant, real, and effective regular wave characteristics. Table 2 shows the input wave features for different numerical model simulations.

Table 2: Characteristic of generated wave in numerical models.

d/R	(H_{in}, T_{in})									
0.67	(0.04, 1.9)	(0.055, 1.95)	(0.07, 2)	(0.085, 2.05)	(0.1, 2.1)	(0.115, 2.15)	(0.13, 2.2)	--	--	--
1.0										

1.33								(0.16, 2.3)	(0.19, 2.4)	(0.22, 2.5)

Wave heights implemented within the range of applicability, in which wave height does not exceed breaking condition $H_b = 0.78\ d$, the wave impinges the structure. Table 3 summarizes the result of the analyzed data for the numerical model. It illustrates the structure's efficiency in dissipating waves by values of coefficient of reflection (*Kr*), transmission (*Kt*), and dissipation (*Kd*).

Table 3: Summary for results analysis.

Coefficient	$d/R = 0.67$	$d/R = 1$	$d/R = 1.33$
Kr	0.98 to 0.99	0.39-0.67	0.37-0.52
Kt	0.01- 0.08	0.46-0.65	0.61-0.75
Kd	0.03- 0.20	0.65-0.8	0.5-0.67

Fig. 6 shows that the reflection coefficient decreases with the increase in the water depth and increases wave steepness. It also demonstrates that the transmission coefficient rises with increasing water depth and decreases with increasing wave steepness. As a result, one of the main drawbacks of this type of structure is wave reflection. As a result, using SBW as a submerged coastal protection structure with the lowest reflection coefficient is ideal.

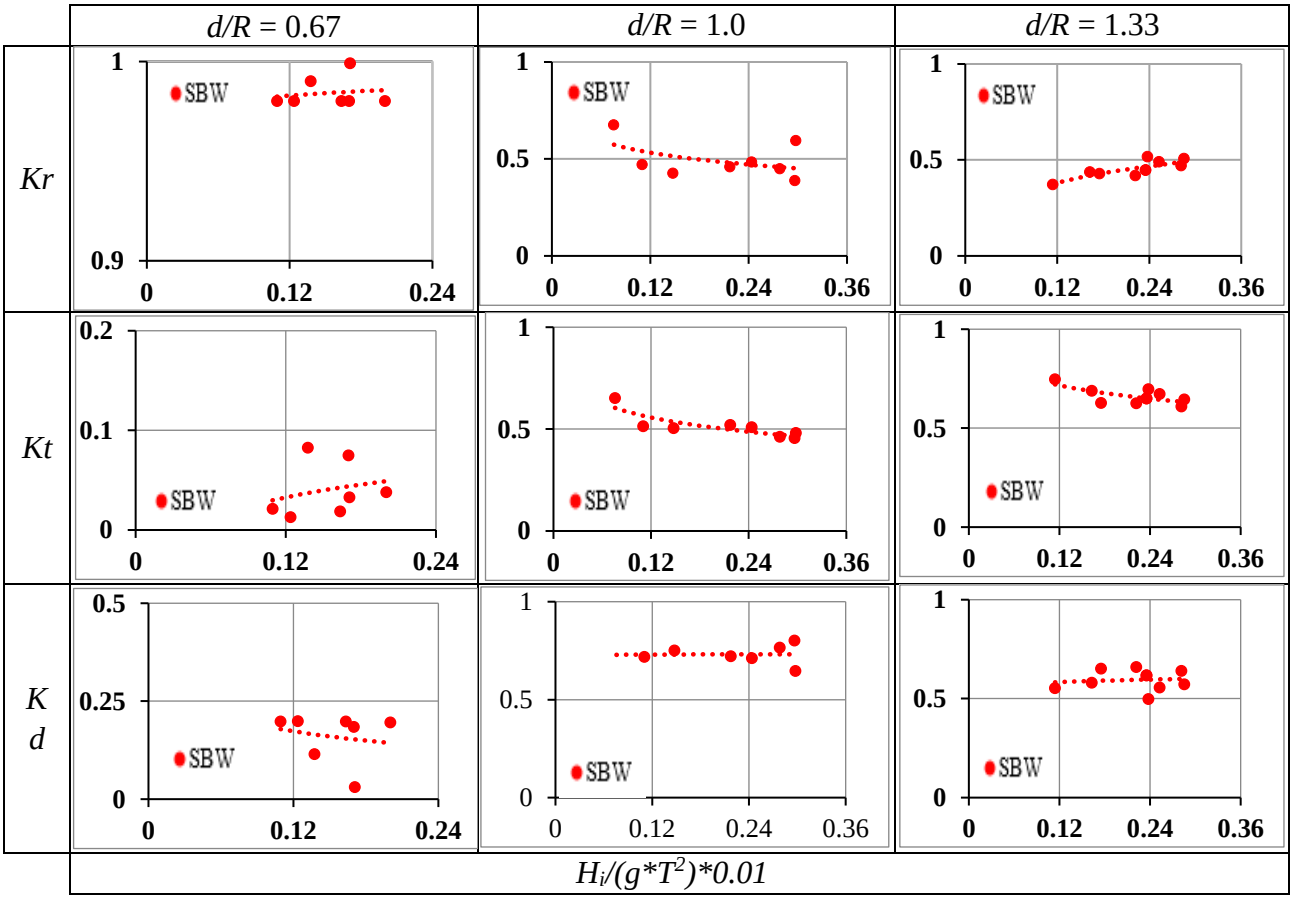

Fig. 6: Effect of the emerged, partially submerged, and Submerged structure on the wave characteristics.

Conclusions and Recommendations

This study aims to identify the hydraulic performance of semi-circular breakwater. Besides experiment measurements, numerical simulations have been executed to widen the physical model results and check the structure under different hydrodynamic conditions. The flume without and with

SBW was tested physically under the same conditions. The results were used to calibrate and validate the numerical Flow 3D model based on the Reynold Average Navier-stocks equation and Large-eddy simulation turbulent model. The calibration revealed that the agreement correlation coefficients ranged from 93 to 98 percent. The study represents the efficiency of SBW coastal protection structure in dissipating waves by 3 - 20 %, 65 - 80 %, and 50 - 67 % for different depths of submergence 0.67, 1, and 1.33, respectively. The structure, on the other hand, substantially amplifies the reflected wave. So, to improve the structural efficiency, it is advised that the structure be changed to a corrugated semi-circular or perforated semi-circular breakwater.

Acknowledgments

This work is supported by the Coastal Research Institute (CoRI).

References

[1] S. A. Hughes, *Physical Models and Laboratory Techniques in Coastal Engineering*. World Scientific Publishing Co., 1993.

[2] M. J. Briggs, "Basics of Physical Modeling in Coastal and Hydraulic Engineering," *US Army Corps Eng.*, vol. 1, no. September, p. 11, 2013, [Online]. Available: https://www.researchgate.net/publication/258440862_Basics_of_Physical_Modeling_In_Coastal_and_Hydraulic_Engineering.

[3] T. Kasem, "Development of a Generic Numerical Wave Tank Coupling Solid, Liquid and Air," Yokohama National University, 2010.

[4] Y. Goda and Y. Suzuki, "Estimation of incident and reflected waves in random wave experiment," *Coast. Eng.*, pp. 828–845, 1976, doi: 10.1061/9780872620834.048.

[5] Flow Science, "Flow 3D user manual," 2020.

[6] C. W. Hirt and B. D. Nichols, "Volume of Fluid (VOF) method for the dynamics of free boundaries," *J. Comput. Phys.*, vol. 39, pp. 201–225, 1981, doi: https://doi.org/10.1016/0021-9991(81)90145-5.

[7] G. Wei and M. Barkhudarov, "Surface wave models in FLOW-3D," *Flow Sci. Inc.*, 2012.

[8] A. Paci, "Numerical analysis of floating structures for off-shore and harbour engineering," 2018.

Influence of Upstream Impervious Blanket with Vertical Cutoff on Seepage through Earth Dam

Mohamed Amer[1, a], M.A. Abourohiem[1,b] and Ahmed M. Abdelrazek[1,c]

[1]Irrigation Engineering and Hydraulics Dept., Faculty of Engineering, Alexandria University, Alexandria, Egypt.

[a]eng.mohamed.amer@alexu.edu.eg, [b]mohammed.abourohiem@gmail.com, [c]ahmedmrazek@alexu.edu.eg

Keywords: *Analytical solution, Control measures, upstream impervious blanket, confined seepage, Unconfined seepage.*

Abstract. Dam failures result in the loss of lives and money; therefore, reducing seepage and enhancing dam stability are essential. As a result, seepage control measures must be installed on earth dams to be safe and stable against the harmful effects of seepage through them. The upstream impervious blanket, linked with the dam core, is an acceptable measure for controlling seepage through earth dams based on previous foundations of great or infinite depths. The effect of the upstream impervious blanket on seepage features, such as seepage discharge, head loss, and the free surface location, is investigated in this work using an analytical solution based on both confined and unconfined seepage ideas. Analytical formulas are developed to calculate the seepage discharge, the maximum height of the free surface, the head loss, and the free surface position. Results revealed that the proposed control measure could reduce the seepage discharge, increases head loss, and lowers the free surface to a large extent when applied on Shiwashok earth dam, in Iraq, as a case study.

Introduction

Earth dams are commonly constructed on alluvial layers with high permeability, allowing water to seep through the soil pores and create mechanical drag forces on soil particles. If these forces exceed the resistance force of the soil grans, movements of grans may occur, especially at the seepage exit, leading to undermining of soil particles by piping or upheaval, which may lead to irreversible damages in the long term of use. In addition, a huge amount of water may be lost by under-seepage, which is of great economic concern in storage dams.

According to the foundation depth, several techniques can be employed to control seepage through earth dams, such as clay trench for shallow depths, vertical cutoff walls for moderate depths, and upstream impervious blanket for deep depths [1]. According to [2], penetration of the vertical cutoff by 90 % and 50 % reduces discharge by 64 % and 25%, respectively, which is economically unacceptable. Therefore, the upstream impervious blanket is the best choice to control seepage through earth dams based on pervious foundations with great or infinite depths.

Despite the effectiveness of the upstream impervious blanket as a seepage control measure, few works were oriented to analyze its effect on seepage through earth dams. Recently, some numerical models based on the finite element method were applied to study the performance of the upstream impervious blanket [3,4,5]. A few analytical solutions, mostly close to empirical forms, were presented in the previous studies [6,7].

It is seen from the previous studies that there is no exact or complete solution to analyze the performance of the upstream impervious blanket. Also, the free surface location behind the blanket is not accounted for, although it is only the determiner parameter to evaluate the pore water pressure. Therefore, it is urgent to establish a complete analytical solution to estimate the seepage characteristics, seepage discharge, head loss, and location of the free surface. In the present work, a closed-form solution is presented to define the above seepage parameters.

Definition of the studied problem

2. The statement of the current study is to develop an analytical solution for analyzing the effect of the upstream impervious blanket when used to control the seepage through earth dams resting on a deep pervious foundation. For this purpose, the main parameters involved in the present problem are defined considering a physical model for an earth dam based on a pervious foundation of depth (T) and provided with an upstream impervious blanket, as shown in Fig. (1). The dam embankment has a height (H_d), top width (b), base width (B), and slope factors $m_1 = cot\alpha$ and $m_2 = cot\beta$ where α and β are the angles of the embankment faces. The upstream impervious blanket has a length (L_b) and thickness (t_b). The blanket is connected to a thin core and extends upstream the dam to a distance (X_b). A vertical cutoff of depth (S) is fixed to the blanket at its connection with the core to increase its effectiveness. (h_1) and (h_2) are the head and tailwater depths, while (h_3) is the height of the seepage surface. The head loss due to the blanket is (ΔH), and (h_f) is the height of the free surface at any fractional distance (X_f) from the point of the origin (O).

3.

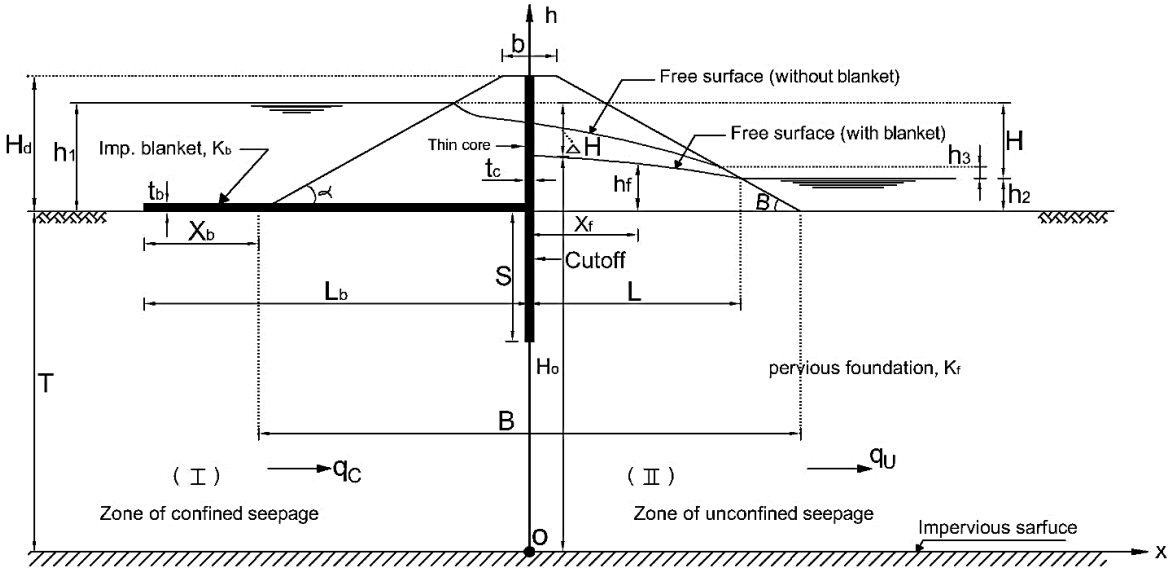

4. Figure (1) Definition sketch for the studied problem

Analytical solution

First of all, some assumptions must be made to facilitate the solution; (i) The embankment and foundation are of homogeneous soil, having the same conductivity coefficient (k_s), (ii) Effect of thickness of both core and blanket is neglected since it is too small compared to the seepage field dimensions, and (iii) The height of the seepage surface (h_3) is not considered because the free surface is flatter compared to the case without a blanket. Considering a complete impervious blanket of conductivity coefficient k_p = 0.0, the blanket with the cutoff act as a solid floor with a sheet pile for a hydraulic gravity structure, overlying a pervious layer of depth (T). As shown in Fig. (1), the seepage field is divided into two zones: (I) and (II). Zone (I) of a length (L_b) is equipped by confined seepage, while in Zone (II) of length (L), unconfined seepage occurs. The two types of seepage are, simultaneously take place in the same seepage domain.

Confined seepage. The seepage flow below the impervious blanket of length (L_b) and provided with cutoff with depth (S) typically presents the confined seepage problem, under a floor of a hydraulic gravity structure, due to an effective head ($\boldsymbol{H}$) [8], Pavlovsky's solution (1956) can be used to define the seepage discharge for this case due to the effective head ($\Delta\boldsymbol{H}$), where

$$q_c = K_s\,\Delta H\,\frac{K'}{K}, \tag{1}$$

5. where, Ks is the conductivity coefficient for the foundation soil, H is the effective head, and K', K are the constants of the complete elliptic integral of the first kind. Values of K'/K can be found from special tables [9], as a function of the modulus (m), where,

$$m = \cos\left(\frac{\pi}{2}\frac{S}{T}\right)\sqrt{tanh^2\left(\frac{\pi}{2}\,\frac{L_b}{T}\right) + tan^2\left(\frac{\pi}{2}\frac{S}{T}\right)}\quad , \tag{2}$$

$\Delta H = (T + h_1) - H_o,$ and

H_o is the maximum height of the free surface, just behind the core, at point of origin (O). Substituting for ΔH in Eq. (1), yields

$$q_c = K_s(T + h_1 - H_o)\frac{K'}{K}\ , \tag{3}$$

Unconfined seepage. Considering a two-dimensional flow on a horizontal impervious boundary and satisfying Depuit assumption, the seepage discharge, using Darcy's law, is

$$q_u = \frac{K_s}{2L}\left[{H_1}^2 - {H_2}^2\right], \tag{4}$$

6.

7. where; H_1 and H_2 are the elevations of two points on the free surface, with distance (L) in between.

8. Applying Eq. (4) on the unconfined seepage, in the zone (II), where $H_1 = H_o,$ and $H_2 = T + h_2$, the seepage discharge, (q_u) is

$$q_u = \frac{K_s}{2L}\left[{H_o}^2 - (T + h_2)^2\right], \qquad and\ . \tag{5}$$

$$L = \frac{b}{2} + m_2\,(\ H_d - h_2) \tag{6}$$

Correlation between confined and unconfined seepage. For a steady seepage condition, the discharge of both confined and unconfined seepage is the same, then $q_c = q_u = q$. Thus, equating the right-hand sides of Eqs. (3) and (5) gives

$K_s(T + h_1 - H_o)\frac{K'}{K} = \frac{K_s}{2L}\left[{H_o}^2 - (T + h_2)^2\right]$, Then

$${H_o}^2 + 2\,L\,H_o\frac{K'}{K} = (T + h_2)^2 + 2\,L(T + h_1)\frac{K'}{K}, \tag{7}$$

9. Adding the term $(\mathrm{L}\frac{K'}{K})^2$ to each side of Eq. (21), and rearranging yields

10.

$$H_o = \sqrt{(T+h_2)^2 + 2\,L(T+h_1)\frac{K'}{K} + \left(L\frac{K'}{K}\right)^2} - \left(L\frac{K'}{K}\right), \quad (8)$$

11. Once the value of (H_o) is found, the seepage discharge can be calculated using Eq. (3) or Eq. (5). The height of the free surface (h_f) at any fractional distance (X_f) can be found using Eq. (5), but in the form,

$$h_f = \sqrt{{H_o}^2 - \frac{2q}{K_s}X_f} - (T), \quad (9)$$

12.

13. The effectiveness of the upstream impervious blanket is evaluated by defining the percentage reduction in the seepage discharge $(\Delta q\%)$. The seepage discharge(q_o), for the case of earth dam without a blanket (reference case) can be found using Nedrigy solution (1983) [10]. If q is the discharge in the case of the dam with a blanket, then the percentage seepage reduction $\Delta q\%$ is,

14.

$$\Delta q\% = \frac{q_o - q}{q_o} \times 100, \quad (10)$$

Applications of the analytical solution

15. Based on Eq. (2), the presented analytical solution can be applied considering three cases; (i) blanket without cutoff, (ii) blanket with cutoff, and (iii) cutoff without a blanket. In all cases, both the maximum height of the free surface (H_o) and the seepage discharge (q) are estimated using Eqs. (8) and (3), respectively.

Blanket without cutoff. This case is the most existed in practice. To satisfy such a case, substitute for S = 0.0 in Eq. (2), yields,

$$m = tanh\left(\frac{\pi}{2}\frac{L_b}{T}\right). \quad (11)$$

16.

Blanket with cutoff. In this case, the blanket has a cutoff with depth (s), for which Eq. (2) is valid to find the value of the modules (m).
Cutoff without a blanket. Substituting for the blanket length L_b= 0.0, in Eq. (2), the modules (m) becomes,

$$m = \mathrm{Sin}(\frac{\pi}{2}\frac{S}{T}), \quad (12)$$

17. In this case, the cutoff is vertically joined to the core, which is out of scope in the present study.

Case study (Shiwashok dam)

18. As a case study, the established analytical solution was applied to the Shiwashok earth dam. Shiwashok earth dam is proposed for construction in Iraq's Kurdistan region. However, because of the economic downturn, the dam had not yet been completed. Concerning the data reported [5], the dam cross-section is as given in Fig. (2). The final proposed design of the Shiwashok dam did not include a clay blanket. Therefore, in the present study, a blanket with cutoff is suggested to control the seepage flow through

the foundation below the dam. In the following analyses, two cases will be considered; (i) blanket without cutoff, and (ii) blanket with cutoff at its connection with the core.

19.

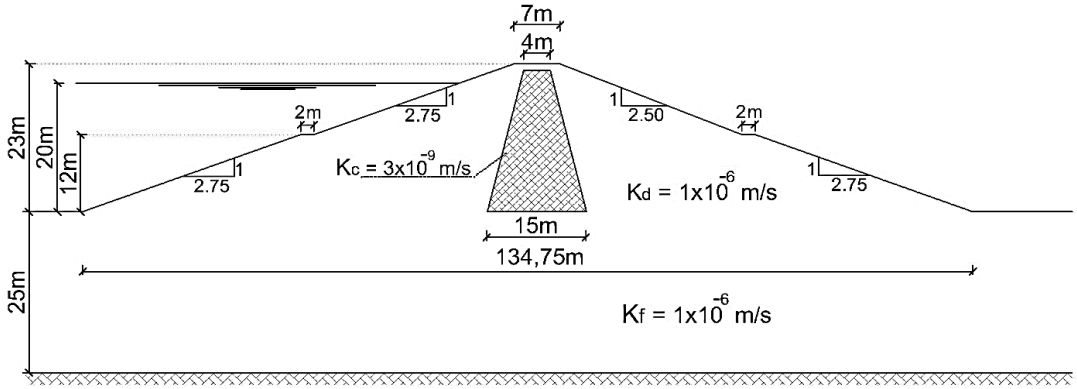

Fig. (2) Section through Shiwashok dam, [5]

Blanket without cutoff. Using values of the dam base B = 135 m and H= 20m in Eqs. (11) and (12), the effect of the blanket length (L_b) on the relative values of both seepage discharge (q/K_sH) and the loss of head ($\Delta H/H$) is analyzed considering the foundation depth T=25m. Different relative values of the blanket length (L_b/B) = 0.50, 1.00, 1.50, 2.00 are used to declare the effect of blanket length, as shown in Fig. (3). The seepage discharge is rapidly decreased up to L_b/B= 0.75, followed by a slight decrease up to L_b/B= 1.50, after which a poor effect is found. Thus, the effective length of the blanket is then equal to five times the head H, which agrees well with the numerical solution [5]. Regarding the relative head loss (ΔH/H) effect, the same result is found where the head loss significantly increases up to L_b/B= 0.75, beyond which a slight increase exists.

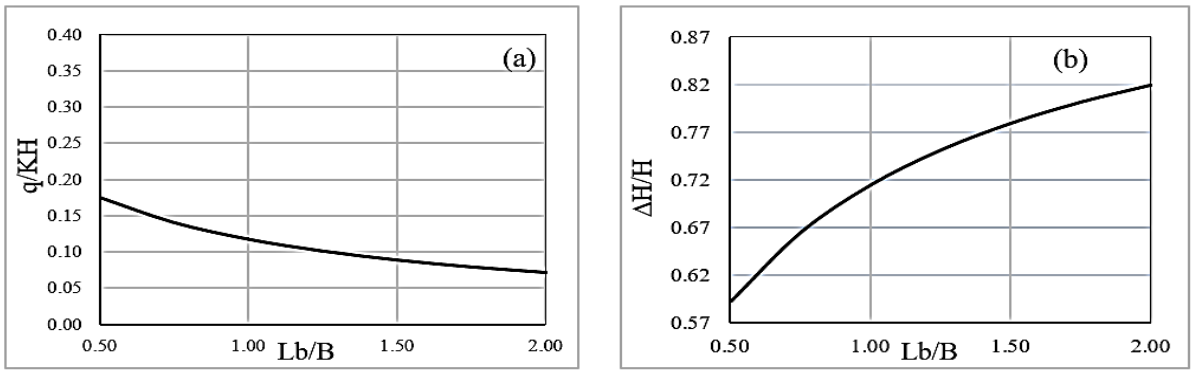

Fig. (3) Effect of relative blanket length (Lb/B) on (a) relative discharge (q/K_sH), and (b) loss of head ($\Delta H/H$) for T=25m

20.

Considering Shiwashok earth dam, a comparison is conducted between the current solution's results and those obtained analytically and numerically by [5,7], as shown in Fig (4). It is seen that a more reduction in the seepage discharge is obtained using the present solution refers to the effect blanket conductivity, which is assumed to be zero. On the other hand, a good agreement exists between the current solution and the numerical one presented by [5] within the range of L_b/B= 5 H.

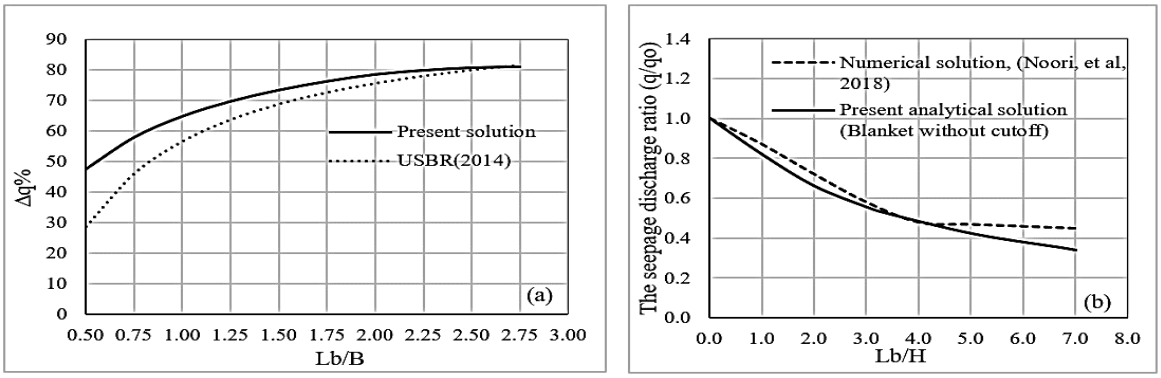

Fig. (4) Comparison of the present analytical solution with; (a) solution of [7] and (b) numerical solution presented by [5]

Blanket with cutoff. Using a relative blanket length L_b/B= 0.75, the relative cutoff depth (S/T) effect, on both seepage discharge and head loss, is tested for a relative cutoff depth S/T= 0.1 ~ 0.8, as shown Fig. (4). It is seen that the seepage discharge decreases while the head loss increases but with a very small rate (2.0%) for both. Thus, the cutoff nearly does not affect the small depth of foundation, T=25m, which presents 0.186 of the dam base width. In fact, for deeper foundation depth, T = 50, 75, 100, and 150m, the cutoff depth has a significant effect, as shown in Fig. (5). The poor effect of the cutoff in shallow foundation depth is referred to that the seepage flow field simulates flow in a long pipe, in which local losses due to cutoff is too small compared to length losses caused by the blanket. For long pipes with a small diameter, the local losses are too small compared to friction losses.

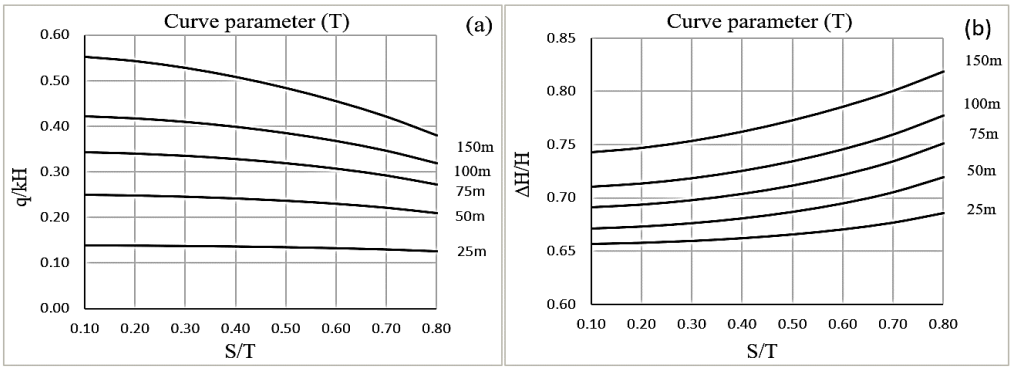

Fig. (5) Effect of the relative cutoff depth (S/T) for blanket length (Lb/B) = 0.75 on; (a) relative discharge (q/K_sH), and (b) Relative loss of head ($\Delta H/H$).

Conclusions

As a result of the above analyses, the obtained conclusions are given below.

1- A new analytical solution is developed for seepage through an earth dam controlled by an upstream impervious blanket with a vertical cutoff.
2- Applying such a solution, one can get the values of seepage discharge, loss of head, and location of the free surface.
3- For the Shiwashok dam, the cutoff has a negligible effect due to the shallow foundation depth. However, the cutoff significantly addresses more impacts for deeper foundation, where the foundation depth $T \geq 0.50$ of dam base width (B).

References

[1] USBR, Embankment Dams, Chapter (5), Seepage Analysis, U.S Department of the Interior, Bureau of Reclamation, Washington, D.C. (1987).

[2] Punmia, B.C., Lal, P.B.B, Jain, Ashok, K., and Jain, Arun, k. Irrigation and Waterpower Engineering. (An ISO 9001: 2015 Company) New Delhi, India, (2019).
[3] Alam, I. and Ahmad, I., Sensitivity study of different parameters affecting design of the clay blanket in small earthen dams, Journal of Himalayan Earth Sciences Volume 48(2) (2015), 139-147.
[4] Salmasi, F. and Noori, M., Effect of upstream semi-impervious blanket of embankment dams on seepage, ISH Journal of Hydraulic Engineering 25 (2), (2017), 143-152.
[5] Noori, M. Ibrahim, H. and Hasan, A. Influence of upstream blanket on earth dam seepage, 4th International Engineering Conference on Developments in Civil & Computer Engineering Applications (ISSN – 2409-6997), (2018).
[6] Bennett, P.T., The Effect of Blanket on Seepage through Pervious Foundation, trans. American Society of Civil Engineers, 3, (1946), 52-61.
[7] USBR, Embankment Dams, Chapter (8), Seepage phase 4, US Department of the Interior, Bureau of Reclamation, Washington, D.C., (2014).
[8] Harr, M. E., Groundwater and seepage Dover publications, INC. New York., (1962)
[9] Abramowitz, M., and Stegum, I. A., Handbook of mathematical functions with formulas, Graphs, and mathematical tables. National Bureau of Standards Applied Mathematics Serie, USA., (1970).
[10] Nedrigy, V. P., Hydraulic Structures. In Russian Gostroyzdat, Moscow, Russia., (1983).

Flow Over Side Weirs with a Parabolic Shape: an Experimental Investigation

Ramadan A. Moutawee[1,a], M.A. Abourohiem[1,b] Ahmed M. Abdelrazek[1,c]

[1]Irrigation Engineering and Hydraulics Dept., Faculty of Engineering, Alexandria University, Alexandria, Egypt.

[a]ramadan.metawee2018@gmail.com, [b]mohammed.abourohiem@gmail.com
[c]ahmedmrazek@alexu.edu.eg

Keywords: Broad crested weir, Sharp-crested weir, Side weir, Parabolic shape.

Abstract. A side weir is a hydraulic structure that diverts water from the main channel to a side one. It is widely used in irrigation engineering, sewer networks, and flood protection. Previous research had focused on flow over side weirs with a rectangular shape, and a little attention was paid to side weirs with a triangular shape. Side weirs with a parabolic shape, on the other hand, had never been addressed before. As a result, the current paper focuses on analyzing flow characteristics over side weirs with parabolic shape, discharge coefficient, and discharge ratios. The experiments are carried out on two types of weirs: broad and sharp-crested side weir with three parabolic parameters. The main channel Froude number, parabola's parameter, and weir length are the main parameters influencing flow characteristics. The study's findings are represented graphically in the form of charts and formulae with no dimensions.

Introduction

A side weir is an open, formed in the side of the main channel, to divert or spill part of the main flow into the side channel when rises above the crest level. Side weirs are widely used in many practical situations; (i) irrigation and drainage networks to control, and regulate both discharges and levels, distribute irrigation water on branches and distributaries, escape excess discharges of the main canals at the intermediate escapes and spill river floods at dam spillways, (ii) stormwater overflow from urban sewage systems, and (iii) water plants as discharge measurement devices.
The side weir open may have, rectangular, triangular, or trapezoidal shape with a sharp or broad crest. The hydraulic characteristics of flow over rectangular side weirs, discharge coefficient, and surface water profile along the weir open, had been extensively investigated in the previous studies) [1, 2, 3, 4, 5, 6, 7, 8], and with a little extent for triangular and trapezoidal shapes [9, 10, 11, 12, 13, 14, 15]. In contrast, side weirs with parabolic shape had not been dealt with in the previous works. Therefore, the present paper is intended to study the flow characteristics over parabolic side weirs with a sharp or broad crest, as shown in Fig. (1). An experimental study is conducted to study the influence of various parameters on the discharge coefficient and relative side weir discharge

Theoretical approach

Flow over side weirs is a typical example for spatially-varied flow with decreasing discharge expressed by the following equation,

$$dy/dx = \left(S_o - S_f - \left(\frac{dQ}{dx}\right)\left(\alpha\left(\frac{Q}{gA^2}\right)\right)\right) \Big/ \left(1 - \left(\alpha\frac{Q^2T}{gA^3}\right)\right), \quad (1)$$

Concerning Fig. (1), *y* represents the depth of flow at any section, *x* represents the distance along the side weir between sections 1 and 2, *g* is the gravity acceleration, and *dy/ dx* represents the water

surface slope. For the main channel, S_o is the bed slope, Q is the discharge, S_f is the friction slope, α is the kinetic energy correction factor, and A is the cross-sectional area. For the side weir, $-dQ/dx$ is the discharge per unit length over the side weir, and T is the top width of the flow.

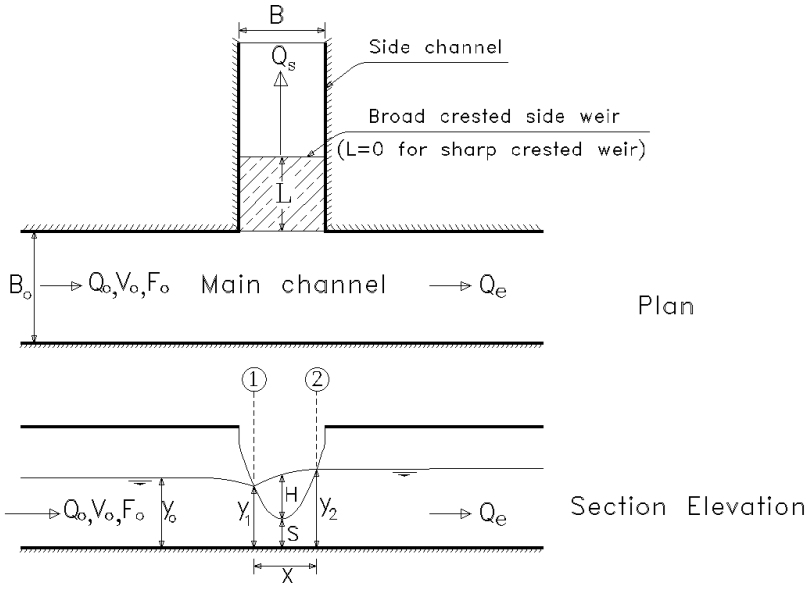

Fig. (1) Definition sketch for flow over Parabolic side weir

Assuming that both the main and the side channels are rectangular sections and prismatic, therefore α =1, and $S_o - S_f = 0$, Eq (1) is simplified as

$$dy/dx = \left(Q\, y \left(-\frac{dQ}{dx}\right)\right) \Big/ \left(g\, {B_o}^2\, y^3 - Q^2\right), \tag{2}$$

Where B_o is the main channel width. The discharge equation for a side weir with a parabolic shape per unit length is

$$-dQ/dx = \left(\frac{\pi}{2\sqrt{2}}\, C_d \sqrt{2g}\ \sqrt{P}\, (y-s)^2\right) \Big/ \left(2\sqrt{2}\, \sqrt{P}\, (y-s)^{0.5}\right) = \frac{\pi}{8}\, C_d \sqrt{2g}\, (y-s)^{1.5}, \tag{3}$$

Where C_d is the discharge coefficient, P is the parameter of the parabola, and S is crest height. Assuming that the specific energy, E is constant along the length of the side weir, the discharge in the main channel is given by

$$Q = B_o\, y \sqrt{2g(E-y)} \tag{4}$$

From the system of equations (2) through (4)

$$dx = \frac{4\, B_o}{\pi\, C_d} \left((3y - 2E) \Big/ \sqrt{(E-y)\, (y-s)^3}\right) dy \tag{5}$$

Integrating between section 1 and 2 yields,

$$C_d = \frac{8\, B_o}{\pi\, x}\, (\phi_2 - \phi_1), \quad \text{and} \tag{6}$$

$$\phi_i = \frac{2E-3S}{E-S} \sqrt{\frac{E-y_i}{y_i-S}} - 3 \sin^{-1} \sqrt{\frac{E-y_i}{E-S}} \tag{7}$$

Equations (7) is the varied flow function for flow over side weirs, while y_i denotes depths y_1 or y_2. Using the measured value of flow depths y_1, y_2, crest height S, and the distance x, the discharge coefficient C_d can be defined.

Main parameters

Considering the parabolic side weir with a broad crest, the parameters affecting the discharge coefficient $\boldsymbol{C_{db}}$ are expressed as

$$C_{db} = f_1(g, \rho, V_0, H, L, P, B), \tag{8}$$

where V_o is the average velocity in the main channel, H is the head over the side weir, B is the side channel width, and L is the side weir length. Applying the dimensional analysis technique (π – theorem), Eq (8) becomes;

$$C_{db} = f\left(F_o, \frac{P}{B}, \frac{H}{L}\right), \tag{9}$$

and for the parabolic side weir with a sharp crest C_{ds} is

$$C_{ds} = f\left(F_o, \frac{P}{B}\right) \tag{10}$$

Experimental study

The experiments are conducted in the Hydraulic Laboratory, Faculty of Engineering, Alexandria University. The experimental setup is represented schematically in Fig. (2). The main channel has 9.0 m long, 0.4 m wide, 0.6 deep, and zero bed slope. The side channel has 1.0 m long, 0.4 m wide (B), and 0.6 m deep. The models of both sharp and broad crested parabolic weirs were fabricated from coated wood. Three models, for both types, having a crest height S = 3.0 cm and parabola's parameter P = 5, 7.5, and 10 cm.

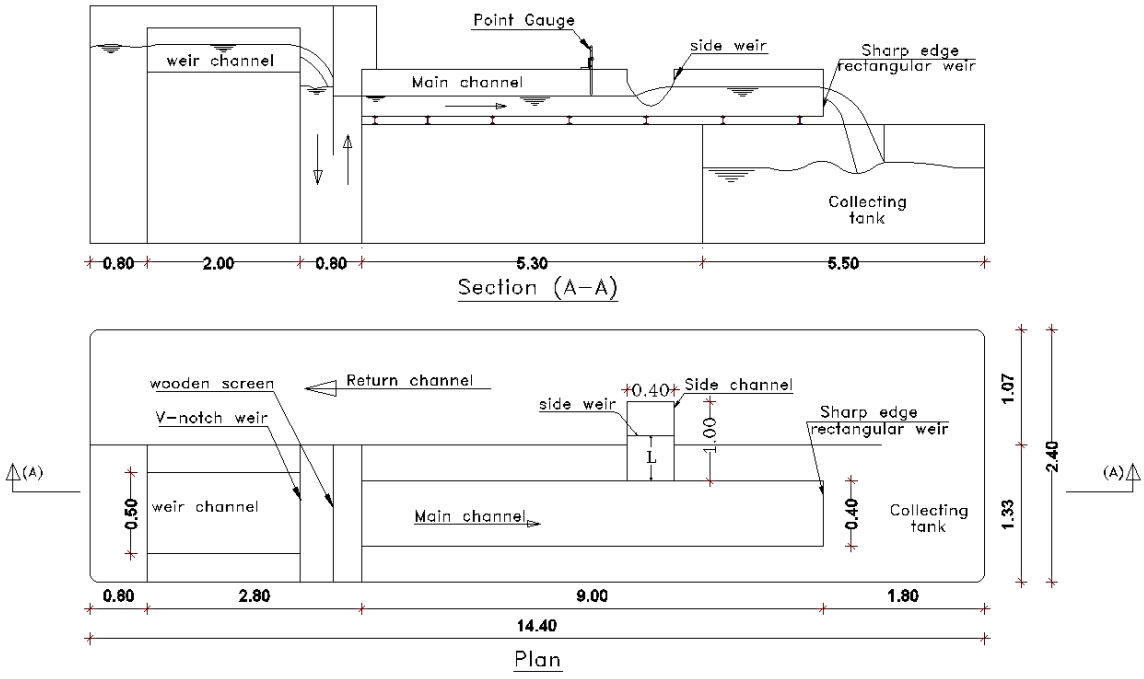

Fig. (2) Definition sketch for Experimental Set-up

A 90° V-notch sharp-edged weir is installed upstream of the main channel for the discharge measurements, while a rectangular sharp-edged weir is located at the end of the main channel extension. A tailgate adjusts the flow depth in the main channel. For a given side weir model, flow depth in the main channel $\boldsymbol{y_o}$ as well as $\boldsymbol{y_1}$ and $\boldsymbol{y_2}$ and distance x, between section (1) and (2), in addition to the main and branch channel discharges, are measured. The above measurements are reported for various values of the main channel Froude number $\boldsymbol{F_o}$. Table (1) illustrate the details of the tested models and ranges of the flow parameters.

Table (1) Tested model dimensions and ranges of flow parameters

Type of weir	Parameter of parabolic, P cm	Relative parabola's parameter P/B	Crested length L, cm	Crest height S, cm	Discharges		Froude number F_o
					Q_o, L/s	Q_s, L/s	
Broad-crested	5.0 7.5 10	0.125 0.1875 0.25	60	3.0	3.64 - 31.33	0.67-4.11	0.2 - 0.55
Sharp-crested			-		3.84 - 23.32	0.9 - 0.29	0.2 - 0.5

Results analysis

The main objective of the present study is to define the discharge coefficient C_d and the side-discharge ratio Q_s/Q_o for the parabolic side weir, either broad or sharp-crested one. The measured values of Q_o , Q_s , y_1 , y_2 and x are used to calculate C_d from Eqs (6) and (7) for both weirs (C_{db}) and (C_{ds}).

Parabolic broad-crested side weir. Referring to the relation (9), the coefficient C_{db} is a function of F_o , P/B and H/L. Therefore, the calculated values of C_{db} are plotted against such parameters, as illustrated in Figs. (3) and (4). It is obvious that the coefficient C_{db} increases by increasing the relative parameter of the parabola P/B while it decreases due to increasing F_o and H/L for all values of P/B. On the other hand, the side-discharge ratio $(Q_s/Q_o)_b$ increases with increasing P/B and decreases when F_o increases, as shown in Fig.(5). The discharge coefficient ratio $C = C_{db}/C_{ds}$ is plotted against H/L as shown in Fig. (6).

Parabolic sharp-crested side weir. The discharge coefficient C_{ds} is affected by F_o and P/B as expressed by the relation (10). The discharge coefficient C_{ds} has the same trend that for the broad crested weir. C_{ds} increases due to increasing P/B and decreases when F_o, increases as given in Fig. (7). The side discharge ratio $(Q_s/Q_o)_s$ increases by increasing P/B while it decreases with increasing F_o, as presented in Fig. (8).

It is useful to formulate values of both C_{db} , C_{ds} and Q_s/Q_o as a function of the main parameters, in dimensionless relationships. Applying the nonlinear regression analysis technique, a dimensionless formula for both C_d, and Q_s/Q_o are developed in the forms.

$$C_{db} = -0.317F_o - 0.32\frac{H}{L} + 0.54\frac{P}{B} + 0.51, \qquad R^2 = 0.99 \qquad (11)$$

$$(Q_s/Q_o)_b = -0.20\,F_o + 0.55\,\frac{P}{B} + 0.14, \qquad R^2 = 0.97 \qquad (12)$$

$$C = 0.8 + 0.1\frac{H}{L}, \qquad R^2 = 0.99 \qquad (13)$$

$$C_{ds} = -0.48F_o + 0.717\frac{P}{B} + 0.627, \quad and \qquad R^2 = 0.99 \qquad (14)$$

$$(Q_s/Q_o)_s = -0.30\,F_o + 0.73\,\frac{P}{B} + 0.175 \qquad R^2 = 0.98 \qquad (15)$$

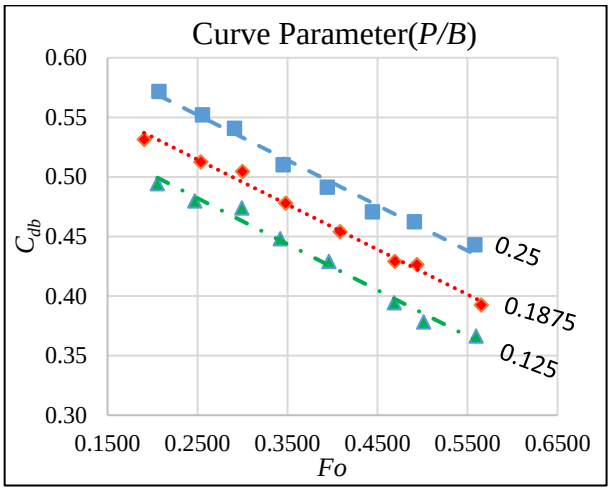

Fig. (3) Variation of C_{db} with F_o for broad-crested

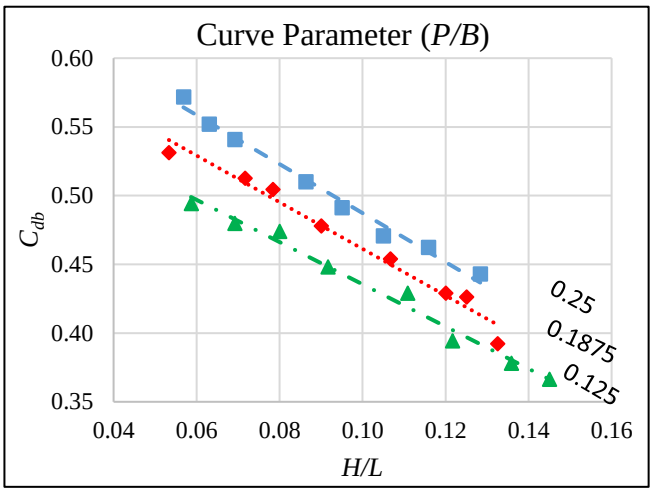

Fig. (4)Variation of C_{db} with H/L for broad-crested

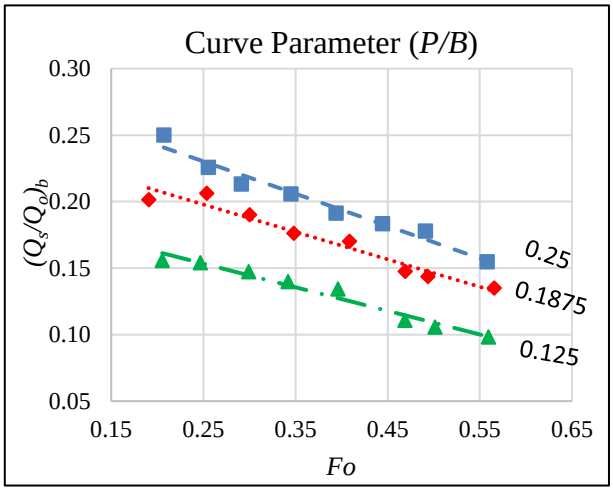

Fig. (5) Variation of $(Q_s/Q_o)_b$ with F_o for broad-crested

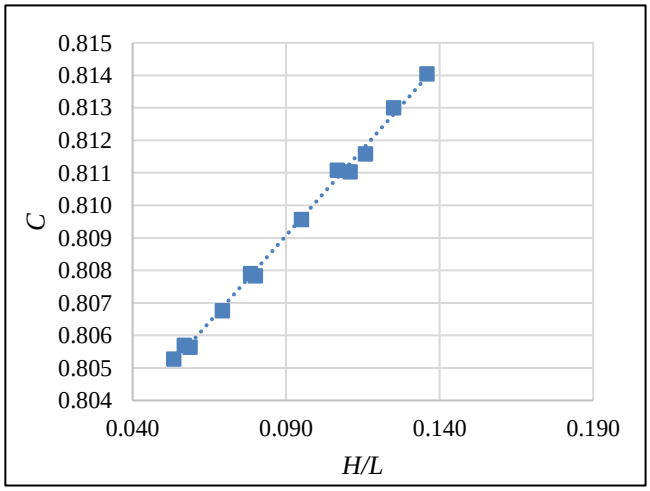

Fig. (6) Variation of C with H/L for broad-crested

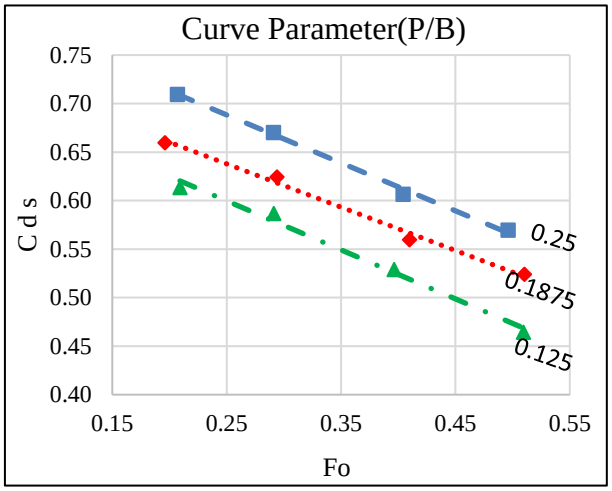

Fig. (7) Variation of C_S with F_o for sharp-crested

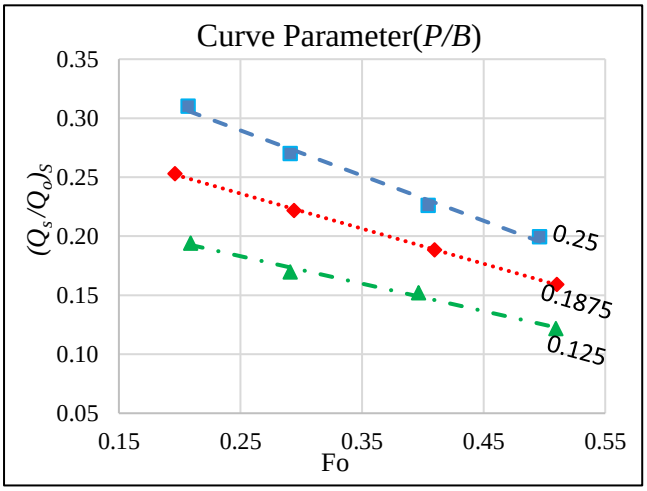

Fig. (8) Variation of $(Q_s/Q_o)_S$ with F_o for sharp-crested

Conclusions

The effect of the main parameters on the discharge coefficient and the side-discharge ratio for the parabolic side weirs with sharp and broad-crested ones are analyzed. The discharge coefficient either with broad or sharp crest and the side-discharge increases due to increasing the parameter of parabola while it decreases when the main flow Froude number and the crest length increase. As a result, the discharge coefficient, as well as the side-discharge ratios, are correlated to such parameters and expressed in dimensionless formulas

References

[1] W. H. Hager, "Lateral Outflow Over Side Weirs," *J. Hydraul. Eng.*, vol. 113, no. 4, pp. 491–504, (1987).

[2] P. K. Swamee, S. K. Pathak, and M. S. Ali, "Side-weir analysis using elementary discharge coefficient," *J. Irrig. Drain. Eng.*, vol. 120, no. 4, pp. 742–755, (1994).

[3] R. Singh, D. Manivannan, and T. Satyanarayana, "Discharge Coefficient of Rectangular Side Weirs," *J. Irrig. Drain. Eng.*, vol. 120, no. 4, pp. 814–819, (1994).

[4] H. Agaccioglu and Y. Yüksel, "Side-weir flow in curved channels," *J. Irrig. Drain. Eng.*, vol. 124, no. 3, pp. 163–175, (1998).

[5] M. E. Emiroglu, O. Bilhan, and O. Kisi, "Neural networks for estimation of discharge capacity of triangular labyrinth side-weir located on a straight channel," *Expert Syst. Appl.*, vol. 38, no. 1, pp. 867–874, (2011).

[6] A. R. Vatankhah, "Analytical solution for water surface profile along a side weir in a triangular channel," *Flow Meas. Instrum.*, vol. 23, no. 1, pp. 76–79, (2012).

[7] A. Parsaie and A. Haghiabi, "The Effect of Predicting Discharge Coefficient by Neural Network on Increasing the Numerical Modeling Accuracy of Flow Over Side Weir," *Water Resour. Manag.*, vol. 29, no. 4, pp. 973–985, (2015).

[8] E. Elalfy, M. Elkholy, C. K. Riahi-Nezhad, and M. H. Chaudhry, "Estimation of Discharge through a Levee Breach with Constant Cross Section," *J. Hydraul. Eng.*, vol. 144, no. 4, p. 06018005, (2018).

[9] A. Coşar and H. Agaccioglu, "Discharge Coefficient of a Triangular Side-Weir Located on a Curved Channel," *J. Irrig. Drain. Eng.*, vol. 130, no. 5, pp. 410–423, (2004).

[10] M. E. Emiroglu, O. Kisi, and O. Bilhan, "Predicting discharge capacity of triangular labyrinth side weir located on a straight channel by using an adaptive neuro-fuzzy technique," *Adv. Eng. Softw.*, vol. 41, no. 2, pp. 154–160, (2010).

[11] N. Kaya, "Effect of upstream crest length on flow characteristics and discharge capacity of triangular labyrinth side weirs," *Sci. Res. Essays*, vol. 5, no. 13, pp. 1702–1712, (2010).

[12] M. E. Emiroglu and N. Kaya, "Discharge coefficient for trapezoidal labyrinth side weir in subcritical flow," *Water Resour. Manag.*, vol. 25, no. 3, pp. 1037–1058, 2011).

[13] M. Rahimpour, Z. Keshavarz, and M. Ahmadi, "Flow over trapezoidal side weir," *Flow Meas. Instrum.*, vol. 22, no. 6, pp. 507–510, (2011).

[14] H. Haddadi and M. Rahimpour, "A discharge coefficient for a trapezoidal broad-crested side weir in subcritical flow," *Flow Meas. Instrum.*, vol. 26, pp. 63–67, (2012).

[15] M. E. Emiroglu and O. Kisi, "Prediction of Discharge Coefficient for Trapezoidal Labyrinth Side Weir Using a Neuro-Fuzzy Approach," *Water Resour. Manag.*, vol. 27, no. 5, pp. 1473–1488, (2013).

Study Group Of Wells Fed From Multi Confined Aquifers

Salwa Adel Abdel Rahman Abdel Malek[1,a], Mohamed Abdel Razek Rezk[2,b], and Rabiea Ibrahim Nasr[3,c].

[1, 2, 3] Irrigation and Hydraulics Department, Faculty of Engineering, Alexandria University, Alexandria, Egypt.[a]engsalwaadel@gmail.com, [b]Mohamedabdelrazek1953@hotmail.com, [c]profrabiea@yahoo.com

Keywords: Multiaquifer wells, Hele-Shaw model, combined aquifer system.

Abstract. Multiaquifer wells, that are open across more than one aquifer, can have a great effect on the hydraulics of groundwater system. These wells change the physical system by establishing direct links between otherwise isolated strata. Several methods are available to simulate multiaquifer Wells.. In this paper an experimental study is used using Hele-Shaw model to represent multiaquifer wells. Four groups of experiments are formed to find effect of piezometric heads (H) and aquifer permeability (k) on measured well discharge (Q) due to abstraction. First group are carried out for a well penetrating a single confined aquifer that is easily solved using Dupuit equation in order to calibrate the model before running the experimental testes. Second group is performed for a well penetrating a two confined aquifers in order to verify the model accuracy by comparing results with Sokol equation. Third group is carried out for a well penetrating a two confined aquifers. Forth group is done for a multiple well system forming a square with a well in the center and fed from two confined aquifers. It is concluded that Dupuit equation is agree very well with the experimental results for a well fully penetrating a confined aquifer and not recommended to be applied for a combined aquifer system. Permeability of aquifer plays an important role for increasing well discharge. Results are presented in graphical forms using dimensionless parameters to determine the well discharge for different values of piezometric head and water depth in well (h_w).

Introduction

Horizontal Hele-Shaw model is among the most widely used wet models in studies of groundwater flow. It consists of a viscous liquid flow in the laminar range, located between two closely spaced parallel plates. The interspace between the plates represents the aquifer. An important feature of Hele-Shaw model is that the plate spacing is related to conductivity. The viscous liquid imitates the ground water. Withdrawing groundwater can be simulated by extracting specific amount of fluid at the required position. Flow towards wells was analytically studied in different ways of approach. Some analytical solutions were presented by Dupuit[1], , Harr [2],and Sokol [3]. Many pervious researches have demonstrated the versatility of the Hele-Shaw model to simulate groundwater flow problems such as Marino(1967) [4], and Rezk and Moghazi (1995) [5], (1966) [6].The history of the well hydraulics and well testing started in 1863 with Dupuit , who developed the first analytical solution to model radial flow to a well in steady state. The hydraulic gradient is equal to the slope of the free surface and is invariant with depth Darcy's law. Thus

$$Vr = -K\frac{dh}{dr} \quad (1)$$

and the well discharge Q

$$Q = 2\pi\, r\, h\, k\frac{dh}{dr} \quad (2)$$

Integration for the boundary conditions at the well for confined aquifer.

$$Q = 2\,\pi\, K\, b\,\frac{H_O - h_w}{\ln(\frac{R_O}{r_w})} \quad (3)$$

And for unconfined aquifer

$$Q = \pi K \frac{H_O^2 - h_w^2}{\ln(\frac{R_o}{r_w})} \quad (4)$$

In 1962, M . E . Harr derived relationship about interference among wells. He indicated from his observations that, when a number of wells are introduced within a feed contour, the output increases, but the efficiency of each additional well decreases. This effect is due to the so-called interference among wells.

Daniel sokol in 1963 showed that The water level in a no pumping well perforated in more than one artesian aquifer is affected by each aquifer in proportion to the transmissibility of that aquifer. The ratio of the water-level fluctuation in a well to the potentiometric-surface fluctuation in an aquifer perforated by that well is equal to the ratio of transmissibility of the aquifer in which the fluctuation occurs to the total transmissibility's of all aquifers perforated by the well. He derived the following formula:

$$\frac{\Delta h_w}{\Delta H_1} = \frac{T_1}{\sum_{i=1}^{n} T_i} \quad (5)$$

Description of the experimental model

Fig. (1-a) shows the outlines dimensions of the model. Fig. (1-b) illustrates a schematic diagram of the horizontal Hele-Shaw model used to simulate the problem. It consists of three Perspex cylinders (10 mm thick) at base (1) to represent radial flow towards the well, closed at the bottom and have inner diameters of 30,50 and 70 cm. The outer radius of the inner cylinder represents the well radius of influence R_o, while the middle and outer cylinder represents a constant head reservoir to represent the original piezometric head of the two aquifer H_1,H_2 respectively. They have a height of 20 cm. The big cylinder is amounted on a horizontal steel table (2) and the upper face of its bottom is considered as a datum for all head measurements during the tests. The middle cylinder is placed inside the big one and a narrow spacing between the bottoms of the two cylinders is kept constant with the aid of individually fiber washers (0.102 cm thick. Each). This space simulates the thickness of the lower aquifer (a_2) (layer II), which can be increased by adding more washers. The vertical space between the outer and the middle cylinders simulates a reservoir that feeds layer II (the lower aquifer) under a piezometric head H_2. The small cylinder is placed inside the middle cylinder, making sure that the vertical axes of the three cylinders are the same. The spacing between the bottoms of the inner and middle cylinders is also kept constant with fiber washers to simulate the upper aquifer thickness (a_1) (layer I). The vertical space between the inner and middle cylinders simulate also another reservoir that feeds layer I (the upper aquifer) under a piezometric head H_1.The bottoms of the three cylinders are fixed together with brass bolts, equally distributed all over the bottom's areas of the three cylinders. In order to simulates the wells, five holes of 10 mm diameters are made in the three cylinder's bottom. Four of these holes are forming a square pattern of side width 14 cm and wells locate at the square corners, while the fifth one is made in the center of the square, as shown in Fig. (1-c). The four holes are symmetrical and located at 10 cm from the centric well. Five glass tubes (10 mm diameter) are fixed into these holes to represent the multiple well systems (3). Discharge tubes (4) are fitted to the bottom of the holes in the outer cylinder and opposite to the wells. A viscous oil (supper 7500-20W/50) (5) is used to simulate the ground water flow. The collected oil from well can be controlled by a control discharge valve (6). The rate of well discharge Q is measured by collecting an amount of oil in a graduated tube (7) in a certain time. The corresponding oil depth in the well h_w and temperature are recorded. An over flow pipe (8) is provided to each reservoir to maintain the desired piezmetric head during the tests. A small centrifugal pump(9) is used to lift oil from a collection tank(10) to an elevated tank(11) through a delivery tube (12),which in turn feeds the two reservoirs through a feeder tube (13) using a control valve (14). To facilitate the reading of data, vertical strips of millimeter papers are placed on the outer cylinder, the middle cylinder and the well. In order to observe any change in the piezometric heads during experiments, Three piezometer tubes (15) are fixed into the inner cylinder's bottom , in one line with the centric well and passing in the

mid distance between wells 3 and 4. They are fixed at distance 2.50 , 7.50 and 12.50 cms from the centric well axis. Temperature is measured in each experiment.

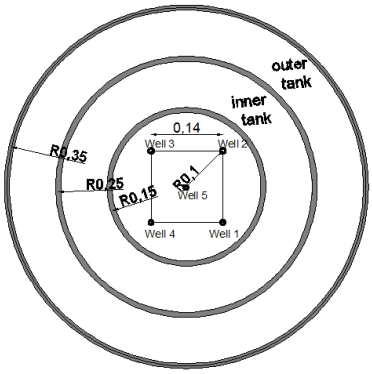

Fig.(1-a) Plan of the Hele-Shaw

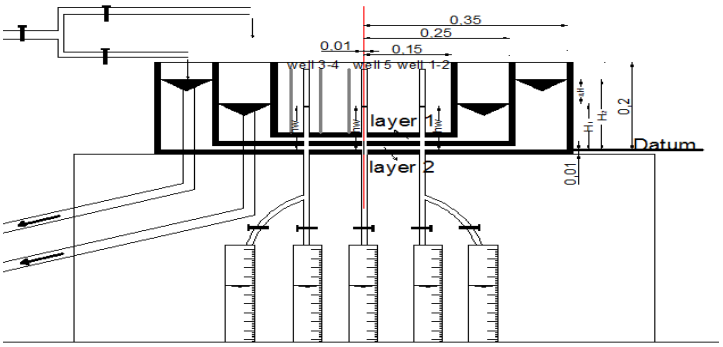

Fig.(1-c) Dimensions in (m)of the Hele-Shaw

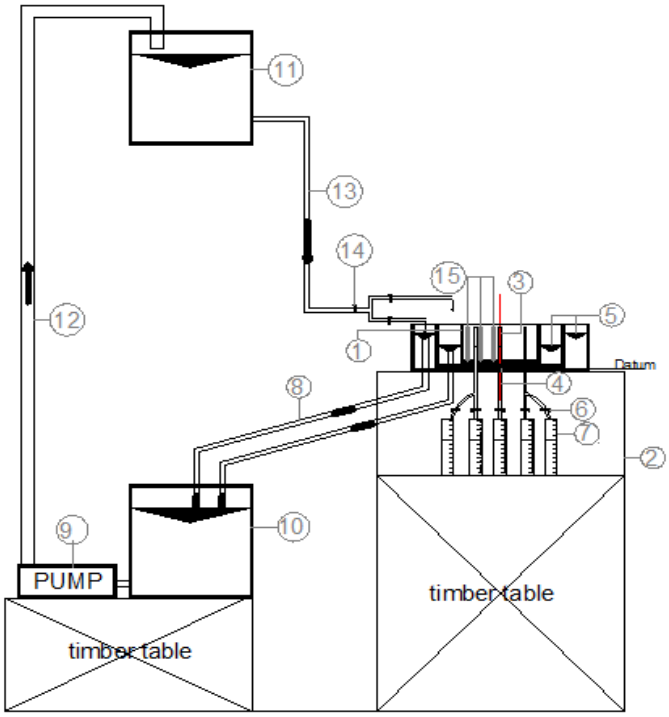

A Schematic Diagram of the used Hele-shaw model

1. Cylinder tanks
2. Steel base
3. Glass tube
4. Discharge tube
5. Viscous oil
6. Control discharge valve
7. Graduated tube
8. Over flow tube
9. Centrifugal pump
10. Collected tank
11. Main supply tank
12. Delivery tube
13. Feeder tube
14. Control valve
15. Piezometers

Fig. (1-b) Experimental Hele-Shaw Model.

Procedure of the experimental work

First group of experiments are carried out for a well penetrating a single confined aquifer that is easily solved using Dupuit (Eq. 3) in order to calibrate the model before running the experimental testes. The first test is carried out by considering the thickness of the aquifer a_1=0.102 cm, the radius of influence Ro=15 cm and the piezometric head of the aquifer H_o=10 cm. The second test is carried out for the same aquifer thickness a_1=0.102 cm, the radius of influence R_o=25 cm and the head of the aquifer H_o= 10 cm. The third test is carried out by considering the thickness of the aquifer a_1=0.204 cm, the radius of influence R_o=15 cm and the piezometric head of the aquifer H_o=10cm. The forth

test is carried out by considering the thickness of the aquifer a_1=0.204 cm, the radius of influence R_o=25 cm and the piezometric head of the aquifer H_o= 10 cm.
Second group of experiments are carried for a well penetrating a two confined aquifers in order to verify the model accuracy by comparing results with Sokol (Eq.5). Three sets of tests are carried out for k_1/k_2 =0.5,1.0 and 2 without discharging from well.
Third group of experiments are carried out for a well penetrating a two confined aquifers in order to demonstrate the effect of the piezometric head and permeability of each aquifer on the measured well discharge. Three sets of tests are carried out for k_1/k_2=0.5,1.0 and 2.
Forth group of experiments are carried out for an artesian multiple well systems. Six complete tests are made for well diameter 1.0 cm. The centric well denoted with No.5 while the other four wells by the numbers 1,2,3 and 4. All experiments are operated at a fixed value of the difference head ΔH=15 cm, and for well diameters 1.0 cm. Discharge is measured in case of operating wells No. (5), (1), (1&3), (1,3&5), (1,2,3&4),and(1,2,3,4&5).

Analysis and discussions of results

A horizontal Hele-Shaw model is developed firstly to solve problem of steady radial flow to artesian well in order to verify its efficiency to handle horizontal flow problems. For the case of abstracting from well 5 only which penetrating a confined aquifer, comparison between the measured and the calculated well discharge Q, based on Dupuit Eq, is done. For a constant value of the piezometric head (H_o); the relation between the relative measured well discharge ($Q / K a_o H_o$) and relative drawdown in the well ($(H_o - h_w)/H_o$) is drawn as shown in Fig.2, For H_o= 10 cm, R_o=15,25 cm, and a_o=0.102 cm after that for H_0= 10 , R_O=15,25 cm and a_o=0.20 cm. Experimental results agree very well with those obtained by the Dupuit equation in case of increasing aquifer thickness (a_1),well radius of influence (R_o),and height of the original piezometric surface above the impervious stratum (H_o) where when a_1 =0.20 cm, R_o=25 cm, and H_o=10cm gives more a gratifying agreement than when a_1 =0.102 cm, R_o=15 cm, and H_o=10cm .

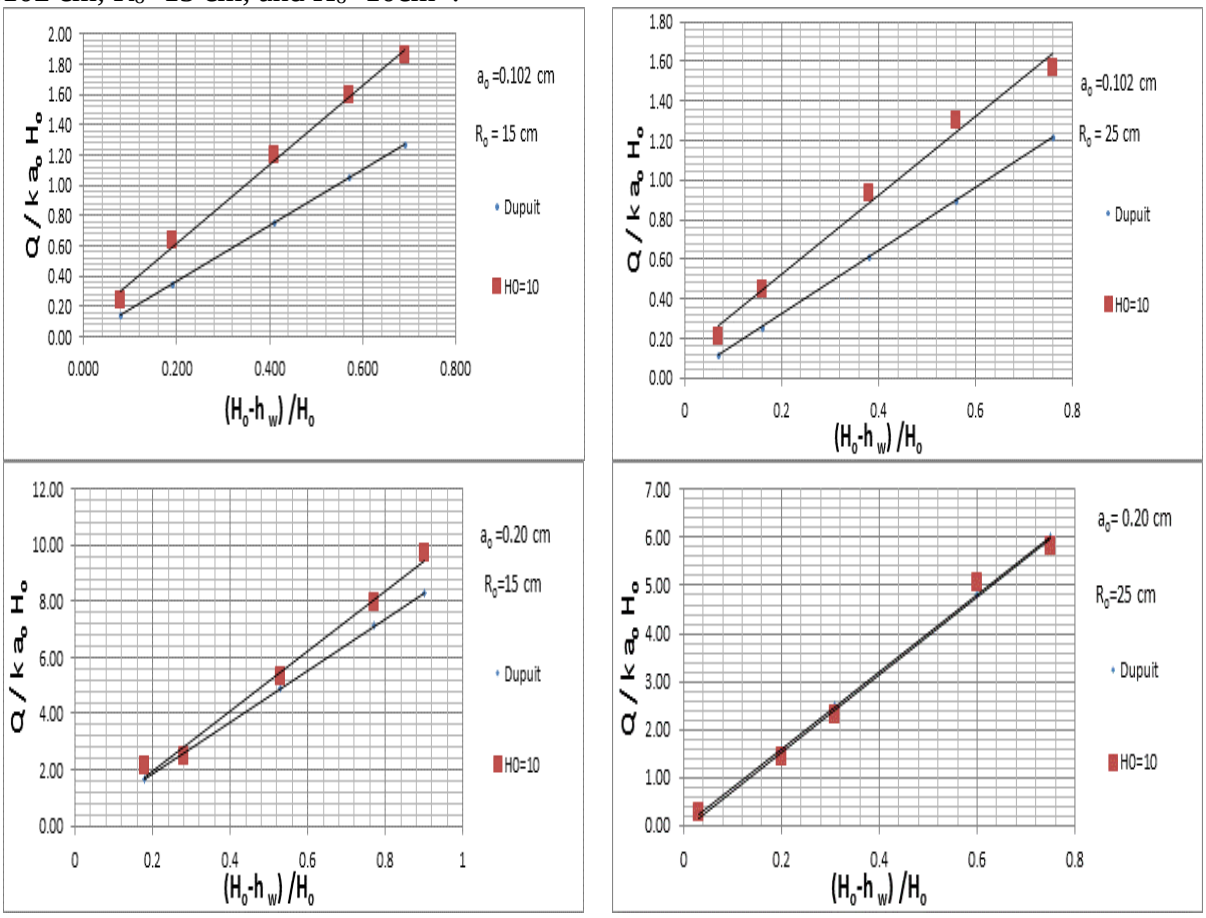

Fig. 2 comparison between experimental and theoretical results (Dupuit Eq).

In the second test for a well penetrating a two confined aquifers in order to verify the model accuracy. Three sets of tests are carried out for k_1/k_2=0.50,1.0 and 2 respectively without abstracting from the well. In each set of tests, H_1 is allowed to increase by an amount ΔH_1 while H_2 is kept constant. The corresponding fluctuation of oil level in the well Δh_w is, then, recorded. The above procedure is repeated by allowing H_2 to increase by an amount ΔH_2 while H_1 is kept constant and the corresponding Δh_w are also recorded. Temperature is measured in each experiment. Results are compared with SOKOL(Eq.5). It may be noticed from Fig.(3) that the differences between both results are often very small and drop to nil in some cases.

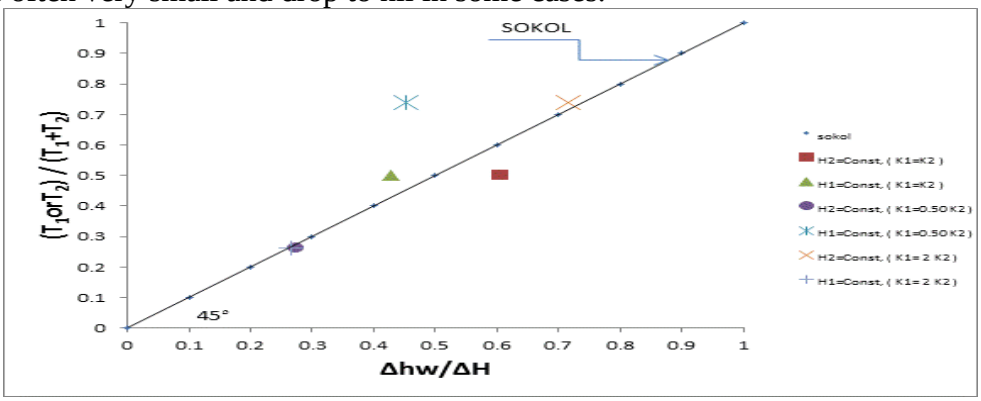

Fig.3 comparison between measured and calculated fluctuation of the well level by sokol.

The model is thirdly used to demonstrate the effect of the piezometric head and permeability coefficient of each aquifer on the well discharge measured .Three sets of tests are carried out for k_1/k_2=0.50,1.0 and 2. During these tests, h_w is kept constant at 5.2 cm and H_1 is first kept constant while H_2 is allowed to increase to get $\Delta H=H_2-H_1$=3,5,8,11and 13 cm. Then H_2 is kept constant and H_1 is allowed to increase to get the same above values of ΔH. Fig. (4-a),(4-b),(4-c) show the relationship between relative discharge ($Q/k\ a\ h_w$)and difference ($\Delta H/h_w$) for k_1/k_2=0.50,1.0 and 2 respectively. It may be noticed from Fig. (4-a) that at a certain value of ΔH and when$H_2>H_1$ the well discharge is bigger compared to the corresponding case when $H_1>H_2$.Although the source of the upper aquifer (I) is closer to the well compared to the lower aquifer (II).Since the permeability of aquifer (II) is bigger than that of aquifer (I). Fig.(4-b) shows that at the same value of ΔH the difference H_1-H_2 produces more well discharge compared to the difference H_2-H_1 although the permeability of both aquifers are equal. This is because the source of aquifer (I) is nearer to the well compared to the source of aquifer (II). Meanwhile when the permeability coefficient and the piezometric head of the upper aquifer is bigger than the corresponding values of the lower aquifer the inverse is occurred as shown in Fig.(4-c).

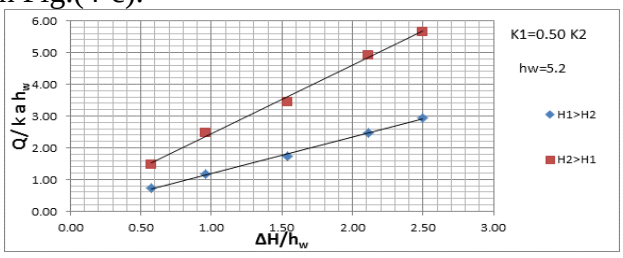

Fig.(4-a) comparison between discharge.

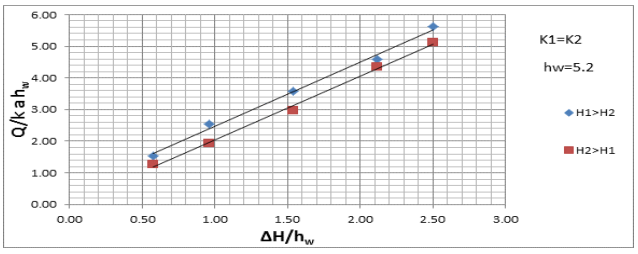

Fig.(4-b) comparison between discharge.

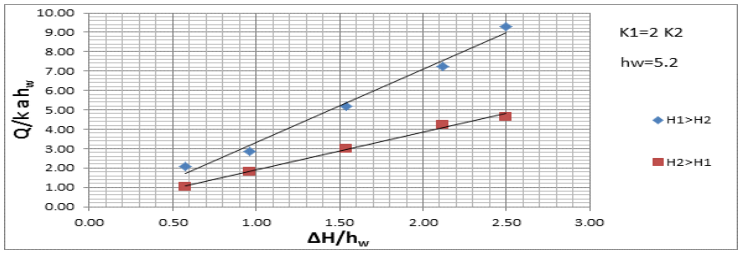

Fig.(4-c) comparison between discharge.

For the case of abstracting from an artesian multiple well systems. For single well No.5 which fed from multi aquifers, two sets of experiments for (H_1>H_2) and (H_2>H_1) are carried out for constant K_1=K_2, values of ΔH=15 cm, and d_w=1.0 cm. comparison between the two sets of experiments are done, where the first set for H_1-H_2=15, is kept constant while (h_w) is changed many times and the corresponding well discharge (Q) is measured. The second set is prepared for H_2-H_1=15 and the same procedure of the first set is followed. The first and second sets of experiments which are performed on well No.5 are repeated for wells No. 1, (1,3), (1,3,5), (1,2,3,4) and (1,2,3,4,5).Results are drawn as shown in Fig.5. It may be noticed from Fig.5 that at a certain value of (h_w) and when H_1>H_2 the well discharge is bigger compared to the corresponding case when H_2>H_1. This is because the pizometric head of aquifer (I) is nearer to the well compared to the piezometric head of aquifer (II).

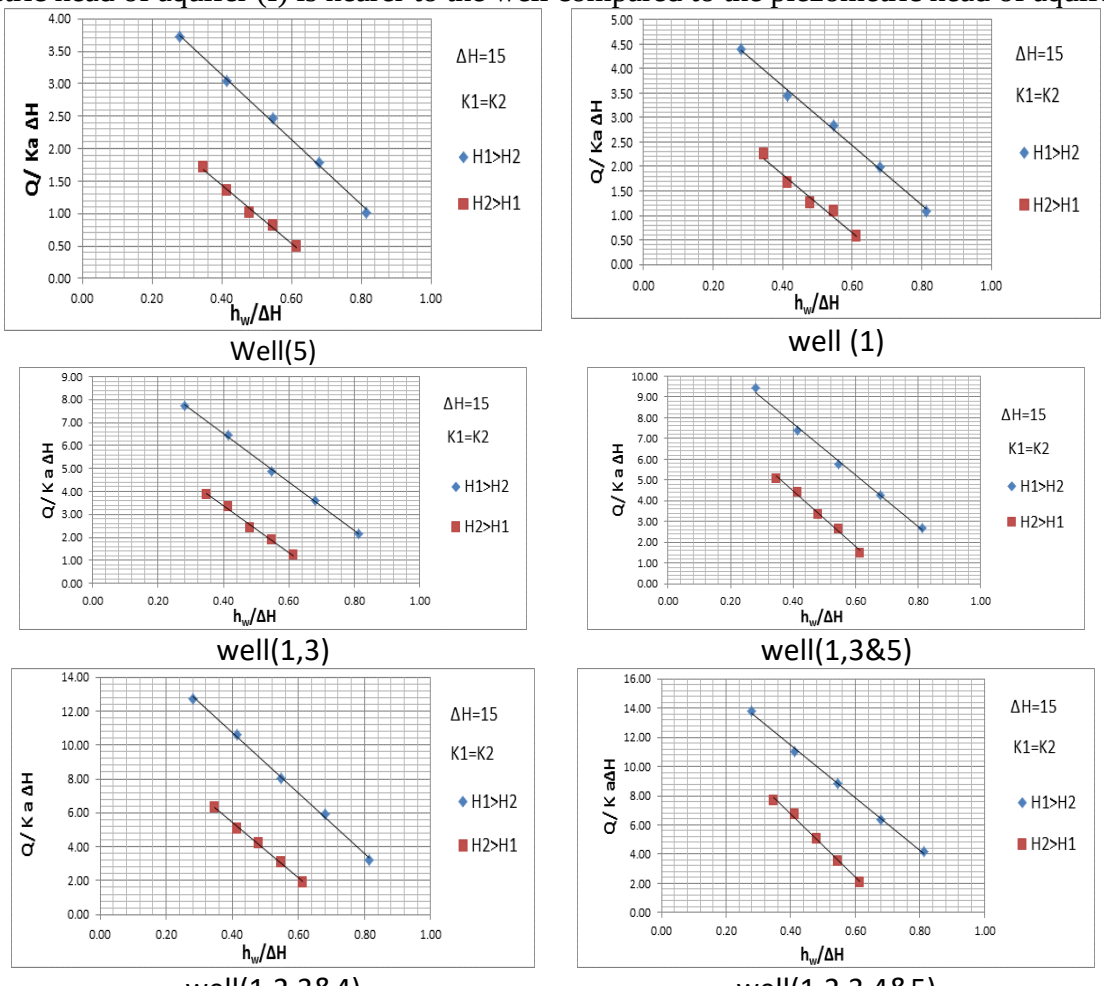

Fig.5 discharge from well (5),(1),(1,3),(1,3,5),(1,2,3,4)and(1,2,3,4,5).

- **Conclusions.** The current study focuses on simulating the abstracting from artesian multiple well systems under different boundary conditions As a result, the main conclusions could be arranged as follows:

- The designed Hele-Shaw model showed an excellent accuracy with the result obtained by Sokol equation.
- Permeability of aquifer plays an important role in increasing well discharge; however for two aquifers position of aquifer piezometric head is not contribute in increasing well discharge if one of them has less permeability.
- For a constant equal permeabilities of the two aquifers I&II, and when aquifer I subjected to higher piezometric head than aquifer II, the discharge interring the well is bigger due to ($H_1 > H_2$), this is because of existence piezometric head of aquifer No.I is nearer to the well than the piezometric head of aquifer No II.

References

[1] D.K., Todd. (1980). Groundwater Hydrology. John Wiley&Sons, U.S.A.
[2] Harr, M. E. (1962). Groundwater and Seepage. McGraw-Hill Book Company, New York.
[3] Sokol, D. (1963). Position and fluctuations of water level in wells perforated in more than one aquifer. J.of geophysical Res,PP.1079-1080.
[4] Marino, M. (1967). Hele-Shaw model study of the growth and decay of groundwater ridges. J.of Geophysical Research, PP.1195-1205.
[5] Rezk, M. and Moghazi,H. (1995). An experimental study of a well in a leaky aquifer, J. of Modeling Measurements and Control, AMSE Press, PP.5-21, France.
[6] Rezk, M. and Moghazi,H. (1996). A viscous flow analogy for studying pumping from multiple artesian well system, Alexandria Engineering Journal, March, Alexandria, Egypt.

Environmental Impacts of the Grand Ethiopian Renaissance Dam (GERD) on Egypt

Lamiaa Abdallah

Alexandria higher Institute of Engineering and Technology (AIET), Alexandria, Egypt

Lamiaa_Abdallah@yahoo.com

Keywords: *Grand Ethiopian Renaissance Dam (Dam), Environmental Impacts of GERD, Egypt's Water Deficiency*

Abstract. Since 2011, Egypt's water security was sharply threatened when Ethiopia announced construction of the Grand Ethiopian Renaissance Dam (GERD). Ethiopia started filling the dam in 2020, and the second filling is to take place July 2021. This action will have severe political, economic, social and environmental impacts on Egypt. The GERD is currently a matter of fact, it is not a questionable issue. In this paper, we will focus on the expected environmental damages on Egypt. The environmental impacts studied in this paper includes fresh water deficiency from current 59.5 billion cubic meter (bcm), of which 55.5 bcm are from the Nile, leading to an annual ~ 600 m^3 of fresh water per capita, far below the global standard of 1000 m^3. The associated impacts of water deficit include loss of agricultural lands, banning of growing some crops that are water-intense (like rice), increased salinization of agricultural lands in the Nile Delta and deficiency of hydropower production from the Aswan High Dam (AHD). Other concerns include long period droughts and the GERD refilling, especially if this happens immediately after the initial fill, and finally floods in case of destruction of the GERD and its consequences on Egypt. Some countermeasures for these problems are discussed and proposed to decrease the effects of filling and operation of the GERD. In conclusion, upstream countries have the right to invest in their water resources, but at the same time in a cooperative, no-harm policy, to decrease the possible negative effects on downstream countries.

Introduction

The Nile River. The Nile is the world's longest river. It flows across 11 African countries. It has two main tributaries; 1) the Blue Nile with its origins in Ethiopia and that shares by 85% of the water that reaches the downstram countries (Sudan and Egypt), and 2) the Whit nile that originates from Lake Victoria and shares by the remainder 15%. The average water flow that reaches the downstream countries is approximately 84 billion cubic meters (bcm) annually [1].

Egypt and the Nile. The Nile River Sharing Agreement between Egypt and Sudan, signed in 1959 distributed the annual 84 bcm flow as 55.5 bcm to Egypt and 18.5 bcm to Sudan and 10 bcm are for evaporation. Egypt harvests about 2 bcm of fresh water from groundwater and another 2 bcm from rainfalls. This makes the total freshwater resources in Egypt reach 59.5 bcm. Egypt's annual freshwater needs are 80 bcm, which means that Egypt already has a deficit of 20.5 bcm, even without taking into consideration the consequences of the GERD. This amount is compensated by re-using the agricultural water and treated sewage water [2]. the United Nations sets a water scarcity level of 1000 m^3 per capita annually. Currently, the per capita in Egypt is 600 m^3 annually. Egypt's population is expected to increase by 2% annually, and given that the share of Egypt's from the freshwater is maintained constant, the problem will be very critical, as shown in Table 1.

Table 1. Egypt population and the corresponding annual freshwater share per capita

year	1960	1990	2020	2025	2030
Population (million)	27	60	100	110	120
m^3 of water / capita	2200	1000	600	550	500

The GERD. After 2 months of the Egyptian 2011 revolution, Ethiopia announced that it will construct the GERD on the Blue Nile near the Ethiopian-Sudanese border, as shown in Fig. 1. The GERD reservoir will cover an area of approximately 1900 km^2 (bigger than the area of London), and the water level at full supply is 640 m above sea level. The total storage capacity of the dam is approximately 74 bcm, which is equal to Egypt's and Sudan's shares of the Nile River annually. The actual volume that will be needed to fill-up the basin may even reach up to 110 bcm if we account for the losses due to seepage and evaporation. Two hydroelectric power stations are installed at the right and left banks of the downstream river comprising of 16 Francis turbines that will grant a total installed power capacity of 6 GW (approximately three times that of AHD), and estimated yearly potential production of 15 GWh. The project costs were estimated by 5 billion USD. Upon completion, the GERD will become the largest hydropower dam in Africa [3-4]. The 2015 Agreement of Principles was signed in Khartoum between Egypt, Sudan and Ethiopia. Under this agreement, Egypt agreed to Ethiopia's right to build the dam and gave legitimacy to the dam construction that it was denied before. The agreement just focused on resolving the dam's technical framework. Negotiators among Ethiopia, Sudan, and Egypt on the design, initial filling, and long-term operation was ongoing, but no agreement has yet been reached [5].

Ethiopia started filling the reservoir by ~ 5 bcm in July 2020 and announced that the full filling will take 3~5 years. Egypt demands that the filling process of the reservoir be not less than 7 years, and that its water share should not be less than 40 bcm annually during the filling phase. Egypt also demands that, storage must be only in the rainy season and stops in drought times [6]. In addition to the water deficiency, the GERD could adversely impact fish, aquatic plants, and biodiversity in the downstream due to possible changes in water temperature, salinity, and oxygen content. With a maximum reservoir area of 1904 km2, surface evaporation could increase. The aforementioned impacts could have transboundary ecological, agricultural, and health implications and, therefore, should be taken into consideration [7].

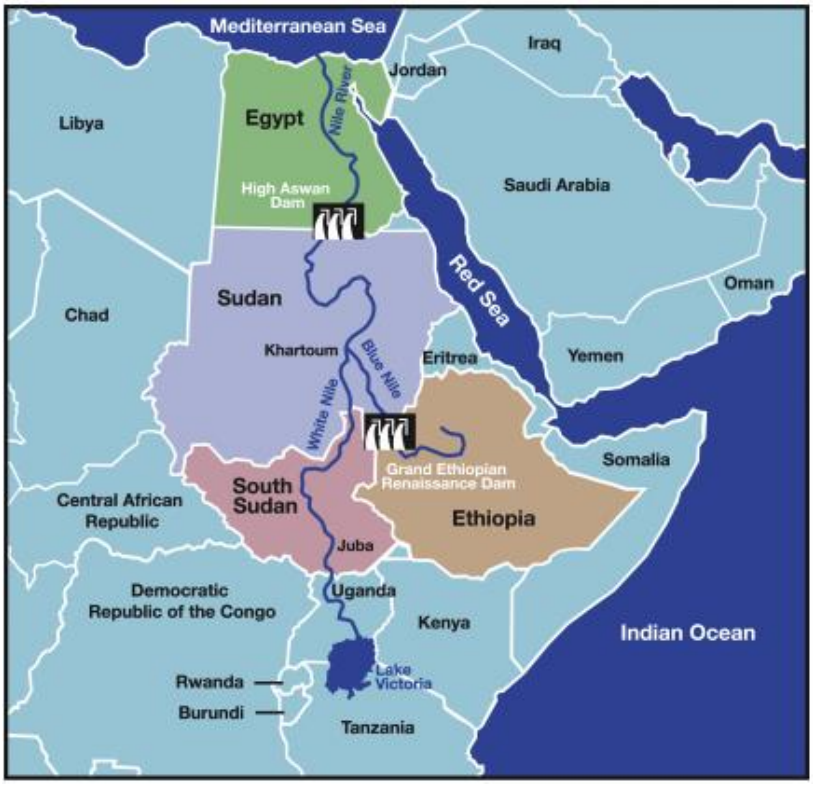

Fig. 1 Map showing the Nile River and the site of the GERD

GERD Impacts under Different Scenarios

The published data on the GERD is very limited concerning key environmental factors. No Environmental Impact Assessment (EIA) was done (or if done, was not published), in violation of international laws. To assess the GERD impacts, we have to consider the following four different scenarios with several possibilities:

Scenario (1): Impacts during the filling period of the GERD Reservoir. Ethiopia would like to fill the reservoir as quickly as possible to acheive its hydropower energy production (energy target policy). However, any fill rate must consider minimum water requirements for Egypt and Sudan (cooperation policy) [8]. According to [9], a five-year filling period of the GERD will force the AHD reservoir to reach its minimum water level by the fifth year. Reference [10] showed that a 100% fill rate policy (equivalent to complete filling of the GERD reservoir in 2.5 years) will result in a 55% reduction of water stream flow to Egypt. On the other hand, annual reservoir fill rates of 8–15% can be beneficial for hydroelectric power generation for Ethiopia with a minimal effect on stream flow to Egypt. Reference [11] showed that impounding 10% or 25% of streamflow will result in a 6% or 14% average reduction in streamflow into Egypt during the first 5 years, respectively. Reference [12] suggested that Egypt should apply an AHD drought management policy during the filling period together with an agreement with the Ethiopian side on a GERD-AHD safeguard policy to release additional amount of water from the GERD if the AHD reservoir elevation falls below a critical level. Authors of [13] used a multi-source satellite imagery technique using Google Earth Engine (GEE) to monitor the changes in water level during the first filling of the GERD reservoir from 9 July–30 November 2020. The volume of water at GERD increased by 3.6 bcm, which accounts for about 5.3% of its planned capacity. Reference [14] estimated that GERD will worsen Egypt water budget from currently ~ 20 bcm to a total annual deficit between 26 to 38 bcm according to the GERD filling policy.

Scenario (2): Normal operation after filling the reservoir. The primary use of the GERD will be the generation of hydroelectric power. Once the GERD reservoir is filled, the average release from the GERD will be equal to its average annual inflow. Operation may aim at representing the natural flow regime to a certain extent with peak flow during flood season (August) and lower flows in the dry season; if inflow and hence volume/water level are high, released discharges are also high; if reservoir volume is low, discharges and hydropower are reduced depending on the season. A non-cooperative operation scenario (from the Ethiopian perspective) would only consider the optimization of the reservoir operation to maximize hydropower generation [15].

Scenario (3): Operation during a severe multi-year drought. The third scenario will begin when a sequence of very low flows occurs in the Nile Basin. The probability, severity, and timing of specific sequences of low flows are unknowable, especially as climate change unfolds. For example, a severe multi-year drought might begin during or immediately after filling the GERD Reservoir, so it cannot be assumed that scenario (2) will precede scenario (3). In severe drought conditions, feelings about the loss of water security may become especially acute, which could lead to a water panic among irrigators and civil society in Egypt if people feel that they are unjustly denied access to water or if the burden falls disproportionately on poor, vulnerable farmers [16].

Scenario (4): Collapse (destruction) of the dam. A catastrophic event such as dam failure, caused by geological/foundation weakness (example: earthquakes), extreme storms, structural problems, old age, and terrorism or military attack etc., would lead to a major humanitarian disaster. the most important of which would be the huge amount of water trapped behind the GERD that would flow in the Blue Nile, which when combined with the water coming from the White Nile and smaller tributaries like Atbara, would collapse the Sudanese dams which would cause the sinking of Khartoum underwater at the level of 3 meters. After 18 days, the water would reach the High Dam in Egypt [17].

Consequences of GERD on Egypt's Environment

Besides their benefits of generating clean and cheap hydropower, maintaining steady flow of water along the year and protecting against floods and droughts, mega dams have also several negative impacts. These impacts include changes in the aqua fresh water living patterns, increased soil salinity after absence of natural frequent annual leaching of soil by flooding, overuses of chemical fertilizers and pesticides due to preventing of fine earth fertility particles by the dam and which causes contamination of groundwater, and increases the vulnerability of delta lands against climate change and the raise of the Mediterranean Sea level. The most significant effects that Egypt is trying to overcome are the destruction of agricultural farmland due to the reduction in the water share, seawater intrusion in the Nile Delta, increased land salinity, threats to the fisheries and reduction of Aswan High Dam capacity to produce hydroelectric power [18].

Impacts on agricultural system. The GERD has a clear effect at the end of the irrigation network in the Egyptian Delta. The manifested effect is reducing the surface water level (SWL). As a remedial action, cultivating water-intensive crops (like rice) are being banned in some areas and limited in others. Changing the crop pattern through cultivating non-voracious crops will affect the groundwater (especially in the shallow aquifers where there will b no or very little recharge). The soil quality will also be damaged over time as a result of salt accumulation, no bleaching and the extensive use of fertilizers to compensate for the low soil fertility. A shortage of surface and groundwater, a decrease in soil quality, and reducing the area cultivated by economic crops (like rice and maize) could affect the Egyptian economy [19].

Impacts on groundwater. Groundwater faces 2 main problems: quantity and quality. In 2016, the estimated discharge from groundwater aquifer in the Nile Delta was about 7 bcm. In the Nile Delta, the groundwater extraction increases linearly by about 0.1 bcm / year. The use of groundwater in the Nile Delta is strongly linked to availability of Nile water and any shortage as a result of the GERD will be covered by drilling more of groundwater wells, whether legally or illegally. Many factors cause the quality deterioration of the groundwater aquifer in the Nile Delta including: agriculture fertilizers, pesticides, wastes, seawater intrusion and increased saline water due to aquifer over-pumping [20].

Impact on seawater intrusion on Nile Delta. Filling the reservoir of GERD in 3 years would reduce the annual average fow in the Nile River from 55.5 to 30.9 bcm. If the filling time is extended to 6 years, the average annual fow would be reduced to 43.2 bcm. The Nile River will be completely drained if the GERD is filled in 1 year as all the fow will be diverted to the reservoir of the GERD. Under natural conditions, a delicate balance between freshwater bodies in coastal aquifers and seawater bodies is acheived. During the filling phase of the GERD, this balance will be affected and seawater will migrate through the bottom layers of the coastal aquifers causing the seawater intrusion problem [21].

Impact on hydropower generation from AHD. Reference [22] estimated that in a scenario of filling the GERD in seven years, Egypt will face a significant shortage in water quantity associated with a reduction of 20% to 30% of electricity production from the AHD. According to New & Renewable Energy Authority (NREA) in Egypt, the total electrical energy generated in Egypt during 2019 (just before the COVID-19 crisis) was ~ 200 TWh. The share of hydropower in the electricity energy mix during the same year was 13 TWh (6.5%). The generating capacities in Egypt exceeds 58 GW, with a maximum load of 32 GW. All hydropower generating capacities in Egypt represent only 2.8 GW (4.8%) of the total generating capacities. This means that the hydropower energy can be completely omitted from the energy mix without much affecting the security of electrical energy in Egypt. The only concern is in fact environmental. This amount of electricity will most probably be compensated by adjusting the loading of the new Siemens combined cycle power plants with an equivalent CO_2 emissions of approximately 7 Million Ton annually, based on an emission intensity of approximately 0.55 kg CO_2/kWh [23].

Recommended Mitigation Actions

Upstream countries have the right to invest in their water resources, but at the same time the possible negative effects on downstream countries must be considered. Since the beginning of GERD construction on the Blue Nile in 2011, no agreement has been reached between the Eastern Nile countries on the critical issues of dam capacity, initial flling policy, and dam operation [28].

Egypt has to develop a plan that include firm and fast procedures including increasing the efficiency of water distribution by lining water canals to prevent water leakage in distribution system, switching from surface to drip irrigation, apply new irrigation systems that use sensors to track moisture levels in soil, shift to cultivating agricultural products which needs less water like grapes that can be exported while importing water-intensive crops like rice (importing virtual water), set a program for seawater desalination and another program for wastewater treatment and reuse. In [29], the authors suggested that Egypt can build or finance solar and wind power plants in Ethiopia and couple their intermittent variable operation with the operation of the GERD to decrease the power requirements from the GERD and allow sufficient amount of water flow to Egypt.

Conclusions

Egypt has to adapt strategies to face the expected reduction in Nile water supply, which, when combined with the existing ~ 20 bcm freswater deficit, may lead to severe consequences on the national security of Egypt concerning political, economical, social and environmental aspects of life. The main target now is to use all the possible tools, diplomatic relations and soft power to force the Ethiopian side to commit to a binding agreement concerning a fair, midterm filling interval (in the range of 7 years) that can acheive his energy targets of generating hydropower and in the mean time will cause minimum harm to the downstream countries. The agreement should include procedures for operating the GERD in cooperation with the downstream countries, especially during drought periods. All documents concerning the construction of the dam should be available to the scientific community so that risk of failure analysis can be assessed. Internally, Egypt has to develop a plan that include several procedures for rational utilization of freshwater, including efficient and modern agriculture methods, changing crop patterns, applying seawater desalination, wastewater treatment, utilizing groundwater and harvesting rainfall. In addition, firm procedures for water conservation among domestic users and land farmers should be applied.

References

[1] N. V. Pemunta et al.: The Grand Ethiopian Renaissance Dam, Egyptian national security, and human and food security in the Nile River basin, Cogent Social Sciences, 7:1 (2021).

[2] R. G. Abd Ellah: Water resources in Egypt and their challenges, Lake Nasser case study, Egyptian Journal of Aquatic Research, 46, 1–12 (2020).

[3] A. I. El-Moghraby: On the Grand Ethiopian Renaissance Dam (GERD), International Journal of Environmental Science and National Resources, 11:2 (2018).

[4] W. Y. El-Nashar and A. H. Elyamany: Managing risks of the Grand Ethiopian Renaissance Dam on Egypt, Ain Shams Engineering Journal, 9, 2383–2388 (2018).

[5] A. Hijazi: The GERD Conflict: Challenges to Egypt's water security, Center for Middle Eastern Studies, Ankara, Turkey, (2020).

[6] A. Aroussi: Nations clash over giant Nile dam, Nature, Vol. 574, 159-160 (10 Oct. 2019).

[7] N. A. Elagib and M. Basheer: Would Africa's largest hydropower dam have profound environmental impacts? Environmental Science and Pollution Research, 28, 8936–8944 (2021).

[8] A. M. Sharaky et al.: Model-Based optimization for operating the Ethiopian Renaissance Dam on the Blue Nile River, in "Grand Ethiopian Renaissance Dam Versus Aswan High Dam", Springer, 119-148 (2017).

[9] N. Donia and A. Negm: Impacts of filling scenarios of GERD's reservoir on Egypt's water resources and their impacts on agriculture sector, in: "Conventional Water Resources and Agriculture in Egypt", Springer, 391-414 (2018).

[10] B. Keith et al.: Considerations in managing the fill rate of the Grand Ethiopian Renaissance Dam reservoir using a system dynamics approach, Journal of Defense Modeling and Simulation: Applications, Methodology, Technology, 14:1, 33–43 (2017).

[11] Y. Zhang et al.: Ethiopia's Grand Renaissance Dam: Implications for downstream riparian countries, Journal of Water Resources Planning and Management, 05015002, 1-11 (2015).

[12] K. G. Wheeler et al.: Cooperative filling approaches for the Grand Ethiopian Renaissance Dam, Water International, 41:4, 611-634 (2016).

[13] P. Kansara et al.: An assessment of the filling process of the Grand Ethiopian Renaissance Dam and its impact on the downstream countries. Remote Sensing, 13, 711 (2021).

[14] E. Heggy et al: Egypt's water budget deficit and suggested mitigation policies for the Grand Ethiopian Renaissance Dam filling scenarios, Environmental Research Letters, in press, (2021).

[15] S. Liersch et al.: Management scenarios of the Grand Ethiopian Renaissance Dam and their impacts under recent and future climates, Water, 9, 728 (2017).

[16] K. G. Wheeler et al.: Understanding and managing new risks on the Nile with the Grand Ethiopian Renaissance Dam, Nature Communications, 11, 5222 (2020).

[17] A. T. Ahmed and M. H. Elsanabary: Hydrologicalc and environmental impacts of Grand Ethiopian Renaissance Dam on the Nile River, 18th International Water Technology Conference, Sharm ElSheikh, Egypt, 12-14 March 2015.

[18] S. M. Ramadan et al.: Environmental impacts of Great Ethiopian Renaissance Dam on the Egyptian water resources management and security, 23rd International Conference on: Environmental Protection is a Must, Alexandria, Egypt, 11-13 May 2013.

[19] S. Abdel Aziz et al.: Assessing the potential impacts of the Grand Ethiopian Renaissance Dam on water resources and soil salinity in the Nile Delta, Egypt, Sustainability, 11, 7050 (2019).

[20] O. M. Sallam: Vision for future management of groundwater in the Nile Delta of Egypt after construction of the Ethiopian dams, Hydrology: Current Research, 9:3 (2018).

[21] H. Abd-Elhamid et al.: Evaluation of potential impact of Grand Ethiopian Renaissance Dam on seawater intrusion in the Nile Delta aquifer, International Journal of Environmental Science and Technology, 16, 2321–2332 (2019).

[22] E. E. Omran and A. Negm: Environmental impacts of the GERD project on Egypt's Aswan high dam lake and mitigation and adaptation options, in: "Grand Ethiopian Renaissance Dam Versus Aswan High Dam", Springer, 175-196 (2018).

[23] New & Renewable Energy Authority (Egypt): Annual Report (2020).

[24] N. Abdelazim et al.: Operation of the Grand Ethiopian Renaissance Dam: Potential risks and mitigation measures, Journal of Water Management Modeling, 27, C469 (2020).

[25] S. Sterl et al.: Linking solar and wind power in eastern Africa with operation of the Grand Ethiopian Renaissance Dam, Nature Energy, 6, 407–418 (2021).

Optimum Design of Flexible Water Network Taking into Account Reducing CO2 as Egypt's participation in Paris Agreement

M.Mousa[1, a], S. Aly [2, b] and M. Awad [3, c]

[1] Alexandria National Refinery & Petrochemical Company, Alexandria, Egypt

[2] Suez University, Faculty of Petroleum & Mining Engineering, Suez, Egypt

[3] Suez University, Faculty of Petroleum & Mining Engineering, Suez, Egypt

[a] Email address: mohammed.ibMo@pme.suezuni.edu.eg

Abstract: During Paris agreement, Egypt's nationally contributed on carbon dioxide reduction to 1.5 % by 2100 and since water distribution network release billions of pounds of CO2 every year in addition to the amount emitted in construction phase or pipeline repairing, thus pronounced interest is required for designing flexible, sustainable and least cost systems to cope with future challenges. The main purpose of this study is to find an optimum design of flexible water network among several alternatives via combining water network cost, carobn disoxide esmmisions resultant from water network and flexibility too as objective functions to establish a multi-objective model.The model used in this research is integration between GA and EPANET software. Objective functions used in the model cares about optimization of total network cost, carbon dioxide emissions, meanwhile network's flexibility is considered as a constraint. Three flexibilities metrics had been investigated in this research for efficient design of water network then the best flexibility metric is added to the model as an objective function. Three studies had been presented in this paper to tradeoff between flexibility, CO2 emissions and total. The developed model was tested, validated with both of the results obtained from the literature for a simple & large water network for Suez in Egypt and the results were satsfacroily. This research helps scientists, water managers and decision makers for better understanding how to move towards for having sustainable and flexible infrastructure systems and put guidelines for reducing greenhouse gas emissions to comply with Paris agreement requirements.

Keywords: water network design, flexibility, Genetic Algorithm, EPANET, carbon life cycle, tradeoff, Paris Agreement.

1. Introduction

Water is considered to be a main resource for human kind survival. It can be used in irrigation purposes, cleaning activities, chemical industries as solvents, coolant, etc. According to the end usage, water requires to be stored, transported and treated till reaching to the end user. Water is treated in treatment plants where several chemical and physical procedures are made to purify it till be capable for using in drinking according to the regulations of the Environmental Impact Agency. Water distribution networks (WDNs) are the infrastructure that carry and transport water from the treatment plant to the end users. Any WDNs consists of the following components; reservoirs, pipes, pumps and valves.Mohan and Jinesh stated that among different components of WDNs pipelines that transport water from one point to customer are considered to be the main expenditure [1]. In addition to capital cost of WDN, there are huge operational costs such as, energy cost for water transportation water from certain place to other. Egypt's nationally determined contributions to Paris agreement that's targeted to reduce global warming as a first attempt 2°C till reaching 1.5°C by 2100.These actions can be done by strictly applying the environmental regulations besides cooperation with local resources. It was found that it's possible to reduce carbon dioxide emissions by 20 % (i.e., 250 Mton CO2) stated by Lamiaa Abdallah[2]. Several million tons of Carbon dioxide is emitted from water distribution system all over the world. In addition to the amount of CO2 emitted to the atmosphere during rehabilitation or construction new WDNs leading to making these infrastructures unfortunately polluting the environment and increase greenhouse gas effects. In this paper, several WDNs design alternatives are presented with taking into account cost reduction and reducing CO2 emissions too [3]. Flexibility in WDNs design becomes essential after cascading terror attacks on

New York on September,11, hurricanes and earthquakes in Japan 2011.[4].The aim of this research is as follows; developing a multi-optimization model for WDNs for optimizing WDNs, trade-off between cost, emissions and flexibility and investigating the flexibility as a metrics for reliability and incorporate it as an objective function in model formulation. This can achieve by enhancing existing GA model and integrate it with EPANET then compare the result from the study with the previous one.

2. Literature Review

2.1.Optimization in WDNs

2.1.1. Linear / Non-Linear Models

Diameter of pipelines in WDNs had been considered to be the decision variable by Shamir, for cost optimization by building a steady state hydraulic solution [5]. A random sample technique was used by Pitachi for selecting an optimum diameter of pipe network [6] by considering the diameter of pipe network is the continuous variable and hence the solution is rounded off to the nearest commercial diameter, which leads to a lot of infeasible designs [7].Gupta et al., focused on branched WDNs and optimize the cost by considering the length of pipe as a decision variable via LP [8].Same work had been made by Kally but for looped network [9].Later on, Bahave classified network to be either branched or looped, where the former can be used in agricultural, industrial or small countries [10]. The early work in design of WDNs is based on LP or NLP which consider as a complicated. In addition to that using pipe diameter as the discrete variable leading to not find the optimal solution, that's why from 1990's researchers are using meta-heuristics modeling techniques in WDNs design.

2.1.2. Meta-heuristics Models

It's based on making several iterations for the optimization problem to improve the solution. Researchers used stochastic techniques in WDNs optimization e.g., GA, simulated annealing, harmony search, etc. GA was firstly used by Murphy & Simson for optimize small WDNs [11]. Simpson et al. used GA for optimizing large size WDNs [12]. Studying the effect of both using an adequate population size and tournament effect was made by Goldberg [13], then integration of GA with EPANET software produced by EPA was made by Walters,1999 &Lippai et al.[14,15] and the optimal solution was found to be sensitive to Hazen-William's equation linked in EPANET by Rossman [16]. For interested water engineers and designers they can find more details on references section) [17, 18, 19, 20].

2.1.3. Reliable system

A reliable system performs its function for a given time and within specified conditions [21]. WDNs must be reliable enough in order to perform its function in case of different scenarios such as, fire, pipe break, etc. Unfortunately, there is no direct measure for reliability since it's not a system's property [22], but since pipe break leads to loss water and high repairing cost, researchers indicate it as a reliability indicator. Usually there are two reasons for pipe break which are as follows; mechanical failure and hydraulic failure due to demand variation or presence of uncertainties. Resilience index is estimated by Todini and can be calcualted from Eq.1[23]. Several techniques were made by researchers to evaluate system's reliability based on neuro fuzzy and regression models and available in references [24, 25, 26].

$$RI = 1 - \frac{\boldsymbol{P}_{\mathbf{in}}}{P_{max}} \qquad (1)$$

$$\boldsymbol{P}_{\mathbf{in}} = \mathrm{P_{tot}} - \gamma \sum_{i=1}^{nn} qihi \qquad (2) \qquad \boldsymbol{P}_{\mathbf{max}} = \mathrm{P_{tot}} - \gamma \sum_{i=1}^{nn} qih' \qquad (3) \qquad P_{\mathrm{tot}} = \gamma \sum_{k=1}^{nr} Q_k H_k + \sum_{j=1}^{np} P_j \qquad (4)$$

Where, RI = resilience index , $\boldsymbol{P}_{\mathrm{tot}}$ = power at begining of WDN , γ= water specific weight , Q_k = discharge flowrate of reservoir K ,n_r = resevoirs number and n_p = pumps number.

Modified RI is defined as the percentage of the amount of addtional power at deamand node to the summation of minimum power at demand nodes [27]. It can be noted that MRI can be larger than 1 , while the value of RI is less than 1.

3. Model Formulation

The model used in this paper aims to develop an optimum water distribution network with least cost, minimum CO2 emissions and with a maximum flexibility. This is made by integration GA with EPANET and reliability as a constraint.

3.1. Genetic Algorithm

The input to GA is objective function(s) and randomly potential solution to the problem. Solutions are like chromosomes with a mathematical encoding and capable of reproducing. Usually, any two solutions from chromosomes are combined together depending on the rate of mutation. Average fitness for the population allows a combination of several generations to have a good result in any problem [28 ,29].

3.2. GANetXL

It was developed by university of Exter, Centre of water system . GANetXL can be used in single and multi-objective optimization by using GA for problem optimization, which makes GA using an easy task for researchers and many water engineering applications. It's available as an add- in Microsoft excel and considered as a flexible, user-friendly program which can work with more than thousands of variables. A set of decision variables, objective function(s) and constraints are required to run the program and the optimization progress can appear in the toolbar [30].

3.3. EPANET

It was developed by EPA; it's a steady state simulation problem, which combines water quality, flowrates and hydraulic behavior of network. WDNs are governed by mass and energy conservations, where the former can be described in Eq.5. The latter is based on understanding the system energy's loss /gain, length, diameter, coefficient of friction of pipe network, which can be calculated from Hazen's William method as shown in Eq.6 [31].

$$Q_{in,\,i} = Q_{out,\,i} + Q_{d,\,i} \quad (5)$$

Where, $Q_{in,\,i}$ = Total input water flow to node i, $Q_{out,\,i}$ = Total output water flow to node i and, $Q_{d,\,i}$ = Demand water to node i.

$$H_{f,\,j} = 10.4397\ L_j \frac{(C_j Q_j)^{1.85}}{D_j^{4.6855}} \quad (6)$$

Where, $H_{f,\,j}$= Head loss in pipe j in m, L_j= Pipe length in m, C_j = Coefficient of friction to node j and D_j = pipe inside diameter in inches.

3.4. Objective Function

In this research, the objective function varies with scenarios to trade-off between different design alternatives. A general formula for the optimization problem's objective function are as follows;
Obj. 1= Minimize Life Cycle Cost (7), Obj. 2=Minimize Life Cycle CO2 Emission (8)
Obj. 3 = Maximize reliability & Flexibility (9)

3.5. Constraints

Constraints can be classified as follows; systematic constraints like mass and energy conservations, users restricted constraints such as, pressure requirement in each node where its values reach from 30-75 psi [32]. Finally, reliability constrains are added in some alternatives for better trade-off between different design scenarios and it's assumed its equal =0.8 over the design period. Eq. 10 to 12 describe constrains respectively as mentioned above.

$$H_{f,\,j} = H_{j,\,1} - H_{j,\,2} \quad (10)$$

$$H_{p,\,k} = H_{k,\,1} - H_{k,\,2} \quad (11)$$

$$H_{min} < H_m \quad m = 1,2,3, \ldots . n \quad (12)$$

Where, $H_{f,\,j}$ = head loss in node j estimated from eq.2, $H_{j,\,1}$& $H_{k,\,1}$= nodal head at high pressure at node j or k. $H_{j,\,2}$& $H_{k,\,2}$ nodal head at low pressure at node j or k, $H_{p,\,k}$ = head added by pump, n = node number and H_m = pressure at node m.

3.6.Working Procedures

In this paper, different scenarios had been studied to trade-off between different design alternatives when subjected to different objective functions. Table.1 illustrates different design alternatives dealt with in this research.

Table.1: Different design alternatives

#	Objective Function	Constrains	#	Objective Function	Constrains
1	Fixed Cost	Network	6	CO2 emissions	Network &Flexibility
2	Fixed Cost	Network , Flexibility	7	Life Cycle Costs , CO2 emissions	Network
3	Life Cycle Costs	Network	8	Life Cycle Costs , CO2 emissions	Network &Flexibility
4	Life Cycle Costs	Network , Flexibility	9	Life Cycle Costs , Flexibility	Network
5	CO2 emissions	Network	10	Life Cycle Costs, CO2 , Flexibility	Network & Flexibility

4. Case Studies

WDN-I was first introduced by Shamir [33] and had been used by several researchers. Layout of WDN-II is shown in figure.2. It's a pumped network; pump addition to the network increases both of capital and operating costs and contributes in CO2 emissions [34]. WDN-II is popular used in the literature, called ''anytown'' water network and was first introduced by Walski.et.al. [35]. The model used was tested too in a real network to check its ability in dealing with complicated systems, compare its results with work done with Rayan. et.al. [36]. WDN-III is related to Suez water network. Suez is located at the north of Suez Gulf. Suez's total population is 744,189 inhabitants according to census 2017. [37]. WDN-III consists of three reservoirs, three pumps, 389 pipelines and 341 nodes with demand = 6656 m³/hr. [38]. It's assumed that Hazen's Williams coefficients equal 130 &144 for ductile iron pipe and PVC pipes respectively for all networks. Further description for networks is available in appendix section. Figures 1, 2&3 illustrate the layout for the three case studies where marked area in figure.3 indicate pumps location after that, evaluation strategies for estimating (RI), (MRI) and (NRI) and finally, investigation different indices efficiency over different failures scenarios was made.

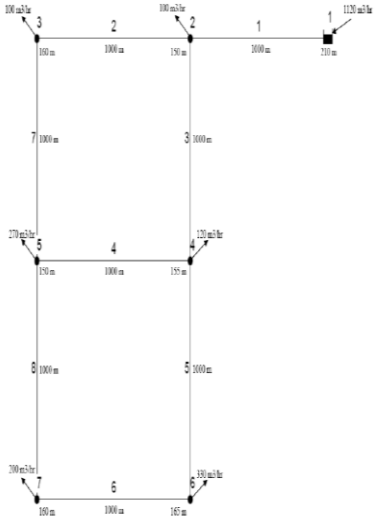

Figure.1. WDN-I

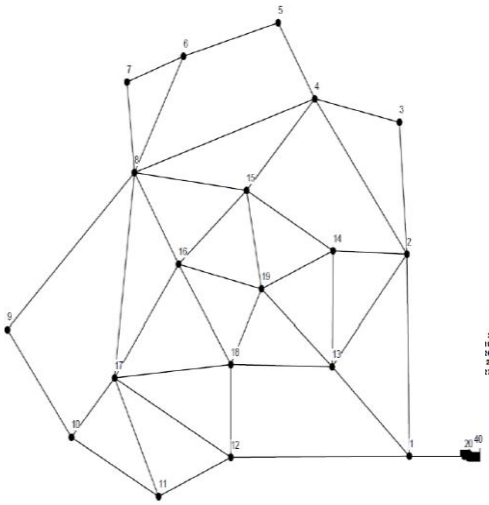

Figure.2. WDN-II

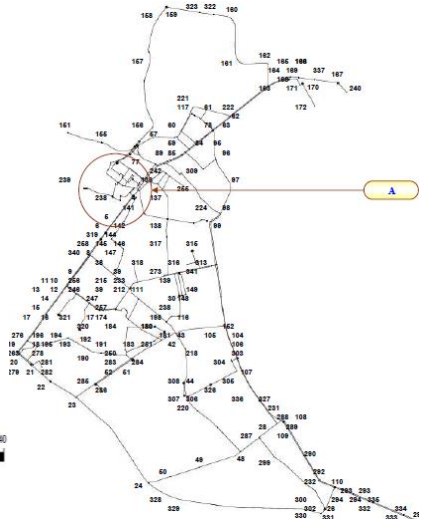

Figure.3. WDN-III

5. Results & Discussions

5.1.WDN-I

5.1.1. Simultion for WDN-I

Although WDN-I looks simple problem , it was found that there are 11^8 solutions unfotunately, the system reliability in the first alternative is 55 % which is not a good value in order to have reliable and flexible network to be capable of dealing with uncertanties such as pipe failures. In order to test the developed model, the model had been run by the same cost data presented by Alperovits [33] and it was found that the optimal value had been obtained at the eighth run with a total cost 662760 L.E., which is as the same obtained by stochastic optimization traditional techniques. Table.2 shows the

results of different design alternatives related to WDN-I, where cost expressed in milion L.E and CO2 in Kg.

Table.2 Results of optimum different design alternatives related to WDN-I

#	Reliability %	Fixed Cost	LCC	LCE	#	Reliability %	Fixed Cost	LCC	LCE
1	**55**	**31.4022**	86.79	2370	5	**55**	**31.4022**	86.79	2700
2	84	36.6096	96.258	2990	6	84	36.6096	96.258	2990
3	0	36.72006	64.0668	3022	7	60	31.56	83.634	2670
4	88.7	42.606	69.432	3400	8	88.7	37.872	88.368	3035

5.1.2. Trade-off Alternatives

5.1.2.1. Cost vs. Reliability

It was found that to have reliable network it's required to pay 5.094 , 6.312 mililon L.E. as a fixed cost for WDN-I for reiability reaches 84 and 88.7 % respectively.

5.1.2.2. Cost & Life Cycle CO2 emissions

By considering minimizing CO2 emissions as an objective function as in the fifth alternative as work prensented by Wu.et al. [39]. It was found that CO2 emissions had been reduced to 2.7 k tons. After addition of reliability as another objective function as in the sixth alternative , CO2 emissions increased to 2.99 K tons. The seventh alternative is similar to that reported by Wu.et al. considered as a multi-objective optimization, but unfortunately network isn't reliable. Finally, system flexibility is increased to 88.7% in the last alternative with an increase in both of life cycle costs &CO2 emissions by 7 and 13% respectively.

5.2. WDN-II

5.2.1.Simultion for WDN-II

Simulation had been made using GANetXL & EPANET. The first alterntive hadn't been made since the model had been tested in WDN-I. Firstly, a simulation was carried to optimize WDN-II without considering flexibility. Table.3 shows the results of different design alternatives related to WDN-II, where cost expressed in milion L.E and CO2 in S/T and related pumps data are presented in appendix.

Table.3 Results of optimum different design alternatives related to WDN-II

Alternative No.	Fixed Cost	LCC	LCE * 10^{14}	Alternative No.	Fixed Cost	LCC	LCE * 10^{14}
3	274	485.8121	2.89	7I	288	488.7731	2.72
4	328	547.1276	3.09	7II	289	489.5157	2.72
5	350	518.8292	2.4	8I	362	564.9904	2.89
6	391	592.5271	2.88	8II	355	561.4658	2.92

5.2.2.Trade-off Alternatives

5.2.2.1. Cost vs. Reliability

To have reliable network , it's required to pay 76 millions L.E. as a fixed cost for reliable system. This value increases to 88 millions L.E for having a maximum reliability (i.e. an excess ranges from 11-13.5 % from total fixed costs).

5.2.2.2. Cost & Life Cycle CO2 emissions

It was found that the cost of reducing one ton of CO2 in WDN-II is 160 L.E for non reliable systmm and this value raises to 316 L.E for reliable systems , which nearly double the cost in case of non- reliable systmes.

5.3. WDN-III

5.3.1.Simultion for WDN-III

The optimum solution results for WDN-III was 87.5 millions L.E. for minimum pressure= 25 m. Working was made with same piping and diameters cost data for testing the model illustrated above and validate it in large networks and it was found that the optimum cost is 87.46 millions L.E . After that, the model used above was used for trading-off different alternatives.

Table.4 Results of optimum different design alternatives related to WDN-III

Alternative No.	Fixed Cost	LCC	LCE * 10^{14}	Alternative No.	Fixed Cost	LCC	LCE * 10^{14}
3	96	201.69	4.46	7I	97	217.3	4.23
4	112.038	340.15	5.15	7II	98.5	218.65	4.36
5	150.48	370.65	3.1	8I	175.39	312.3	3.67
6	193.6	390.6	3.76	8II	180.3	375.3	3.25

5.3.2.Trade-off Alternatives

5.3.2.1.Cost vs. Reliability

To have reliable network , it's required to pay 54.5 millions L.E. as a fixed cost for reliable system. This value increases to 84.3 millions L.E for having a maximum reliability. (i.e. an excess ranges from 15.7-18.8 % from total fixed costs).

5.3.2.2.Cost vs. Life Cycle of CO2 emissions

It was found that the cost of reducing one ton of CO2 in WDN-III is 140 L.E for non reliable system and this value raises to 278 L.E for reliable systems.

5.4.Flexibility vs. reliability

RI, MRI and NRI had been investigated for failures events probabilities [40]. It was found that the probability of breaking two or more than two pipes simultaneously is low. A visual basic code had been written, linked to EPANET. Systems' performance is analyzed by using average percentage of feasible scenarios. Figure.4 shows optimal metric indices values for break scenarios.

Table.5. shows optimum metrics indices value for WDN-III vs. LCC in million L.E.

Life Cycle Costs	RI	NRI	MRI	Life Cycle Costs	RI	NRI	MRI
22	0.3	0.285	0.03	33.138	0.8	0.78	0.092
23.9856	0.41	0.405	0.05	34.716	0.85	0.8	0.096
25.564	0.57	0.55	0.07	39.45	0.87	0.85	0.099
28.404	0.63	0.6	0.09	71.01	0.9	0.88	0.1

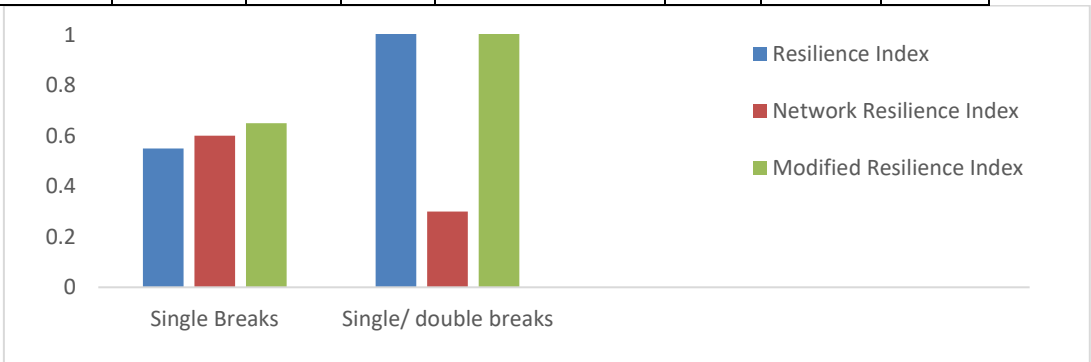

Figure.4 shows optimal metric indices values for break scenarios for WDN-III

6. Conclusions

Several tons of carbon dioxide is emitted from WDNs all over the world. In addition to that it's a must to consider the flexibility during the design phase or rehabilitation of any infrastructure and particularity in WDNs in order to make the system capable of supplying water with sufficient demands and pressure to all customers especially in case of uncertainties such as, demand pattern variation or emergencies. Egypt's contributed in Paris agreement for climate change to reduce the amount of carbon dioxide so a trade-off among different design alternatives is required. Different objective functions such as, flexibility, life cycle costs and carbon dioxide emissions had been investigated for three WDNs. Model was tested & validated with the results obtained from the literature and for a real case too in Suez, Egypt to check it in large systems and it was found that the obtained results are satisfactorily. For the first case study, it was found that depending on reliability considerations a reduction of the life cycle costs could reach to 28 %, meanwhile an increase in life cycle costs up to 9 % is observed if reliability reaches 88.7% and it needs around 63 LE. per ton carbon dioxide reduction this value increases for WDN-II&WDN-III due it's large size and presence

of pumps, which contributes in CO2 emissions. Finally, this research presents a trade-off technique among different alternatives for optimal WDNs designing and according to project specifications & decisions makers the desired solution could be selected.

Funding sources
This research received no external funding.

Conflicts of interest
There are no conflicts to declare.

Acknowledgements
The author would like to thank ***University of Exter, the Centre for Water systems, UK*** for developing and providing a free version of GANetXL software and ***Eng. Mohamed Ali*** for his aid in simulaion.

Recommendations

- It's recommended from decision makers to work with scholars, researchers, and organizations such as, Japan International Cooperation's Agency for developing a framework to comply with Paris agreement regulations. Finally, further work is required to investigate other pollutions resultant in water network structures and add it to the model.

Nomenculture

LCC	Life Cycle Cost	LCE	Life Cycle carobn Emissions
$\boldsymbol{P}$tot	Power at begining of WDN	Qd,i	Demand to water node i
γ	Water specific weight	Hf, j	Head loss in pipe j
Qk	Discharge flowrate of reservoir K	Lj	Pipe length
nr	Resevoirs number	Cj	Coefficient of friction to node j
np	Pumps number.	Dj	Pipe inside diameter
RI	Resilience index	Obj.	Objective Function
MRI	Modified Resilience index	H$j1$	Nodal head at high pressure at node j
NRI	Network Resilience index	H$k1$	Nodal head at high pressure at node K
Qin,i	Total input water flow to node i	Hj2	Nodal head at low pressure at node j
$Qout,i$	Total output water flow to node i	Hk2	Nodal head at low pressure at node K
Hpk	Head added by pump	n	Number of nodes

Refernces

1. S. Mohan and J. Babu: submitted to Journal of Computing in Civil Engineering (2010).
2. L. Abdallah: submitted to International Journal of Industry and Sustainable Development (2020).
3. Natural Resources Defense Council: Water efficiency saves energy: Reducing global warming Pollution through water use strategies New York (2009).
4. I.Basupi and Z. Zapelan: submitted to Journal of Water Resources Planning and Management (2013).
5. Y. Yuan, Y. Liu and M. Zhang: submitted to Mathematical Problems of Engineering (2015).
6. U. Shamir “Minimum Cost design of Water Distribution Networks”, Cambridge University Press, New York, (1964).
7. R. Pitchai “Model for Designing Water Distribution Pipe Networks”, PhDThesis, Harvard University, Cambridge, MA, (1966).
8. D. Karmeli, Y.Gadish and S. Meyers: submitted to Journal of Pipelines Divisons (1968).
9. M. Gupa, Y. Hassan :Water Supply System with Multiple Points.Vol.4 (3) ,(1972) ,p.200-204.
10. E. Kally, “Computerized Planning of the Least-Cost Water Distribution Network”, Water and Sewage Works Reference, R121 to R127 (1972).
11. P. R. Bhave and R. Gupta, “Analysis of Water Distribution Networks,” Alpha Science International, Technology & Engineering, University of Michigan, Michigan, (2006).
12. C. Dandy, R. Simpson, A., and J. Murphy: An improved Genetic Algorithm for Pipe Network Optimization. Water Resources Research,32(2): 449–458, (1996).

13. D. E. Goldberg and K. Deb, "A comparative analysis of selection schemes used in genetic algorithms," Foundations of genetic algorithms, vol. 1, pp. 69–93, (1991).
14. G.A. Walters, "Optimal Design of Water Distribution Networks" in E. Cabrera and F. Martinez (eds.), Water Supply Systems, State of the art and future trends, Computational Mechanics Publications, pp. 91-117, (1993).
15. I. Lippai, P. Heaney and M. Laguna: submitted to Journal of Computing in Civil Engineering, (1999).
16. Lewis A. Rossman, "The EPANET Programmer's Toolkit for Analysis of Water Distribution Systems", 29th International Conference: "Annual Water Planning Resources & Management", (2004).
17. L. Abdallaha and T. El-Shennawy, "Evaluation of CO2 emissions from electricity generation in Egypt", 1st International Conference on Chemical, Energy and Environmental Engineering (ICCEEE), Alexandria, Egypt, 19-21 March, 2017.
18. Cl. Aranha, Y. Lavinas and Marcelo Ladeira, "Experimental Analysis of the Tournament Size on Genetic Algorithms", International Conference on Systems, Man, and Cybernetics (IEEE), 2018.
19. O. Calvo, C. Quintiliani, L.lfonso and Gi.Demarinis: submitted to Journal of Water Resources Planning & Management ,(2019).
20. L.Sela and M.Housh: submitted to Journal of Hydraulic Engineering, (2019).
21. O. Fujiwara, U. Silva: submitted to Journal of Environmental Engineering, (1990).
22. M. Salman , R. Mazumder , Y.Li and X. Yu :submitted to Journal of Water Resources Planning & Management ,(2018).
23. E. Todini, "Looped water distribution networks design using a resilience index based heuristic approach." Urban Water, 2(2), 115–122. (2000).
24. A. Assad, O. Moselhi and T. Zayed: submitted to Water Journal, (2019).
25. A. Gheisia, S. Shabania and G. Nasera, "Flexibility ranking of water distribution system designs under future mechanical and hydraulic uncertainty", 13th Computer Control for Water Industry Conference, CCWI, (2015).
26. A. Gheisi and G. Naser: submitted to Urban Water Journal, (2013).
27. N. Jayaram, K. Srinivasan, Performance-based, "optimal design and rehabilitation of water distribution networks using life cycle costing", Water resources research 44 (2008).
28. S. Katoch, S. Chauhan and V.Kumar: submitted to Multimedia Tools and Applications, (2020).
29. D. A. Savic, and G. A. Walters: Submitted to Journal of Water Resources Planning & Management, (1997).
30. A. Savić, J. Bicik and S. Morley, "GANETXL: A DSS Generator for Multi-objective Optimization of Spreadsheet-Based Models, the Centre for Water Systems, College of Engineering, Mathematics and Physical Sciences, University of Exeter, UK(2011).
31. L. A. Rossman, EPANET: User's manual, U.S. EPA, Cincinnati. (2000).
32. Y.Guo , V. Ghorbanian and W Karney, " Minimum Pressure Criterion in Water Distribution Systems : Challenges & Consequences", Conference: World Environmental & Water Resources Congress :Flood ,Droughts and Eco-systems , Austin,(2015).
33. E. Alperovtis and U. Shamir: submitted to Water Resources Research, (1977).
34. K. Pirtla"Investigation of Sustainable and Reliable Design Alternatives for Water Distribution Systems ", PhD Thesis, Arizona StateUniversity, USA, (2012).
35. T. Walski: submitted to Journal of Water Resources Planning and Management, (1987).
36. B. Djebedjian , A. Yaseen , and M. Rayan, "Optimization of Large Water Distribution Network Design Using Genetic Algorithm", 10th International Water Technology Conference, (IWTC10), Alexandria, Egypt , (2006).
37. Information on :https://knoema.com/atlas/Egypt/Suez/Population.

38. United Nations Development Programme, "Suez Master Plan," March 1976.
39. Z.Wu, W. Cheng, J.He, P. Gao and S. Xu in , Carbon emission control strategies for China: A comparative study with partial and general equilibrium versions of the China MARKAL model, edited by W. Chen et al. / Energy,(2005), in press.
40. H. Liu, A. Savić, Z. Kapelan, E. Creaco and Y.Yuan : submitted to Submitted to Journal of Water Resources Planning & Management, (2016).

APPENDICES

Table.1 U.S. Energy-Related CO2 Emissions by Sector and Source (Tg CO2 Eq.) (EPA2020)

Sectors and Source	2005	2010	2015	2020
Electric Power	**2,381**	**2,342**	**2,382**	**2,466**
Petroleum	102	47	38	40
Natural Gas	320	322	261	285
Coal	1,958	1,962	2,071	2,129
Other	0.4	12	12	12
Transporation	**1,882**	**1,835**	**1,858**	**1,853**
Petroleum	1,8484	1,800	1,823	1,817
Natural Gas	33	35	35	36
Electricity	5	4	5	6
Industrial	**828**	**805**	**839**	**840**
Petroleum	330	336	326	321
Natural Gas	382	370	389	387
Coal	116	99	124	132
Electricity	731	580	607	610
Residental	**358**	**363**	**346**	**344**
Petroleum	95	93	83	78
Natural Gas	262	268	262	265
Coal	1	1	1	1
Electricity	849	879	855	882
Commercial	**222**	**225**	**223**	**224**
Petroleum	50	45	42	41
Natural Gas	163	173	174	176
Coal	9	6	6	6
Electricity	797	879	916	968
U.S Territories	**53**	**63**	**74**	**86**

Table.2 EPANET'S Different Functions an its Defintions

Function	Defintion
openNetwork	Opens then load a certain network for simulation
closeNetwork	Closes a certain network after being analyzed
getNodePressure	Recover a certain node's pressure
getNodeHead	Recover a certain node's head
getLinkCount	Calculate the total number of links in the loaded network
getNodeCount	Calculate the total number of nodes in the loaded network
getLinkId	Recover an id number for certain link
getNodeId	Recover an id number for certain node
getLinkDiameter	Recover a certain link's diameter
getLinkLength	Recover a certain link's length
setLinkDiameter	Define a diameter's value in certain link
setLinkStatus	Modify link status from open to close and vice versa
Solve	Perform Hydraulic's network

Table.3 Costs of Piping Installation for Different Diameters for WDN-I&II

Dia. (cm)	Dutile Iron (L.E /m)	HDPE (L.E./m)	Piping Installtion Costs(L.E./m)
10	873.27	106.42	970.3
15	1025.075	231.62	1064.2
20	1272.345	391.25	1361.55
25	1616.645	607.22	1643.25
30	209.71	854.49	1893.65
35	2449.225	1031.335	2018.85
40	3001.67	1347.465	2394.45
45	3455.52	1704.285	3192.6
50	4062.74	2103.36	4069
55	4695	2546.255	4695
60	5186.41	3029.84	5164.5
65	5956.39	3555.68	5743.55
70	6578.165	4123.775	6353.9
75	7180.22	4734.125	6948.6
90	9577.8	6817.14	8764

Table.4 Costs of Repair for different diameters

Dia. (cm)	Break Rate (Break/ Year/ km)	Reapiring Costs (L.E./ Single Break)
10	0.52	8951.8
1.5	0.43	9796.9
2	0.26	10454.2
2.5	0.16	11158.45
3	0.1	12504.35
3.5	0.09	15024
4	0.07	15775.2
4.5	0.05	16260.35
5	0.042	17637.55
5.5	0.029	19562.5
6	0.016	22050.85
6.5	0.019	22504.7
7	0.013	23866.25
7.5	0.008	25243.45

Table.5 Different Pipe Materials emoided energy coeffiecient according to Ambrose et al., 2002

Type of Pipe	Emboided energy (J / kg)
Ductile Iron	38200000
DICL	40200000
PVC	74900000
PE80B	75200000
PE100	75200000
PVC	76600000

Table.6 Carbon dioxide emissions from the emboided energy in ton / m.

Dia. (cm)	Dutile Iron	HDPE	Dia. (cm)	Dutile Iron	HDPE
10	0.095796	0.039966	45	0.502711	0.638242
15	0.140618	0.086506	50	0.593234	0.787897
20	0.185441	0.146541	55	0.650363	0.953297
25	0.238172	0.227684	60	0.710123	1.134614
30	0.305845	0.320245	65	0.85036	1.331501
35	0.355061	0.386163	70	0.936125	1.544306
40	0.43328	0.50433	75	1.015089	1.722855

Table.7 Resultants Emissions Amount from using Horizontal Directional Drilling Equipment in Kg.

Equipment	Hydrocarbons	Carbon Monoxide	Nitrogen oxides	Partiaculate Matters	Carbon Dioxide	Sulfur Oxides
Backhole	0.353808	2.580984	2.17728	0.208656	905.728	0.58968
Excavator	0.231336	1.886976	3.56076	0.358344	1471.808	0.95256
Truck	0.09072	0.6804	1.365336	0.117936	877.424	0.567
Rig	0.6804	4.050648	9.498384	1.76904	5519.28	3.587976
Roller	0.009072	0.086184	0.163296	0.013608	56.608	0.04536
Total	**1.3608**	**9.2988**	**16.7832**	**2.44944**	**8774.24**	**5.76072**

Table.8 Emissions of CO2 in Ib in case of Pipe breaks

Dia. (cm)	Clamp Length (cm)							
	15	19	25	32	38	50	60	75
5.08	0.08157	0.08157	0.085979	0.085979	0.098192	N/A		
7.62	0.08157	0.085979	0.085979	0.092747	0.109105			
10.16	0.085979	0.092747	0.098192	0.10366	0.114572	0.136398	0.14731	0.174603
15.24	N/A	0.098192	0.109105	0.114572	0.136398	0.152756	0.174603	0.207341
20.32	N/A	0.10366	0.114175	0.120018	0.141843	0.16369	0.190961	0.223699
25.4	N/A	0.120018	0.136398	0.14731	0.190961	0.212787	0.234612	0.289198
30.48	N/A	0.13093	0.14731	0.158223	0.207341	0.223699	0.256437	0.321936

Table.9 WDN-I characteristics

Node No.	Elevation (ft.)	Demand L/hr.	Redquired Pressure (ft.)
1	64.008	-	-
2	45.72	100000	9.144
3	48.768	100000	9.144
4	47.244	120000	9.144
5	45.72	270000	9.144
6	50.292	330000	9.144
7	48.768	200000	9.144

Table.10 Piping Cost Data for WDN-I using Shamir prinicle for model validation

Dia. (m)	Cost (L.E./m)	Dia. (m)	Cost (L.E./m)
0.0254	31.56	0.4572	2051.4
0.0508	78.9	0.508	2682.6
0.0762	126.24	0.5588	4734
0.1016	173.58	0.6096	8679
0.1524	252.48	0.0254	31.56
0.2032	362.94	0.0508	78.9
0.254	504.96	0.0762	126.24
0.3048	789	0.1016	173.58
0.3556	946.8	0.1524	252.48
0.4064	1420.2	0.2032	362.94

Table.11 Pumps characteristics for WDN-II , Discharge and head are in Lit./ hr and ft. respectively.

First Pump			Second Pump		
Discharge	Head	Efficiency	Discharge	Head	Efficiency
0	27.87091	0	106680	32.51606	0
454250	27.1272	50	103600	31.58703	50
908000	25.08504	65	97000	29.72897	65

Proposed Indices for Prioritizing Energy Efficiency Measures (EEMs) in Existing Office Buildings

Tarek ElShennawy
Alexandria National Refining & Petrochemicals Co. (ANRPC), Alexandria, Egypt
tshennawy@yahoo.com

Keywords: Energy and Environmental Indices, Energy Efficiency Measures (EEMs), Retrofitting Office Buildings, Energy and Environment

Abstract. The building sector plays a pivotal role in achieving the climate goals of Paris Agreement to limit global warming below 1.5°C or 2°C by 2100. Buildings are responsible for almost one third of energy consumption and 40% of CO_2 emissions worldwide. Almost 90% of the building stock was built when there was neither awareness of the climate change challenges nor energy efficiency regulations. In order to achieve the goals of energy efficiency and CO_2 emission reductions from the building sector, major retrofits are required. In many cases, there is no sufficient budget to finance most of the EEMs, and a decision support tool is required to help the decision maker to prioritize such measures. Normally, financial indices like payback time (PBT) or net present value (NPV) or internal rate of return (IRR) are used to prioritize EEMs. Such indices lack important information concerning the quantity of saved energy or the amount of reduced CO_2 emissions. In this context, we propose the use of any of the following two alternative indices to prioritize EEMs taking into consideration the energy / environmental viewpoint with respect to the invested money; The Energy Saving Index (kWh saved/$ spent) where projects with the highest kWh saved/$ spent are preferred, and the Emission Reduction Index (kg CO_2 reduced/$ spent) where projects with the highest CO_2 reduction/$ spent are preferred. A company with multi-office buildings in Alexandria, Egypt, is taken as a case study to examine the effectiveness of the proposed indices in prioritizing the suggested EEMs.

Introduction

The Paris Agreement, signed in December 2015, sets an ambitious target to limit global temperature rise (the main reason for climate change), within this century, below 2°C (and hopefully 1.5°C) compared to pre-industrial levels. The building sector is responsible for a large share of greenhouse gas emissions and their reduction can bring to a signifcant cut of the environmental impacts [1]. CO_2 emissions from the building sector is responsible for 38% of total global CO_2 emissions [2]. Without stringent climate policies, buildings energy demand is expected to increase due to demographic trends and socio-economic developments. Limiting global warming below 1.5°C or 2°C by 2100 requires strong actions to reduce the impact of buildings activities [3]. To achieve the 1.5°C pathway, we require a building emissions reduction of 80–90% by 2050. Staying under a 1.5°C global temperature increase is no longer possible due to the current insufficient actions. However, staying under 2°C is still achievable, but the longer the sector waits to make a transition the more abrupt this transition will have to be [4]. For new constructions, high energy performances are required by mandatory codes and standards. All new constructions should be Nearly Zero Energy Buildings (NZEB). However, a large part of the building stock is quite old and built without any regulations about energy efficiency; consequently, its energy consumptions are very high. The potential energy saving that can be obtained from very simple EEMs retrofits is very high [5]. Office buildings have major characteristics that differentiate them from other building types. These major characteristics include high energy consumption capacity due to high dependence on mechanical heating and cooling systems and artificial lighting. Office Heating, Ventilation and Air Conditioning (HVAC) accounted for between 40% and 68% of electrical consumption, followed by energy for lighting, which accounts for between 13% and 37% and office equipment that consumes between 12% and 25% of energy [6].

Retrofit has similar terms in literature such as refurbishment, rehabilitation, renovation, improvements, and repairs on existing buildings. Sustainable retrofit is defined as the upgrade of components or elements or fabric system or controls of a building with the aim of improving the building's energy and environmental performance [7]. Because of financial constraints, not all the EEMs can be applied at once, making it necessary to define a criterion for ranking them. Several indicators were proposed in literature to rank or prioritize such EEMs [8]. Prioritizing the most economically promising investments is not straightforward because apart from cost-effectiveness calculations, several real-world constraints have to be taken into account [9]. Although several papers in literature deal with energy retrofits in existing buildings, yet a limited number of these papers combine energy savings, environmental benefits and cost of the EEMs into one index that can be used to judge these EEMs. In [10], three Energy Performance Indicators (EPIs) are defined, which are annual electricity use intensity, annual natural gas use intensity, and annual energy cost and a standard regression coefficient sensitivity analysis method is applied to determine the sensitivity of each EEM with respect to the three EPIs, and the relative sensitivity of all EEMs are calculated to evaluate their energy impacts. The proposed indices are applied to a medium size office building in USA. In [11], a free online toolbox was developed to select and prioritize the energy efficiency interventions in public buildings in terms of costs, energy savings, CO2 emissions' reduction and return on investments. The proposed method was applied on a public building (municipality) in Italy.
It should be noted that energy saving and CO_2 emission reduction are two facets of the same coin. The CO_2 emission intensity is based on the energy mix used to generate electricity. According to the global energy mix of 2020, approximately 63% of generated electrical energy came from carbon-based sources (37% coal, 22% natural gas and 5% oil) whereas 37% of the generated electrical energy came from carbon-free sources (17% hydropower, 10% nuclear and 10% renewables of wind, solar and biomass). It is worth noting that the coal is approximately equal to all non-fossil energy sources, including hydropower, nuclear, wind and solar. In 2020, the worldwide electrical energy generated was approximately 27,000 Tera Watt Hours (TWh), and the corresponding CO_2 emissions were approximately 14 Giga Tons (40% of global CO_2 emissions). This means that the global average CO_2 intensity is approximately 0.5 kg CO_2/kWh. In other words, each 1 kWh of saved electric energy corresponds to 0.5 kg of CO2 not emitted to the atmosphere [12].

Methodology

Step (1): Energy Audit. Normally this step is done as a part of a continuous Energy Management System (EnMS) such as ISO 50001:2018 [13]. The company or the organization's top management should assign an energy audit team (internal or external), who plans and conducts an audit plan that is compatible with the company's size and energy consumption. The required data may include the building type, building area, year of construction, electricity, natural gas and water bills for at least 12 months, number of employees, working hours, number and power of elevators, type of HVAC system and its power, number and power of computers, printers, copiers, and other office equipment, available area of the roof, maximum and minimum recorded temperatures during the year, types of glazing (windows), numbers and power of lighting fixtures, number and power of electric water heaters in addition to any other loads that consumes energy. The audit report should conclude with a list of EEMs.
Step (2): Evaluation of the EEMs. Each EEM will be evaluated in terms of energy saving potentil (kWh) and its equivalent CO_2 emission reduction. Each EEM will be financially evaluated in terms of its money investment including capital and installation costs, expected annual money savings and the familiar financial index of the PayBack Time (PBT) in years. In our study, we will use this index thanks to its high popularity and simplicity to the decision makers. Other indices may also be used such as Net Present Value (NPV) or Internal Rate of Return (IRR), Return on Investment (ROI), Life Cycle Cost (LCC) or Total Cost of Ownership (TCO), in accordance with the company / organization internal system.

Step (3) Apply Organization's Constraints. Each organization may have certain constraints such as funding problems which may limit the application of high investment projects, need to comply with laws and regulations concerning carbon footprint (prefer environmental projects even if not economically feasible), preferring of projects with short payback period), etc. Within these constrains some opportunities may be ignored even if technically and/or economically attractive.

Step (4) Prioritize EEMs. We propose the use of any of the following two equivalent indices:

- *Energy Saving Index (kWh saved/$ spent)*

From the energy management viewpoint, projects with the largest kWh savings are the best projects. However, the comparison based on the saved kWh alone may not be fair. A project with the highest kWh savings may be financially unfeasible and the vice versa. To normalize the amount of kWh savings with the investment over the project lifetime, we have to combine both indices; the financial and the energy saving. The kWh saved / $ spent index is proposed, where projects with the highest kWh saved / $ spent are preferred.

- *Emission Reduction Index (kg CO_2 emission reduction/$ spent)*

Applying he same discussion, and combining this time the environmental point of view with the financial one, the kg CO_2 emission reduction / $ spent index is proposed. Again, projects with the highest CO_2 emission reduction / $ spent are preferred.

It is clear that both indices are related. Actually, these two indices are the same index, expressed once in terms of energy units and once in environmental units, with the reference always made with respeect to financial units.

Case Study

To validate the effectiveness of the proposed indices in the process of decision making concerning prioritizing the EEMs, a case study is considered for Alexandria National Refining & Petrochemicals Co. (ANRPC) in Alexandria, Egypt. Applying the aforementioned four-step methodology, we get:

Step (1). ANRPC contains seven office buildings. Fig. 1 shows the main administrative building. The buildings work 8 hours per day, 5 days a week. The building is shutdown during weekends and national and religious vacations. The effective operating hours of the building are in the range of 2000 hours annually. The total consumed electrical energy during 2020 was approximately 2,500,000 kWh. The electrical consumed energy peaks during the summer months due to HVAC loads, as shown in Fig. 2. The HVAC loads consumes about 40% of the buildings energy, the lighting consumes about 30% of the energy and the office equipment and other loads (elevators, water heaters, water pumps, . .) consume the remainder 30%. The price of 1 kWh of electrical energy is approximately 0.1 USD.

Step (2). After performing an energy audit, the following EEMs are identified:

1. Replace the glazing system such that new glass allows sunlight to enter without heat energy. This will decrease both the artificial lighting load and the air-conditioning (A/C) load.
2. Replace ~ 2000 fluorescent lighting fixtures (80 Watt each) with equivalent LED panels (40 Watt each). There will be no heat emitted from LED, and hence, the A/C loads will decrease.
3. Replace old individual split units with central A/C system.
4. Replace inefficient appliances with newer ones with energy label A (or green color), with lowest consumption and highest efficiency.
5. In elevators, use motors with variable speed drives (VSDs) instead of two-speed motors.
6. Use solar water heaters instead of electric heaters.
7. Install Photo-Voltaic (PV) solar panels The panels may serve as shading plates for the roof and hence, decrease the A/C loads.

Step (3). After discussions with the top management and applying the company's constraints, only EEMs involving replacing lighting loads with LED, replacing the old split A/C units with central A/C system and installing PV solar panels were approved for further in-detail analysis.

Fig. 1. The entrance and the main office building of the case study

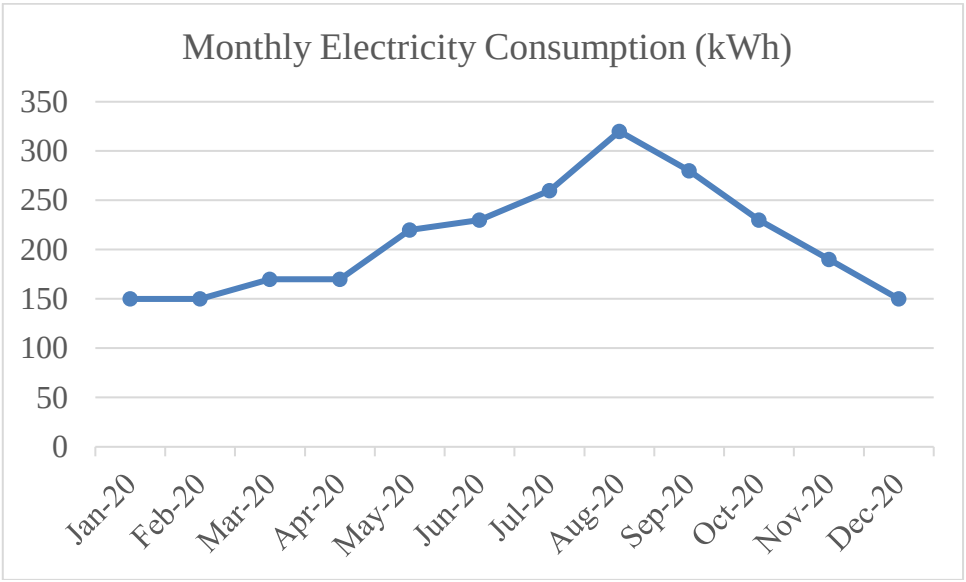

Fig. 2. Monthly electrical energy consumed for the seven buildings of the case study

Step (4). For the selected EEMs, the investment cost (USD), the annual energy savings (kWh), the annual money savings (USD), the annual CO_2 emission reduction (kg), the Payback Time (years) and the proposed indices; saved kWh / $ spent) and CO_2 emission reduction / $ spent are calculated and presented in Table 1.

Table 1. Energy saving, environmental and financial indices for the proposed EEMs

	Capital cost ($)	Annual kWh saved	Annual money saving ($)	Annual reduced CO_2 (kg)	PBT (years)	kWh saved / $ spent	CO_2 reduced / $ spent
LED Lights	75,000	160,000	16,000	80,000	4.7	2.13	1.06
Central A/C	250,000	350,000	35,000	175,000	7.14	1.4	0.7
PV panels	50,000	100,000	10,000	50,000	5	2	1

Results & Discussions

From Table 1, we can see that the highest values of the proposed indices are those for the LED lighting, followed by installing PV panels and finally the replacement of the A/C system. The meaning of the emission reduction index for the PV project for example, is that for every 1 $ spent on this project, there will be a reduction of the CO_2 emission by 1 kg. If this 1 $ was to spent on the replacing the A/C project, then, there will be a reduction of the CO_2 emission by only 0.7 kg. this index can be used when selling such EEMs to any international authority for funding such projects within a national climate change plan or as a part of the finance required for nationally-determined contributions (NDC) submitted by each country to the United Nations as a mandatory document for each country's commitment to Paris Agreement. For example, Egypt CO_2 emissions are currently ~ 250 Million Ton in 2020 [14]. If we want to decrease this quantity (say by 10% or by 25 Million Ton) by wide spreading the installation of PV panels on a country level, then we need 25 Billion USD.

Conclusions

In this paper, the problem of prioritizing EEMs was discussed. It gives the decision maker a decision support tool when comparing among several energy efficiency projects, especially when the available budget is limited and all EEMs cannot be executed simultaneously. The proposed four-steps methodology for such prioritization follows in its first three steps the normal procedure suggested in other studies and that are recommended by any energy management system; 1) performing an energy audit, 2) determining the EEMs, and evaluate such EEMs in terms of potential kWh savings, CO_2 emission reduction in addition to financial evaluation using any familiar financial index such as the Pay Back Time, 3) apply the organization constraints such as available budget or need to comply with laws and regulations. The fourth step differs from most related studies, in which the prioritization was done using financial indices only. In this study, combining the energy saving and the CO_2 emission reduction data with the financial indices help to configure the physical meaning of the index, rather than blind numbers. The two proposed indices could be used interchangeably, as they are actually the same index, expressed once as an energy saving index and once as an emission reduction index, and both are referenced to the dollars needed to perform the EEM in question. The proposed indices could be used to compare and prioritize EEMs within buildings or industries. The case study was applied on the office buildings in a refinery, where projects such as replacing conventional lighting fixtures with LED panels and installing PV solar panels have the highest benefit / cost ratio, compared to projects such as replacing the individual split units of the HVAC system by a central A/C system or replacing the glazing system by a special glazing system that allows the passage of daylight and block the passage of heat energy. Such indices could be used to quantify any financing required to perform energy saving or environmental projects within a national plan to mitigate climate change and rationalize the energy resources.

References

[1] United Nations Environment Program (UNEP): 2020 Global Status Report for Buildings and Construction: Towards a Zero-emission, Efficient and Resilient Buildings and Construction Sector (2020).

[2] A. Levesque, R. C. Pietzcker, L. Baumstark and G. Luderer: Deep decarbonisation of buildings energy services through demand and supply transformations in a 1.5°C scenario, Environmental Research Letters, 16, 054071 (2021).

[3] Global Alliance for Buildings and Construction: Buildings and Climate Change Adaptation: A Call for Action (2021).

[4] N. Suman, M. Marinic and M. Kuhta: A Methodological framework for sustainable office building renovation using green building rating systems and cost-benefit analysis, Sustainability, 12, 6156 (2020).

[5] F. Asdrubali and G. Grazieschi: Life cycle assessment of energy effcient buildings, Energy Reports, 6, 270–285 (2020).

[6] E. M. Erebor, E. O. Ibem, I. C. Ezema and A. B. Sholanke: Energy efficiency design strategies in office buildings: A literature review, IOP Conference Series: Earth and Environmental Science, International Conference on Energy and Sustainable Environment, 665, 012025 (2021).

[7] B. Benzar, M. Park, H. Lee, I. Yoon and J. Cho: Determining retrofit technologies for building energy performance, Journal of Asian Architecture and Building Engineering, 19:4, 367-383 (2020).

[8] U. F. Oberegger, R. Pernetti and R. Lollini: Bottom-up building stock retrofit based on levelized cost of saved energy, Energy & Buildings, 210, 109757 (2020).

[9] T. Zachariadis et al.: Determination of cost-effective energy efficiency measures in buildings with the aid of multiple indices, Energies, 11, 191 (2018).

[10] Y. Ye, K. Hinkelman, Y. Lou, W. Zuo, G. Wang and J. Zhang: Evaluating the energy impact potential of energy efficiency measures for retrofit applications: A case study with U.S. medium office buildings, Building Simulation (2021).

[11] F. Pietrapertosa, M. Tancredi, M. Giordano, C. Cosmi and M. Salvia: How to prioritize energy efficiency intervention in municipal public buildings to decrease CO_2 emissions? A case study from Italy, International Journal of Environmental Research and Public Health, 17, 4434 (2020).

[12] Internatonal Energy Agency (IEA): Global Energy Review 2021: Assessing the effects of economic recoveries on global energy demand and CO_2 emissions in 2021 (2021).

[13] International Standardisation Organization: Energy management systems - Requirements with guidance for use, ISO 50001:2018.

[14] L. Abdallah and T. El-Shennawy: Evaluation of CO_2 emission from Egypt's future power plants, Euro-Mediterranean Journal for Environmental Integration, 5:49 (2020).

Environmental and Energy efficiency assessment of electric propulsion systems for ships

Hossam M. Hussien[1, a], Mohamed M. ElGohary[1, b], Maged M. AbdElnaby[1, c]

[1]*Department of Naval Architecture and Marine Engineering, Faculty of Engineering, Alexandria University, Alexandria, Egypt*

[a] Eng.hosam1980@gmail.com, [b] *Mohamed.elgouhary@alexu.edu.eg,* [c]*maged.abdelnaby@alexu.edu.eg*

Keywords: Diesel electric propulsion, Energy Efficiency, Passenger ships, Ship exhaust emissions, IMO regulations.

Abstract. The maritime industry faces many challenges regarding the adverse environmental impact, whether at the level of legislation set by the International Maritime Organization (IMO) or the economic crises that arising from the Covid-19 pandemic. IMO has found that the highest percentage of ship emission is mainly coming from the ship propulsion systems. Therefore, the current research proposes an electric propulsion system to drive the ship instead of the conventional one to reduce ship emissions and enhance energy efficiency. As a case study, a passenger ship is investigated. The results showed that the proposed electric propulsion system has lower emission rates than the conventional one by 10%, 21%, and 88% for CO_2, NOx, and SOx emission, respectively. From an energy efficiency point of view, the diesel-electric propulsion system enhances the energy efficiency and complies with the required IMO values as actual energy efficiency is about 66%, 70%, 83%, and 95% of the required IMO values at baseline, phase 1, phase 2 and phase 3, respectively.

Introduction

Recent regulations set by the International Maritime Organization (IMO) and financial challenges that arising from the Covid-19 pandemic made the shipping industry faces numerous difficulties [1,2]. Latest measurements from IMO shows that ships emitted 2.6% of the total worldwide Carbon dioxide (CO_2) emissions [3,4]. Therefore, IMO has given a few enactments to lessen the unfriendly ecological effect [5]. Mohseni et al [6] pointed that the most elevated level of ship outflow is fundamentally comes from the propulsion system. The solution is to propose a more efficient system than conventional propulsion system [7,8]. The most efficient solution is electric propulsion system as it can be adopted to different vessel types at different speeds [9].

Lim et al [10] presented an application of electric system in a ship to reduce nitrogen oxides (NOx) to be accepted with the regulations released from IMO. Offshore supply vessels and Liquefied Natural gas ships can use the electric propulsion system incorporated with Azipod propeller as shown in [11]. Another research investigated the evaluation of power and other dynamic specifications for electric propulsion system [12]. Zahedi & Norum [13] Validate the electric propulsion system components and its design through a simulation software. Moreover, Bassam et al [14] investigated the hybrid system included electric system and found that an environmental and economic benefits from the application. Therefore, the application of electric propulsion system onboard ship is very hot research issue because of its economic and environmental benefits resulted from the previous literature survey.

The aim of the research is to propose an electric propulsion system to drive the ship instead of the conventional system to reduce ship emissions and enhance energy efficiency. The environmental assessment will be based on a comparative analysis between the proposed electric propulsion system and the conventional system through evaluation of greenhouse gas emissions. As a case study, a passenger ship will be investigated.

Case study description

The case study for the assessment process of energy efficiency and environmental impacts is selected to be a passenger ship. The ship is operated by Holland America line passenger vessels under name (MS Westerdam) with a capacity of 2366 passengers and 820 crew members. The ship was built in 2004 and sailing under the flag of the Netherlands. Principal specifications of the ship are shown in Table 1 [15]. The ship is suggested to be operated by a diesel-electric propulsion system as shown in Fig. 1 with a total power of 51,840 kW covers both the electric propulsion and auxiliary/hotel power requirements for the ship.

Table 4 Main specifications of the studied passenger ship

Ship Name	MS Westerdam
IMO number	9226891
Length overall, [m]	285
Beam, [m]	32
Draft, [m]	7.8
Service speed, [knots]	22
Number of passengers	2366
Gross tonnage, [ton]	82,897
Electric power, [kW]	51840

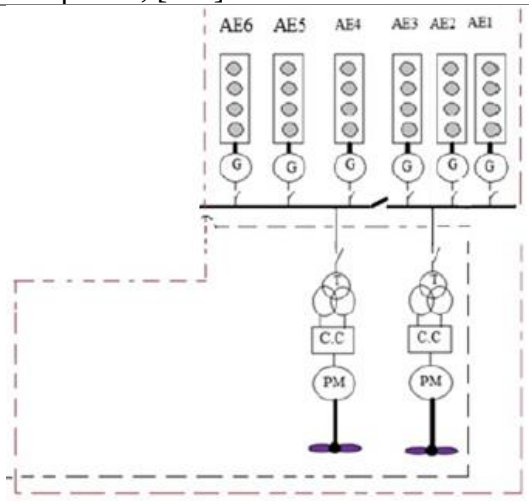

Fig. 7 Proposed electric propulsion system arrangements for the case study

The propulsion system can be provided with the required electric power from 6 generators (G) through transformers. Cyclone convertor (C.C) regulates the frequency according to the required propulsion motor speed (P.M). The diesel generator will be operated by ultra-low sulfur heavy fuel oil (ULSHFO) with 0.1 sulfur and a specific fuel consumption of 155.6 g/kWh with load factor of 90% and efficiency equals to 41.3 %.

The ship is sailing from Canada (Vancouver port) to Japan (Tokyo port) to attract more passengers to increase the financial benefit of the ship. This sailing route is 10,560 nautical miles (NM) and takes 20 days in one trip the average number of trips per year is five.

Performance evaluation methodology

The environmental performance can be assessed by evaluating the exhaust emissions from ships. The energy efficiency can be assessed by using the procedure recommended from IMO by using Energy Efficiency Design Index (EEDI) procedure [16].

Firstly**,** the total emissions during ship cruise can be evaluated by using Eq. (1) which depending also on the type of engine (Eng) like main engine and auxiliary engine.

$$M_{trip,n} = \sum_{.}\left[T * \sum_{Eng}(P \times L \times F_n)\right] \quad (1)$$

Where (P) is the power of engine in [kW], L is the load factor of engine, T is the operating time of ship in [hour], (n) is the type of pollutant, and (F) is the fuel emission factor in [g/kWh]. The emission factors for NO_x, Sulfur oxide (SOx) and CO_2 are 13, 0.4, and 485 [g/kWh], respectively for diesel electric engine operated with ULSHFO 0.1%S [1]. On the other hand, the emission factors are 539 g/kWh, 16.4 g/kWh and 3.29 [g/kWh] for CO_2, NOx and SOx respectively for conventional diesel engine operated with MDO (1%S) [17].

Furthermore, the energy efficiency of the case study can be assessed by using the EEDI procedure [3]. EEDI can be assessed by calculated the reference value $EEDI_{ref}$ through Eq. (2) and the attained value $EEDI_{att}$ set by IMO through Eq. (3) and measured in [gCO_2/GT-NM] [3,17].

$$EEDI_{ref} = \left(\frac{170.84}{GT^{0.214}}\right)\left(1 - \frac{X}{100}\right) \quad (2)$$

Where, (GT) is the gross tonnage of passenger ship, (X) is the reduction rate set by IMO as follow; 5% in phase 1 (2015-2019), 20% in phase 2 (2020-2024) and 30% in phase 3 (2025-onwards) [18,19].

$$EEDI_{att} = \frac{\left(\frac{HL_{max.}}{\eta_{gen.}} + \frac{\sum_{i=1}^{n}(0.75.MPP(i))}{\eta_{PTI} \cdot \eta_{gen.}}\right).(C_F \cdot SFC_{AE})}{GT \cdot v_{ref.}} \quad (3)$$

The previous equation depends on the electric power during ship cruise in kW (HL_{max}), the efficiency of generator (η_{gen}), the electric propulsion motor power in kW (MPP), the electric propulsion systems efficiencies at 75% of the electric motor output rated power $\eta_{PTI,}$ the fuel conversion factors of the consumed fuel to CO_2 (C_F), the average specific fuel consumption for all engines (SFC_{AE}) at 75% of the maximum continuous rating (MCR) power in [g/kWh] and ($V_{ref.}$) which is the operational vessel speed in knots.

Results and discussions

The environmental performance can be assessed by evaluating the exhaust emission rates per trip. The examined emission types are NOx, SOx, and CO_2 as these types are related with IMO regulations. The assessment process depends on the comparative study between the proposed diesel electric propulsion system operated with ULSHFO (0.1% S) and the conventional one operated with MDO (1%S), therefore, the different emissions rates can be compared in Fig. 2. The emissions rates are in ton/trip as discussed in Eq. (1). As shown in Fig. 2, the conventional diesel engine emitted more NOx emission rates than the diesel electric engine as NOx emission have a solid relation with the combustion temperature inside the engine and the combustion of MDO (1%S) will produce higher NOx rates than ULSHFO [20]. The conventional diesel engine will produce higher SOx emission than the diesel electric as SOx emission depends on the sulfur content of the combustion fuel. On the other hand, the CO2 emission rates in two options are very closely as it depends on the carbon content of the fuel, but the diesel electric will produce fewer CO_2 emission than the conventional one.

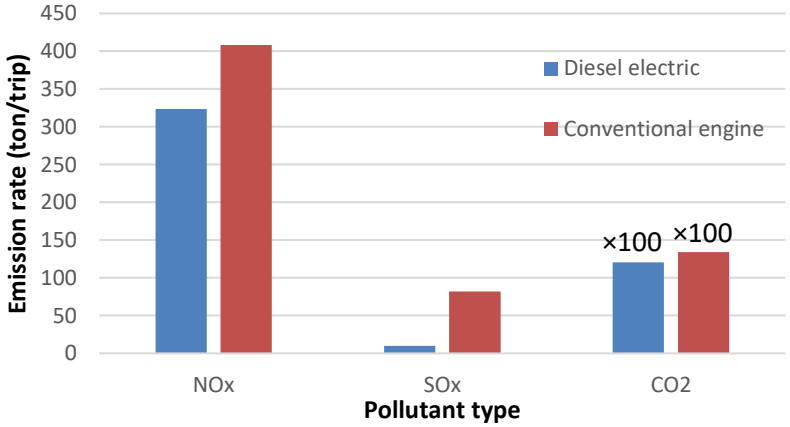

Fig. 8 Exhaust emission rates for diesel electric engine compared with conventional one

NOx and SOx emission rates have been compared with the IMO 2016 and 2020 emission-limit rates, respectively. The IMO 2020 SOx and tier III 2016 NOx limits are 1.555 kg/min and 2.008 kg/min, respectively. Fig. 3 shows a comparative diagram between IMO limit and the SOx and NOx emission rates for diesel electric propulsion system. It can be noticed that SOx emissions rates for the diesel electric engine comply with the IMO 2020 limits because of it use ULSHFO with a little amount of sulfur. On the other hand, it can be noticed that NOx emissions from diesel electric engine isn't comply with IMO 2016 limits, therefore, it is recommended to use selective catalytic reduction (SCR) technique which can reduce NOx emission rate from the proposed diesel electric engine by up to 90% [1].

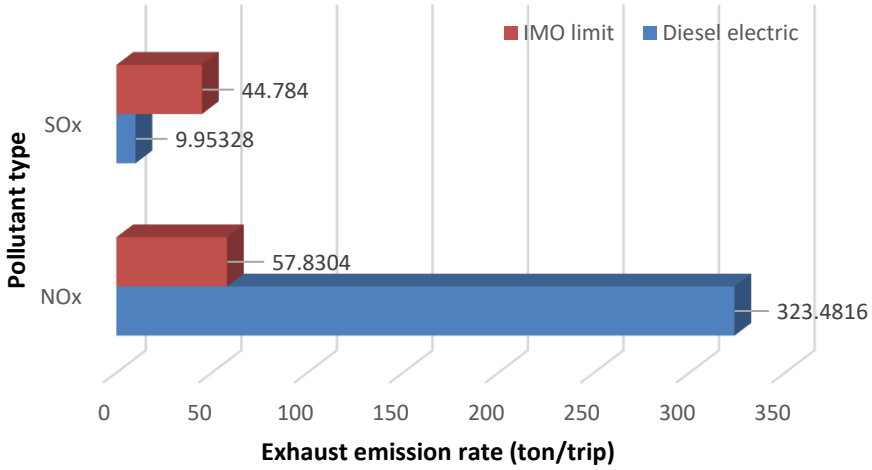

Fig. 9 IMO NOx and SOx emissions for the DE and COGES propulsion options

Finally, the energy efficiency can be assessed by the calculation of EEDI for electric propulsion system as recommended from IMO. By conducting the procedure in section 3 to the case study, it is shown that the reference EEDI and its value in the three phases can be calculated based on the gross tonnage of passenger ship as investigated in Fig. 4.

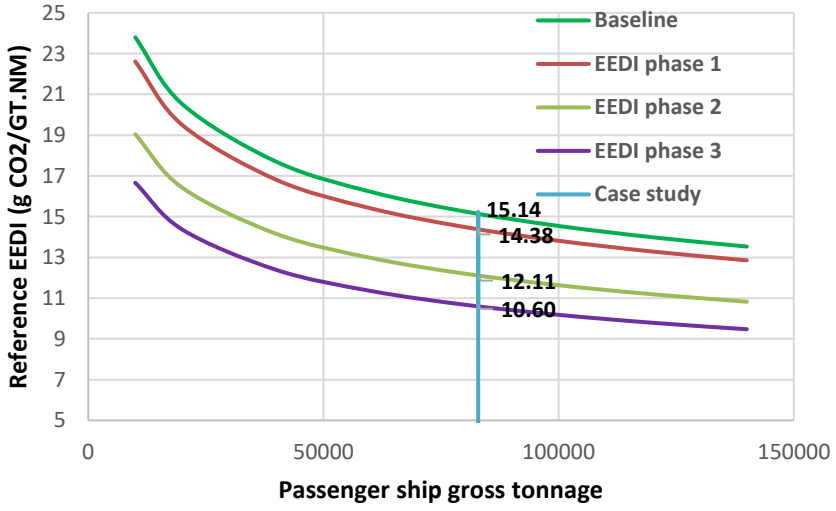

Fig. 10 Reference EEDI values for passenger ship

This reference value will be compared with the actual attained EEDI which can be calculated by using Eq. (3) based on 22 knots service speed, 3.114 ton-CO_2/ton-fuel conversion factor of fuel to CO_2 and 82,897 gross tonnages. The attained EEDI will be 10.03 g CO_2/GT-NM. The relative attained EEDI value to the reference value at different phases for the proposed diesel electric propulsion system can be described in Fig. 5.

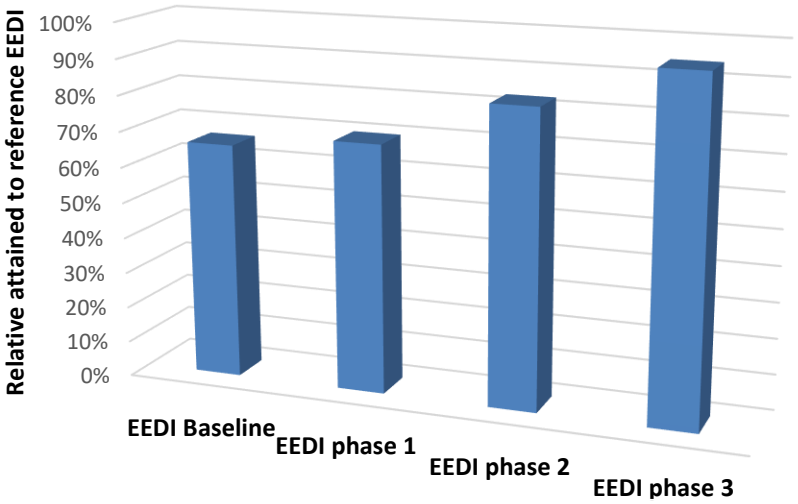

Fig. 11 Relative attained to the reference EEDI and the average EEOI values for the case study

It is shown that, the proposed diesel electric propulsion system will comply with the required IMO phases now and in the future as the attained EEDI is about 66%, 70%, 83%, and 95% of the reference EEDI value at baseline, phase 1, phase 2 and phase 3, respectively.

Conclusions

The present research discusses the electric propulsion system for a passenger ship from environmental and energy efficiency point of view. The diesel electric propulsion system operated by ULSHFO (0.1% S) is proposed to propel the ship instead of the conventional diesel engine which operated by MDO (1% S). The main conclusions from the current paper are:

- From environmental point of view, diesel electric engine operated by ULSHFO (0.1%S) comply with IMO SOx and not comply with NO_x emission. Be comparing the exhaust emissions rates between diesel electric and conventional engine, it is shown that diesel electric has lower emission rates than the conventional one by 10%, 21% and 88% for CO_2, NOx, and SOx emission, respectively.
- From energy efficiency point of view, the diesel electric propulsion system enhances the attained EEDI and complies with the required IMO values as it is about 66%, 70%, 83%, and 95% of the reference EEDI values at baseline, phase 1, phase 2 and phase 3, respectively.

References

[1] N.R. Ammar, I.S. Seddiek, Enhancing energy efficiency for new generations of containerized shipping, Ocean Eng. 215 (2020) 107887. https://doi.org/10.1016/j.oceaneng.2020.107887.

[2] D.K. Lee, Y.K. Jeong, J.G. Shin, D.K. Oh, Optimized design of electric propulsion system for small crafts using the differential evolution algorithm, Int. J. Precis. Eng. Manuf. - Green Technol. 1 (2014) 229–240. https://doi.org/10.1007/s40684-014-0029-9.

[3] N.R. Ammar, I.S. Seddiek, Evaluation of the environmental and economic impacts of electric propulsion systems onboard ships: case study passenger vessel, Environ. Sci. Pollut. Res. (2021). https://doi.org/10.1007/s11356-021-13271-4.

[4] M.M. El-Gohary, The future of natural gas as a fuel in marine gas turbine for LNG carriers, Proc. Inst. Mech. Eng. Part M J. Eng. Marit. Environ. 226 (2012) 371–377. https://doi.org/10.1177/1475090212441444.

[5] A. Halff, L. Younes, T. Boersma, The likely implications of the new IMO standards on the shipping industry, Energy Policy. 126 (2019) 277–286. https://doi.org/https://doi.org/10.1016/j.enpol.2018.11.033.

[6] S.A. Mohseni, E. van Hassel, C. Sys, T. Vanelslander, Economic evaluation of alternative technologies to mitigate Sulphur emissions in maritime container transport from both the vessel owner and shipper perspective, J. Shipp. Trade. 4 (2019). https://doi.org/10.1186/s41072-019-0051-8.

[7] R.D. Geertsma, R.R. Negenborn, K. Visser, J.J. Hopman, Design and control of hybrid power and propulsion systems for smart ships: A review of developments, Appl. Energy. 194 (2017) 30–54. https://doi.org/https://doi.org/10.1016/j.apenergy.2017.02.060.

[8] M.M. Elgohary, Energy Conservation: passenger and container ships case studies, Alexandria Eng. J. 48 (2009) 151–159.

[9] C. Nuchturee, T. Li, H. Xia, Energy efficiency of integrated electric propulsion for ships – A review, Renew. Sustain. Energy Rev. 134 (2020) 110145. https://doi.org/https://doi.org/10.1016/j.rser.2020.110145.

[10] C. og Lim, B. cheol Park, J. chul Lee, E.S. Kim, S. chul Shin, Electric power consumption predictive modeling of an electric propulsion ship considering the marine environment, Int. J. Nav. Archit. Ocean Eng. 11 (2019) 765–781. https://doi.org/10.1016/j.ijnaoe.2019.02.011.

[11] A.M. Bassam, A.B. Phillips, S.R. Turnock, P.A. Wilson, An improved energy management strategy for a hybrid fuel cell/battery passenger vessel, Int. J. Hydrogen Energy. 41 (2016) 22453–22464. https://doi.org/https://doi.org/10.1016/j.ijhydene.2016.08.049.

[12] P. Prempraneerach, J. Kirtley, C. Chryssostomidis, M.S. Triantafyllou, G.E. Karniadakis, Design of the All-Electric Ship: Focus on Integrated Power System coupled to Hydrodynamics, in: Proc. Am. Soc. Nav. Eng. Soc. Nav. Archit. Mar. Eng. Electr. Sh. Des. Symp., 2009: pp. 563–568. https://doi.org/10.1109/SPEEDHAM.2008.4581214.

[13] B. Zahedi, L.E. Norum, Modeling and Simulation of All-Electric Ships With Low-Voltage DC Hybrid Power Systems, IEEE Trans. Power Electron. 28 (2013) 4525–4537. https://doi.org/10.1109/TPEL.2012.2231884.

[14] A.M. Bassam, A.B. Phillips, S.R. Turnock, P.A. Wilson, Development of a multi-scheme energy management strategy for a hybrid fuel cell driven passenger ship, Int. J. Hydrogen Energy. 42 (2017) 623–635. https://doi.org/https://doi.org/10.1016/j.ijhydene.2016.08.209.

[15] Hollandamerica, MS Westerdam, Cruise Ships. (2021). https://www.hollandamerica.com/en_US/cruise-ships/ms-westerdam/5.html (accessed June 1, 2021).

[16] A.G. Elkafas, M. Khalil, M.R. Shouman, M.M. Elgohary, Environmental Protection and Energy Efficiency Improvement by using natural gas fuel in Maritime Transportation, Environ. Sci. Pollut. Res. (2021). https://doi.org/10.21203/rs.3.rs-194729/v1.

[17] A.G. Elkafas, M.M. Elgohary, M.R. Shouman, Numerical analysis of economic and environmental benefits of marine fuel conversion from diesel oil to natural gas for container ships, Environ. Sci. Pollut. Res. 28 (2021) 15210–15222. https://doi.org/10.1007/s11356-020-11639-6.

[18] A.G. Elkafas, M.M. Elgohary, A.E. Zeid, Numerical study on the hydrodynamic drag force of a container ship model, Alexandria Eng. J. 58 (2019) 849–859. https://doi.org/10.1016/j.aej.2019.07.004.

[19] M.M. El Gohary, N.R. Ammar, Thermodynamic analysis of alternative marine fuels for marine gas turbine power plants, J. Mar. Sci. Appl. 15 (2016) 95–103. https://doi.org/10.1007/s11804-016-1346-x.

[20] V. Mrzljak, T. Mrakovčić, Comparison of COGES and Diesel-Electric Ship Propulsion Systems, J. Marit. Transp. Sci. Special ed (2016) 131–148. https://doi.org/10.18048/2016-00.131.

Parametric study of a hybrid adsorption-vapor compression cooling system

Mohamed G. Gado [1,a], Tamer F. Megahed [2,b], Shinichi Ookawara[1,c], Sameh Nada [1,d], Ibrahim I. El-Sharkawy [1,e]

[1]Energy Resources Engineering Department, Egypt-Japan University of Science and Technology (E-JUST), New Borg El-Arab City, Alexandria 21934, Egypt
[2]*Electrical Power Engineering, Egypt-Japan University of Science and Technology (E-JUST), New Borg El-Arab City, Alexandria 21934, Egypt*
[a]*mohamed.gado@ejust.edu.eg*, [b]tamer.megahed@ejust.edu.eg, [c]ookawara.s.aa@m.titech.ac.jp, [d]sameh.nada@ejust.edu.eg, [e]ibrahim.*elsharkawy.ejust.edu.eg*

Abstract. Sorption-based hybrid vapor compression chillers have been identified as a possible replacement for energy-intensive conventional compression chillers. The objective of the current work is to evaluate the system performance and the corresponding energy savings of a hybrid adsorption-compression chiller. The adsorption chiller works with silica gel/water pair whilst using R410A as a refrigerant for a standalone compression chiller. Herein, the computational model is verified with the relevant observed experimental data. A parametric study of the proposed system with a nominal cooling capacity of 18.5 kW is conducted based on a wide range of driving (55°C to 95°C), recooling (25°C to 40°C), and chilled (12°C to 18°C) water inlet temperatures. Simulation results revealed that introducing a hybrid adsorption-compression chiller could reduce the electricity bills by 65.4% at 95°C) compared to 5.6% at the driving water inlet temperature of 55°C. Energy savings can be declined to 41.6% at 40°C, compared to energy savings of 65.4% at 25°C. It was found that peak energy savings (82.3%) can be attained at a chilled water inlet temperature of 18°C. Furthermore, simulation results of R410A are compared against R134a and R600a, revealing that R600a presents superior performance.

Keywords: Adsorption, Energy savings, Hybrid chiller, Refrigerants, Compression chiller

Introduction

Cooling and air conditioning applications are a key contributor to electricity usage, which made up 17% of the global consumed electricity [1]. Thus, enhancing the performance of a compression system can share in reducing the exerted electric power. Improving the performance of the compression system can be accomplished by decreasing the condensation temperature of the compression system [2]. Therefore, using hybrid cooling systems to reduce the intermediate temperature can improve the COP of the compression facility [3]. Absorption, adsorption, ejector, solid desiccant, and liquid desiccant systems are combined with compression chillers to present hybrid cooling chillers. Integration of adsorption units with the compression cycle can reap the inherent advantages of the adsorption chillers, such as the operation using low-grade waste heat or solar energy [2].

Several authors have studied the amalgamation of adsorption chillers with standalone compression cycles [4]. Vasta et al. [5] performed experimental work on an adsorption cascaded compression chiller. Their results indicated that isobutane and propane seemed viable alternatives for R717, R744, and R410A. Palomba et al. [6] examined series, parallel, and cascade connections by examining various layouts of adsorption-assisted hybrid compression chillers. Their findings showed that the attainable energy savings of a hybrid chiller might be enhanced in higher temperature lift for the compression subcycle.

The combination of an adsorption chiller and a standalone chiller can benefit from (i) operating at lower evaporating temperatures than adsorption systems, (ii) operating at lower heat source temperatures without a significant performance loss when compared to adsorption chillers, and (iii) lowering electricity bills by utilizing hybrid chillers relatively with standalone chillers. In summary, the current work focuses on analyzing system credibility on the basis of driving, recooling, and chilled temperatures utilizing multiple refrigerants using lumped parameter models (R410A, R134a, and R600a).

Working principles

Fig. 1 demonstrates a typical illustration of an adsorption-assisted cascaded compression chiller. The indicated system comprises two main subsystems: (i) adsorption chiller and (ii) compression chiller. On the one hand, the adsorption chiller comprises mainly four principal parts; desorber, adsorber, condenser, and evaporator. Desorber and adsorber work as thermal compressors [7]. On the other hand, the compression chiller encompasses a compressor, a condenser, an expansion device, and an evaporator. Amalgamations of such two systems can share in reducing the intermediary temperature between these two subsystems.

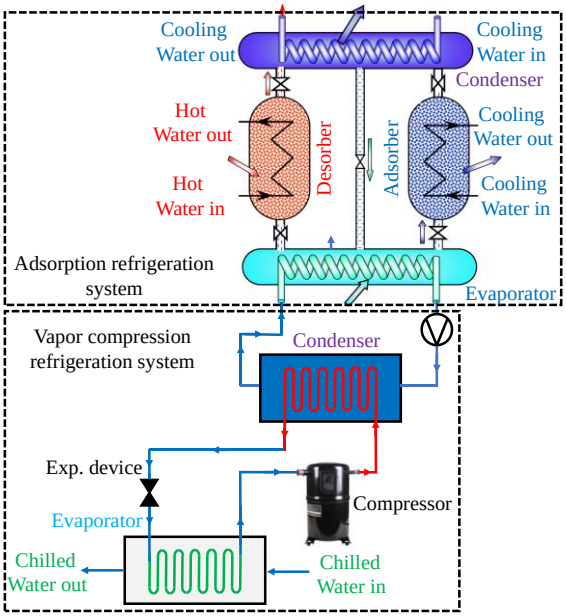

Fig. 1 Layout of adsorption-integrated compression chiller.

Mathematical modeling

The mathematical modeling of a adsorption-integrated compression chiller is presented as follows:

Adsorption system modeling

The mathematical modeling of the silica gel-based adsorption chiller is based on solving simultaneously the adsorption isotherm, the adsorption kinetics, mass, and energy balance of the system's major components, namely, an adsorber, adsorber, a condenser, and an evaporator. Main operating parameters and constants are invoked from ref. [8].

Compression system modeling

The vapor compression cooling system is simulated using lumped parameter modeling of the heat exchanger of the system per se. Additional information about the modeling can be found in ref. [9].

Performance indicators

The performance of the proposed chiller is examined using the COP and energy saving as below:

$$\begin{cases} COP = \dfrac{Q_{eva,Conv}}{P_{elec}} \\ ES = 1 - \dfrac{COP_{hybrid}}{COP_{conv}} \end{cases} \quad (1)$$

Results and discussion

As shown in Figs. 2 and 3, the mathematical model was confirmed using reported experimental data from the literature. The assorted temperatures were then altered from 55°C to 95°C for driving temperatures, 25°C to 40°C for recooling temperatures, and 12°C to 18°C for chilled temperatures to evaluate the system performance with the resulted energy savings of using such a hybrid chiller.

Model validation

The system model is validated against experimental data of refs. [9] and [5]. To ensure the mathematical model's fidelity, the adsorption and compression chillers are separately validated.

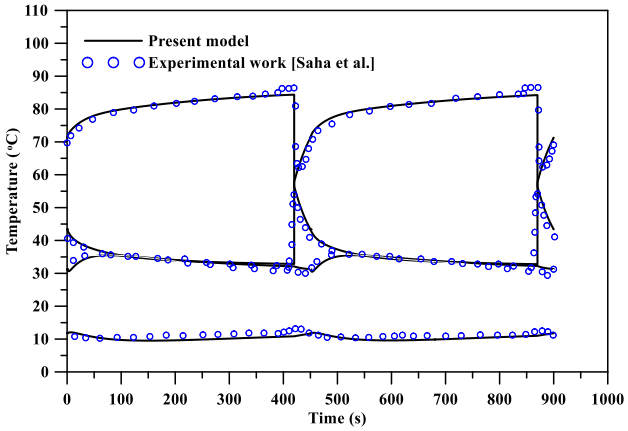

Fig. 2. Water outlet temperature profiles comparison comparison for the simulated and experimental data.

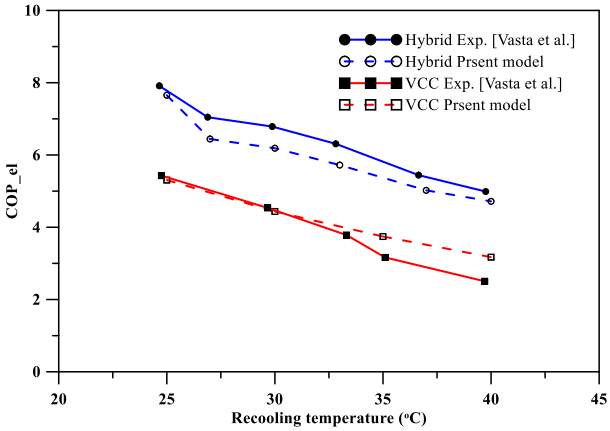

Fig. 3. Comparison between simulated and experimental compression performance.

Transient response of adsorption-integrated compression chiller

Fig. 4 reveals the temporal histories of the heat transfer fluids (inlet/outlet) temperatures for the desorber, adsorber, condenser, cascade condenser, and evaporator of the adsorption-integrated compression chiller. The driving temperature is held as 90°C, while the recooling temperature is taken as 30°C. The chilled temperature is 12°C for the evaporator of the standalone chiller. Fig. 4 depicted that the hybrid cycle is accomplished almost steady-state within three half-cycles. Also, it is worth mentioning that the reduction of the cascade water temperature compared with the conventional system, which in turn enhances the performance. Also, Fig. 5 depicts the equivalence of the transient-variant cooling capacity of the adsorption chiller with the variant steady state condensation power of the standalone chiller.

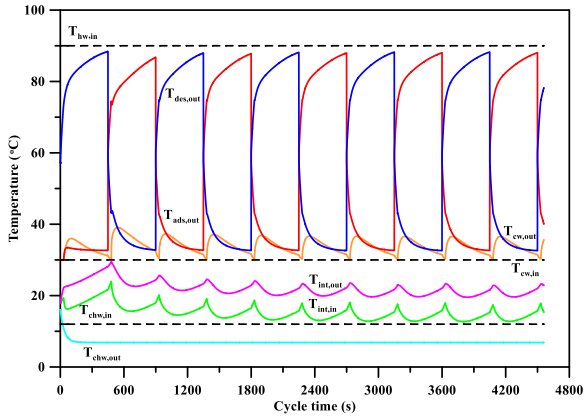

Fig. 4. Outlet temperature profiles of an adsorption-integrated compression chiller.

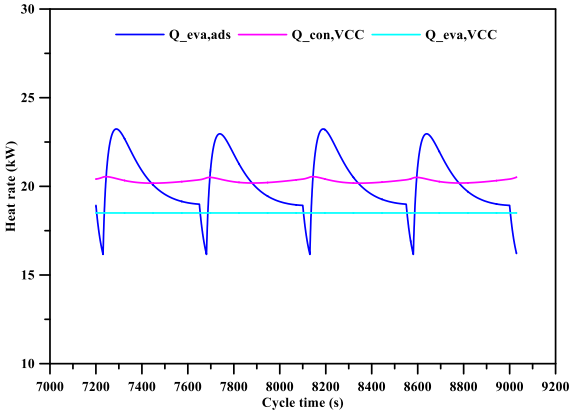

Fig. 5. Heat rate variation for the cooling capacity of the adsorption chiller and the condensation power of the standalone chiller.

Influence of driving temperature

Variation of the conventional, hybrid performance, and energy savings are investigated against variation of driving temperatures (55°C to 95°C), keeping recooling and chilled temperatures fixed at 25°C and 12°C. The coefficient of performance of the hybrid chiller increases proportionally from 6.9 to 17.7, as the regeneration temperature alters from 55°C to 95°C as depicted in Fig. 6. This is because of the dwindling of the adsorption's evaporator outlet temperature (intermediate temperature). The COP of the standalone chiller remained constant at 6.5; this can be attributed to the persistent temperature values of secondary fluids. Therefore, introducing an adsorption-integrated compression chiller might diminish the electricity bills by 65.4% at 95°C) compared to 5.6% at the driving temperature of 55°C as shown in Fig. 7.

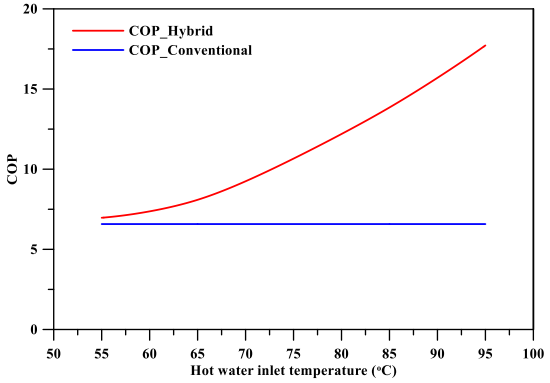

Fig. 6. Effect of the driving temperature on the system performance.

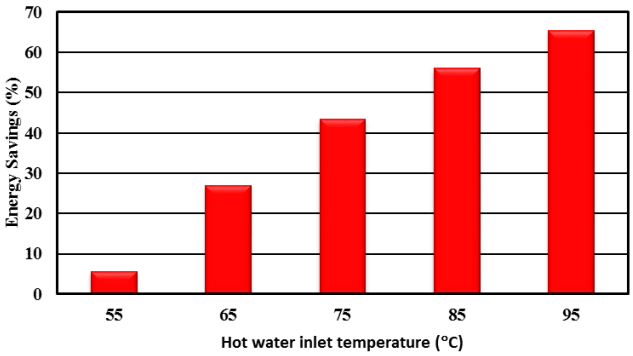

Fig. 7. Energy savings at different driving temperatures.

Influence of recooling temperature

By maintaining driving and chilled temperatures constant at 95°C and 12°C, increment of the recooling temperature from 25 °C to 40 °C, the conventional and hybrid performance and energy savings could be predicted depicted in Fig. 8. It can be perceived that the coefficient of performance of the hybrid chiller decreases from 17.7 to 5.7, as the recooling temperature modifies from 25°C to 40°C. This is due to the decline of the produced cooling capacity of the adsorption chiller, which abates the standalone chiller's waste heat. This feature reduces the intermediate temperature of the standalone chiller, diminishing the system performance. Similarly, the coefficient of performance of the conventional chiller decreases from 6.5 to 3.7. This might be due to the decrease in the recooling

temperature. As a result, Fig. 9 reveals that the energy savings can be declined to 41.6% at 40°C) compared to 65.4% at 25°C.

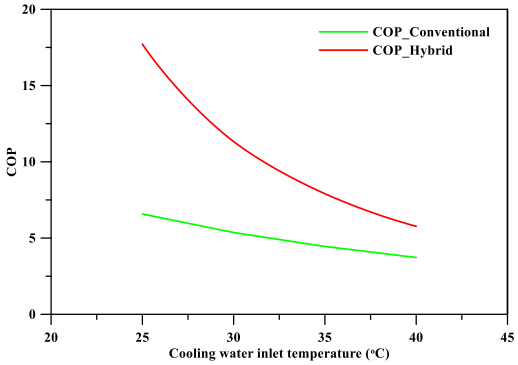

Fig. 8. Variation of the recooling temperatures with the system performance.

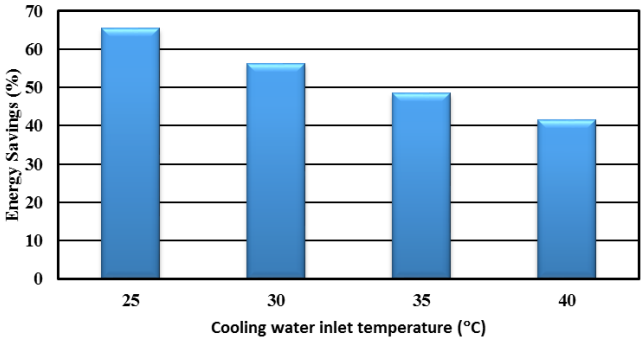

Fig. 9. Energy savings at different recooling temperatures.

Influence of chilled temperature

To evaluate the system performance, a varied chilled temperature from 12°C to 18°C. Increasing the chilled temperature results in increasing the evaporation temperature of the standalone chiller. Therefore, the compression COP increases, and subsequently, the condensation heat decreases relatively with the cooling capacity of the adsorption chiller at a constant cooling power of the standalone chiller. Fig. 10 reveals that as the chilled grows from 12°C to 18°C, the compression COP escalates from 6.5 to 8.7 while hybrid COP increases from 17.7 to 43. As a result, 65.4% to 82.3% of electricity can be saved as the chilled temperature changes from 12°C to 18°C, as demonstrated in Fig. 11.

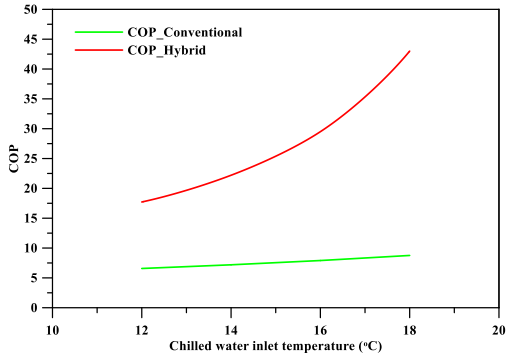

Fig. 10. Influence of chilled temperatures on the system performance.

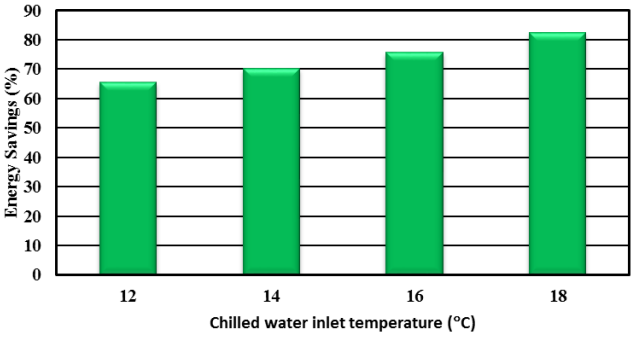

Fig. 11. Energy savings at different chilled temperatures.

Comparisons of different refrigerants

Fig. 12. depicts the attainable coefficient of performance for different refrigerants, namely, R410A, R134a, and R600a with variant driving temperatures (55°C to 95°C). It was found that R600a represents a superior coefficient of performance while R410A has lower values of COP. It is worth noting that using several refrigerants does not affect the whole system's energy savings. Therefore, hybrid adsorption-compression cooling systems can share in using environmentally benign refrigerants without a considerable loss of the system energy savings.

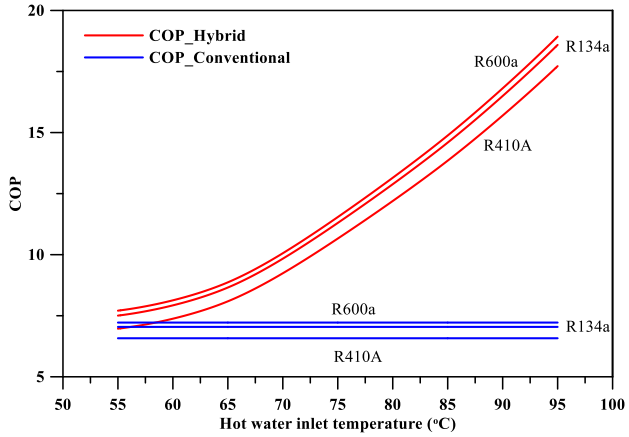

Fig. 12. System performance comparison based on different refrigerants.

Conclusion

In this paper, a simulation program is developed and proven by observed data in the literature. The influence of regeneration, recooling and chilled water temperatures was investigated to inspect the system functioning of an adsorption-integrated compression chiller. Based on the simulation key findings, the following conclusion can be drawn: (i) As the driving temperature elevates from 55°C to 95°C, hybrid COP increases from 6.9 to 17.7 whereas conventional COP is maintained invariant at 6.5, (ii) Increasing recooling temperature from 25°C to 40°C, resulting in reducing the hybrid system energy savings from 65.4% to 41.6%, and (iii) Superior energy savings (82.3%) can be attained at regeneration, recooling and chilled temperatures of 95°C, 25°C and 18°C.

References

[1] X. Liu, M. Qu, X. Liu, L. Wang, Membrane-based liquid desiccant air dehumidification: A comprehensive review on materials, components, systems and performances, Renewable and Sustainable Energy Reviews. 110 (2019) 444–466. https://doi.org/10.1016/j.rser.2019.04.018.

[2] M.G. Gado, S. Ookawara, S. Nada, I.I. El-Sharkawy, Hybrid sorption-vapor compression cooling systems: A comprehensive overview, Renewable and Sustainable Energy Reviews. 143 (2021) 110912. https://doi.org/10.1016/j.rser.2021.110912.

[3] M.G. Gado, T.F. Megahed, S. Ookawara, S. Nada, I.I. El-sharkawy, Energetic analysis of a PVT-based solar-driven hybrid adsorption-compression refrigeration system, in: In: Proceeding of 9th Eur. Conf. Ren. Energy Sys, Istanbul, Turkey, 2021: pp. 171–176.

[4] V. Palomba, U. Wittstadt, A. Bonanno, M. Tanne, N. Harborth, S. Vasta, Components and design guidelines for solar cooling systems: The experience of ZEOSOL, Renewable Energy. 141 (2019) 678–692. https://doi.org/10.1016/j.renene.2019.04.018.

[5] S. Vasta, V. Palomba, D. La Rosa, W. Mittelbach, Adsorption-compression cascade cycles: An experimental study, Energy Conversion and Management. 156 (2018) 365–375. https://doi.org/10.1016/j.enconman.2017.11.061.

[6] V. Palomba, G.E. Dino, A. Frazzica, Coupling sorption and compression chillers in hybrid cascade layout for efficient exploitation of renewables: Sizing, design and optimization, Renewable Energy. 154 (2020) 11–28. https://doi.org/10.1016/J.RENENE.2020.02.113.

[7] M. Gado, E. Elgendy, K. Elsayed, M. Fatouh, Performance enhancement of an adsorption chiller by optimum cycle time allocation at different operating conditions, Advances in Mechanical Engineering. 11 (2019) 1–12. https://doi.org/10.1177/1687814019884780.

[8] M. Gado, E. Elgendy, K. Elsayed, M. Fatouh, Parametric Study of an Adsorption Refrigeration System Using Different Working Pairs, Journal of Engineering Science and Military Technologies. 17 (2017) 1–15. https://doi.org/10.21608/ejmtc.2017.21172.

[9] M.G. Gado, T.F. Megahed, S. Ookawara, S. Nada, I.I. El-Sharkawy, Performance and economic analysis of solar-powered adsorption-based hybrid cooling systems, Energy Conversion and Management. 238 (2021) 114134. https://doi.org/10.1016/j.enconman.2021.114134.

The environmental and economic assessment of using liquefied natural gas (LNG) as a fuel for bulk carrier ships

M M El Gohary [1, a] , I S Saddiek [2, b] and A Anwar [1, c]

[1]*Department of Naval Architecture and Marine Engineering, Faculty of Engineering, Alexandria University, Alexandria, Egypt*

[2]*Department of Marine Engineering Technology, Arab Academy for Science, Technology and Maritime Transport, Alexandria, 1029, Egypt*

[a] *Mohamed.elgouhary@alexu.edu.eg,* [b] *isibrahim@aast.edu,* [c] *anwarmarine82@gmail.com*

Keywords: *air emissions reduction, natural gas, environmental and economic benefits, dual fuel engine*

Abstract. As International Maritime Organization emission regulations become more rigorous, the marine industry is submitting to transformation. As well as managing today's mounting operational costs and achieving cost effective environmental acquiescence, ship owners are faced with decisions about technology, fuels and the possibility of enduring their fleet. Moreover, clean air and human health awareness during this pandemic gained renovated interest and continues to be a key determinant of renewable port activity. The alternative fuels′ debate has been dominated by the potential of liquefied natural gas. LNG-fuelled vessels count to approximately 13% of the running new build order book and estimates for 2021 and demonstrates continue growth in many classifications of society of vessels. This paper studies the environmental and economic assessment of using liquefied natural gas liquefied natural gas as a fuel for bulk carrier ships; the reduction of air pollutant emissions, such as oxides of nitrogen, oxides of sulphur, particulate matter and carbon dioxide by 80.7%, 98.5%, 97.6% and 21.8% , respectively, and annual saving damage due to atmospheric emissions per year of 2.27, 11.97, 0.82 and 0.18 million dollars, respectively, in addition to saving annual fuel cost of 2.367 million US dollar, compared to heavy-fuel oil for marine shipping. These results have been investigated by using low pressure dual fuel engine.

1- Introduction

The greenhouse gas emissions, which are announced from IMO, are coming more and more into common focus [1],and ship owners are now concerned with growing the international shipping which is considered the back-bone of world trade by 93% between 2000 and 2018;[2], shipping represents 2.5%–3.5% of global CO2 emissions; [3], because of COVID-19, global maritime trade immersed by 4.1% in 2020, see fig. 1; [4], with expectations of trade growth to return to a positive range by 4.8% in 2021;[5], in addition, ships are responsible for global air pollutant emissions, such as oxides of nitrogen (NOx) and oxides of sulphur (SOx) of 6.6% and 4%, respectively [6]. with IMO expectations, GHG emissions from shipping industry will grow between 50% and 250% by 2050. [7, 8]. Many ships travel in environmentally sensitive areas. To do so, their engines need to meet very strngent emission regulations. IMO Tier III, Emission Control Area (ECA) and Energy Efficiency Design Index (EEDI) regulations define the limits for all vessels sailing in international waters. The global response to the devastating effects of pollution and global warming on marine ecosystems is to adopt even tougher rules for emissions

to meet IMO expectations which target to reduce carbon emissions by 40% by 2030 and 70% by 2050, compared to 2008 levels [9]. Fig.2 presents annual carbon-dioxide emissions per vessel, by vessel type, 2019. [3] Recently there are numerous technologies that have been implemented to reduce emissions [8, 10, 11] such as selective catalytic reduction, exhaust gas re-circulation to reduce NOX, Sea water scrubbing, exhaust below water line to reduce SOX, electrostatic filters to reduce particulates and closed crankcase ventilation.

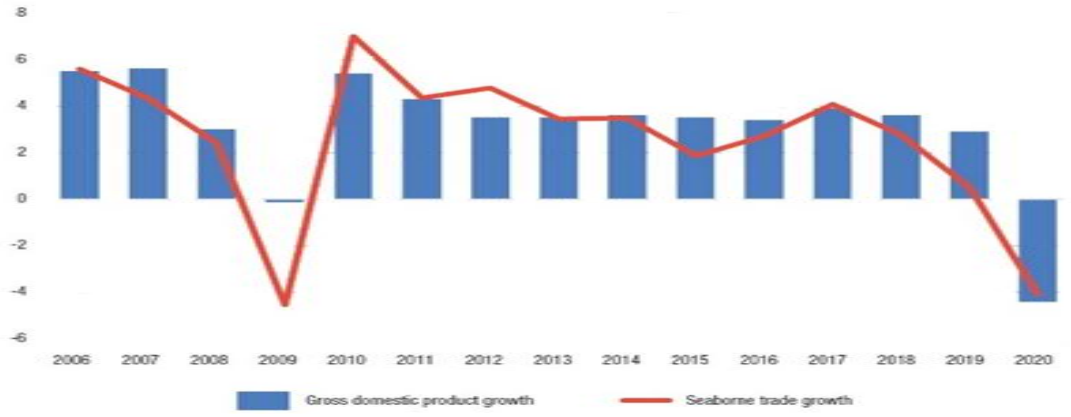

Fig. 1 development percentage of international maritime trade and global output, 2006-2020

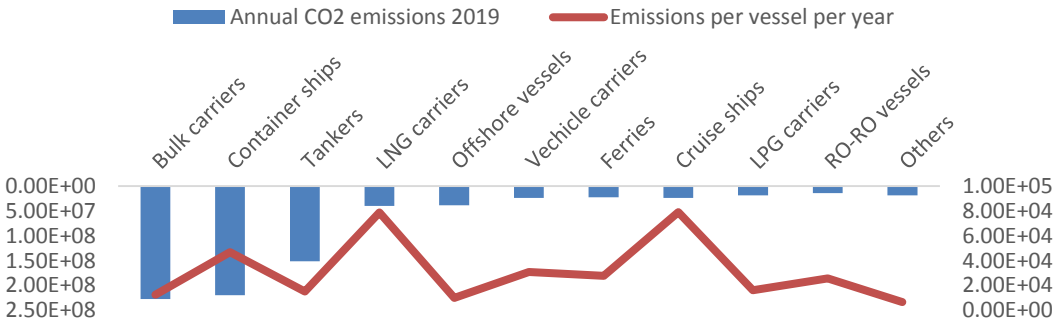

Fig. 2 Annual carbon-dioxide emissions per vessel by vessel type, 2019

2- Alternative marine fuel overview

Recent researches reveal that many alternative fuels can be used in shipping. Among the proposed alternative fuels for shipping, LNG, methanol, hydrogen (particularly for use in fuel cells), and liquefied petroleum gas (LPG) are identified as the most promising solutions [12]. All these fuels are virtually sulfur-free and can be used for compliance with sulfur content regulations, which is considered to be the most urgent challenge for shipping. They can be used either in combination with conventional, oil-based marine fuels, thus covering only part of a vessel's energy demand, or to completely replace conventional fuels for some ships. Despite the merit of low sulfur content, many of them have serious issues; for example, biodiesel has bad starting in cold weather and causes an increase in NOx emissions [8,13]; other researches showed the possibility of using methanol and the emission of aldehyde, vapor lock, cold starting, and cost-effectiveness [8, 1]. In addition to these disadvantages, there are some criteria that control choosing the suitable alternative fuel, such as adaptability, availability, safety, cost, renewability, performance, and environmental impact [1, 10, 11] which recommend hydrogen and natural gas see fig. 3, Unfortunately, hydrogen has some safety issues that need resolution; it has a low energy density and would need a hydrogen supply infra-structure to make it viable for the marine industry [14]. Furthermore, many scientists showed the possibility of using natural gas for marine application, either for ship's powering system [10, 11, 15] or for electric

generation, using fuel cells [13]. This means that it is highly likely that natural gas comes at the top of list as an alternative marine fuel in the near future.

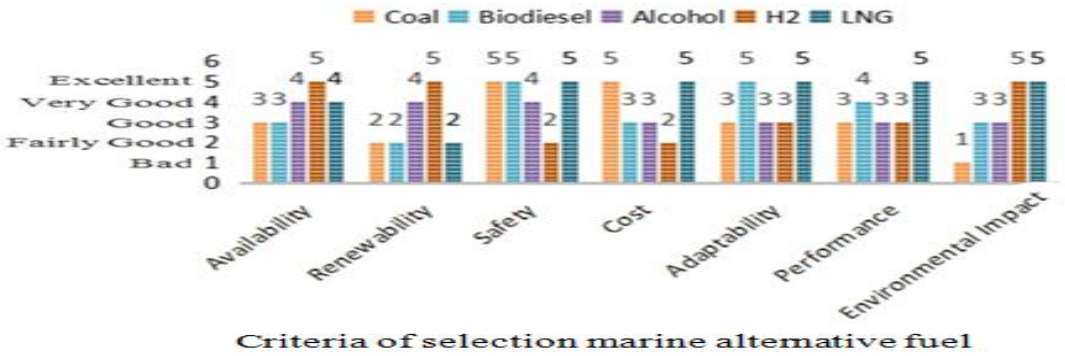

Fig. 3 weighting matrix chart of alternative marine fuels

3- Natural gas characteristics

Natural gas consumption increased by 78 billion cubic meters (bcm), or 2%, well below the exceptional growth seen in 2018 (5.3%). Nevertheless, the share of gas in primary energy rose to a record high of 24.2%. Fig.4 shows the distribution of proved reserves in 2019, which are generally taken to be those quantities that geological and engineering information indicates with reasonable certainty can be recovered in the future from known reservoirs under existing economic and operating conditions. From the graph, Africa shares with 7.0% from total distribution and Egypt with 1.1% (2.1 Trillion cubic meter, 32.9 reserve/production ratio) [16].

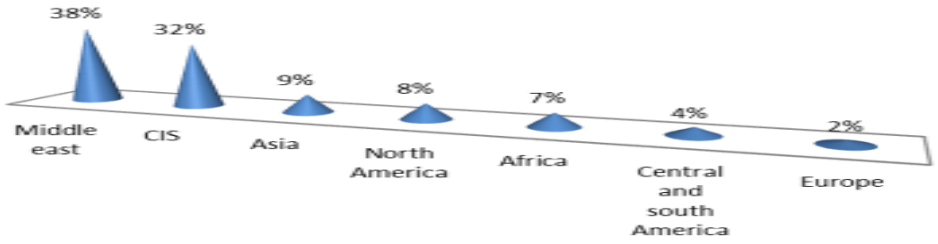

Fig. 4 LNG distribution of proved reserves in 2019

5- Case study:

This study discusses both the environmental and economic assessment of using liquefied natural gas (LNG) as a fuel; the chosen bulk carrier ship is Wadi Safaga that belongs to a national navigation company, which is considered the largest shipping Egyptian company specialized in shipping dry cargo among the world's largest ports. Table1. ship principals.

Ship name	WADI SAFAGA
Flag	EGYPT
IMO NO.	9460734
L.P.P. / Molded Breadth	229 m / 32 m
Port of registry	Alexandria
Fuel consumption per year	11579.3 ton
Main engine	STX-MAN B&W 7S50MC-C, 11060 KW @ 127 RPM
Build	2010
Gross tonnage	43736

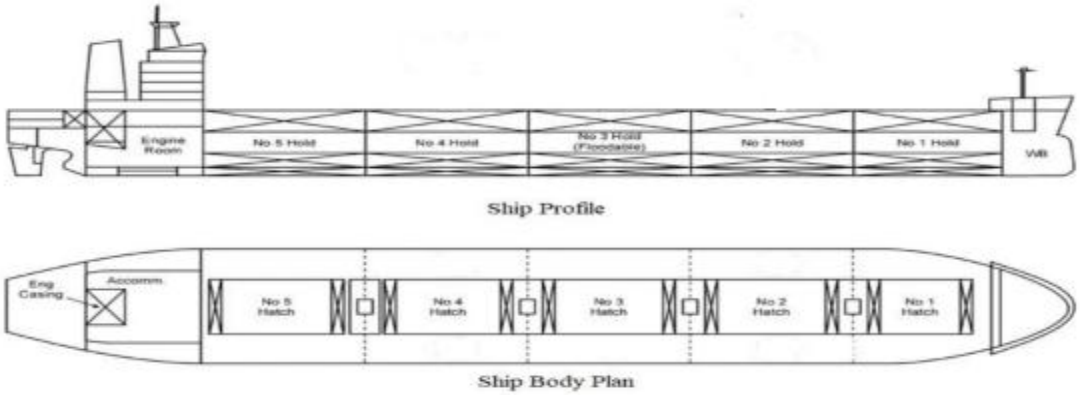

6-Environmental and economic assessment

This section introduces the methodology applied to assess the environmental impacts of the ship with a focus on the most influential pollutants on the environment, such as CO_2, NOx, SOx, and PM with emphasis on the calculations, and, the methodology applied to assess the economic benefits of the conversion process from diesel to dual-fuel engine.

6.1 Environmental assessment

Calculating quantity of gaseous emissions from diesel and dual fuel engines is considered the main crucial factor for environmental benefits evaluation. Calculating the quantity of gaseous-emissions from The Environmental Protection Agency (EPA) inventory method thereby includes defining the input parameters related to the type of vessel, the type of fuel consumed and the mode of operation. Consequently, the emission quantity can be estimated using the following formula [11]: E =P x LF x efd x t where ‘‘E’’ is the emission quantity (g), ‘‘P’’ is the engine power at MCR (kW), ‘‘LF’’ is the load factor (85%), ‘‘efd’’ is the emission factor (g/kWh) in diesel mode and ‘‘t’’ is the engine running time (hr). By substituting the average HFO and LNG for two stroke diesel engines [17, 19] at the same power and running hours, it was possible to estimate the environmental benefits due to shifting from HFO to LNG (in case of dual-fuel engine). Figure 7 shows the results of this estimation. It is clarified that from these results that the shift from HFO to LNG has led to reduction in (NOx), (SOx) , (PM) and (CO2) by 81.5%, 98.6%, 97.7% and 25%, respectively.

Table 2 Emission factors g/kwh

Emission g/kwh	Diesel	Dual fuel
CO2	549	412
NOx	14.5	2.68
Particulates	0.44	0.01
SO2	11.73	0.17

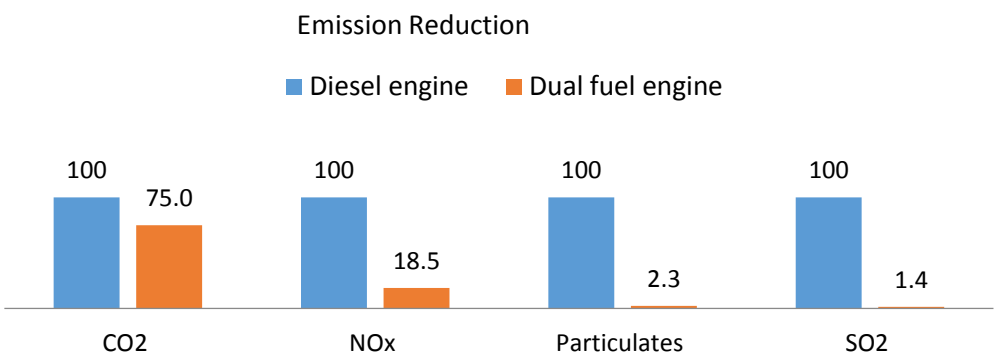

Fig. 7 Emissions reduction due to dual fuel engine.

Because the ship does not have a regular line, it sails among the world's largest ports almost all the year. From the ship owning company, the total days at sea are 250 days a year. Table 3 shows the environmental benefits of the conversion from diesel to dual fuel engine, lower emissions of CO_2 (24.95 per cent), NOX (81.5 per cent), PM (97.7 per cent) and SO2 (98.55 per cent). These results match the ones that are reported in reference [6, 10].

Table 3 the environmental benefits of the conversion from diesel to dual fuel engine:

Pollutant	Engine mode	Emission / trip (ton)	Emissions / year(ton)	Reduction ton/year
CO2	diesel	6384.34	30966.89	7727.62
	NG	4990.43	23239.27	
NOx	diesel	168.62	817.89	666.72
	NG	32.46	151.17	
PM	diesel	5.12	24.82	24.25
	NG	0.12	0.56	
SO2	diesel	136.41	661.64	652.05
	NG	2.06	9.59	

6.2 The progress in analysis of environmental damage

In the past two decades, there has been much progress in the analysis of environmental damages; the results provide substantial evidence that the classical air pollutants (CO2, particles, NOx and SO2) from the combustion of fossil fuels impose significant damage costs. The costs of global warming from the emission of greenhouse gases are also large. We present results of the damage costs per ton of emitted pollutants for typical conditions in UK. [21, 22]. Table 4 the cost of damage due to atmospheric emissions (million dollar /year) and the reduction due to the conversion process.

From table 4, we can deduce that the reduction cost of damage due to atmospheric emissions percentage in CO2, NOx, SO2 and particulates is as follows: 12.34%, 81.52%, 97.73% and 98.55%, respectively.

Pollutant	Engine mode	Cost of damage in MUSD	Reduction in MUSD
CO2	diesel	1.47	0.18
	NG	1.29	
NOx	diesel	2.79	2.27
	NG	0.52	
PM	diesel	0.84	0.82
	NG	0.02	
SO2	diesel	12.15	11.97
	NG	0.18	

6.3- Economic assessment

Recent researches claim that NG can be stored on ship, either compressed with density 0.19 ton/m3 at 250 bar in steel bottles or liquefied temperature -162Co with density 0.45 ton/m3 at 1 bar, in a cylindrical cryogenic tank that is made from arm-reinforced plastic, which typically sustains pressure from 0.3 to 10 bar. But owing to the higher quantity of NG used during the trip in this case study, it will not practically possible to store in compressed form. This means that there is a priority to use the liquefied natural gas [1, 6, 10]. From our case study it requires 290.7m3 of NG, equivalent to each cubic meter of diesel oil. As we mentioned above, the ship has not got a regular line so it is prepared for 1262 hours of sailing that needs 2127.4 m3 of LNG during this period, so we need two tanks, each with 20m length x8.25m diameter and 5mm wall

thickness, which was obtained from equation: ; where r is the tank radius, P is the operating pressure 4.14 bar, F is the tensile strength 1029 MPa and E is the safety factor taken to be 3. To convert from diesel to dual fuel engine, diesel fuel and LNG consumption per year will be 121.9 and 10113.7 ton respectively, so we can deduce that LNG offers a lower energy cost per cubic meter, against heavy fuel oil by nearly 40% because it contains more energy for the same power. Table 5 displays operational costs of diesel engine, average price of diesel in the end of 2020 was 349.5$/ton (source [23, 24]). More over diesel fuel bunkering is 3.5$/ton; we get oil lubrication quantity for system and cylinder from reference [27], whereas the cost of maintenance, repair and oil lubrication cost from the company that owns the ship. Table.8 explains operational costs of Dual fuel engine, average price of LNG in the end of 2020 was 304$/ton [25], price of Main engine, Gen-sets, LNG tanks, Gas system , maintenance & repair (M&R) cost and gas storage & vaporization (M&R) cost were obtained from Wartisla company and [26]. Design price was obtained from reference [28], shipyard installation, the information was obtained from Alexandria Shipyard-Egypt (around 10000hrs with labor cost 25$/hr). From Table 5, we get total annual savings operational costs million USD, with reduction 47.4% (Fig.8). For the assumption that the average maximum ship age is 28 years and that it was launched ten years ago, so the expected reaming ship saving after conversion for the expected remaining ship life with different value of interests (MUSD/year), the yearly capital cost recovery is 2.04 million $ per year at an interest rate of 10%. At the end of the ship life cycle, the total annual saving for using DF engine equal 24.62M $.

Table 5. Diesel engine economy

Operational costs/trip (M$)				Operational costs / year in
	M$	$/ton	ton	
Diesel fuel bunkering	0.008	3.5	2339.2	0.039
Diesel fuel	0.818	349.5	2339.2	3.887
Oil	0.027	2203.50	12.41	0.130
Maintenance & repair (M&R) cost	0.05			0.250
Total	0.906			4.31

Table 6. Dual Fuel engine economy

capital costs in MUSD				
Supply	10.45			
Design	1			
Shipyard installation	0.25			
Total capital costs	11.7			
Operational costs/trip				Operational costs/year
	M$	$/ton	Ton	
Gas fuel	0.291	304	957.34	1.3836
Gas fuel Bunkering	0.029	30.4	957.34	0.1384
Diesel fuel	0.0076	349.5	21.8	0.0362
Diesel fuel bunkering	0.00007	3.5	21.8	0.0004
Oil	0.027	2203.50	12.41	0.1300
Maintenance & Repair	0.05125			0.4095
Gas storage & vaporization	0.00236			0.1672
Total operational	0.4087			2.2652

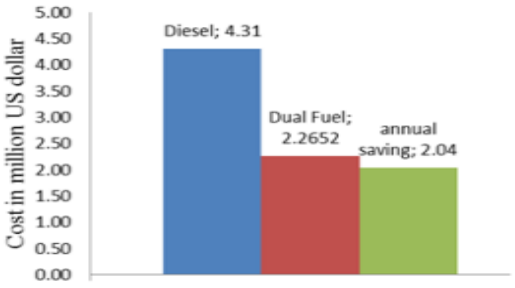

Fig.8 Annual Saving Cost in MUS

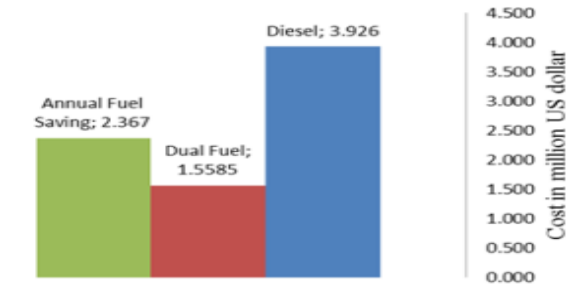

Fig.9 Annual Fuel Saving Cost in MUS

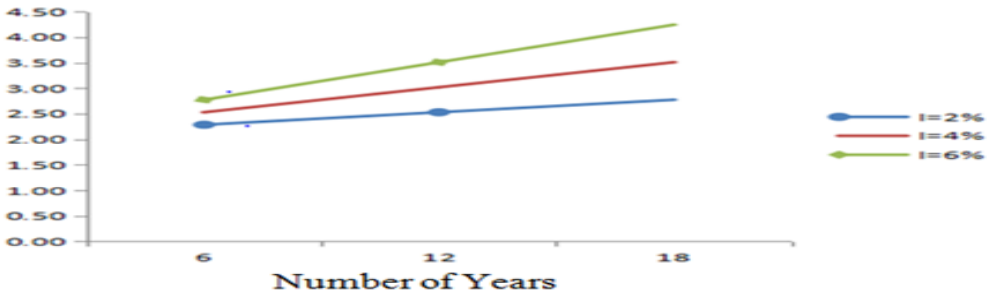

Fig. 10 Annual fuel saving after conversion for the expected remaining ship life with different value of interests (MUSD/year).

The total annual fuel cost for diesel and dual-fuel engines are US$ 3.926 million and 1.5585 million US$, respectively; therefore, the annual fuel saving cost equals 2.36 million US$ By assuming that the remaining ship age is 18 years, the total annual saving for using dual-fuel engines will be 21 million US$, assuming 3% fuel price increment. From equations: CA= Ci CRF , where CA is the annual cost and Ci is the capital cost. CRF is given by, where N is the expected ship working year after conversion. Figure 11 reveals the relationship between annual cost conversion and expected reaming ship life, for example, with 12% interest, the minimum working years to recover the conversion cost is close to 10 years, and due to this case.

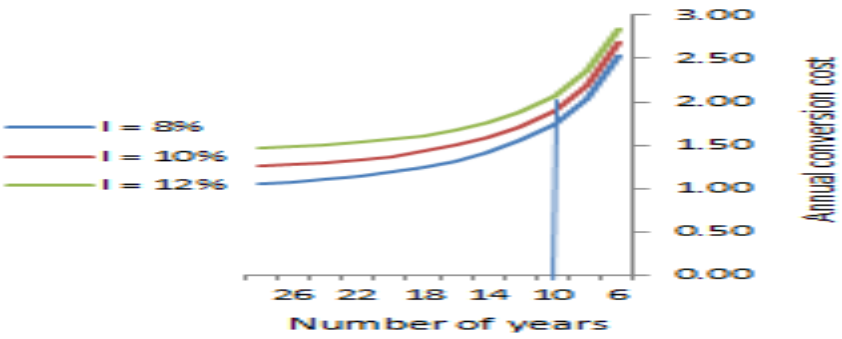

Fig. 11 the relation between annual cost conversions and expected reaming ship life

Acknowledgments: Special thanks are due to Wartsila Company. Also, many thanks are due to Mr. Ibrahim Aboustait , the superintendent in National Navigation Company for all the essential provided information.

7. Conclusion

With demonstrating liquefied natural gas and its ability as an alternative fuel to reduce environmental emissions such as oxides of nitrogen (NOx), oxides of sulphur (SOx) , particulate matter (PM) and carbon dioxide (CO2) by 80.7%, 98.5%, 97.6% and 21.8%, respectively, and annual saving damage due to atmospheric emissions per year of 2.27, 11.97, 0.82 and 0.18 million dollars respectively as well as saving annual fuel cost of 2.04 million US dollar compared to heavy-fuel oil (HFO) for marine shipping, there is no wonder to take on liquefied natural gas as a top of the list fuel in marine shipping.

8. References:

[1] Elkafas, A. G., Elgohary, M. M., & Shouman, M. R. (2020). Numerical analysis of economic and environmental benefits of marine fuel conversion from diesel oil to natural gas for container ships. Environmental Science and Pollution Research, 28(12), 15210–15222. https://doi.org/10.1007/s11356-020-11639-6

[2] Review of Maritime Transport 2018UNCTAD.unctad.org/webflyer/review-maritime-transport-2018.

[3] Review of Maritime Transport 2019 |UNCTAD.unctad.org/webflyer/review-maritime-transport-2019.

[4] Review of Maritime Transport 2020 UNCTAD.unctad.org/web flyer/review-maritime-transport-2020

[5] Review of Maritime Transport 2021 |UNCTAD,COVID-19 and Maritime Transport. unctad.org/web flyer/review-maritime-transport-2021

[6] Ammar, N. and I. Seddiek, An environmental and economic analysis of emission reduction strategies for container ships with emphasis on the improved energy efficiency indexes. Environmental Science and Pollution Research, 2020. 27.

[7] Smith, T.W.P., Jalkanen, J.P., Anderson, B.A., Corbett, J.J., Faber, J., Hanayama, S., et al., 2014. Third IMO greenhouse gas study 2014. International Maritime Organization (IMO).

[8] Salem, A., M. Elgohary, and I. Seediek, Overview of alternative fuels with emphasis on the potential of LNG as future marine fuel. Proceedings of the Institution of Mechanical Engineers, Part M: Journal of Engineering for the Maritime Environment, 2014.

[9] IMO (2018), initial IMO stategy on reduction of GHG emissions from ships

[10] Banawan, A., M. Elgohary, and I. Seediek, Environmental and economic benefits of changing from marine diesel oil to natural-gas fuel for short-voyage high-power passenger ships. Proceedings of The Institution of Mechanical Engineers Part M-journal of Engineering for The Maritime Environment, 2010. 224: p. 103-113.

[11] Seddiek IS, Elgohary MM (2014) Eco-friendly selection of ship emissions reduction strategies with emphasis on SOx and NOx emissions. Int J Nav Archit Ocean Eng 6:737–748. https://doi.org/10. 2478/IJNAOE-2013-0209

[12] (Engineering, Royal Academy of, July 2013), Future Ship powering options Exploring alternative methods of ship propulsion.

[13] Ammar NR (2019a) An environmental and economic analysis of methanol fuel for a cellular container ship. Transp Res Part D Transp Environ 69:66–76.

[14] Elgohary, M., N. Ammar, and I. Seediek, Steam and sofc based reforming options of pem fuel cells for marine applications. Brodogradnja, 2015. 66.

[15] El-Gohary, M.M., The future of natural gas as a fuel in marine gas turbine for LNG carriers. Proceedings of the Institution of Mechanical Engineers, Part M: Journal of Engineering for the Maritime Environment, 2012. 226(4): p. 371-377.

[16] BP Statistical Review of World Energy 2020.pdf

[17] Keller, P. (2019, February 3). 2019 Will be the Year of Acceleration for LNG as Marine Fuel. The Maritime Executive.https://maritime-executive.com/editorials/2019-will-be-the-year-of-acceleration-for-lng-as-marine-fuel.

[18] Energy demand and exhaust gas emissions of marine engines and Energy Policy by Hans Otto Kristenen The Technical University of Denmark Harilaos Psaraftis Project no. 2014-122: Mitigating and reversing the side-effects of environmental legislation on Ro-Ro shipping in Northern Europe Work Package 2.3, Report no. 03 September 2015

[19] Side-effects of environmental legislation on Ro-Ro shipping in Northern Europe Work Package 2.3, Report no. 03 September 2015

[20] Sharafian, Amir & Blomerus, Paul & Mérida, Walter, 2019. "Natural gas as a ship fuel: Assessment of greenhouse gas and air pollutant reduction potential," Energy Policy, Elsevier, vol. 131(C), pages 332-346.

[21] Rabl, A. and J. Spadaro, Damage Costs of Air Pollution and Policy Implications.

[22] Transportation Cost Analysis - Air Pollution Costs. (n.d.). https://vtpi.org/tca/tca0510.pdf.

[23] Information on http:// www.shipandbunker.com, (access date February 2, 2021)

[24] Information on http:// www.shipandbunker.com/worldbunkerprices, (access date February 2, 2021)

[25] Information on http:// www.DNV-GL end of December 2020

[26] Low pressure X-DF engines by WinGD 2020 Winterthur Gas & Diesel Ltd.pdf

[27] Shaft generators for the MC and ME Engine MAN B&W, Copenhagen, Denmark

[28] 144-Car Ferry LNG Fuel Conversion Feasibility Study Life Cycle Cost Analysis Prepared for Washington State Ferries Seattle, WA File No. 11030.01 1 July 2011

Effect of aspect ratio on the whole performance of direct contact membrane distillation

Mohammed Rabie[1, 2, a, *], M. F. Elkady[1, 3, b], A. H. El-Shazly[1, 4, c]

[1]Chemical and Petrochemicals Engineering Department, Egypt-Japan University of Science and Technology, Alexandria 21934, Egypt
[2]Mechanical Power Engineering Department, Mansoura University, El-Mansoura 35516, Egypt
[3]Fabrication Technology Department, Advanced Technology and New Materials Research Institute (ATNMRI), City of Scientific Research and Technological Applications, Alexandria, Egypt
[4]Chemical Engineering Department, Faculty of Engineering, Alexandria University, Alexandria 11432, Egypt

[a]mohammed.rabie@ejust.edu.eg, [b]marwa.elkady@ejust.edu.eg, [c]ahmed.elshazly@ejust.edu.eg

Keywords: Membrane distillation; Feed inlet temperature; Permeate flux; Membrane aspect ratio.

Abstract. Membrane distillation is a thermally driven technique which mainly depends on the difference in temperature between the hot (saltwater) and cold (pure water) on both sides of the membrane. The current work presents the effect of aspect ratio on the whole performance of direct contact membrane distillation system. The effect of performance parameters (i.e., feed inlet temperature and flow rate) on the system performance is also introduced to highlight the key operating conditions. The selected performance parameters in the current study were the overall thermal efficiency and system productivity. Ansys 2020 software was used for the numerical simulation process, which solved the governing equations using finite volume method. The numerical model was validated with experimental work from literature. The results show that the minimum aspect ratio has the highest performance; for instance, at feed inlet temperature and feed flow rate of 80 °C and 1800 ml/min, respectively, the permeate flux was 36.3 kg/m2 h at the minimum aspect ratio, whereas it produced 26.9 kg/m2 h at the highest aspect ratio. Moreover, feed inlet temperature and flow rate were noticed to considerably affect the whole system performance. Overall, the maximum system productivity was noticed at the minimum aspect ratio, highest feed inlet temperature and highest flow rate.

Introduction

The freshwater shortage all over the world is the motivation key for developing new techniques for water desalination and improving it to attain the optimum performance. Membrane distillation (MD) process mainly depends on the vapor pressure difference (i.e., the driving force), as a consequence of temperature difference across the membrane surfaces [1]. This technique has a noticeable lower operating pressure compared to other techniques. There are four types of membrane distillation, amongst the most popular type is the direct contact membrane distillation (DCMD) [2]. The major design of the system is composed of two flow channels separated by a hydrophobic porous membrane.

Recently, there are a lot of improvements for the MD system to be competitive with other desalination techniques. Integrating MD with solar energy was proposed and studied for simultaneous fresh water and electricity generation [3–5]. Fabrication of new membranes was also introduced to improve the productivity of the system via improving the membrane hydrophobicity and porosity [6]. Additionally, spacer could be used in the feed channel to promote evaporation and consequently improve the system performance and productivity [7, 8]. The effect of working factors such as saltwater temperature on the system performance were well investigated [9].

For sustainable fresh water production a HCPV with active cooling [10, 11] ,using water as a coolant, could be utilized to supply electric power and hot water, which totally enhance the unit's economy.

The aim of the current work is to introduce the effect of aspect ratio of the membrane on the overall operation of the system. A three-dimensional model was designed to study the effect of membrane's aspect ratio besides the system operating parameters (i.e., feed inlet temperature and flow rate) on the system performance. Ansys fluent 2020 software was used for the simulation process. The originality of this research is divided into two aspects, the first one is the investigation of aspect ratio and operating parameters for DCMD, and the second aspect is the designed model for simulation which could be modified for any further improvements.

Model description

The current study is considering DCMD type, which composed of two flow channels separated by the hydrophobic porous membrane. The effect of aspect ratio, which is defined as the ratio of channel length to channel width, on the system performance is introduced numerically. Fig. 1 shows the proposed system with defining the channel's length and width.

Governing equations. Mass, momentum, energy equations are controlling the proposed system, and these governing equations are as follows:

Mass conservation:

$$\nabla.\vec{V} = \frac{MS}{\rho}. \quad (1)$$

Momentum conservation:

$$\rho(\vec{V}.\nabla)\vec{V} = -\nabla P + \mu\nabla^2\vec{V}. \quad (2)$$

Energy conservation:

$$\vec{V}.\nabla T = \frac{\nabla^2 T}{\alpha} + \frac{ES}{\rho}. \quad (3)$$

where $\vec{V}$, P, ρ, μ, T and α are velocity vector, pressure, density, dynamic viscosity, temperature, and thermal diffusivity, respectively, whereas MS and ES are the mass and energy sources, respectively.

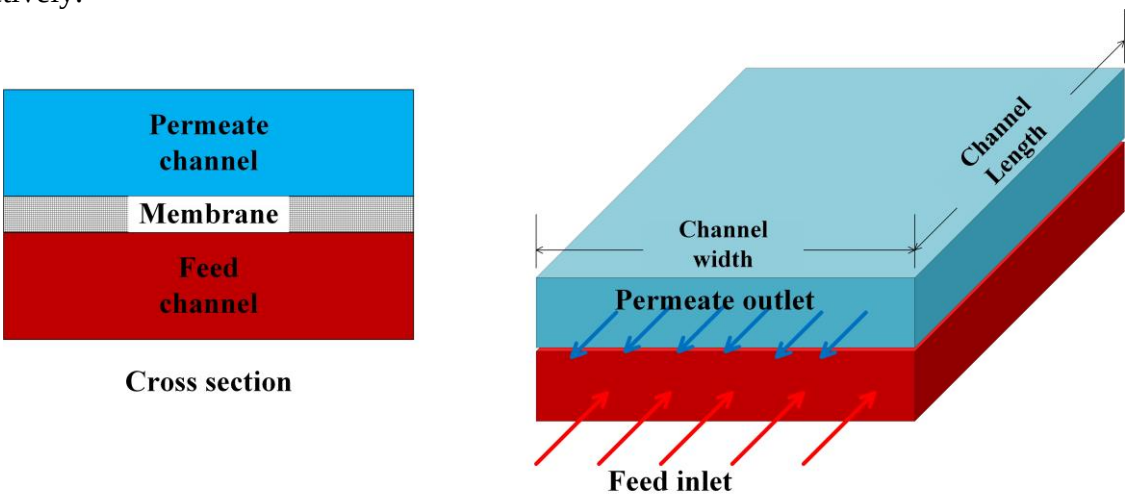

Fig. 1 Schematic drawing for the proposed system.

System performance parameters. The most important performance parameters used in this technique is the permeate flux and system thermal efficiency. The former is measuring the amount of pure water produced per membrane's unit area per unit time, while the latter is calculating how much energy is consumed for evaporation process (which is favorable) out of the total energy consumed. Permeate flux could be calculated as follows [12]:

$$J = \omega\left(P_v^f - P_v^p\right). \quad (4)$$

And the thermal efficiency could be expressed as follows [13]:

$$\eta = \frac{JA\Delta H}{\dot{m}C_p(T_{fi}-T_{fo})} \quad (5)$$

Numerical solution. A three-dimensional model was designed using Ansys 2020 software, then a reasonable boundary conditions were set on the system boundaries, then a mesh dependence test was performed, and finally the model was validated with [14]. Fig. 2(a) shows the mesh dependence test with selected number of cells of 500,000 element, and Fig. 2(b) shows the model validation with the experimental work of [14] with very good agreement.

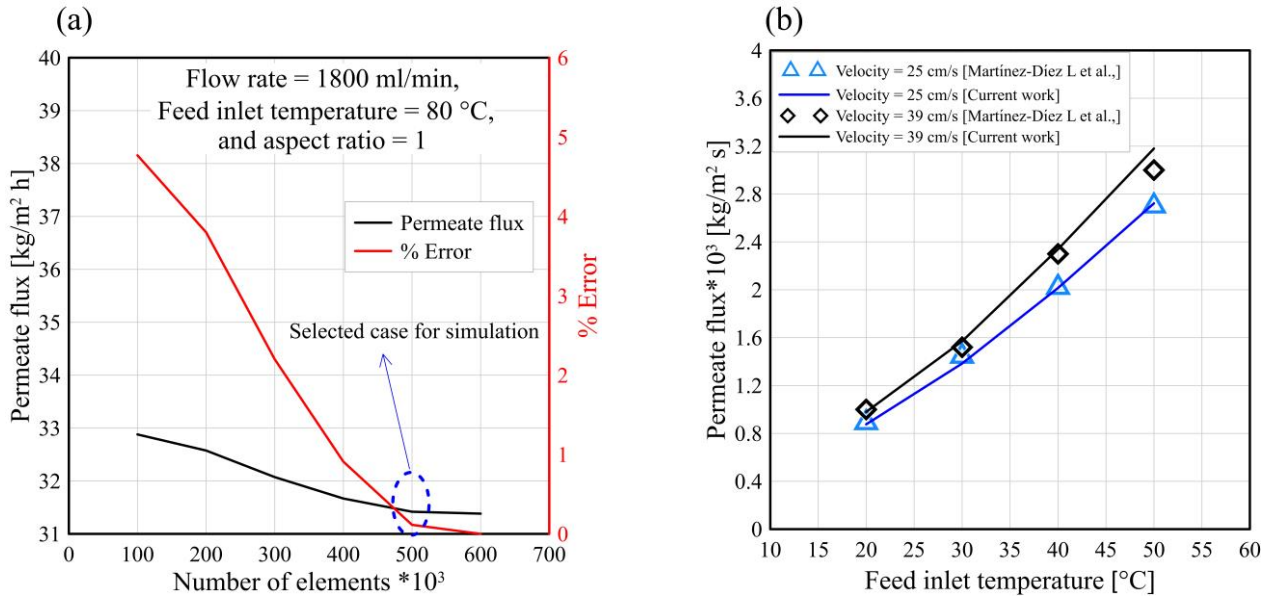

Fig. 2 (a) Mesh dependence test result, and (b) Model Validation with [14].

Result and discussion

The response of the system performance to the change in saltwater temperature is illustrated in Fig. 3(a) and (b), respectively, at different aspect ratios. It could be seen from the figures that feed inlet temperature is positively affecting both permeate flux and thermal efficiency, and this is a consequence of increasing the process driving force. Furthermore, increasing the aspect ratio has a negative effect on the overall performance as could be noticed form Fig. 3(a) and (b). The concept here is that, increasing the aspect ratio allows more heat to be transferred and hence decreasing the temperature difference, which consequently decreasing the driving force.

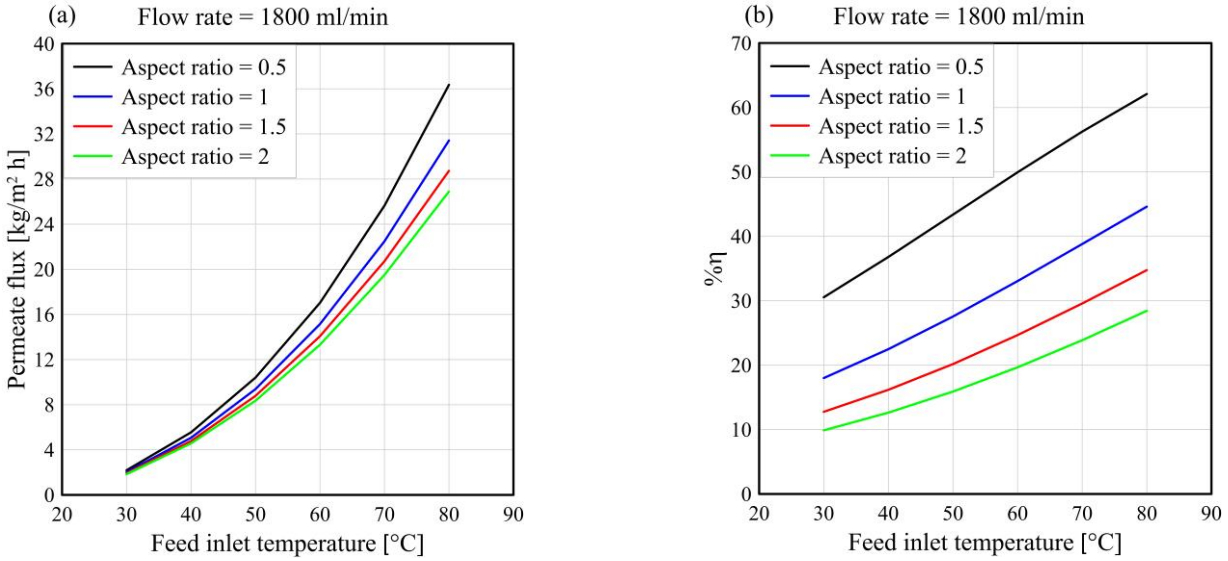

Fig. 3 Effect of Saltwater temperature on (a) the permeate flux, and (b) efficiency, at different aspect ratios.

The impact of fluids' flow rate on the system performance parameters is presented in Fig. 4(a) and (b), respectively, at the highest studied feed inlet temperature (80 °C) and different aspect ratios. Increasing the feed flow rate has a significant effect on the produced pure water, for instance, rising the flow rate from 300 to 2400 ml/min has increased the permeate flux from 21.5 to 33 kg/m2 h, respectively. On the other hand, increasing the flow rate is slightly increasing the thermal efficiency, this is because both the useful and consumed heat is increased (numerator and denominator), and the increase in numerator is higher than that of denominator, therefore according to Eq. 5 the efficiency is slightly increased. The effect of aspect ratio has the same trend as that illustrated in the previous paragraph.

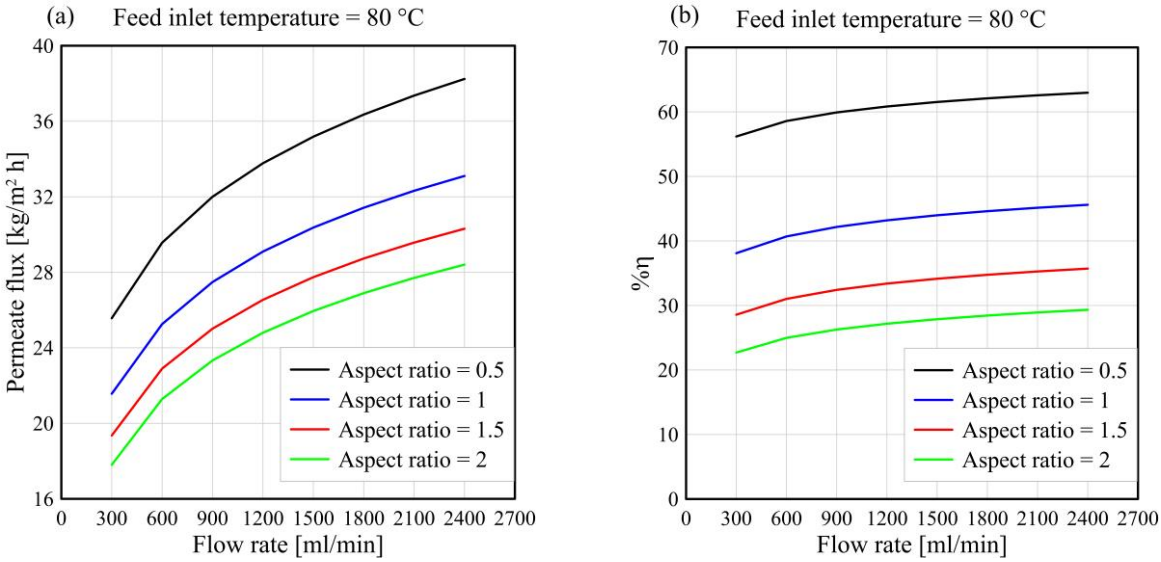

Fig. 4 Impact of flow rate on (a) permeate flux, and (b) efficiency, at different aspect ratios.

Fig. 5 shows the temperature contours at the membrane/feed interface for the different studied aspect ratios. The contours sections are scaled for comparison purpose. As could be seen from the figure, increasing the aspect ratio has reduced the red colored area (highest temperature), and so the temperature difference on the two surfaces of the membrane has been reduced. This effect has reduced the driving force and then it negatively affected the whole system performance.

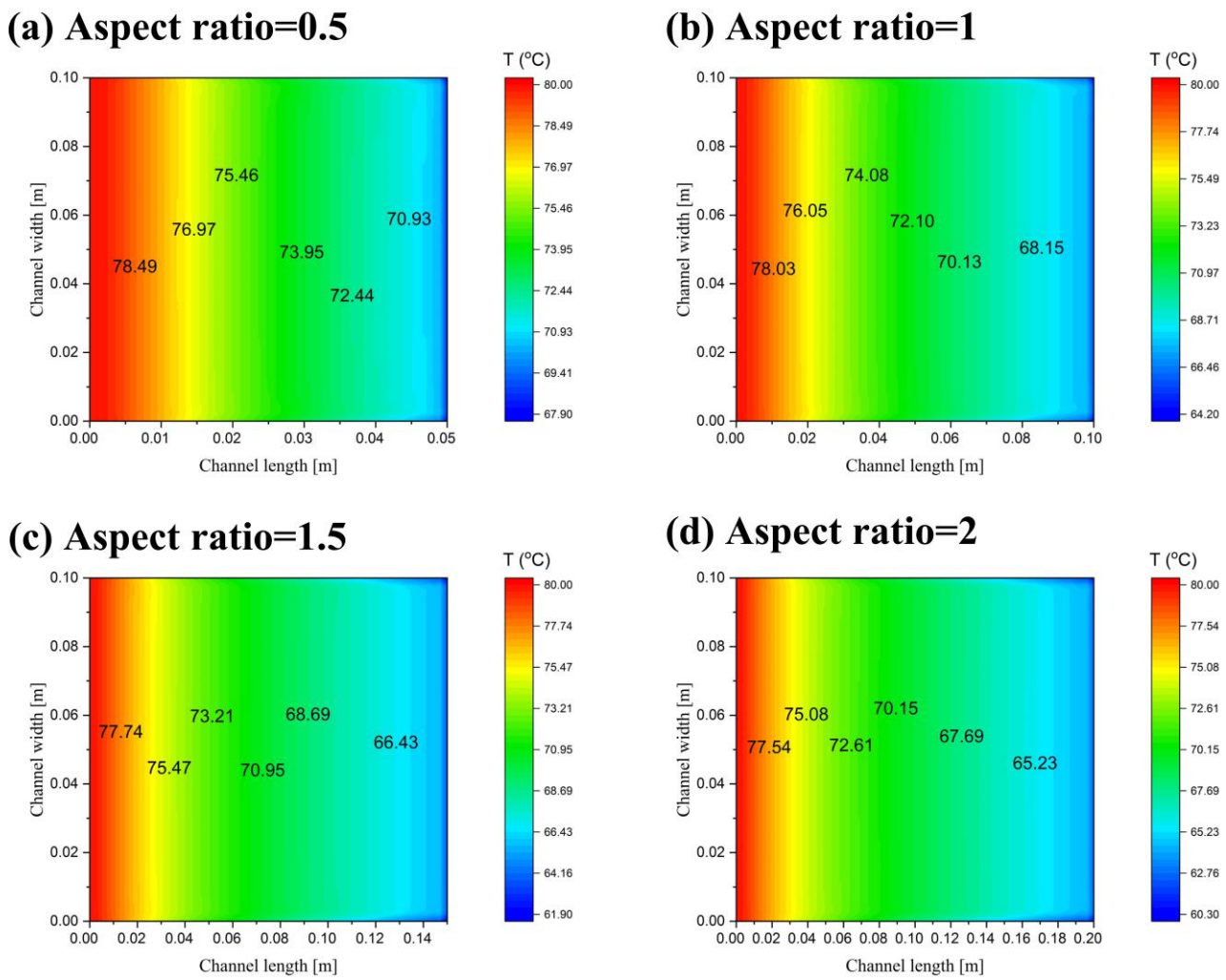

Fig. 5 Temperature contours at membrane/feed interface at all studied aspect ratios.

Conclusion

The current work is numerically investigating the impact of aspect ratio, saltwater inlet temperature, and flow rate on the overall performance of DCMD. Aspect ratio has a negative effect on system productivity and efficiency at any operating conditions as it generally decreases the driving force. Furthermore, increasing feed inlet temperature and feed flow rate has a positive effect on the system performance as it increased the permeate flux and thermal efficiency. Finally, it is recommended for the designer to manufacture a cell that could incorporate membranes with small aspect ratio.

Acknowledgement

The authors would like to express their appreciation to Minister of Higher Education (MoHE) and Egypt-Japan University of Science and Technology (E-JUST), for continuous support.

References

[1] Alkhudhiri A, Darwish N, Hilal N. Membrane distillation: A comprehensive review. Desalination 2012;287:2–18. https://doi.org/https://doi.org/10.1016/j.desal.2011.08.027.

[2] Ahmed FE, Lalia BS, Hashaikeh R, Hilal N. Alternative heating techniques in membrane distillation: A review. Desalination 2020;496:114713. https://doi.org/https://doi.org/10.1016/j.desal.2020.114713.

[3] Rabie M, Salem MS, Ali AYM, El-Shazly AH, Elkady MF, Ookawara S. Modeling of an

integrated air gap membrane distillation unit utilizing a flat plate solar collector. Energy Reports 2020;6:1591–6. https://doi.org/https://doi.org/10.1016/j.egyr.2020.10.046.

[4] Rabie M, Ali AYM, Abo-Zahhad EM, Elqady HI, Elkady MF, Ookawara S, El-Shazly AH, Salem MS, Radwan A. Thermal analysis of a hybrid high concentrator photovoltaic/membrane distillation system for isolated coastal regions. Sol Energy 2021;215:220–39. https://doi.org/https://doi.org/10.1016/j.solener.2020.12.029.

[5] Zhao Q, Zhang H, Hu Z. Hybridizing photovoltaic cell with direct contact membrane distillation for electricity and freshwater cogeneration: Concept and performance evaluation. Desalination 2020;496:114701. https://doi.org/https://doi.org/10.1016/j.desal.2020.114701.

[6] Elrasheedy A, Rabie M, El-Shazly A, Bassyouni M, Abdel-Hamid SMS, El Kady MF. Numerical Investigation of Fabricated MWCNTs/Polystyrene Nanofibrous Membrane for DCMD. Polymers (Basel) 2021;13. https://doi.org/10.3390/polym13010160.

[7] Ve QL, Rahaoui K, Bawahab M, Faqeha H, Date A, Faghih A, Akbarzadeh A. An experimental heat transfer investigation of using spacer in direct contact membrane distillation. Energy Procedia 2019;160:223–30. https://doi.org/https://doi.org/10.1016/j.egypro.2019.02.140.

[8] Alwatban AM, Alshwairekh AM, Alqsair UF, Alghafis AA, Oztekin A. Performance improvements by embedded spacer in direct contact membrane distillation – Computational study. Desalination 2019;470:114103. https://doi.org/https://doi.org/10.1016/j.desal.2019.114103.

[9] Manawi YM, Khraisheh M, Fard AK, Benyahia F, Adham S. Effect of operational parameters on distillate flux in direct contact membrane distillation (DCMD): Comparison between experimental and model predicted performance. Desalination 2014;336:110–20. https://doi.org/https://doi.org/10.1016/j.desal.2014.01.003.

[10] Y.M. Ali A, M. Abo-Zahhad E, Elqady HI, Rabie M, Elkady MF, Ookawara S, El-Shazly AH, Radwan A. Thermal analysis of high concentrator photovoltaic module using convergent-divergent microchannel heat sink design. Appl Therm Eng 2021;183:116201. https://doi.org/https://doi.org/10.1016/j.applthermaleng.2020.116201.

[11] Ali AYM, Abo-Zahhad EM, Elqady HI, Rabie M, Elkady MF, El-Shazly AH. Impact of microchannel heat sink configuration on the performance of high concentrator photovoltaic solar module. Energy Reports 2020;6:260–5. https://doi.org/https://doi.org/10.1016/j.egyr.2020.11.248.

[12] Kuang Z, Long R, Liu Z, Liu W. Analysis of temperature and concentration polarizations for performance improvement in direct contact membrane distillation. Int J Heat Mass Transf 2019;145:118724. https://doi.org/https://doi.org/10.1016/j.ijheatmasstransfer.2019.118724.

[13] Suwwan D, Hashaikeh R, Janajreh I. Low Energy Direct Contact Membrane Desalination: Conjugated Heat and High Fidelity Flow Simulation. Energy Procedia 2015;75:1722–7. https://doi.org/https://doi.org/10.1016/j.egypro.2015.07.438.

[14] Martínez-Díez L, Vázquez-González MI. Temperature and concentration polarization in membrane distillation of aqueous salt solutions. J Memb Sci 1999;156:265–73. https://doi.org/https://doi.org/10.1016/S0376-7388(98)00349-4.

3rd International conference of Chemical, Energy and Environmental Engineering
July 2021 Egypt Japan University of Science and Technology, Alexandria, Egypt.

CROP WATER REQUIREMENT FOR ZANZIBAR ISLAND IN TANZANIA STATE UP TO 2100

Othman Juma Suleiman[1,a], Mohammad. Abourohiem[2,b], Nesma Abdel Meged[2,c]
[1]Ministry of agriculture, natural resources and irrigation, Zanzibar, Tanzania.
[2]Department of Irrigation and Hydraulic, Faculty of Engineering, Alexandria University, Alexandria, Egypt.
[a]osuleiman1281@yahoo.com, [b]mrohim76@yahoo.com, [c]eng_nesma_adwy@yahoo.com

Keywords: Climate Change, Bias Correction, Climate Model Scenario, Cropwat, CWR

Abstract. Climate changes are a major problem that directly affect agricultural economy since lead to increase the crop water requirements for major crops. The present study aims to analyse the impact of climate change on crop water requirements for different crops irrigated in Zanzibar Island in the long term. Zanzibar Island is a part of the United Republic of Tanzania, located offshore Tanzania mainland coast. The current study is conducted to estimate crop evapotranspiration (ETc) as well as crop water requirements (CWR) of rice, banana, tomato, watermelon and maize crops. For this purpose, data of Kizimbani station is used during the period (1983-2013) based on the observed climate data and period (2020-2100) based on Representative Concentration Pathways (RCPs), RCP 4.5. The delta change was applied to obtain the corrected value both future temperature and Precipitation using CMHyd software. The CWR for the different crops was both computed using CROPWAT 8.0. Zanzibar will be affected by climate extremes which leads to large climate variability with heavy precipitation and dry periods. These changes will affect precipitation trends and water management issues for floods and droughts. Future temperatures are projected to rise on Zanzibar with increases of 1.3 to 2 °C by the 2050s and 1.8 to 3.1°C by the 2100 relative to the baseline period (1983–2013). The sum CWR volumes for rice, banana, tomato, watermelon and maize will increase by 13.05% and 28.6% by 2050 and 2100 in average respectively .

Introduction

Climate changes will accelerate the global hydrological cycle, with increase in the surface temperature, changes in precipitation patterns, and evapotranspiration rate. The magnitude of climatic changes including variations in temperature and rainfall differs in various parts of the world [2]. Changes in temperature and precipitation patterns as consequence of the increase in concentrations of greenhouse gases may affect the hydrology process, availability of water resources, and water use for agriculture, population, aquatic life in rivers and lakes, and hydropower. The shortage and excess of crop water availability affects the growth and development of the plants, yields production and quality of produces. This leads to, mostly increase of evapotranspiration rate which in turn increase crop water requirements (CWR.).

General circulation models (GCMs) are currently the most widely used tools for simulating the global

climate system response to increase greenhouse gas concentrations, as well as for estimating the climate variables on a global scale. For evaluation of the atmospheric composition, a set of possible future scenarios are illustrated such as, Representative Concentration Pathways (RCPs) were adopted [3,4]. The RCPs form a set of greenhouse gas concentration and emission pathways designed to support research on impacts and potential policy responses to climate change[4,5]. On the basis of multi-gas emission scenarios, it is used four RCPs (i.e. RCP 8.5, 6, 4.5 and 2.6) for various impact studies. IPCC (2013)[1] reported that under RCP 8.5 the all changes in the mean annual temperature exceeds 2°C in the middle of this centurycompard to baseline period of 1990.

Makame, (2015) showed that most of east coast area in Zanzibar received low rainfall which led to shortage yield production for example in 2010 to 2011 more than 7000 people at Micheweni did not have enough food due to rainfall fluctuation.

Zainab Hassan Moyo, (2013)[6] studied vulnerability of rainfall rice producing households to climate change and variability. It was found that an annual increase in temperature of approximately 0.025. The historical return period of extreme flood occured of different years 1972 to 1984 and 1985 to 1990 , and drought condition due to climate variability in the year 1964 to 1972 and 1990 to 2000. These factors hindered the decline of clove production and supply in the world market from 80% in (1970s) to 7%.

It is clearly from the above review of literature that the climate in Zanzibar has undergone a marked change. Thus, the agriculture sector is likely to suffernfrom water stress. Therefore, the objective of the present paper is to evaluate the impact of climate change on reference evapotranspiration and CWR of rice, banana, tomato, watermelon and maize crops in Zanzibar Island due to data collected fron Kizimbani station.

STUDY AREA

Zanzibar is an island of the United Republic of Tanzania, which located in the Indian Ocean approximately 30 km east of the Tanzania mainland. The island is located between latitude 4°50' and 6°30' South, and longitude 39°10' and 39° as shown in Figure 1. Zanzibar has a tropical climate with average temperatures that are quite constant throughout the year. It has relatively high levels of average precipitation, and it is exposed to strong rains in March to May, with shorter rains in November and December. The dry season lasts from June to October.

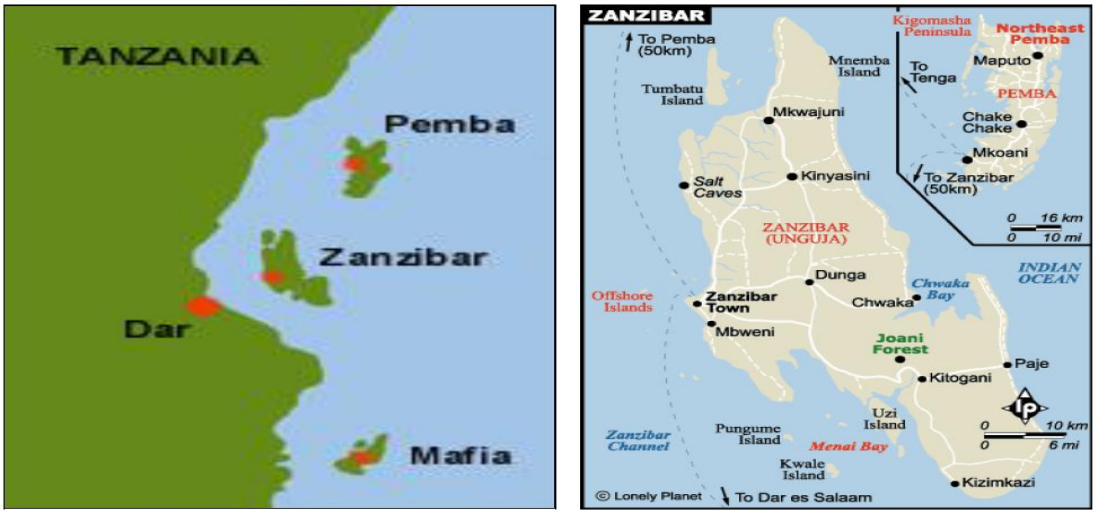

Fig.1 Location map of Zanzibar, cited in Sheha, (2009).

Data and Methodology

According to Tanzania Meteorological Agency (TMA), Zanzibar Zonal Office, Zanzibar has a tropical climate with annual rainfall of on average 1600 mm and 1900 mm for Zanzibar and Pemba, respectively. The climate of Zanzibar is dominated by two rainy seasons Masika and Vuli with drier periods in between. Masika is the main and long rainy season extends from the end of March to May and is responsible for most of the total annual rainfall. The highest rain is recorded in the month of April while from end of May until early November is the dry season. In the other hand, Vuli has short rainfall in the months of October to December. Figure 2 gives an average of monthly rainfall for Kizimbani station for the period (1981– 2013).

According to the information collected from Tanzania Meteorological Agency, Zanzibar Zonal Office shows that, the monthly maximum temperature ranges from 28ºC during the coldest month (May - July) to 32ºC during the hottest month of February. The mean monthly minimum temperature ranges from 19ºC during the month of September to 23.4ºC during the hottest month of April. The average monthly temperature of Zanzibar range from 1983 to 2013 is shown in the Fig 3.

Based on the observed data, it is concluded that there is strong observational data to show that the climate of the Zanzibar is changing. Temperatures have been rising over the last thirty years in Zanzibar Island, with a strong increase in average and maximum temperatures.

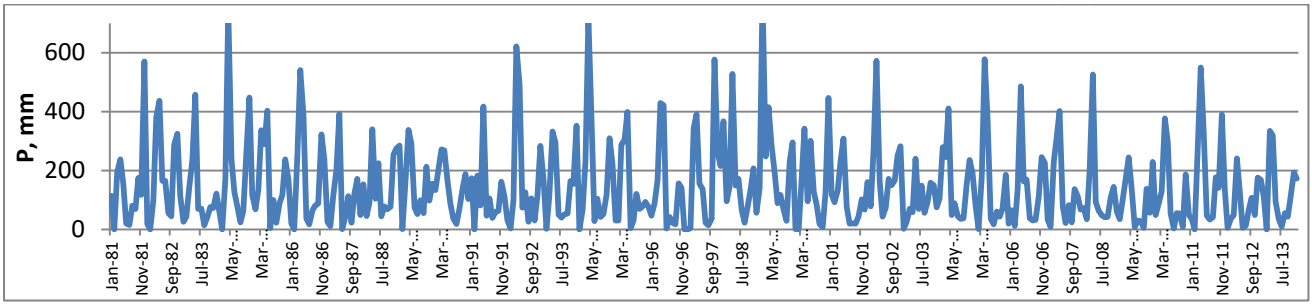

Fig 2 rainfall for Kizimbani station from 1981 to 2013

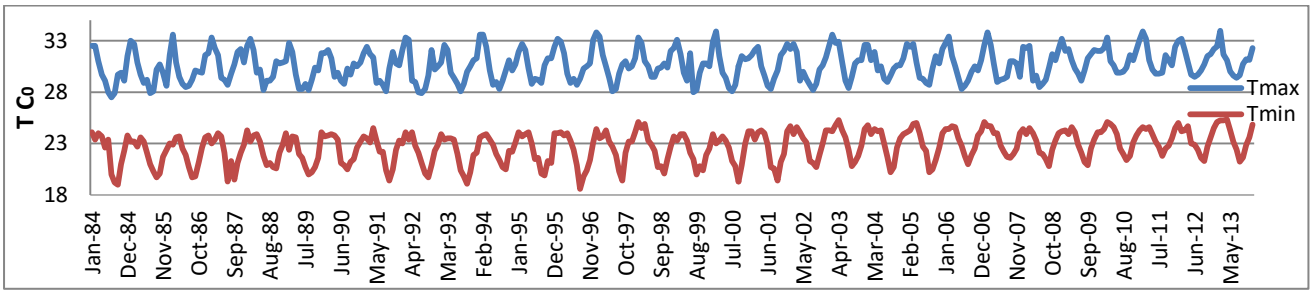

Fig 3 Max and Min Temperature for Kizimbani station from 1984 to 2013

The increases are highest in the months December to May and the highest temperature recorded on the island was in at over 39 degrees in 2007 . The changes in rainfall are complex, and there does not appear to be a simple precipitation trend across the islands. However, there are some indications of change in rainfall variability, and there have been higher rainfall intensity events recorded in recent years. There are observational trends of increasing wind speeds on the islands over the last 20 years, with an increasing tendency to extreme wind events.

The main goal of the International Coordinated Regional Climate Downscaling Experiment (CORDEX) Initiative, sponsored by the World Climate Research Program (WCRP), is to fill this gap in a selection of pre-defined domains. Practically, the CORDEX data are obtained by downscaling with a Regional Climate Model (RCM) the outputs of a GCM embedding the simulation domain and used as a driving model. In the current paper climatic data performed in the frame of CORDEX-Africa with different combinations of GCMs and RCMs are used. Several meteorological data including precipitations and daily max and min temperatures are available in four different runs: Historical for the 1950–2005 period and the RCP45 scenario for the 2006–2100 period. For the evaluation runs, it is used RCM (RCA4) and for the future period combinations of this RCM with GCM (ICHEC-EC-EARTH). The model was run over an African domain covering the Ethiopian territory with a horizontal resolution of 0.44o. The results of the simulations were downloaded from the website of the Earth System Grid Federation (https://esg-dn1.nsc.liu. se/projects/cordex/).

A comparison of the baseline data from GCM under RCP 4.5 with the observed data of Kizimbani station from 1983 to 2013 was carried out. To get a reasonably accurate estimate of future temperature and precipitation, for the calculation of future, ETo and CWR, was considered essential to apply bias correction to the temperature and precipitation data. For bias correction of temperature and precipitation data, the delta change was used [21]. The data were downloaded in Net CDF file format and extracted by a tool called CMhyd.). It was designed to work with the CORDEX data archive, which provides downscaled regional climate model data.

RESULTS AND DISCUSSIONS

The future climate model projections of climate change on Zanzibar are to explore the potential future trends and risks. The rainfall regime of Zanzibar will change but the projections vary. After bias correction, results are shown in Fig .4 and Fig. 5.

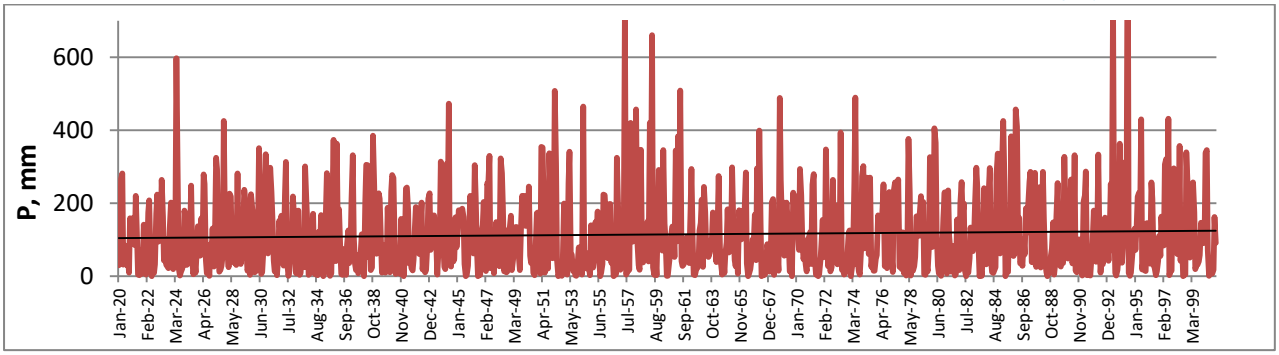

Fig. 4 rainfall for Kizimbani station from 2020 to2100

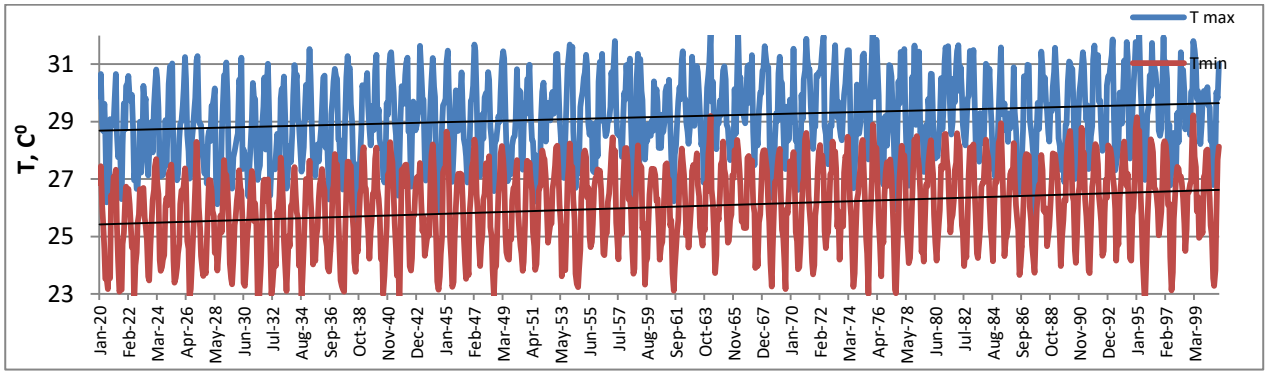

Fig. 5 Max and Min Temperature for Kizimbani station from 2020 to2100

It can be noticed that, Rainfall is projected to increase in future climate in almost island under RCP 4.5 emission scenario. Zanzibar will be affected by climate extremes which leads to large climate variability with heavy precipitation and dry periods. These changes will affect precipitation trends and water management issues for floods and droughts. There are consistent trends projected of increasing rainfall during the Mar-May wet or rainy season, and an increase in January and February. There is also a trend of decreasing rainfall during the dry season (June – October). It should be noted that the relative humidity ranges from 70% to 85% during the period 2020 to 2100.

Estimation ETc Using Cropwat 8.0 Software. The increase in temperature was believed to contribute to an increase in evapotranspiration which can result in high amount increase CWR and decrease in crop water available. Therefore, to calculate the predicted increase or decrease in crop water requirement for the crops in Zanzibar, the types of crops and cultivated area for each crop must be identified. The different crops with the irrigation area for each crop as well as the growing stages for different crops and values of Kc, obtained from FAO database for each crop, at different growing stages for various crops also are shown in Table1.

Kizimbani future data station were used to calculate Crop water requirements from 2020 to 2100 using Cropwat 8.0 software. For rice maximum crop water requirement was 797.1mm found in the year 2091 and minimum CWR was 573.5mm found in the year 2100. The variation of higher water demand for rice crop in 717.8mm in the year 1993 means evaporation loss was more, low humidity, higher wind speed and shortage of effective rainfall. These factors influence higher amount of water needed to compensate in order to sustain water required for rice production. For banana; mximum and minimum CWR were 1226.1mm and 924.5mm calculated in the year 2069 and 2020 respectively. For tomatoes maximum and minimum crop water requirement were 663.2mm and 488.4mm were calculated in the year 2100 and 2025 respectively. For watermelon and maize maximum CWR was 476mm and 493.5mm in the both year 2100 respectively and minimum CWR was 348.1mm and 341mm both in the year 2025 respectively

Based on the corrected future climate data by Bias, Cropwat 8.0 software is used to estimate the forcasting ET_c up to2100 . Average ET_c values for different selected years is shown in Fig 6

Table 1 Area, planting, harvesting dates, crop growth period and Kc for different crops in Zanzibar Island

Crop type	Irrigated Area (ha)	Planting date	Harvesting date	Yield response	Critical depletion fraction	Crop Growth Periods(days)				Crop growth stage coefficient (Kc)			
						Initial	crop dev	Mid season	Late season	initial stage	deve	mid	late
Rice	8000	January	April	1.1	0.2	20	30	40	30	1.1	1.05	1.2	1.05
Banana	3000	January	August	1	0.55	60	60	75	45	1	1	1.2	1.1
Tomatoes	2500	January	May	1.05	0.4	30	40	45	30	0.6	0.6	1.2	0.8
watermelon	2000	January	April	0.81	0.6	25	35	40	20	0.5	0.5	1.05	0.75
maize	500	January	May	0.8	0.8	20	35	40	30	0.3	0.3	1.2	0.35

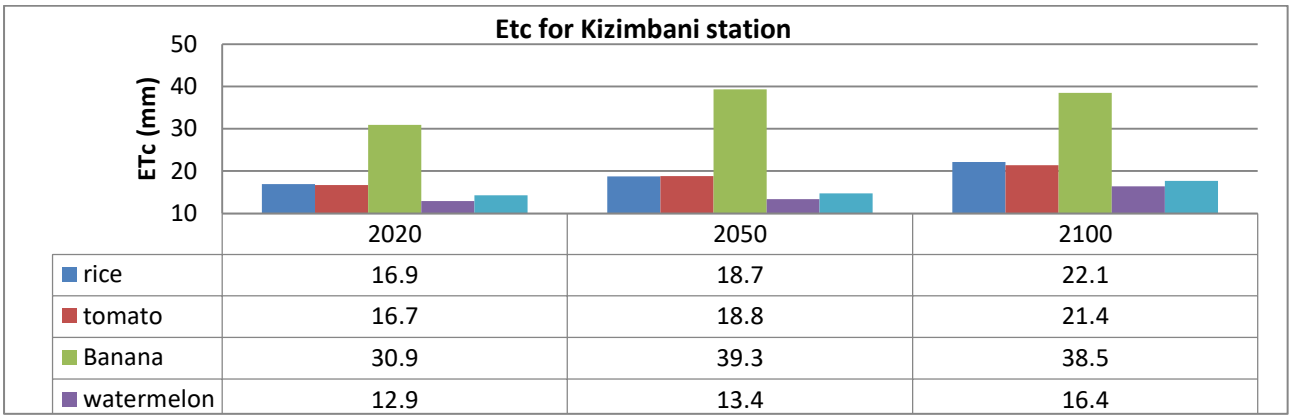

Fig. 6 Future ETc for rice, tomato, banana, watermelon and maize through 2020, 2050 and2100

Future Crop Water Requirement in Volumes. Considering a pilot area of 100 ha cultivated with 50 ha rice, 15.5 ha tomato, 19.0 ha banana, 12.5 ha watermelon and 3.0 ha maize, the future CWR for each crop is given in table 2 for the years 2050 and 2100. The total CWR for all crops is 31.17 x 10^5 m^3 and 30.82 x 10^5 m^3, or 0.3117m^3 /ha and 0.3082 m^3, for 2050 and 2100 ,respectively

Table 2 Future Crop water requirement in volume in Kizimbani station data based on 2050 and 2100

Month	Rice	Tomato	Banana	Watermelon	Maize	Rice	Tomato	Banana	Watermelon	Maize
	month/ 100 ha X 10^5 / m^3 2050					month/ 100 ha X 10^5 / m^3 2100				
Jan	1.581	0.806	1.643	0.744	0.496	1.581	0.868	1.43	0.744	0.000
Feb	1.42	0.957	1.653	1.015	1.102	1.83	1.334	1.68	1.334	0.256
Mar	1.12	0.837	1.767	0.992	1.085	1.80	1.736	1.71	1.612	0.697
Apr	1.53	1.44	1.38	1.29	1.2	1.47	1.53	1.53	1.26	0.026
May	0	1.023	1.519	0	0.558	0	1.023	1.30	0	0.000
Jun	0	0	1.44	0	0	0	0	1.35	0	0
Jul	0	0	1.271	0	0	0	0	1.36	0	0
Aug	0	0		0	0	0	0	1.36	0	0
Sep	0	0	0	0	0	0	0	0	0	0
Oct	0	0	0	0	0	0	0	0	0	0
Nov	0	0	0	0	0	0	0	0	0	0
Dec	0	0	0	0	0	0	0	0	0	0
Total	5.65	5.063	11.975	4.041	4.441	6.68	6.49	11.72	4.95	0.98
∑. Vol./100ha	31.17					30.82				
Σ. Vol./1ha	0.31					0.30				

Conclusions

The present paper is intended to estimate, temperature (T), Rainfall (P), reference evepotranspiration (ETo) and in turn Crop Water Requirements (CWR) during (2020-2100) under RCPs 4.5 for Zanzibar Island, Tanzania state. The overall specific conclusion drawn from the current study revealed that:

1- Future temperatures are projected to rise on Zanzibar with increases of 1.3 to 2 °C by the 2050s and 1.8 to 3.1°C by the 2100 relative to the baseline period (1983–2013).
2- There are trends projected of increasing rainfall during the wet season (Mar-May), and an increase in January and February with extreme floods. There is also a trend of decreasing rainfall during the dry season (June – October) with occurring drought periods.
3- During the rainfall season, the temperature will decrease and the humidity will increased. Due to the rising humidity, the estimated evapotranspiration will decrease in the future.
4- Probable floods might occur in the periods 2024, 2057 to 2061 and 2092 to 2095.
5- Overall, The CWR volumes for rice, tomato, banana, watermelon and maize is projected to increased by 10.72%, 12.68%, 27.31%, 3.99%, 2.87% and 30.88%, 28.20%, 24.63%, 27.38%, 23.93% respectively by 2050 and 2100 respectively . relative to the baseline year 2020.
6- The sum of CWR for the identified crops will be increase by 12.6% and 28.7% by 2050 and 2100 years, respectively, compared to those culculated for the year 2020.

6. REFERENCES

[1] Intergovernmental Panel on Climate Change (IPCC), "Climate change 2013: The Physical Science Basis", Contribution of working group 1 to the forth Assessment Report of Intergovernmental Panel on climate change. Cambridge University Press, UK.), (2013),

[2] Zhang, H.; Zhang, L.L.; Li, J.; An, R.D.; Deng, Y. Climate and Hydrological Change Characteristics and Applicability of GLDAS Data in the Yarlung Zangbo River Basin, China. Wate,r (2018),

[3] Moss, R., Babiker, M., Brinkman, S., Calvo, E., Carter, T.R., Edmonds, J., Elgizouli, I., Emori, S., Erda, L., Hibbard, K., Jones, R., Kainuma, M., Kelleher, J., Lamarque,J-F., Manning, M.R., Matthews, B., Meehl, J., Meyer, L., Mitchell, J.F.B., Nakicenovic, N., O'Neill, B., Pichs, R., Riahi, K., Rose, S.K., Runci, P., Stouffer, R.J., van Vuuren, D.P., Weyant, J.P., Wilbanks, T.J., van,Y.,persele, J.P., Zurek, M., , "Towards new scenarios for analysis of emissions, climate change, impacts, and response strategies", IPCC Expert Meeting Report, 19–21 September 2007. Noordwijkerhout, The Netherlands, (2008), pp: 155.

[4] Moss, R.H., Edmonds, J.A., Hibbard, K.A., Manning, M.R., Rose, S.K., van Vuuren, D.P., Carter, T.R., Emori, S., Kainuma, M., Kram, T., Meehl, G.A., Mitchell, J.F.B., Nakicenovic, N., Riahi, K., Smith, S.J., Stouffer, R.J, Thomson, A.M., Weyant, J.P., Wilbanks, T.J "The next generation of scenarios for climate change research and assessment",
Nature, Vol.463(7282), ., (2010), pp: 747–756.

[5] Van Vuuren, D.P., Edmonds, J., Kainuma, M.L.T., Riahi, K., Thomson, A., Matsui, T., Hurtt, G., Lamarque, J-F., Meinshausen, M., Smith, S., Grainer, C., Rose, S., Hibbard, K.A., Nakicenovic, N., Krey, V., Kram, T., "Representative concentration pathways: An overview", Climatic Change(2011a).

[6] ZAINAB H., MOYO, "Vulnerability Of Rain-Fed Paddy Producing Households To Climate Change And Variability: A Case Of North 'B' District, Unguja" (2013).

[7] Johnson, F. and Sharma, A "Accounting for interannual variability: A comparison of options for water resources climate change impact assessments", Water Resour. Res., Vol.47, W04508. (2011).

Technical and environmental performance investigation of Marine Alternative fuels

Mostafa A. El-Manzalawy [1, a], Mohamed M. ElGohary[1, b], Maged M. AbdElnaby[1, c]

[1]*Department of Naval Architecture and Marine Engineering, Faculty of Engineering, Alexandria University, Alexandria, Egypt*

[a] Mostafa_211177@yahoo.com, [b] *Mohamed.elgouhary@alexu.edu.eg,* [c]*maged.abdelnaby@alexu.edu.eg*

Keywords: *Ship emissions reduction, IMO regulations, Natural gas, Methanol, Energy Efficiency*

Abstract. Environmental issues, for example, the expanded air pollutant emissions from ships are progressively affecting the operation of ships. Therefore, International Maritime Organization (IMO) has adopted many goals to decarbonizing the shipping industry by at least 40% by 2030. Marine fuels play a major role in these goals because of the emissions resulting from the combustion process. Therefore, the present research proposes to convert the conventional engine operated by marine diesel oil (MDO) to a dual-fuel engine operated by either natural gas (NG) or methanol. As a case study, A15-class container ship is investigated. The results showed that the dual-fuel engine operated with (98.5% NG and 1.5% MDO) will reduce CO_2, SOx, and NOx emissions by 28%, 98% and 85%, respectively when compared with their values for conventional diesel engine. On the other hand, the reduction percentages reach to 7%, 95% and 80% when using a dual-fuel engine operated with (95% Methanol and 5% MDO), respectively. The proposed dual-fuel engines operated by either NG and methanol will imrove the ship energy efficiency index by 26% and 7%, respectively.

Introduction

Currently, there are several legislations in addition to many goals adopted by the International Maritime Organization (IMO) to reduce greenhouse gases (GHG) and achieve a blue economy [1]. One of those goals is to reach a 50 percent reduction in the percentage of GHG emitted from ships by 2050 compared to 2008 [2]. There are several mechanisms that can be followed to reduce GHG from ships, include ship design, propulsion systems, alternative fuels [3–6] and renewable energy [7]. Among these methods, alternative fuels of less carbon content are considered one of the best ways to reduce the GHG emitted from ships. The main alternative marine fuel types may be found in two forms: liquid and gaseous fuels. Liquid marine alternative fuels include Methanol, Ethanol, and Bio liquid fuel. On the other hand, the main alternative gasses fuels include Natural gas, Propane, Hydrogen, and Ammonia [8].

Two alternative types will be considered throughout the present project, mainly: Natural gas (NG) and Methanol. Selection of the previous types is the matter of searching for alternative fuels that have less emissions to be applied on board ships in the short term. Methanol has been investigated as an alternative marine fuel in previous research projects such as Swedish EffShip [9], SPIRETH project [10], and Methaship,. Some studies by [11,12] has been carried to evaluate the applicability of using methanol as an alternative marine fuel. Another research by [13] shows that methanol reduce exhaust emissions by a considerable amount and reduce the fuel cost.

The primary segment of natural gas is methane (CH_4), this fuel is the least carbon and sulfur content and consequently with the most promising option to decrease carbon dioxide (CO_2) and Sulfur dioxide (SOx) emissions [5]. Besides, the burning of natural gas in comparison with diesel is characteristically cleaner regarding Nitrogen oxide (NOx). Moreover, natural gas appears as a

financially motivating measure for vessel types spending a long period of their cruising time like handy size tankers, RO-RO vessels, and container ships [4].

All the previous studies, whether research projects or research papers that dealt with the importance of alternative fuels usage onboard ships, confirm that the maritime industry has not benefited the most from alternative fuels. Moreover, it confirms the necessity of conducting many other studies to determine the potential benefits from alternative fuel onboard ships from technical and environmental point of view.

The present research aims at assessing the environmental and technical performance of the proposed alternative fuels (natural gas and methanol). As a case study, A15-class container ship is investigated. The assessment is based on a comparative study between alternative fuels and conventional diesel fuel from environmental and energy efficiency point of view.

Environmental and technical assessment method

The environmental assessment can be performed by calculating the exhaust emissions from ships in case of using the proposed alternative fuels compared with the conventional diesel fuel. The emissions from ships included many kinds of pollutants such as CO_2, SOx and NOx emissions.

The quantity of exhaust emission during one trip (M_{trip}) can be calculated by using Eq. (1) which depending on the engine power.

$$M_{trip,i} = \sum_i MCR_i * L_i * T * E_p \quad (1)$$

Where (MCR) is the maximum continuous rating power of engine in [kW], (i) is the type of engine (main engine or auxiliary engine), L is the load factor of engine and T is the operating time of ship in [hour], and (E_p) is the pollutant emission factor in an energy based form [g pollutant/kWh] [14,15].

The individual emission energy-based rate in differs from type to another. In case of CO_2 emission, it is based on the conversion factor between fuel and CO_2 which depend on the carbon content in fuel, therefore, its value differs from fuel to another. Table 1 show the conversion factor values for different fuels [4].

Table 1 Conversion factors and carbon contents for marine fuels

Fuel type	Carbon content	Conversion factor (g CO_2/ g fuel)
Marine Diesel oil (MDO)	0.8744	3.206
Heavy fuel oil (HFO)	0.8493	3.114
Liquefied natural gas (LNG)	0.75	2.75
Methanol	0.37	1.375

The energy-based rate of CO_2 emission (E_{CO2}) measured in g CO_2/kWh can be calculated using Eq. (2) based on specific fuel consumption (SFC) in g fuel /kWh and the conversion factor CF).

$$E_{CO2} = SFC \times CF \quad (2)$$

Regarding the air pollution emission inventory recommendation from IMO, NOx emission factor expressed in g/kWh for slow speed diesel engine depends on the ship construction date [4]. The first level of control (Tier I) applies for ships constructed on 1 January 2000 or after and can be calculated as shown in Eq. (3) which depends on the engine's rated speed (n).

$$E_{NOx} = 45 \times n^{-0.2} \quad (3)$$

A slow speed diesel engine (SSDE) that is installed on a ship constructed on 1 January 2011 or after (Tier II), a reduction equal to 15% should be fulfilled compared with Tier I NOx emission value [14]. On the other hand, NOx emission factor for natural gas engine and methanol engine is 2.16 g/kWh and 2.47 g/kWh, respectively [4,13].

On the other hand, SOx is proportional to SFC and the content of sulfur in the fuel (S) so that the SOx emission energy-based rate (E_{SOx}) can be calculated by Eq. (4) [8,16,17].

$$E_{SOx} = SFC \times 2.1 \times (S\%) \quad (4)$$

It is seen that lower the sulfur content in fuel is led to reducing the specific emission rate of SOx, which is the reason why more and more strict demands towards lower sulfur content in marine fuel. In case of dual-fuel engine, the emission factor should be evaluated by considering the percentage of each fuel as shown in Eq. (5) [4].

$$E_{p,DF} = x_{gas} \times E_{p,gas} + x_{P.F} \times E_{p,P.F} \quad (5)$$

Where, x_{gas} and $x_{P.F}$ are the percentages of gas and pilot fuels in the dual-fuel engine (DF), E_{gas} and $E_{P.F}$ are the pollutant (p) emission factors for gas and pilot fuels, respectively.

The technical performance can be assessed by using the procedure recommended from IMO through the calculation of Energy Efficiency Design Index (EEDI) [8]. EEDI has two indexes, a restrictive value ($EEDI_{req}$) and the actual value ($EEDI_{att}$) which should be lower than the restrictive value. The restrictive value depends on the ship type and its deadweight (DWT); therefore, Eq. (6) should be used for the calculation of $EEDI_{req}$ in case of container ship.

$$EEDI_{req} = \left(\frac{174.22}{DWT^{0.201}}\right) \times \left(1 - \frac{X}{100}\right) \quad (6)$$

Where (X) is the reduction rate of baseline value each five years as recommended from IMO; 10% in phase 1 (2015-2019), 20% in phase 2 (2020-2024) and 30% in phase 3 (2025-onwards) [3,18].

On the other hand, the actual value is a measure of energy efficiency level for the specified ship and can be calculated as shown in Eq. (7). For the dual-fuel engine, the product of ($SFC_{ME} \times CF_{ME}$) can be calculated by using Eq. (8) depending on the SFC and CF of either gas fuel and pilot fuel [4].

$$EEDI_{att} = \frac{(P_{ME} \times SFC_{ME} \times CF_{ME}) + ((0.025 \times MCR_{ME} + 250) \times SFC_{AE} \times CF_{AE})}{Capacity \times V_{ref}} \quad (7)$$

$$SFC_{ME} \times CF_{ME} = SFC_{gas} \times CF_{gas} + SFC_{P.F} \times CF_{P.F} \quad (8)$$

Where (P_{ME}) is 75% of MCR for each main engine (ME) in kW, (V_{ref}) is the operational ship speed in knots and (capacity) is 70% of the container ship deadweight. The auxiliary engine (AE) power necessary to operate the main engine and the crew accommodation is based on the MCR of the main engine in case of using an engine of more than 10,000 kW as shown in Eq. (7) [4,19].

Case study description

The case study for the assessment process of energy efficiency and environmental impacts is selected to be A15-class container ship. The container ship (Al Jmeliyah) is owned to United Arab shipping company limited Dubai branch and operated by Hapag-Lloyd, Hamburg [20]. The ship was built in 2017 and sailing under the flag of Marshall Islands. Table 2 shows the technical data of the ship [21].

Table 2 Main specifications of the studied container ship

Ship type	A15-class container ship
IMO number	9732357
Length overall, [m]	368
Breadth, [m]	51
Service speed, [knots]	24
Deadweight, [ton]	149360
Container capacity, TEU	14993
Main Engine type	2×Hyundai-MAN B&W 9S90 ME-C
MCR power, [kW]	2×37,620 kW at 72 RPM

The vessel normally serves the Far East route from Asia to Northern Europe through the Suez Canal. The average time for each trip is 47 days from Busan in Asia to Hamburg in Northern Europa [22].

The ship is currently powered by a two SSDE (MAN 9S90 ME-C) with an output of 37,620 kW at 72 rpm which operated with marine diesel oil (0.5% S). The main engine is proposed to be converted to 9G80ME-C10.5-GI dual-fuel engine (DFE) with the same power and speed operated by natural gas and 1.5% MDO as a pilot fuel. On the other hand, it is proposed to be converted to MAN B&W ME-LGI dual-fuel engine that can run on methanol and 5% MDO as a pilot fuel. The proposed engine's cylinder head is equipped with two valves for gas injection and two conventional valves for the pilot fuel oil. ME-GI has the same efficeincy, power and dimensions of ME-C. Based on Hapag-Lloyd reports, around 350 container sites will be lost for the additional gas storage system [23].

Results and discussions

The environmental performance can be assessed by evaluating the exhaust emission rates per trip. The examined emission types are CO_2, SOx, and NOx, as these types are related with IMO regulations. The assessment process depends on the comparative study between the proposed dual-fuel engine operated with natural gas or methanol and the conventional SSDE operated with MDO (0.5%S). The first step in evaluating the environmental benefits of proposed dual-fuel engine is to calculate the energy-based emissions factors as discussed before. The different emissions rates per trip can be calculated based on the specified trip from Busan to Hamburg. The relative emissions rates of the proposed dual-fuel engine compared to diesel engine are shown in Fig.1.

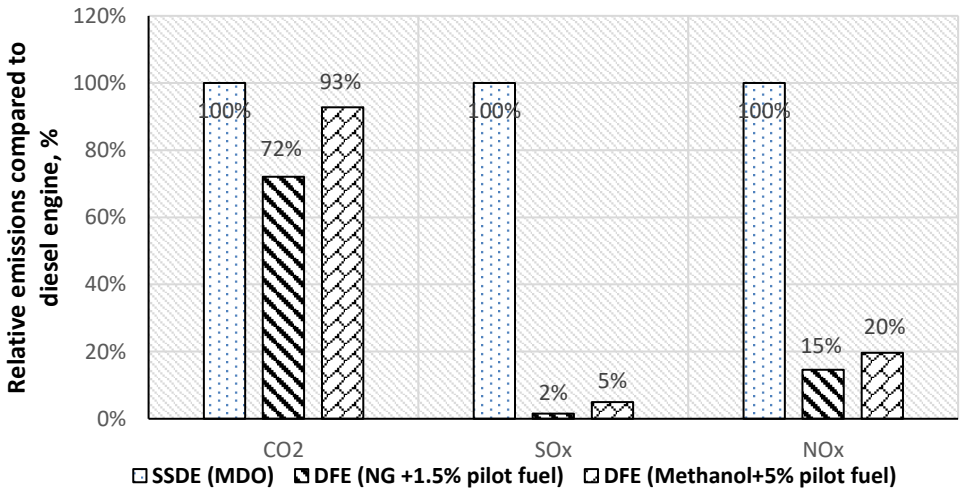

Fig. 1 Relative emissions rates of the proposed dual-fuel engine compared to diesel engine

For the current case study, the emissions rates of SSDE are 39.1 ton/hr, 2.13 kg/min and 20.4 kg/min for CO_2, SOx, and NOx, respectively. These rates are reduced after applying dual-fuel engine (98.5% NG and 1.5% MDO) to 28.2 ton/hr, 0.032 kg/min and 2.97 kg/min with reduction percentages of 28%, 98% and 85%, respectively. These rates are reduced after applying dual-fuel engine (95% Methanol and 5% MDO) to 36.25 ton/hr, 0.107 kg/min and 0.032 kg/min with reduction percentages of 7%, 95% and 80%, respectively.

NOx and SOx emission rates should be compared with the IMO 2016 and 2020 emission-limit rates, respectively [4,8]. IMO 2020 SOx emission limit rate can be predicted based on fuel sulfur content (0.5%) which equals 2.133 kg/min. For the case study, SOx emission rates can be calculated for different pilot fuel percentage in dual-fuel engine to assess the effect of its value on emission rates as shown in Fig.2.

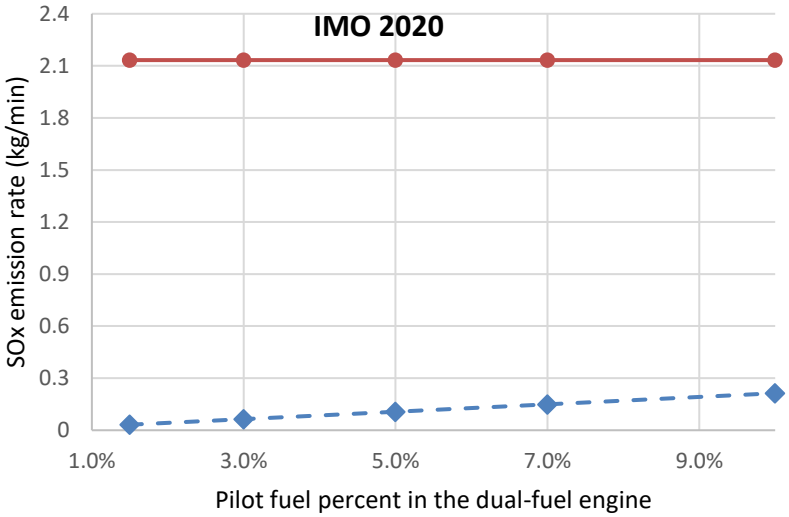

Fig. 2 SOx emission rates at different pilot fuel percentages

It can be noticed that SOx emissions rates for dual-fuel engine are compliant with IMO 2020 limit at different pilot fuel percentage.

IMO 2016 NOx emission limit rate can be predicted based on engine speed which equals 4.26 kg/min. For the dual-fuel engine operated by natural gas and pilot fuel, NOx emissions rates can be calculated for different pilot fuel percentages to evaluate the impact of its value on emission rates as shown in Fig.3.

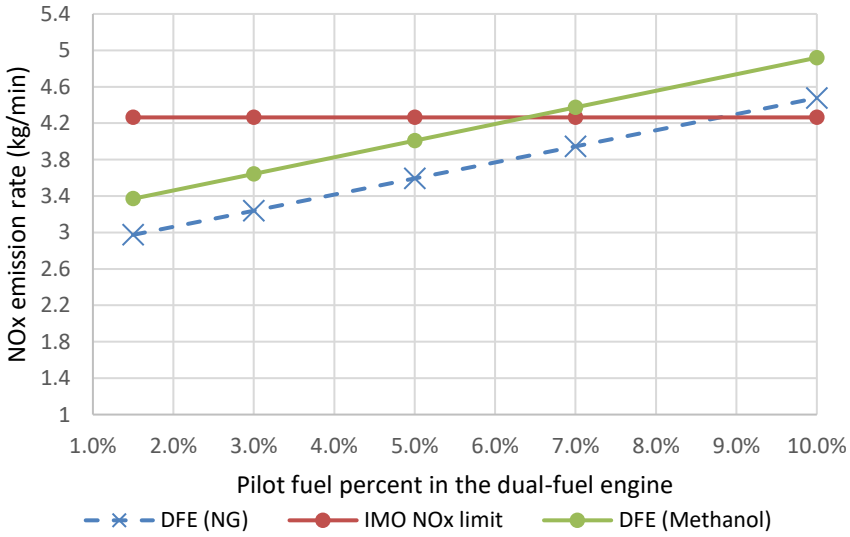

Fig. 3 NOx emission rates at different pilot fuel percentages

As shown in Fig.3, the dual-fuel engine operated by natural gas and methanol will be compliant with the required IMO limit if the percentage of pilot fuel is lower than 8.8% and 6.4%, respectively.

Furthermore, the energy efficiency can be assessed by the calculation of EEDI for the proposed dual-fuel engine as recommended by IMO. By conducting the reference EEDI procedure to the case study, it is shown that the reference EEDI and its value in the three phases can be calculated based on the deadweight of the container ship as investigated in Fig. 4.

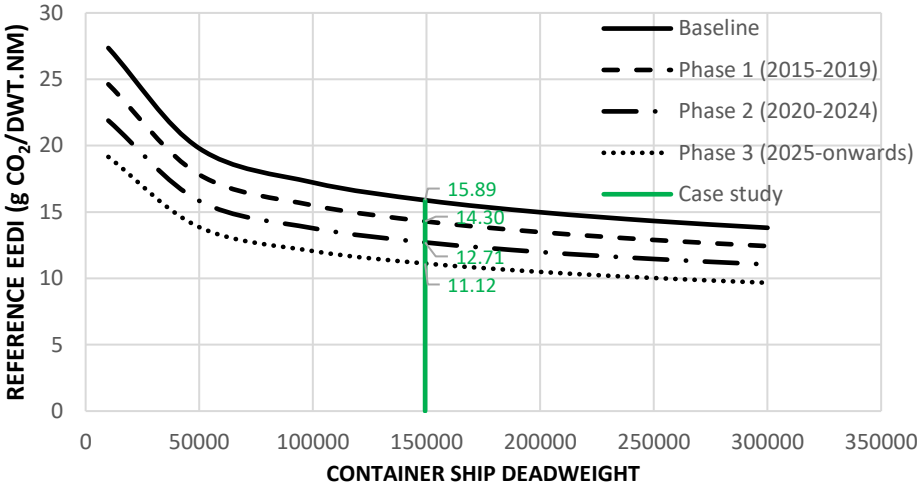

Fig. 4 Reference EEDI values for Container ship

This reference value will be compared with the actual attained EEDI for the case study powered by SSDE which can be calculated by using Eq. (7) based on 24 knots service speed, 3.206 ton-CO_2/ton-fuel conversion factor of fuel to CO_2. The attained EEDI will be 11.91 g CO_2/DWT-NM. It is noticed that the current EEDI of SSDE is fulfilling the EEDI requirement until phase 2 but must be reduced to comply with EEDI phase 3.

To evaluate the energy efficiency benefits for the selected dual-fuel engine operated by either natural gas or methanol, attained EEDI should be calculated. Based on Eq. (7) and Eq. (8), the attained EEDI for dual-fuel engine (98.5% NG and 1.5% MDO) and (95% Methanol and 5% MDO) is 8.77 gCO_2/DWT-NM and 11.07 g CO_2/DWT-NM, respectively. To assess the results, it should be compared with the reference EEDI at different phases as shown in Fig.5.

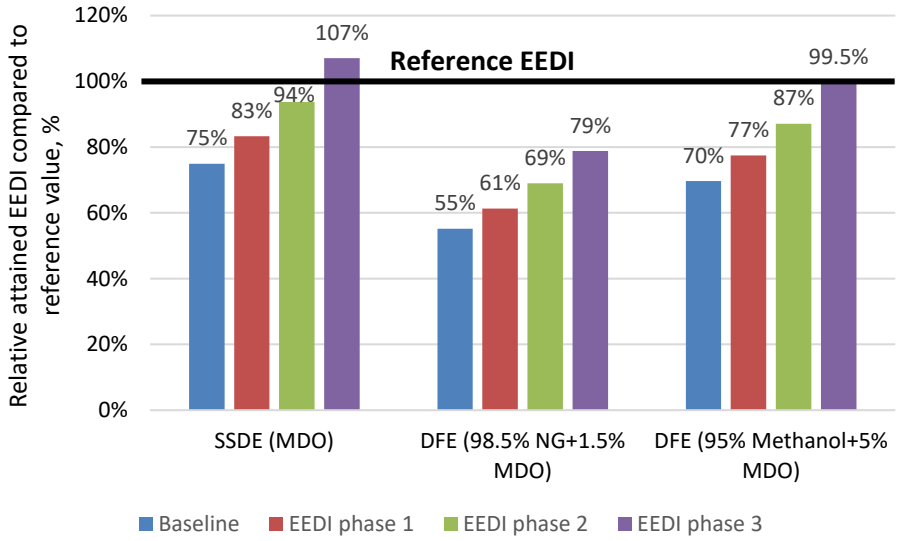

Fig. 5 Relative attained EEDI compared to reference value at different phases

It is shown that, the proposed dual-fuel engine operated by (98.5% NG and 1.5% MDO) will comply with the required IMO phases now and in the future as the attained EEDI is about 61%, 69% and 79% of the reference EEDI at phase 1, phase 2 and phase 3, respectively. On the other hand, the proposed dual-fuel engine operated by (95% Methanol and 5% MDO) will comply with IMO phase 1 and phase 2 as it is about 77% and 87% of the reference EEDI value, respectively. While it will comply with the required IMO phase 3 by a small percentage, as the attained EEDI will reach 99.5% of the required EEDI.

Conclusions

The application of dual-fuel engine operated by natural gas or methanol on A15-class container ship has been investigated from environmental and energy efficiency point of view. The main conclusions from the current study are:

- From environmental point of view, using dual-fuel engine operated with 98.5% NG and 1.5% MDO will comply with the required IMO emissions regulations. This will lead to reductions in CO_2, SOx, and NOx emissions by 28%, 98% and 85%, respectively when compared with their values for SSDE operated by MDO (0.5%S). While the another proposed dual-fuel engine operated by 95% Methanol and 5% MDO will lead to reductions by 7%, 95% and 80%, respectively. Furthermore, the dual-fuel engine operated by natural gas and methanol will be compliant with the required IMO limit if the percentage of pilot fuel is lower than 8.8% and 6.4%, respectively.
- From energy efficiency point of view, the dual-fuel engine operated by (98.5% NG and 1.5% MDO) will comply with the required IMO EEDI phases now and in the future. On the other hand, the dual-fuel engine operated by (95% Methanol and 5% MDO) will comply with IMO EEDI phase 1, phase 2, and phase 3 by about 77%, 87%, and 99.5% of the reference EEDI value, respectively.

References

[1] H.. Psaraftis, C.A. Kontovas, Decarbonization of Maritime Transport : Is There Light at the End of the Tunnel ?, Sustainability. 13 (2021) 237. https://doi.org/10.3390/su13010237.

[2] T.-H. Joung, S.-G. Kang, J.-K. Lee, J. Ahn, The IMO initial strategy for reducing Greenhouse Gas(GHG) emissions, and its follow-up actions towards 2050, J. Int. Marit. Safety, Environ. Aff. Shipp. 4 (2020) 1–7. https://doi.org/10.1080/25725084.2019.1707938.

[3] M.M. El Gohary, N.R. Ammar, Thermodynamic analysis of alternative marine fuels for marine gas turbine power plants, J. Mar. Sci. Appl. 15 (2016) 95–103. https://doi.org/10.1007/s11804-016-1346-x.

[4] A.G. Elkafas, M.M. Elgohary, M.R. Shouman, Numerical analysis of economic and environmental benefits of marine fuel conversion from diesel oil to natural gas for container ships, Environ. Sci. Pollut. Res. 28 (2021) 15210–15222. https://doi.org/10.1007/s11356-020-11639-6.

[5] M.M. Elgohary, I.S. Seddiek, A.M. Salem, Overview of alternative fuels with emphasis on the potential of liquefied natural gas as future marine fuel, Proc. Inst. Mech. Eng. Part M J. Eng. Marit. Environ. 229 (2015) 365–375. https://doi.org/10.1177/1475090214522778.

[6] Y.M.A. Welaya, M.M.E. Gohary, N.. Ammar, A comparison between fuel cells and other alternatives for marine electric power generation, Int. J. Nav. Archit. Ocean Eng. 3 (2011) 141–149.

[7] I. Sadek, M. Elgohary, Assessment of renewable energy supply for green ports with a case study, Environ. Sci. Pollut. Res. 27 (2020) 5547–5558. https://doi.org/10.1007/s11356-019-07150-2.

[8] A.G. Elkafas, M. Khalil, M.R. Shouman, M.M. Elgohary, Environmental Protection and Energy Efficiency Improvement by using natural gas fuel in Maritime Transportation, Environ. Sci. Pollut. Res. (2021). https://doi.org/10.1007/s11356-021-14859-6.

[9] SSPA, EffShip- Efficient Shipping with low emissions, (2013). https://www.sspa.se/environment-and-energy-efficiency/effship-project.

[10] J. Ellis, B. Ramne, Activities and Outcomes of the SPIRETH (Alcohol (Spirits) and Ethers as Marine Fuel) Project, Nord. ENERGI SKNING. (2014) 51.

[11] K. Andersson, S. Brynolf, J. Hansson, M. Grahn, Criteria and Decision Support for A

Sustainable Choice of Alternative Marine Fuels, Sustainability. 12 (2020). https://doi.org/10.3390/su12093623.
[12] J. Dierickx, J. Beyen, R. Block, M. Hamrouni, P. Huyskens, C. Meichelböck, Strategies for introducing methanol as an alternative fuel for shipping, in: Proc. 7th Transp. Res. Arena TRA, Vienna, Austria, 2018.
[13] N.R. Ammar, An environmental and economic analysis of methanol fuel for a cellular container ship, Transp. Res. Part D Transp. Environ. 69 (2019) 66–76. https://doi.org/10.1016/j.trd.2019.02.001.
[14] N.R. Ammar, I.S. Seddiek, Enhancing energy efficiency for new generations of containerized shipping, Ocean Eng. 215 (2020) 107887. https://doi.org/10.1016/j.oceaneng.2020.107887.
[15] N.R. Ammar, A.G. Elkafas, M.M. Elgohary, A. Zeid, Prediction of Shallow Water Resistance for a New Ship Model Using CFD Simulation: Case Study Container Barge, J. Sh. Prod. Des. 35 (2019) 198–206. https://doi.org/https://doi.org/10.5957/jspd.11170051.
[16] ICF, Current Methodologies in Preparing Mobile Source Port-Related Emission Inventories, U.S. Environ. Prot. Agency. (2009).
[17] EPA, Analysis of Commercial Marine Vessel Emissions and Fuel Consumption Data, Energy Environ. Anal. Inc. (2000).
[18] A.G. Elkafas, M.M. Elgohary, A.E. Zeid, Numerical study on the hydrodynamic drag force of a container ship model, Alexandria Eng. J. 58 (2019) 849–859. https://doi.org/10.1016/j.aej.2019.07.004.
[19] IMO, MEPC 308(73): 2018 guidelines on the method of calculation of the attained Energy Efficiency Design Index (EEDI) for new ships, London, 2018.
[20] DNV GL, AL JMELIYAH, DNV GL Vessel Regist. (2021). https://vesselregister.dnvgl.com/VesselRegister/vesseldetails.html?vesselid=34186 (accessed May 25, 2021).
[21] Hapag-LIoyd, Al Jmeliyah ship, Hapag-Lloyd Vessel. (2021). https://www.hapag-lloyd.com/en/products/fleet/vessel/al_jmeliyah.html (accessed April 20, 2021).
[22] Hapag-Lloyd, Far East Loop 2, Servie Finder. (2021). https://www.hapag-lloyd.com/en/service-finder/bydeparture.html/asia/north_europe/FE2.html (accessed April 25, 2021).
[23] Peter Pospiech, Marine Fuel: World First for Megaboxer MV Sajir, Mar. Link. (2019). https://www.marinelink.com/news/marine-fuel-world-first-megaboxer-mv-466448 (accessed April 27, 2021).